Wissenschaftliche Mitteilungen

aus dem
Institut für Meteorologie der Universität Leipzig

ISBN **978-3-9811114-8-4**

Meteorologische Arbeiten (XVI) und Jahresbericht 2010 des Instituts für Meteorologie der Universität Leipzig

Hrsg.: Armin Raabe

Leipzig 2011

Band 48

Wissenschaftliche Mitteilungen aus dem Institut für Meteorologie der
Universität Leipzig Bd. 48

Wissenschaftliche Mitteilungen aus dem Institut für Meteorologie der Universität Leipzig, Band 48

Wissenschaftliche Mitteilungen aus dem Institut für Meteorologie der
Universität Leipzig Bd. 48

Acoustic measurements in air - A model apparatus for education and testing

M. Barth, G. Fischer, A. Raabe

Summary

The speed of sound in air mainly depends on temperature and flow properties along the propagation path of acoustic signals. In turn, distributions of these quantities can be determined from sound speed measurements along different propagation paths. In this article, a modular measurement system is presented which is suited to demonstrate the effects of surrounding conditions on the speed of sound, e.g. for educational purposes, and which can be used for an easy testing of new hardware components or algorithms. Underlying mathematical relations are explained and uncertainties are discussed. A sample application of the system within a laboratory shows the effect of local heating on the sound speed along several propagation paths which differ in their spatial distribution with respect to the heating source.

Zusammenfassung

Die Schallgeschwindigkeit in Luft hängt maßgeblich von der Temperatur und den Strömungsverhältnissen entlang des Ausbreitungsweges akustischer Signale ab. Diese Abhängigkeit kann genutzt werden, um räumliche Verteilungen dieser Atmosphärenparameter aus Messungen der Schallgeschwindigkeit entlang verschiedener Wege durch ein Untersuchungsgebiet zu bestimmen. In diesem Artikel wird ein modular aufgebautes Messsystem vorgestellt. Dieses kann zum Beispiel in der Ausbildung genutzt werden, um den Effekt der Umgebungsbedingungen auf die Ausbreitungsgeschwindigkeit akustischer Signale zu demonstrieren. Es ist jedoch ebenfalls geeignet, um neue Algorithmen oder Hardwarekomponenten zu untersuchen. Die zugrundeliegenden mathematischen Zusammenhänge werden vorgestellt und resultierende Unsicherheiten werden diskutiert. Eine Beispielanwendung des Messsystems im Labor zeigt anschaulich den Effekt, den eine lokal begrenzte Heizquelle auf die Schallgeschwindigkeit entlang verschiedener Schallwege hat, die sich hinsichtlich ihrer räumlichen Nähe zur Heizquelle unterscheiden.

1 Introduction

The speed with which acoustic signals propagate in air depends on the properties along the propagation path. In particular, temperature and flow influence the speed of sound. This dependence can be used to estimate average temperature and flow properties along a sound propagation path from sound speed measurements between a source and a receiver. Subsequently, measurements along distinct paths through an area permit an estimation of spatially distributed temperature and flow fields using tomographic reconstruction techniques.
Such reconstruction techniques are widely used, especially in medicine (e.g. magnetic resonance tomography, computer tomography), but also in materials science (e.g. non-destructive testing of materials) or for geophysical investigations. In the last-

mentioned field of application, the method is used, e.g., to investigate the structure of the Earth's interior (Menke, 1989, Aki and Richards, 2002), the properties of water bodies in oceanography (Munk et al., 1995) or to perform atmospheric investigations (Arnold, 2000, Ziemann, 2000). The basic principle of all tomographic techniques is to reconstruct two- or three-dimensional distributions from line integrated measurements. Hereby, a sounding signal or energy has to be used (which may be actively generated), which is noticeable changed according to the properties along the propagation path.
In atmospheric sciences tomographic techniques are used to remotely measure distributions of temperature and flow properties within a definite area or volume. Detailed reviews on the method, its progress and potential applications are given by Wilson et al. (2001) and Ostashev et al. (2009). An advantage of the method is that no sensors have to be inserted into the area under investigation which might influence the properties of the flow field. In addition, measured temperature values are not influenced by technical properties of the sensor, like effects of radiation. Furthermore, a spatial distribution of parameters (e.g. volume or area averaged values) is estimated which meets the demands of input data for model calculation.
For testing and demonstration a model apparatus has been developed which is suited to test new hardware and software components and which can be used to vividly show the effect of temperature and flow on the propagation speed of acoustic signals. In this article a two-dimensional application of the model apparatus in the laboratory is presented. Thereby, the main focus is on the demonstration of the effect of local heating on the speed of sound along different propagation paths. For this purpose, at first, the theoretical background of sound speed dependencies in air is given. Secondly, uncertainties of the method are discussed. After that, the measurement configuration is shortly described which was used to take the measurements presented in section 5. Reconstructed distributions of temperature and flow fields using tomographic methods are not a primary objectives of this article. Thus, only a brief overview on this topic is given. For further information, the reader is referred to, e.g., Barth (2009) and Barth et al. (2007) for two-dimensional applications or Barth and Raabe (2011) for a three-dimensional set-up of sensors using the model apparatus.

2 Theoretical Background

The acoustic travel time tomographic system is based on the dependency of the speed of sound in air on temperature, flow properties, and to a small extent on humidity, along the sound propagation path. Temperature (as well as humidity) has a scalar influence on the speed of sound, the warmer the air (the more water vapour the air contains) the faster the sound travels, while wind has a vectorial influence: sound travels faster in downwind direction and slower in adverse winds. In the next sections, most important mathematical relations concerning sound speed calculation and subsequent sensitivity estimations are given.

2.1 Sound propagation in air

In a motionless atmosphere, acoustic waves propagate with adiabatic or Laplace sound speed $c_{\mathrm{L}}^2 = \gamma R_{\mathrm{s}} T$, where T is the air temperature along the propagation path, γ is the ratio between specific heat capacities at constant pressure and constant volume

($\gamma = c_p / c_v$) and R_s is the specific gas constant. The latter two quantities depend on the predominant composition of the medium through which the sound propagates. For tropospheric investigations, the composition of dry air can be assumed to be nearly constant. The only constituent which can vary considerably is water vapour. Anyhow, to use constant gas-specific quantities (R_s and γ) for dry air (index d), the acoustic virtual temperature T_{av} is introduced. This temperature includes the influence of the varying water vapour content and is given by

$$T_{av} = T(1 + 0.513q), \tag{1}$$

where q is the specific humidity.
Thus, the speed of sound in a motionless atmosphere is given by

$$c_L^2 = \gamma_d R_d T_{av}, \tag{2}$$

with γ_d = 1.4 and R_d = 287.05 J kg^{-1} K^{-1}.
For further considerations, it is premised that sound propagation takes place along discrete sound propagation paths, referred to as sound rays (geometric acoustics model). This assumption is valid as long as the wavelength of the acoustic signals is much shorter than the spatial extension of the measurement site and inhomogeneities within the medium.
Now, sound propagation in moving air is considered. When the air is moving with velocity **v**, the wave velocity c_L **n** seen by someone moving with the fluid becomes **v** + c_L **n** in a coordinate system at rest. Here **n** is the unit vector normal to the wavefront and **v** = u **i** + v **j** + w **k** denotes the flow vector where **i**, **j** and **k** are the basis unit vectors of a Cartesian coordinate system and (u, v, w) are the flow components in the corresponding directions. Thus, as illustrated in Figure 1, the velocity of sound propagation along the sound ray path $\mathbf{c}_{ray}$ is given by $\mathbf{c}_{ray}(T_{av}, \mathbf{v}) = c_L(T_{av})\mathbf{n} + \mathbf{v}$ (Pierce, 1989; Ostashev, 1997). From this, the sound speed along the sound ray path, c_{ray}, can be estimated to be $c_{ray} = |\mathbf{c}_{ray}| = \mathbf{s} \cdot \mathbf{c}_{ray} = c_L \mathbf{s} \cdot \mathbf{n} + \mathbf{s} \cdot \mathbf{v}$, where **s** is the unit vector in the direction of sound propagation. Provided that |**v**| « c_L, the scalar product **s** · **n** ≈ 1. Thus, the sound speed along the sound propagation path, also referred to as effective sound speed c_{eff}, is given by

$$c_{ray} \approx c_L + v_r = c_{eff} \tag{3}$$

with v_r being the flow velocity in the direction of sound propagation.
For further analyses the two influencing factors on the speed of sound, acoustic virtual temperature and flow, are separated utilising the different character of the quantities. Whereas temperature influences the speed of sound independently from the direction of sound propagation, the effect of air movement depends upon direction. Thus, to separate the influences, sound propagation in opposing directions is considered.
Ideally, reciprocal sound transmission (same sound ray paths for forward and backward sound transmission) should be applied. This requires that acoustic transmitters can act as sound sources as well as sound receivers.

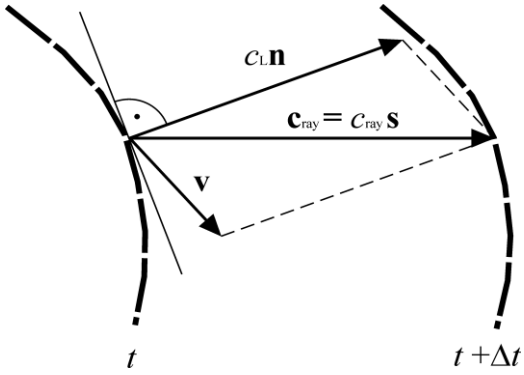

Figure 1: Acoustic signal propagating in a moving atmosphere indicated by its wavefront (dashed lines) at times t and t+Δt. The sound velocity along the ray path $\mathbf{c}_{ray}$ *depends on Laplace sound speed* c_L *and flow velocity* $\mathbf{v}$*. The vectors* $\mathbf{n}$ *and* $\mathbf{s}$ *are unit vectors normal to the wavefront and tangent to the sound ray path, respectively.*

Now, the Laplace content can be separated by summing up the effective sound speed values in forward (index: 1) and backward (index: 2) direction, while the flow value along the ray path is obtained by subtracting the effective sound speed values. Given a definite distance d between acoustic transmitters, measured travel times τ can be used to estimate the effective sound speed

$$c_{\text{eff}} = \frac{d}{\tau} \tag{4}$$

along the sound ray path. From this, the Laplace sound speed and the flow velocity along the ray path can be calculated

$$c_{\text{L}} = \frac{1}{2}\left(c_{\text{eff},1} + c_{\text{eff},2}\right) = \frac{d}{2}\left(\frac{1}{\tau_1} + \frac{1}{\tau_2}\right) \qquad v_{\text{r},1} = \frac{1}{2}\left(c_{\text{eff},1} - c_{\text{eff},2}\right) = \frac{d}{2}\left(\frac{1}{\tau_1} - \frac{1}{\tau_2}\right) = -v_{\text{r},2} \tag{5}$$

For practical reasons, separated speakers and microphones are used resulting in spatially separated sound ray paths. To still separate the influencing factors the sensors are arranged in such a way that pairwise parallel sound propagation paths can be analyzed (bidirectional sound propagation). To minimize errors due to different environmental conditions along the bidirectional sound ray paths, the distance between the ray paths should be as small as possible.

2.2 Sensitivity

According to the mathematical relationship between temperature, humidity and air flow along the propagation path of acoustic signals and the effective speed of sound as described in section 2.1, sensitivity of sound speeds with regard to prevailing atmospheric parameters can be deduced.
First, motionless air is considered. In this case, the effective sound speed equals the Laplace sound speed. Thus, from equations (1) and (2), sensitivity of the speed of sound $u(c_{\text{L}})$ with regard to specific humidity changes $u(q)$ and air temperature changes $u(T)$ can be derived applying the law of error propagation which leads to

$$\begin{aligned} u(c_{\mathrm{L}}) &= \left|\frac{\partial c_{\mathrm{L}}}{\partial T}\right| u(T) + \left|\frac{\partial c_{\mathrm{L}}}{\partial q}\right| u(q) \\ &= \frac{1}{2}\frac{c_{\mathrm{L}}}{T} u(T) + \frac{0.513}{2}\frac{c_{\mathrm{L}}}{(1+0.513q)} u(q) \end{aligned} . \tag{6}$$

Assuming a temperature value of 30 °C (303.15 K), a temperature change of 1 K (which is a comparatively low value) causes a change in sound speed of approximately 0.6 m/s on the one hand. On the other hand, a relative humidity change of 10 % (from 90 % to 100 %) at 30 °C is analyzed. This increase in relative humidity is connected to an increase of specific humidity from 24.0 g/kg to 26.8 g/kg (rise of 2.8 g/kg). This comparably high change results in an increase of the Laplace sound speed of only about 0.2 m/s. From this it can be concluded, that changes in the Laplace sound speed mainly indicate changes in air temperature rather than changes in humidity.
For moving air, sensitivity of the effective sound speed $u(c_{\mathrm{eff}})$ is given by

$$u(c_{\mathrm{eff}}) = \left|\frac{\partial c_{\mathrm{eff}}}{\partial c_{\mathrm{L}}}\right| u(c_{\mathrm{L}}) + \left|\frac{\partial c_{\mathrm{eff}}}{\partial v_{\mathrm{r}}}\right| u(v_{\mathrm{r}}) = u(c_{\mathrm{L}}) + u(v_{\mathrm{r}}) \tag{7}$$

Apparently, a change of the flow component along the sound propagation path v_{r} directly causes a change of the effective sound speed with the same magnitude.

2.3 Tomographic reconstruction

As described in section 2.1, acoustic signals are significantly altered by air properties, especially temperature and flow, along the propagation path. For tomographic reconstruction of distributions from measurements along distinct sound ray paths, algebraic techniques are used as well as stochastic methods.
For algebraic techniques, the area under investigation has to be subdivided into distinct sub-areas (grid cells). Assuming an initial distribution of parameters (e.g. temperatures) for the whole grid, acoustic travel times are calculated for each sound ray path (positions of sources and receivers are known, assumption of straight sound rays). These calculated travel times are compared to the measured values. Based on differences between measured and calculated values, corrections for each grid cell value are calculated in an iterative process until a termination condition (number of iterations or difference between calculated and measured travel time values) is reached. This procedure provides values for discrete sub-areas of the measurement area. Sample applications of such techniques for outdoor investigations can be found in Raabe et al. (2001) and Ziemann et al. (2001) for example.
On the other hand, stochastic inversion (SI) or time dependent stochastic inversion (TDSI) is applied to reconstruct spatially resolved meteorological quantities. Unlike algebraic methods, the distributions reconstructed using SI or TDSI are composed of a mean value within the area under investigation which is calculated first and spatial fluctuations from this mean value at defined points within the tomographic area. For this method additional information on the investigation area, namely the spatial covariance functions of temperature and wind velocity fluctuations, is required (Wilson and Thomson, 1994, Vecherin et al., 2007).

A detailed description of different reconstruction techniques used for tomographic investigations in air, sensitivity studies and sample applications for temperature reconstructions from acoustic measurements can be found in Fischer (2008) and Fischer et al. (2009) or in references therein.

3 Acoustic tomographic system

Acoustic tomographic measurements are performed utilising a standard personal computer (PC) with an acoustic spectrometer card and associated sound sources and receivers. In this section, a short overview of the measurement system is given which is used for testing and demonstration in the laboratory. There are no general restrictions for the method to be limited to indoor applications. Rather, the method itself is scalable. It only has to be ensured that acoustic signals can be properly detected at the receivers to ensure a reliable estimation of travel times. Thus, for longer sound propagation paths, an adjustment of speakers (sound emission) could be necessary.

3.1 Hardware

The core of the acoustic tomographic measurement system is a commercially available acoustic multi-channel spectrometer (SINUS, 2011). This device performs the digital-analogue conversion (DAC) of sound signals which are generated at a PC, the transmission, reception and the analogue-digital conversion (ADC) of the received signals on a common time basis. It operates in the audio range and uses a sampling rate of 51.2 kHz. For the measurements two measurement cards are combined for the use of up to 16 separated receiver channels and 8 separated transmission channels. To apply reciprocal sound transmission for separating temperature and flow influences, an arrangement of 8 source-receiver-pairs around a measurement area of 1.23 m × 1.23 m is built up (Figure 2). For the laboratory set-up 1/4 inch condenser measurement microphones are used as receivers and in-house manufactured speakers are used as transmitters (Barth, 2009).

3.2 Software

The programming environment of MATLAB has been used to develop a modular software package which can be used to generate the sound signals, to control the measurement process, to store received data and to perform subsequent analyses of the acoustic signals up to the plotting of reconstructed distributions. Each module, e.g. the signal generation or the reconstruction algorithm, can easily be changed giving high flexibility for testing and demonstration.

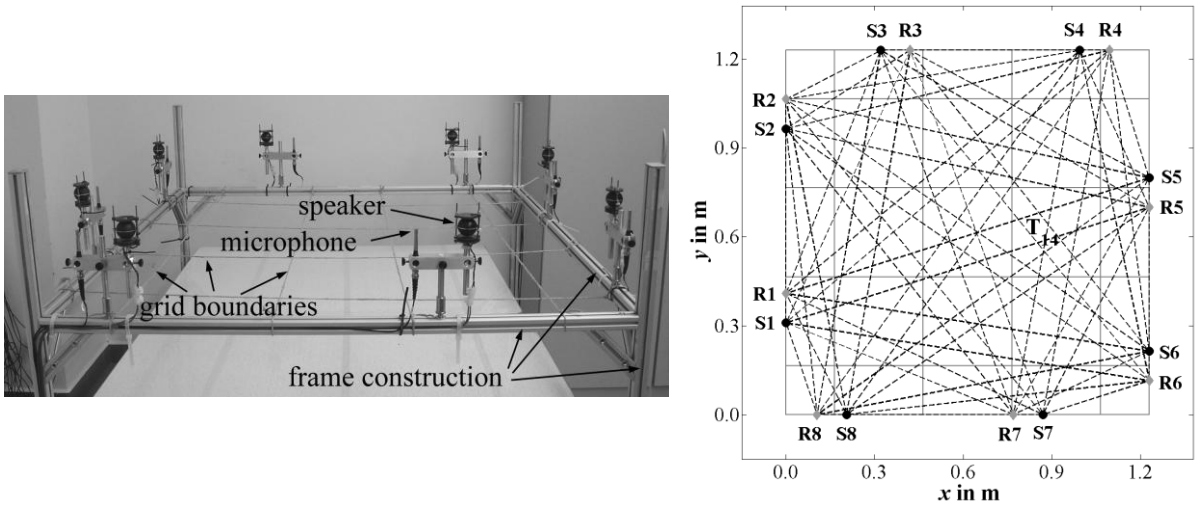

Figure 2: Photograph (left) and schematic top view (right) of the model tomographic apparatus for testing and educational purposes. Eight source-receiver-units (each consisting of one loud speaker and one microphone) are fixed to a frame construction made of aluminium profiles to ensure high flexibility in positioning. The area to be investigated extends to 1.23 m × 1.23 m. For tomographic reconstruction this area is divided into distinct grid cells whose boundaries are indicated by gray straight lines. On the right side, black dashed lines illustrate sound ray paths. Sound sources (black circles) and receivers (grey diamonds) are indicated by S and R, respectively.

4 Measurement uncertainties

According to equation (4), the effective speed of sound is calculated from travel time measurements knowing the positions of the sound sources and receivers, and therefrom knowing the sound ray path lengths. Thus, uncertainties in effective sound speed estimates result from uncertainties in travel time measurements $u(\tau)$ as well as from position uncertainties $u(d)$

$$u\left(c_{\mathrm{eff}}\right)=\left|\frac{\partial c_{\mathrm{eff}}}{\partial \tau}\right| u\left(\tau\right)+\left|\frac{\partial c_{\mathrm{eff}}}{\partial d}\right| u\left(d\right)=\frac{c_{\mathrm{eff}}}{\tau}\,u(\tau)+\frac{c_{\mathrm{eff}}}{d}\,u(d) \tag{8}$$

For the current measurement hardware, travel times can be estimated with an uncertainty of 2 μs using interpolation techniques (Holstein et al., 2004). Uncertainties for measurements of source and receiver positions are assumed to be in the range of few millimetres. Resultant uncertainties for the effective sound speed are plotted in Figure 3.

The total uncertainty of sound speed measurements for sound ray paths which are longer than 1.2 m is about 0.8 m/s for motionless conditions with an acoustic virtual temperature of 30 °C. Thereby, the great deal of uncertainties is connected with uncertainties from measuring the position of the sound sources and receivers (0.6 m/s). To neglect uncertainties from positioning, the system has to be calibrated using alternative measurements of temperature and humidity (e.g. psychrometer data). Therefore, travel times along all sound ray paths are measured for these known conditions (assuming a homogeneous temperature and humidity distributions within the measurement area, no wind). From ambient conditions, expected travel time values are estimated. These values are compared to the measured travel times for every sound

ray path and differences are calculated. For subsequent measurements travel times are adjusted using these differences. Due to this procedure, uncertainties in estimated sound speed values only result from uncertainties in travel time measurements. Thus, for ray path lengths over 1.2 m, an uncertainty for the effective sound speed of 0.2 m/s and below can be achieved.

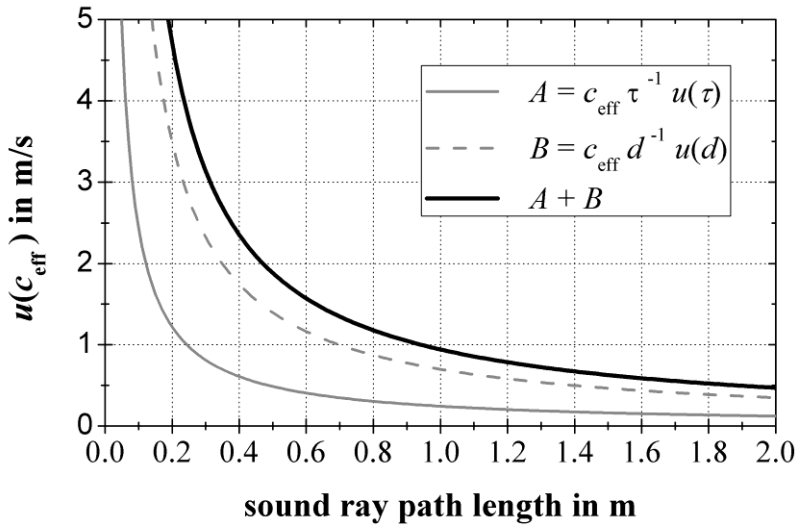

Figure 3: Uncertainties for effective sound speed estimates $u(c_{eff})$ which result from uncertainties of travel time measurements (line A with $u(\tau) = 2\ \mu s$) and uncertainties of position measurements (line B with u(d) = 2 mm) for motionless conditions and an acoustic virtual temperature of 30 °C (c_{eff} = 349.0 m/s).

5 Example measurement

An example measurement using the measurement setup introduced in section 3 has been carried out in a laboratory of our institute to demonstrate the influence of temperature on sound speed along different sound ray paths. Therefore, a series of measurement was taken where the area under investigation was differently heated to generate local differences of temperatures. Over all, the testing time was about four hours, it started at 12:36 CET and ended at 16:39 CET. Single travel time measurements for all sound ray paths were taken every 20 s. For generating locally inhomogeneous temperature distributions, a heating plate was positioned within the measurement area. In Figure 2 (right) the location of the heating plate is indicated by the label ‘T14’. At 13:29 CET the heating plate was turned on and at 14:41 CET it was switched off again.

To calibrate the measurement setup (for elimination of uncertainties due to measurements of sources and receivers positions as described in section 4) initial conditions within the laboratory room (no wind) were measured. The air temperature ϑ was observed to be 22 °C, the relative humidity *rH* was 50 % and the air pressure *p* was 995.3 hPa. From these parameters, the acoustic virtual temperature T_{av} and the Laplace sound speed c_L were calculated according to formulas (1) to (2) (T_{av} = 23.3 °C, c_L = 345.1 m/s). These values were used to estimate temporal corrections for each sound ray path according to the travel time measurements between all sound sources and receivers. For all subsequent measurements, travel times are

calculated from measured travel time values applying these corrections. Thus, changes of travel times along a certain sound ray path represent changes with respect to the initial conditions.
According to the remarks in section 2.1, temperature dependent sound speed was separated considering bi-directional sound ray paths. From the Laplace sound speed c_L (equation (5)), acoustic virtual temperature values (equation (2)) for each parallel pair of sound rays was estimated. From this value the air temperature (equation (1)) was calculated assuming a constant water vapour content (q = 8.3 g/kg).
Figure 4 shows the time dependent course of temperature for six selected sound propagation paths within the measurement area. The line identifiers are chosen in correspondence with the schematic picture of the tomographic measurement system in Figure 2 (right). S/R 1/4 indicates the pair of sound rays from source 1 to receiver 4 and vice versa. Three of the sound propagation paths directly traverse the grid cell which is heated and the other three paths bypass this grid cell.

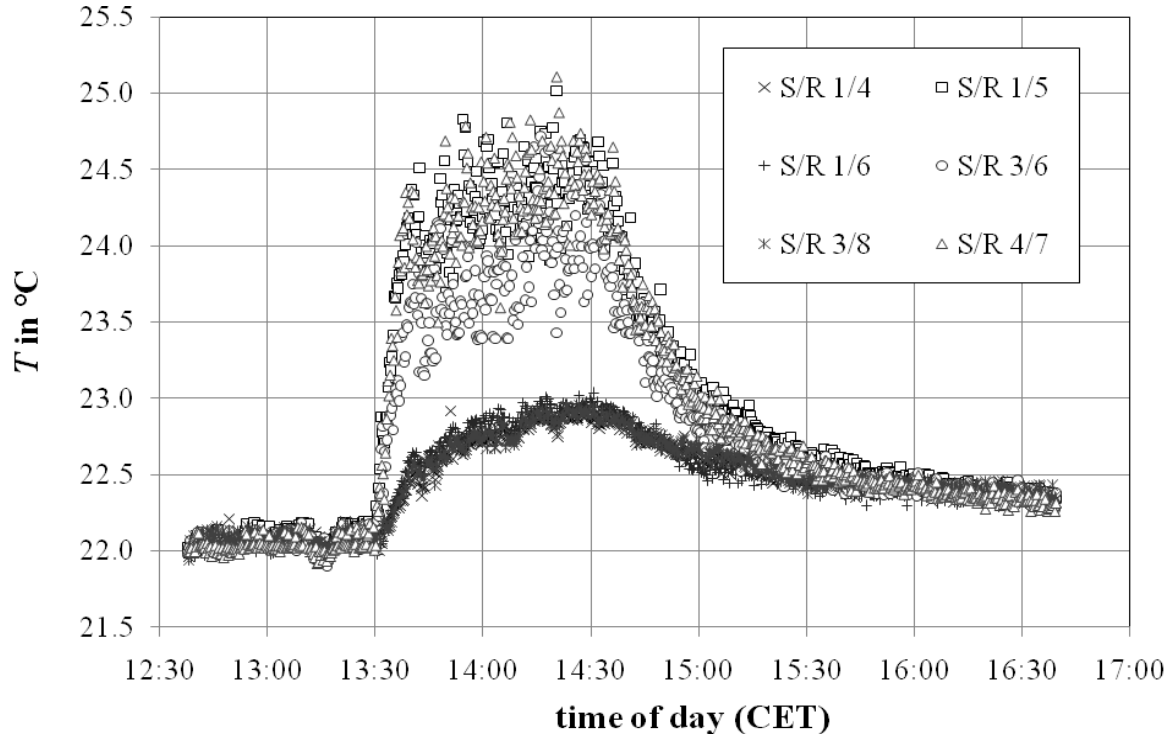

Figure 4: Temporal course of air temperature for selected sound ray paths which traverse the grid cell which is directly influenced by heating (open squares, circles, triangle) on the one hand and which bypass this grid cell (crosses, plus signs, asterisks) on the other hand. The sound ray path is indicated by the source (S) and receiver (R) number (S/R 1/4 indicates the pair of sound rays from source 1 to receiver 4 and from source 4 to receiver 1).

During the first part of the measurements (no heating) estimated temperatures along all sound rays are nearly constant. In this time interval, temperature variability between all sound propagation paths within the area under investigation is less than 0.3 K at a certain point in time.
After turning on the heating plate (13:29 CET) a sudden rise in estimated temperature values for all sound paths is observed. However, it is evident that temperature values along sound rays which do not propagate through the heated grid cell do not increase

as much and as high as temperature values along sound paths which directly traverse the heated area. This clearly shows that the heating is not limited to the air directly above the heating plate but also influences the surrounding air even if the effect is considerably less. Furthermore, estimated temperature values for those sound paths which traverse the heated grid cell, show remarkable higher variations in time than the other values which is due to a technically caused sequential heating of the heating source (to avoid overheating). In addition, it is obvious that the rise in temperature is comparably low (up to a maximum of about 25 °C) even for those paths which are directly influenced by the heating source. Reasons for this are that on the one hand measurements represent line integrated (line averaged) conditions and only a short path section is directly influenced by heating. On the other hand, the heat is not accumulated within the area of investigation, it only passes through it and in addition acoustic measurements are not influenced by radiation.
After switching off the heating plate at 14:41 CET, estimated temperature values along all paths decrease down to a nearly constant value which is slightly above the initial value from the beginning of the measurement. This corresponds to an overall warming of the laboratory. Furthermore, to the end of the measurement, spatial variations for all sound ray paths within the measurement area at a certain point in time decreased down to the value from the first measurement part (0.3 K).
Figure 5 shows examples of tomographically reconstructed distributions of temperature values from travel time measurements within the measuring area at two distinct times. Calculations were made using the simultaneous iterative reconstruction technique, an algebraic method, which was terminated after 50 iterative steps.

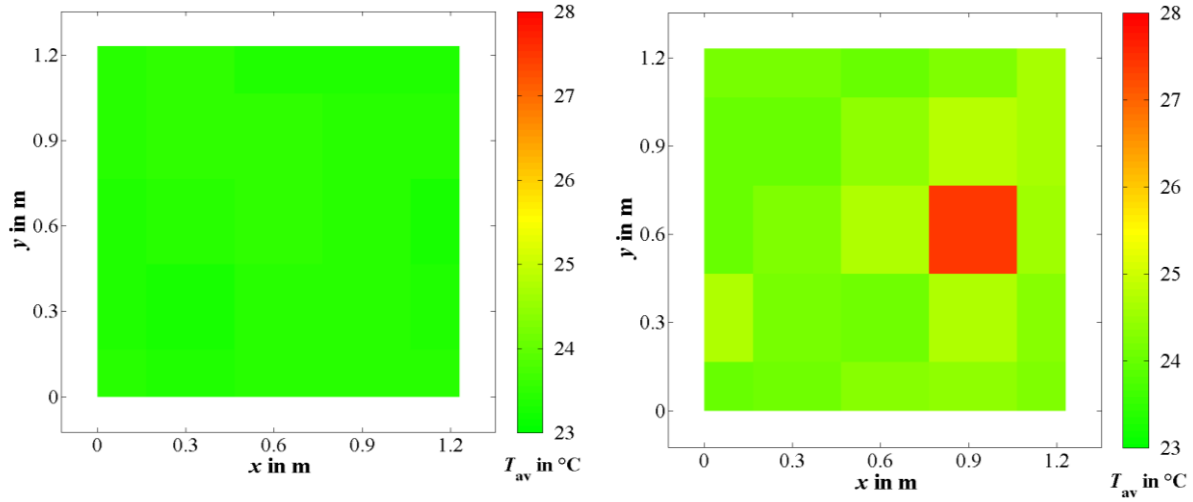

Figure 5: Example tomographic reconstruction of temperature values from travel time measurements at 12:40:43 CET (left) and 14:30:23 CET (right).

The left image of Figure 5 was reconstructed from travel time measurements which were taken at 12:40:43 CET. At this time the heating plate was still switched off. Temperature values are nearly the same within all grid cells with a mean value of 23.4 °C (average temperature for all 25 grid cells) and a standard deviation of 0.06 K. On the right side a reconstructed temperature distribution is shown which was calculated from travel time measurements which were taken at 14:30:23 CET. At this time the heating plate was turned on. The location of the heating source within grid cell T14 is clearly visible (cp. right side of Figure 2 for location of T14), whereas the

surrounding cells are considerably less influenced by heating as expected. The temperature reaches a maximum of 27.4 °C in T14. The mean temperature (spatial average over all 25 grid cells) is 24.4 °C. The standard deviation for this case (with local heating) is substantially higher than the standard deviation for the case without heating. It amounts to 0.67 K for the whole measurement area (all 25 grid cells).

6 Conclusions

In this article, a measurement system is introduced which can be used to vividly demonstrate acoustic techniques to estimate atmospheric parameters (in particular temperature) on the basis of travel time measurements of sound signals along well-known propagation paths. The method itself is scalable and thus not limited to laboratory sized measurement areas but also suited to investigate outdoor distributions. Moreover, it is not limited to two-dimensional measurements but also applicable for three-dimensional investigations as shown, e.g., by Barth and Raabe (2011). Flexibility in sensor positioning easily enables investigations of the effect of different measurement set-ups. Furthermore, the modular structure facilitates an exchange of hardware and software components, e.g., to test different algorithms for signal processing, to investigate characteristics of acoustic signals or properties of sources and receivers.
The measurement method is a remote sensing method. No sensors have to be directly inserted into the measurement area which reduces any disturbances of the fields due to instrumentation. Besides, measurements are not influenced by radiation which is a common problem, e.g. for in situ temperature sensors.
Moreover, the sensitivity consideration showed that for an indoor application with sound ray path lengths of up to a few metres, changes of temperature and flow with respect to an initial distribution should be measured. In doing so, an accuracy of sound speed measurements in the range of 0.2 m/s can be achieved. An example measurement illustrates the sensitivity of the method concerning temperature estimation. The apparatus described here is used for demonstrations and for practical training at the Institute for Meteorology of the University of Leipzig since several years.

References

Arnold, K., 2000: Ein experimentelles Verfahren zur akustischen Laufzeittomographie im Bereich der atmosphärischen Grenzschicht. *Wiss. Mitt. Inst. f. Meteorol. Univ. Leipzig und Inst. f. Troposphärenforsch. e.V. Leipzig*, **18**, PhD thesis, 136pp.

Aki K., Richards P.G., 2002: *Quantitative Seismology.* University Science Books (Sausalito, California), 700 pp.

Barth, M., Raabe, A., Arnold, K., Resagk, C., du Puits, R., 2007: Flow field detection using acoustic travel time tomography. *Meteorol. Z.*, **16**, 443-450.

Barth, M., 2009: Akustische Tomographie zur zeitgleichen Erfassung von Temperatur- und Strömungsfeldern. *Wiss. Mitt. Inst. f. Meteorol. Univ. Leipzig*, **44**, PhD thesis, 279pp.

Barth, M., Raabe, A., 2011: Acoustic tomographic imaging of temperature and flow fields in air. *Meas. Sci. Technol.*, **22**, 035102 (13pp).

Fischer, G., 2008: *Invertierungsalgorithmen für die akustische Laufzeittomographie in der Atmosphäre*. Diploma Thesis, Universität Leipzig, Germany, 83pp.

Fischer, G., Barth, M., Ziemann, A., 2009: Inverse reconstruction techniques and their applicability for acoustic travel-time tomography. *NAG/DAGA 2009, International Conference on Acoustics, Rotterdam, The Netherlands*, publ. on CD-ROM, 4pp.

Holstein, P., Raabe, A., Müller, R., Barth, M., Mackenzie, D., Starke, E., 2004: Acoustic tomography on the basis of travel-time measurements. *Meas. Sci. Technol*., **15**, 1420-1428.

Menke, W., 1989: *Geophysical Data Analysis: Discrete Inverse Theory*. Academic Press, Inc. (San Diego, California) 289pp.

Munk, W., Worcester, P., Wunsch, C., 1995: *Ocean Acoustic Tomography*. Cambridge University Press, 433pp.

Ostashev, V.E., 1997: *Acoustics in Moving Inhomogeneous Media*. London: E & FN SPON, 259pp.

Ostashev V.E., Vecherin S.N., Wilson D.K., Ziemann A., Goedecke G.H., 2009: Recent progress in acoustic travel-time tomography of the atmospheric surface layer. *Meteorol. Z.*, **18,** 125-133.

Pierce, A.D., 1989: *Acoustics—An Introduction to Its Physical Principles and Applications*. Melville, NY: Acoustical Society of America, 678pp.

Raabe, A., Arnold, K., Ziemann, A., 2001: Near surface spatially averaged air temperature and wind speed determined by acoustic travel time tomography. *Meteorol. Z.*, **10** (1), 61-70.

SINUS, 2011: Further information on technical details about the utilized multi-channel spectrometer hardware (Harmonie-PCI Card) available at http://www.sinusmess.de/e

Vecherin, S.N., Ostashev, V.E., Ziemann, A., Wilson, D.K., Arnold, K., Barth, M., 2007: Tomographic reconstruction of atmospheric turbulence with the use of time-dependent stochastic inversion. *J. Acoust. Soc. Am*., **122** (3), 1416-1425.

Wilson, D.K., Thomson, D.W., 1994: Acoustic tomographic monitoring of the atmospheric surface-layer. *J. Atmos. Ocean. Technol*., **11**, 751-769.

Wilson D.K., Ziemann A., Ostashev V.E., Voronovich A.G., 2001: An overview of Acoustic Travel-Time Tomography in the Atmosphere and its Potential Application. *Acta Acustica united with Acustica*, **87,** 721-730.

Ziemann, A., 2000: Eine theoretische Studie zur akustischen Tomographie in der atmosphärischen Grenzschicht. *Wiss. Mitt. Inst. f. Meteorol. Univ. Leipzig und Inst. f. Troposphärenforsch. e.V. Leipzig*, **19**, PhD thesis, 137pp.

Ziemann, A., Arnold, K., Raabe, A., 2001: Acoustic Tomography as a Method to Identify Small-Scale Land Surface Characteristics. *Acta Acust. United Acust*., **87**, 731-737.

Comparison of refractivity profiles derived by Radiosonde soundings and GNSS tomography

B. Brecht, A. Raabe and M. Bender

Abstract

By tomography of GNSS slant delay data the refractivity fields of the atmosphere can be reconstructed. The resolution of the tomography field is about 40 km in horizontal and several 100 m in vertical direction. In 2009 about 270 GNSS stations were available in Germany. The tomographically reconstructed humidity fields have to be validated with other observation methods which are able to detect the refractivity profiles of the atmosphere. The data used to compare is from radiosonde soundings, by which the refractivity can be calculated. The first results of the comparison of GNSS data with radiosonde data from two radiosonde stations in Germany are shown.

Zusammenfassung

Mittels Tomographie der Laufzeitverzögerungen von GNSS-Daten können die Refraktivitätsfelder der Atmosphäre rekonstruiert werden. Die Auflösung des tomographischen Gitters beträgt circa 40 km in horizontaler und einige 100 m in vertikaler Richtung. Im Jahr 2009 waren in Deutschland Daten von etwa 270 GNSS-Stationen verfügbar. Die tomographisch rekonstruierten Feuchtefelder müssen durch andere Messmethoden, die ebenso die Refraktivitätsprofile der Atmosphäre erfassen können, validiert werden. In diesem Fall wurden dazu Vergleichsdaten von Radiosondenaufstiegen genutzt, aus denen die Refraktivität berechnet werden kann. Es werden die ersten Resultate des Vergleichs zwischen GNSS-Daten und Daten zweier Radiosondenstationen in Deutschland dargestellt.

1 Introduction

High resolution weather forecast models require realistic initialization of the synoptic fields. A problem is however that there is a lack of spatially resolved humidity information. This especially holds true on the vertical profile of the water vapor distribution, which is required to make realistic quantitative precipitation forecasts. Such observations with a sufficiently high spatial resolution can only be provided by remote sensing techniques (Bender et al., 2000).

One technique which has recently become widely used is the Global navigation satellite systems (GNSS) based atmosphere sounding. By 2010 the Global Positioning System (GPS) was the only GNSS being fully operational. Further GNSS like the

European Union's Galileo positioning system, scheduled to be fully operational by 2020 at the earliest, are being planned (ESA, 2002).
Several European weather services make use of the GNSS data to improve their operational weather forecasts. Currently the Zenith total delays (*ZTDs*) or the integrated water vapor (*IWV*) are assimilated operationally. Since 2002 the *ZTD* and *IWV* data of an increasing number of German and European GPS stations have been available from the German Research Center for Geosciences (GFZ) in Potsdam (Bender et al., 2011).
Concerning the *IWV*, it is a measure of the total amount of water vapor above a certain station. A dense network of GPS stations (≈ 270 Germany GNSS stations in 2009) provide detailed information on the horizontal water vapor distribution. However, there is no information about the vertical profile. Therefore the GFZ developed a GPS water vapor tomography system in cooperation with the Institute of Meteorology of the Leipzig University (LIM) which is able to reconstruct refractivity or humidity fields from Slant total delays (*STDs*). The system works in near real-time and provides spatially resolved fields with a temporal resolution of less than one hour.
The basic observations required by the GPS tomography are the *STD* data, which are provided by an operational GPS processing system. The temporal resolution of the slant delays is 2.5 minutes. The resolution of the tomography system is about 30 minutes with a horizontal resolution of 40 km and a vertical resolution of 500 m or even higher. Several quantities such as the refraction index, the wet refractivity or the absolute humidity can be reconstructed from slant delay data. In this work the wet refractivity was reconstructed from the slant wet delays (*SWDs*) as it is closely related to the absolute humidity of the atmosphere and only assumptions about the pressure profile have to be made. In order to receive the wet refractivity, information about the *SWDs* have to be estimated. They can be obtained by using the Saastamoinen model (Saastamoinen, 1972, 1973) and surface meteorological observations. Meteorological observations can also be used to initialize the tomography and to estimate the initial atmospheric state (Bender et al., 2011).
In order to validate the results of the GPS tomography, especially the profiles of the wet refractivity, radiosonde soundings were used. Radiosonde soundings provide all observations necessary to obtain the wet refractivity.

2 GPS Atmosphere Sounding

The GPS satellites transmit two signals in the microwave range with frequencies of $L_1 \approx 1{,}575$ GHz and $L_2 \approx 1{,}227$ GHz. GPS processing techniques provide the *STDs* of the GPS signal between the satellite and the receiver. The propagation of the signal and especially the signal path depends on the refraction index of air. According to Fermat principle, the signal propagates along the path with the minimum optical path

length. Due to the fact that the atmosphere is an inhomogeneous medium this does not correspond to a straight line like a geometrical ray path. Earth's atmosphere increases the optical path length between the satellite and the receiver (Bevis et al., 1992).
Both the ionosphere and the neutral atmosphere (troposphere and stratosphere) introduce propagation delays into the GPS signal (Bevis et al., 1992). The slant delay in the ionosphere depends on the concentration of free electrons and the frequency of the signal. Because the ionosphere is a dispersive medium this delay can be removed by a linear combination of both observations. The delay associated with the neutral atmosphere is effectively nondispersive at GPS frequencies and can therefore not be corrected in this way (Bevis et al., 1992). Here the delay results from refraction and diffraction in the atmosphere. The neutral atmosphere consists of dry gases and water vapor. The components are polarized by the electromagnetic field and water vapor itself has a dipole moment which contributes to its refractivity. For microwaves the refractivity is dominated by its dipole moment. The dipole component of the water vapor refractivity can be separated from the nondipole components of the refractivity's of the water vapor and other constituents of the atmosphere. The delay, caused by the water vapor, is called wet delay, the other one hydrostatic delay. Both delays increase from zenith direction to lower elevation angles approximately inverse with the sine of the elevation angle. The hydrostatic delay for zenith direction has a value of about 2.3 m and sea level. The wet delay is about 0 – 10% of the hydrostatic delay. In arid areas it could be nearly zero (Bevis et al., 1992).

2.1 GPS Tomopgraphy

Slant delays are usually expressed as excess phase length, i. e. the path delay multiplied by the vacuum speed of light. The excess phase length as compared to undisturbed propagation in vacuum is given by

$$\Delta L = \int_{\mathrm{L}} n(s)\mathrm{d}s - G = \int_{\mathrm{L}} [n(s) - 1]\mathrm{d}s + S - G \qquad \textbf{(2.1)}$$

where L is the curved path, $n(s)$ the refraction index as a function of the position s along the path, G is the geometrical path length and S the path length along L. While the first term is due to the slowing effect, the second represents the bending term, which is usually negligible. Equation 2.1 can be given in terms of the atmospheric refractivity N, defined by Bevis et al. (1992) with the Slant Total Delay STD:

$$STD = \Delta L = 10^{-6} \int N(s)\,\mathrm{d}s \quad \text{with} \quad N = 10^6 \cdot (n - 1). \qquad \textbf{(2.2)}$$

In case of the GPS tomography the *STDs* represent the measured values while the refractivity field has to be reconstructed from a large number of such observations. The problem is an inverse problem and it turns out to be ill-posed, i.e. solutions are in general not unique and not stable (Bender et. al, 2010). The tomography system used in this work is described in Bender et al. (2010).
The empirical Smith and Weintraub formula gives the refractivity as a function of several atmospheric quantities:

$$N = k_1\left(p_{\mathrm{d}}/T\right) + \mathrm{k}_2\left(e/T\right) + k_3\left(e/T^2\right) \qquad \textbf{(2.3)}$$

where k_1=77,607 K/hPa, k_2=71,6 K/hPa, k_3=3,747·10^5 K^2/hPa, p_{d} and e are the partial pressures for dry air and water vapor in hPa and T is the temperature in Kelvin (Bevis et al., 1994). Different quantities of the empirical constants k_1, k_2 and k_3 have been published (Bevis et al., 1994; Healy, 2011). The first term of Equation 2.3 defines the hydrostatic refractivity and the following two terms describe the wet refractivity N_{wet}. The hydrostatic refractivity is given by the dielectric polarization of the nonpolar gases while the wet term has dielectric and paraelectric contributions from the water molecules, the latter being the dominant term.
In order to reconstruct the N_{wet} field using the GPS tomography the *SWD* must be separated from the *STD*. This is done by calculating the Slant hydrostatic delay (*SHD*) with the Saastamoinen model, which requires precise surface pressure information (Bevis et al., 1992). The Saastamoinen model makes certain assumptions about the vertical pressure profile which in general introduce an additional error into the *SWD* data. Further assumptions about the temperature profile must be made to derive the slant integrated water vapor which would be required to reconstruct the absolute humidity. As the tomography is very sensitive to small variations in the input data the N_{wet} field is reconstructed in this work. The field of the absolute humidity can easily be obtained from N_{wet} making the same assumptions as required to estimate the Slant integrated water vapor (*SIWV*) but without introducing further uncertainties into the tomography.
The basic equation to be solved by the tomography is

$$SWD = STD - SHD = 10^{-6}\int N_{\mathrm{wet}}(s)\,\mathrm{d}s. \qquad \textbf{(2.4)}$$

This equation can be discretised and linearised using a spatial grid and neglecting the ray bending, which leads to the linear equation

$$\boldsymbol{A}x = m, \tag{2.5}$$

where m are the observations (*SWDs* and possibly some meteorological observations), x is the unknown state vector (N_{wet} field) and $\boldsymbol{A}$ is the kernel matrix containing the sub-paths of each slant path in each grid cell. The equation can be solved by several reconstruction techniques, see for example Bender et al. (2010, 2010).

A large impact on the quality of the results has the initial field, which can be implemented with several methods. First it can be used the standard atmosphere as a first guess. More realistic results can be obtained by using the synoptic observations and extrapolating them in a three dimensional field of N_{wet}. Another possibility is to take an analysis field or a forecast of a numerical weather model. The importance of the initial field is inter alia caused by situations where more than 50% of the voxel are not touched by any slant path and will therefore retain their initial value. This can be smoothed a little by applying inter voxel constraints but wrong initial assumptions considerably reduce the quality of the results (Bender et al., 2011).

The GNSS data processing at the GFZ works in near real-time. It provides *ZTDs*, *IWV* and slant delay data operationally. With this large data set of more than 50000 slants per hour the spatially resolved humidity fields are reconstructed by means of tomographic techniques. It can be expected that the additional observations from the future Galileo system will improve the quality of the results. It was demonstrated in a study that by combining the data of the three satellite systems GPS, Galileo and the Russian Glonass-system the spatiotemporal resolution of the reconstructed humidity fields can be increased up to 30 km horizontally, 300 m vertically and 15 minutes temporally.

3 Comparison of Vertical Profiles Obtained from Radio Soundings and GPS Tomography

The results presented below were derived from radiosonde soundings and GPS tomography for July 2007. The GPS tomography data were provided by the GFZ in Potsdam and the data from the radiosondes were provided by the Deutsche Wetterdienst (DWD). The vertical resolution of the reconstructed N_{wet} fields is 500 m. In order to compare the tomographically reconstructed profiles with radiosonde observations the gridded tomography data were interpolated to the radiosonde observations using a bilinear horizontal interpolation and an exponential vertical interpolation. It must be pointed out that the tomography reconstructs voxel means, i. e. mean values for ~40 x 40 x 0.5 km grid cells which are difficult to compare with the radiosonde point observations.

The altitudes which especially should be analyzed are in the range of 0 – 2000 m above the stations, because in this range the atmospheric boundary layer is present; however also higher altitudes are displayed.

Figures 3.1 and 3.2 show the profiles of N_{wet}, given by the radiosonde and the GPS tomography at the site of Emden and Meiningen. Figure 3.1 shows the values of Emden, Figure 3.2 the profiles of Meiningen. In all 4 graphs the profiles of the radiosonde and the GPS tomography show good correlations. In 3 out of 4 graphs the GPS tomography overestimates the values of N_{wet} in the lowest 500 m over the stations. This is caused by the bad initialization of the tomography. Above 500 m the differences between the radiosonde and the GPS tomography are very small, except at a height interval from 2000 – 3000 m on the right picture of Figure 3.1 where the GPS tomography overestimates the values of the radiosonde sounding.

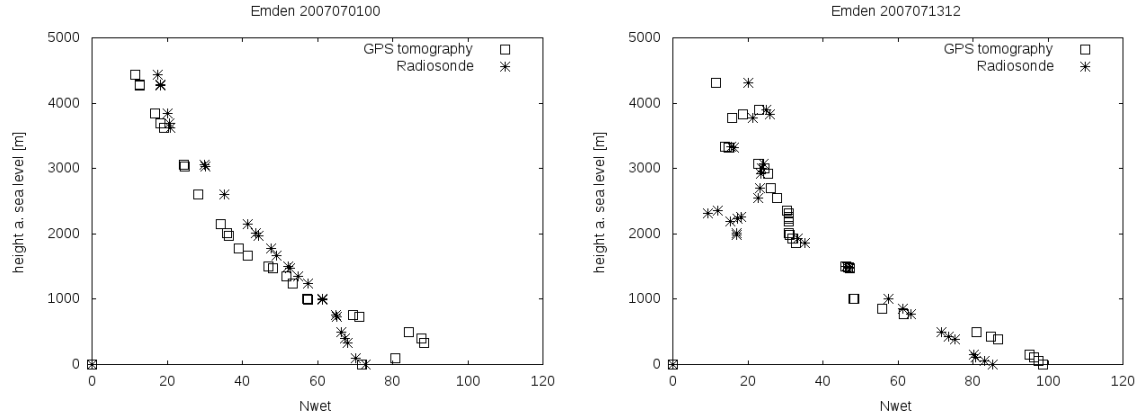

Fig. 3.1: Profiles of N_{wet} versus the altitude (m.a.s.l.) at the site of Emden from radiosondes and the GPS tomography. On the left side the values from the 1th of July 2007 at 00 UTC and on the right side the values from the 13th of July 2007 at 00 UTC are displayed.

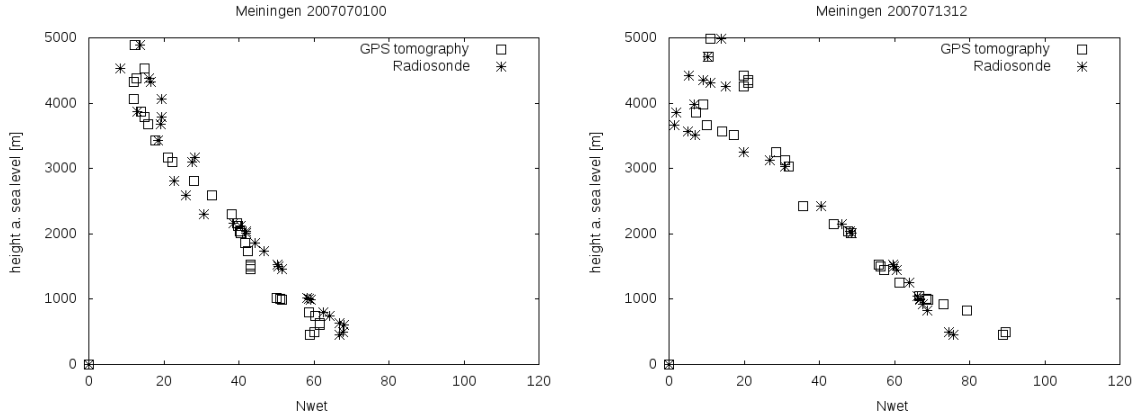

Fig. 3.2: Profiles of N_{wet} versus the altitude (m.a.s.l.) at the side of Idar-Oberstein from radiosondes and the GPS tomography. On the left side the values from the 1th of July 2007 at 00 UTC and on the right side the values from the 13th of July 2007 at 00 UTC are displayed.

The other days of July 2007 (not displayed here) show similar correlations between the radiosonde and the GPS tomography. This can be seen in Figure 3.3, which compares the data pairs of N_{wet} from the radiosonde and the GPS tomography for July 2007 at 12 UTC from Emden. There were plotted the values of N_{wet} from the radiosonde versus the GPS tomography for each vertical layer between 0 - 0,5 km, 0,5 -1 km, 1 – 1,5 km and 1,5 – 2 km over station. The graph shows that the correlation of the radiosonde and the tomography gets significantly higher at altitudes above 500 m over the stations. The same tendencies can be observed in the depictions of 00 UTC (not displayed here). The standard deviation of the lower altitudes is larger (or nearly the same at higher levels than h_1) than the ones from higher altitudes as well ($\sigma(h_1) > \sigma(h_2) \geq \sigma(h_3) \geq \sigma(h_4)$). It can also be seen that the differences between the radiosonde and the GPS tomography become smaller at higher altitudes. But there also occur some significantly differences (for example N_{wet}(radiosonde) ≈ 80 and N_{wet}(tomography) ≈ 110). They cause due to not filtering the data before. That means that there were sometimes insufficient observations to get an expedient solution or there were no slant data available in some regions.

Figure 3.4 also shows these data pairs for Meiningen for the same time as above. There seem to be no significant difference in the results, so that the method of GPS tomography seems to be stable not only for one station but also for another station. To validate this other radiosonde stations have to be involved in this study and have also to be analyzed.

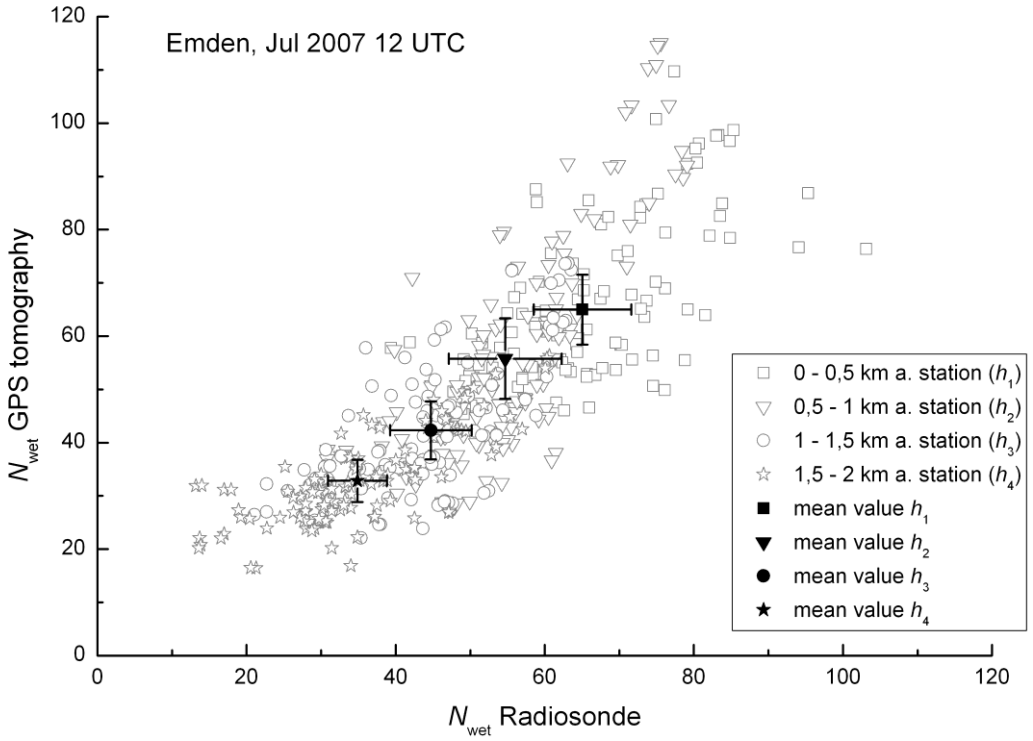

Fig. 3.3: Displayed are data pairs of N_{wet} resulting from radiosonde data versus data from GPS tomography at the side of Emden from July 2007 at 12 UTC. Each data symbol corresponds to a vertical layer illustrated in the legend. The arithmetic average of the standard deviations of the data pairs from one vertical layer is displayed by lines.

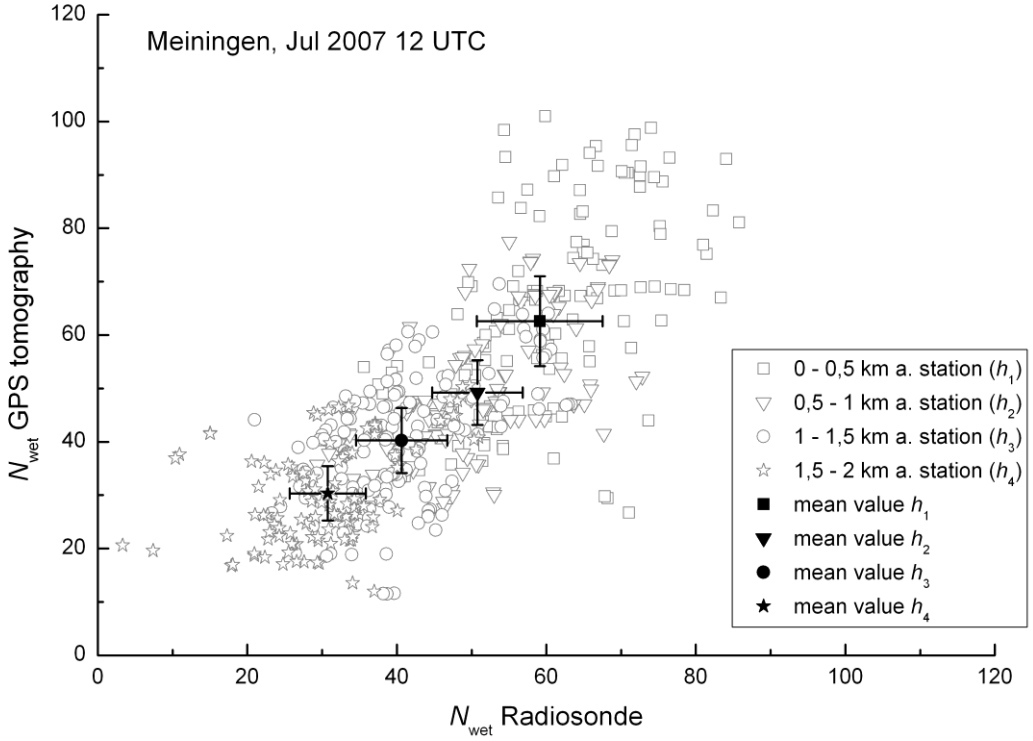

Fig. 3.4: Same as Figure 3.3, but for Meiningen.

4 Conclusions

In order to validate wet refractivity profiles derived by GNSS tomography the profiles were compared with data from radiosonde soundings. This has been done in this study in the cause of one month (July 2007) and carried out for two radiosonde stations (Emden and Meiningen).
The results of the comparison show good correlations between the values of the GPS tomography and the radiosonde soundings. The higher differences in the values in the first height layer (0 – 500 m above station) result from the bad initialization of the tomography. Above this layer the differences become smaller.
There have to be made further analysis by filtering the data of the GPS tomography concerning about the times of insufficient observations and availability of the slant data. There also have to be carried out all available radiosonde stations (13 in 2007 in Germany) with the aim to get a characteristic value, which will be able to describe the quality of the profiles derived by the GPS tomography.
So far it could be said that the GPS tomography seems to be an applicable method for receiving the vertical profile of the water vapor distribution in the atmosphere.

Acknowledgements

We would like to thank the DWD for providing the radiosonde data and the GFZ for providing the GPS tomography data.

References

Baelen, J. V., Aubagnac, J.-P. and Dabas, A., 2005: . American Meteorological Society, Journal of Atmospheric and Oceanic Technology, Vol. 22, 201 – 210.

Bender, M., Dick, G., Wickert, J., Schmidt, T., Song, S., Gendt, G., Ge, M. and Rothacher, M., 2000: Validation of GPS Slant Delays using Water Vapour Radiometers and Weather Models. Meteorologische Zeitschrift, Vol. 1, No. 1, 001-006.

Bender, M., Dick, G., Ge, M., Deng, Z., Schönrock, M., Wickert, J., Kahle, H.-G., Raabe, A. and Tetzlaff, G., 2010: Development of a GNSS Water Vapor Tomography System Using Algebraic Reconstruction Techniques. Advances in Space Research, in press.

Bender, M., Stosius, R., Zus, F., Dick, G., Wickert, J. and Raabe, A., 2011: GNSS water vapor tomography - expected improvements by combining GPS, GLONASS and Galileo observations. Advances in Space Research, Volume 47, Issue 5, 886 – 897.

Bevis, M., Businger, S., Herring, T. A., Rocken, C., Anthes, R. A. and Ware, R. H., 1992: GPS Meteorology: Remote Sensing of Atmospheric Water Vapour Using the Global Positioning System. Journal of Geophysikal Reasearch, Vol. 97, No. D14, 15,787–15,801.

Bevis, M., Businger, S. and Chiswell, S., 1994: GPS Meteorology: Mapping Zenit Wet Delays onto Precipitable Water. Journal Of Applied Meteorology, Vol. 33, 379-386.

Eichler, K., 2009: Untersuchung von atmosphärischen Einflüssen auf simulierte GPS-Laufzeitverzögerungen. Diplomarbeit am Leipziger Institut für Meteorologie.

ESA Mission High Level Definition European Space Agency, 2002: http://ec.europa.eu/dgs/energy_transport/galileo/doc/galileo_hld_v3_23_09_02.pdf.

Healy, S. B., 2011: Refractivity coefficients used in the assimilation of GPS radio occultation measurements. J. Geophys. Res.: 116, D01106.

Rockel, B., Raschke, E. and Weyres, B., 1991: A Parameterization of Broad Band Radiative Transfer Properties of Water, Ice, and Mixed Clouds. Beitr. Phys. Atmosph., Vol. 64, No.1, p. 1-12.

Climatology of the 8-hour tide over Collm (51.3°N, 13°E)

T. Fytterer, Ch. Jacobi

Summary

The horizontal winds in the mesosphere and lower thermosphere (MLT) at heights of about 80-100 km have been measured by the SKiYMET meteor radar at Collm, Germany (51.3°N, 13°E). The radar has been operating continuously since July 2004, and the data from December 2004 – December 2009 were used for constructing a climatology of the 8-h tide. The 8-h tide appears to be a regular feature in the MLT. In particular, the amplitude shows a clear seasonal behaviour, with maximum values around the equinoxes, and generally an increase with height. The largest amplitudes occur in autumn, sometimes reaching values above 15 m/s, but they are significantly smaller during summer (~1 m/s). The phase is early in winter and advances to later times in summer. In general, the phase difference between the zonal and meridional components is close to +2 h. The vertical wavelengths are short in summer (~30 km) but significant longer during the rest of the year. The results were compared with observations from locations of different latitudes.

Zusammenfassung

Der Horizontalwind in der oberen Mesosphäre und unteren Thermosphäre (MLT) in Höhen von 80-100 km wurde mit dem SKiYMET-Meteorradar in Collm, Deutschland (51,3°N, 13°E) gemessen. Das Radar liefert seit Juli 2004 kontinuierlich Daten, wobei nur die Datenreihen von Dezember 2004 bis Dezember 2009 für die Klimatologie der 8-stündigen Gezeit verwendet wurden. Letztere ist eine dauerhafte Erscheinung der MLT. Besonders bei der Amplitude sind ein klarer Jahresgang, sowie eine Höhenzunahme erkennbar. Die Maxima treten während der Äquinoktien auf, mit vereinzelten Werten über 15 m/s, wohingegen sie beim Durchlaufen des Sommers deutlich schwächer (~1 m/s) sind. Die Phase nimmt eine Sommer- und Winterposition ein, wobei erstere später auftritt. Generell liegt die Phasendifferenz zwischen zonaler und meridionaler Phase bei +2 Stunden. Die vertikalen Wellenlängen sind im Sommer mit ca. 30 km sehr kurz und im übrigen Jahr deutlich länger. Letztlich wurden die Ergebnisse mit Beobachtungen von Orten verschiedener Breitengrade verglichen.

1. Introduction

The dynamics of the mesosphere and lower thermosphere (MLT) are strongly influenced by atmospheric waves (Andrews et al., 1987), including the solar tides, which are waves with periods of a solar day and its subharmonics. The latter are excited at lower atmospheric regions (troposphere, stratosphere), propagate vertically and transport momentum and energy upward. The wind amplitudes are comparatively small (~cm/s) near the region of forcing, but increase to significantly larger values above 80 km, maximising around 100-120 km (e.g. Hagan et al., 1995). In these regions, their amplitudes are of the order of magnitude of the mean wind, increasing the amplitudes of the planetary or gravity waves. As a result, the solar tides drive the global circulation and a more accurate knowledge would lead to a better understanding

of the wind fields in the MLT. In general, shorter period waves have smaller amplitudes, so that the diurnal tide (DT) and the semidiurnal tide (SDT) have attracted more attention. But recently, also the terdiurnal tide (TDT, periodicities of 8 hours) has been considered to play an important role, because occasionally their amplitudes are as large as the ones of DT and SDT.

The DT and SDT are mainly excited by the absorption of solar radiation through tropospheric water vapour and stratospheric ozone. In contrast, the cause of the excitation mechanism of the TDT is still uncertain. One theory proposes that the tide could be caused by direct solar heating in the lower and middle atmosphere. Other ones mention a non-linear coupling between the DT and SDT (Teitelbaum et al., 1989) or interactions between the DT and gravity waves. Also possible is a combination of these mechanisms. At least, some proofs for non-linear coupling between SDT and DT were found. Observations in the Arctic mesosphere showed a relationship between the vertical wavelengths of the TDT, SDT and DT, but this was only evident when the TDT had large amplitudes (Younger et al., 2002).

The characteristics of the TDT have been described on some limited occasions. They are a persistent feature (e.g. Beldon et al., 2006), and generally the zonal amplitude is larger than the meridional. Furthermore, a clear seasonal cycle is apparent, including smaller amplitudes in summer and two maxima in spring and autumn, while the latter one is dominating. The amplitudes range from 1-10 m/s at altitudes of ~90 km and depend on season, height and latitude. Observations in high latitudes have shown a missing spring maximum below 95 km (Younger et al., 2002). The phase variability is also differing with latitude and season. At a given altitude, the phase takes a nearly constant summer position from early spring to autumn and is about 1-2 h later than in winter. The phase difference between zonal and meridional components is close to +2 h. Noticeable differences only occur during summer (Beldon et al., 2006). The values of the vertical wavelength strongly vary. Observations made in Arctic regions show wavelengths of about 25-90 km (Younger et al., 2002). Considering the results at mid-latitudes (ranging from ~60-1000 km in the course of a year) made by Namboothiri et al. (2004) and the observations at lower latitudes (~12-32 km) reported by Tokumotos et al. (2007), a significant disagreement is seen.

2. Data collection and analysis

The data used in this study have been measured by a SKiYMET meteor radar located at Collm Observatory, Germany (51.3°N, 13°E). It is operating since July 2004, and the 5-year dataset from December 2004 – December 2009 was used here to investigate

Table 1: *Summarized selection parameters and its limits.*

parameter	limits
radial velocity	$\|v_{rad}\| < 200$ m/s
range	$r < 400$ km
zenith angle	$20° < \theta < 70°$
minimum number of meteors	$n = 5$
zonal and meridional velocity	$\|u,v\| < 150$ m/s
outlier rejection	$\Delta v < 40$ m/s

the TDT. The meteor radar operates at 36.2 MHz with a pulse repetition frequency of 2144 Hz by using a transmitter of 6 kW peak power with a pulse length of 2 km. The VHF radio wave emitted by the radar is either completely (overdense) or only partly (underdense) scattered by ionised meteor trails. The back-scattered energy is detected by the antenna array, which has five elements forming an asymmetric cross, acting as an interferometer, allowing the calculation of azimuth and zenith angle. In combination with range measurements, the exact meteor trail position is determined. Radial wind velocity along the line of sight is obtained from Doppler phase progression with time at each receiver. The number of meteors is varying strongly between altitudes of 80 and 100 km, with a maximum around 89-91 km (Viehweg, 2006). For characterization of the horizontal wind field in the MLT, the observed height interval is divided in six not overlapping height gates centred at 82, 85, 88, 91, 94 and 98 km. The data collection procedure is based on a method, described by Hocking et al. (2001). Individual winds calculated from the meteors are summarized to form half-hourly mean values through projection of the horizontal wind on the individual radial winds, using least-squares fitting. The latter algorithm is done by assuming that vertical winds are small. Furthermore, a data selection is added, including an outlier rejection (Table 1). The amplitude and phase of the TDT are calculated by a multiple regression analysis of one month of half-hourly zonal and meridional wind components, which includes the mean wind, as well as 8-, 12-, and 24 h oscillations. This algorithm is repeated for each height interval.

3. Results

3.1 Basic Results

To give an overview of the MLT dynamics, the results of the mean wind, amplitude and phase of the TDT are given in Figure 1. The mean wind shows a clear seasonal behaviour, marked by a maximum in summer (>30 m/s) and two minima (~0 m/s) during the equinoxes. The meridional component is only about half as strong as the zonal one and consequently a significantly smaller seasonal variability is seen. At the beginning of the year, the zonal/meridional wind is eastward/southward directed and reverses in early spring. This reversal begins at high altitudes and progresses downward. In summer, again westerlies are found at greater altitudes, while in the upper mesosphere easterlies are prevailing. In autumn the wind turns back to westerly/northerly.

Considering the TDT amplitudes, a similar seasonal cycle in both components is evident. The amplitudes are smaller during summer (~2-3 m/s) and show larger values in March (~8 m/s) and October (~12 m/s). The maxima occurring during the equinoxes correlate with the minima of the mean wind. The contrary is the case in summer, when the mean wind is strong and the amplitudes have smallest values. Considering the linear wave theory of the solar tides (Chapman et al., 1970), dependence can be suggested. In general, the amplitudes are small at lower altitudes and increase with height. An exception is seen in October, when the meridional component decreases at altitudes above 91 km. This phenomenon has not been reported in other studies and will be investigated in more detail in section 4.2.

The phase is negative, which implies an upward propagating wave. Only in January the opposite case is observed, indicating a downward directed energy

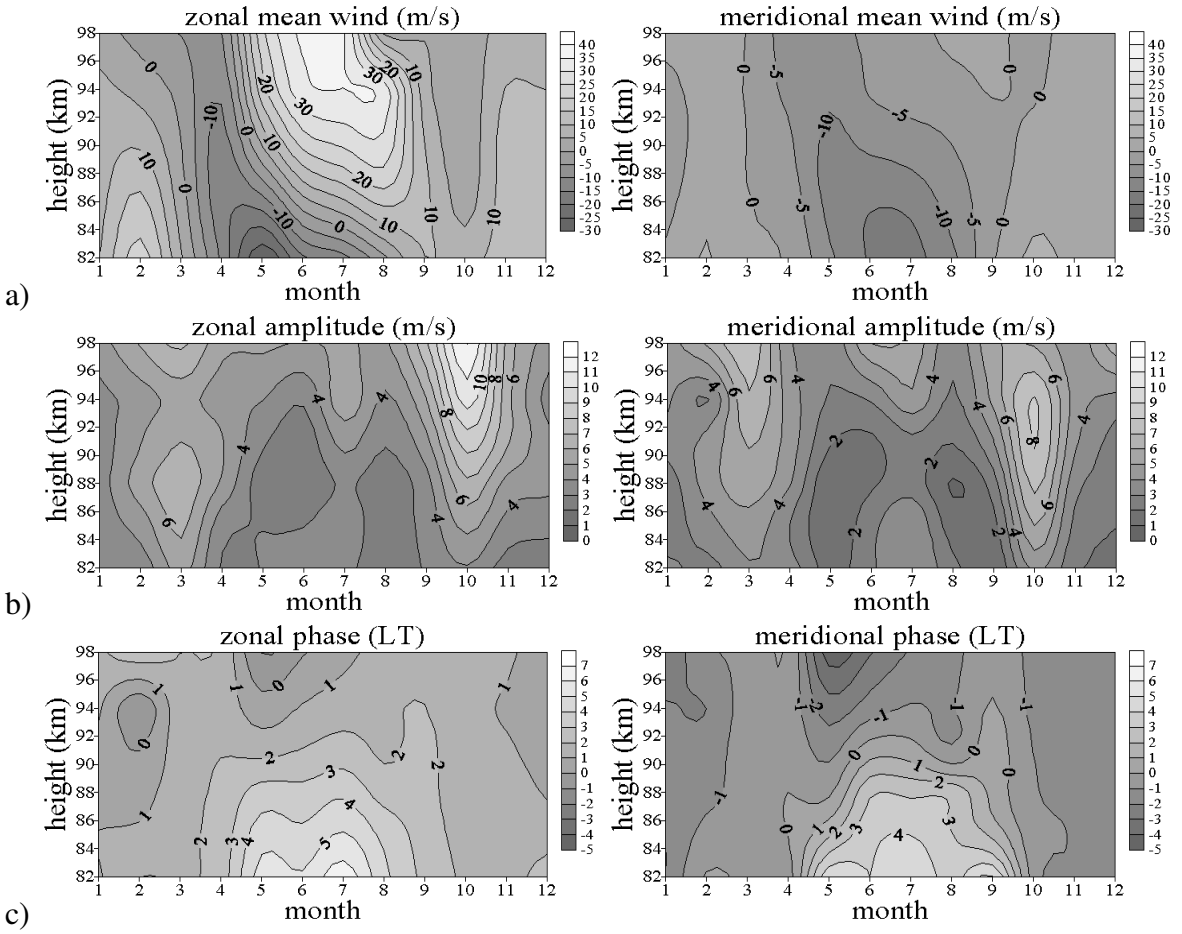

Figure 1: *The seasonal cycle of the zonal (left column) and meridional (right column) components of the a) mean wind, b) amplitude and c) phase of the 8-h tide over Collm, using the data from 2005 – 2009.*

transport. Thus the TDT cannot propagate. A seasonal behaviour is also seen, which shows a similar pattern for both components. The phase difference between the zonal and meridional components is close to +2 h. In winter the phases are the earliest and advance to later times in summer.

3.2 The characteristics of the 8-h tide

The zonal and meridional amplitudes of the TDT at 91 km are presented in Figure 2. This height was chosen, because the statistical errors are smallest there. In general, the observed seasonal cycle includes every significant characteristic, but sometimes differs slightly in detail. The largest amplitudes occur in October (~8 m/s) and March (~6 m/s) and both components reach the smallest values during summer (~2-3 m/s). In July the zonal amplitude shows a weak summer maximum with slightly higher values (~4 m/s). The large error bars indicate a strong inter-annual variability.

Throughout the year, on an average the zonal component is slightly stronger than the meridional (Figure 3). The difference mostly ranges from -1 m/s to +2 m/s, with a few exceptions. There is neither seasonal behaviour nor a clear dependence on height of the amplitude difference. Particularly noticeable is the value at 98 km in October, where the difference is larger than +6 m/s. This is caused by the missing maximum of the meridional amplitude.

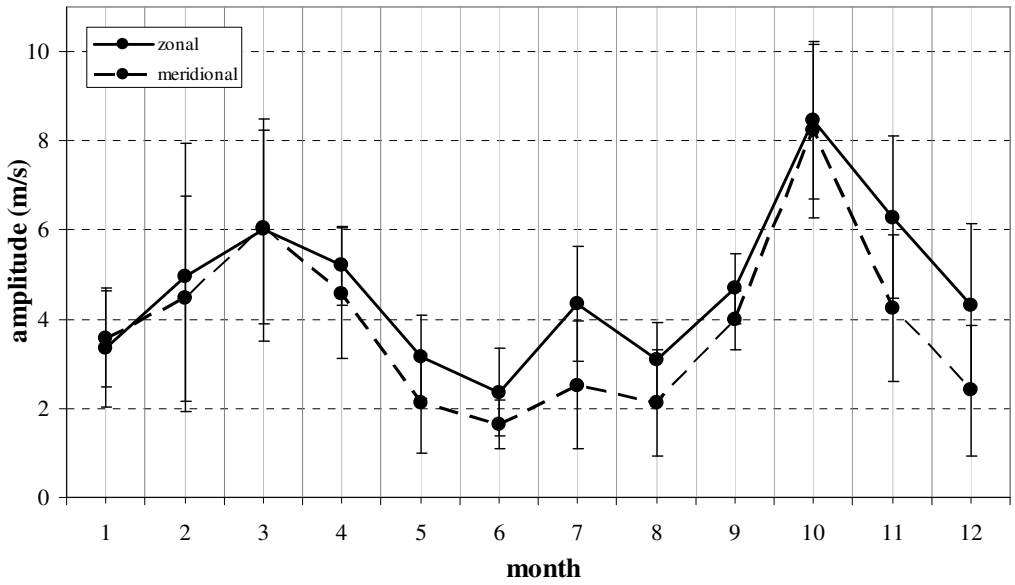

Figure 2: *Seasonal cycle of the zonal (solid line) and meridional (dashed line) amplitude of the 8-h tide at 91 km over Collm, using the data from 2005–2009. The error bars indicate the standard deviation of the individual monthly mean values.*

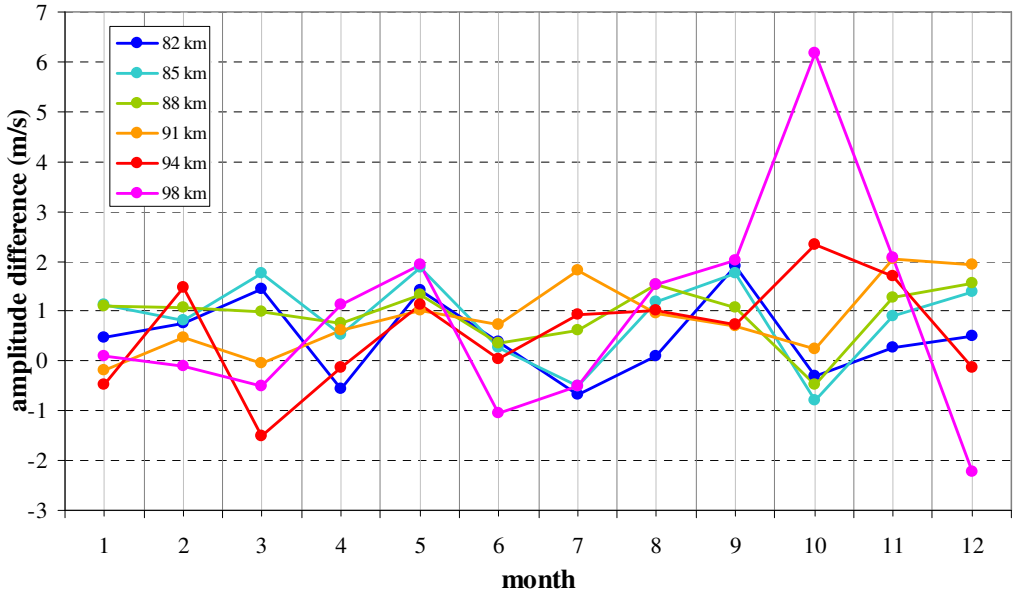

Figure 3: *Seasonal cycle of the amplitude difference between the zonal and meridional component of the 8- tide over Collm, using the data from 2005-2009.*

Figure 4 presents the phase of the TDT at a height of 91 km. Both components show a similar seasonal behaviour and a nearly constant phase difference close to 2 h. The phases are between 0 and 1 LT in winter and change to later times in summer. The phase shifts of 1-2 h occur during the equinoxes, but differ at the individual gates. In general, they are stronger and a bit later at the lower gates (~+4 h). At the highest gate, this relation is reversed, resulting in earlier phases in summer (~3-4 h). Except during the equinoxes, no significant year-to-year variability in phase is evident, also indicated by the comparatively short error bars.

Based on the linear theory of the solar tides, the zonal and meridional phase components differ by +90°. Then for the TDT, a difference close to +2 h is expected.

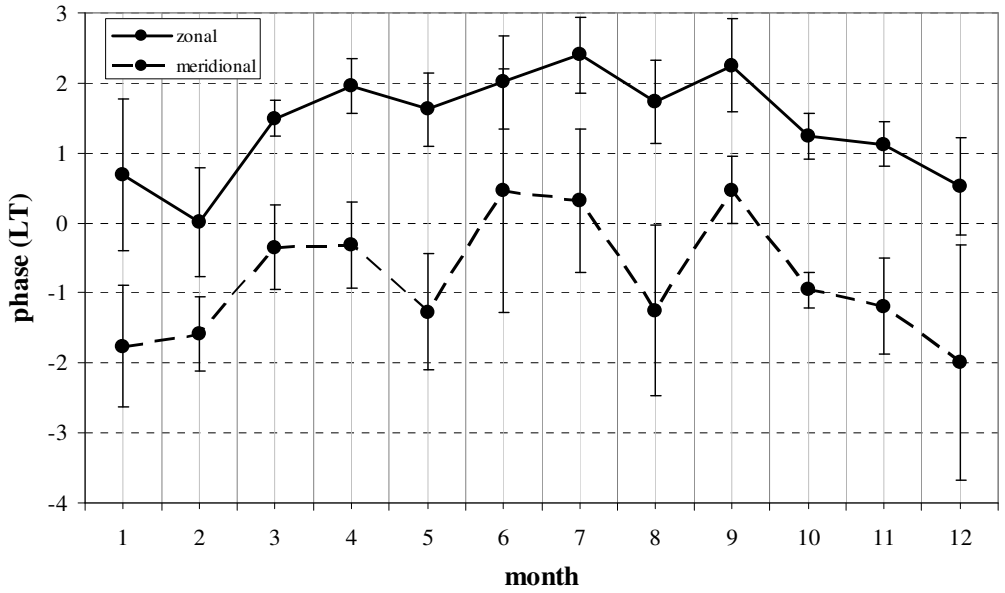

Figure 4: *Seasonal cycle of the zonal (solid line) and meridional (dashed line) phases of the 8-h tide at 91 km over Collm, using the data from 2005–2009. The error bars indicate the standard deviation of the individual monthly mean values.*

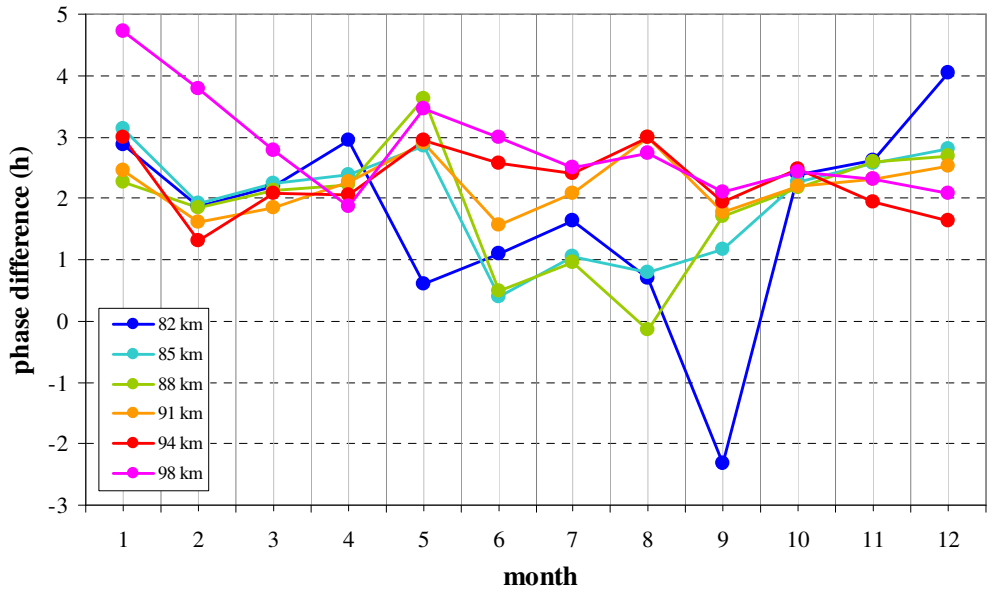

Figure 5: *Time-Height plot of the difference between the zonal and meridional phases of the 8-h tide over Collm, using the data from 2005-2009.*

As seen in Figure 5, this is true on an average, but a few disagreements are observed. In general, the phase difference ranges from 0 h to +3 h. One major exception occurs in summer. In the lower gates being 0-1 h, the phase difference increases to values above +2 h, but remains constant at the upper heights. Variations in gates 1 and 6 are most likely caused by data gaps or small amplitudes (see discussion below). Including the results of the phase variability with height, the observations indicate two different wave modes of the TDT. The first one dominates at heights below 91 km and the second one above 91 km.

To give an overview of the vertical behaviour, a height-profile was constructed for four months (Figure 6). Using a linear regression of the phase with height and also considering the two different wave modes, the vertical wavelengths were calculated

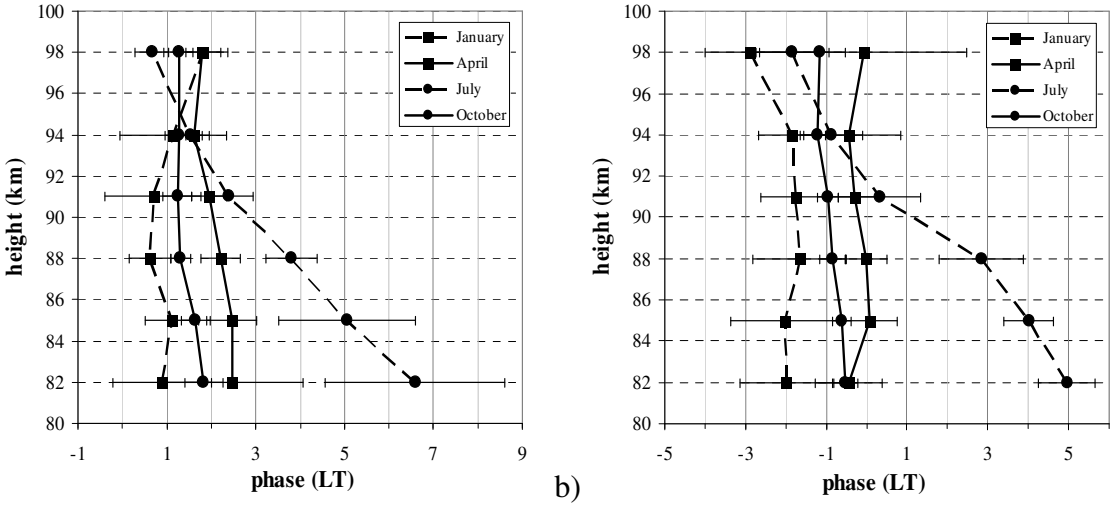

Figure 6: *Height-profile of the a) zonal and b) meridional phases of the 8-h tide over Collm for January, April, July and October, using the data from 2005-2009. The error bars indicate the standard deviation of the individual monthly mean values.*

for each month. Due to large uncertainties, the values of the meridional component at 98 km in February and at 82 km in September were excluded. Finally, the results were summarized for every season and rounded to whole five kilometres (Table 2). It is revealed that the vertical wavelengths are very short in summer (~30 km) and only a bit longer in spring (~50 km). The TDT shows significant longer values in late autumn (~140–175 km) and winter (~75-100 km), sometimes resulting in quasi infinite wavelengths. The chance between winter and summer is smoother than the one from summer to winter. The difference between the zonal and meridional components is most likely caused by the calculating process and the natural variability of the TDT.

4. Discussion

4.1 Comparisons with results from literature

Due to more frequent data gaps in gates 1 and 6, all observations made for these gates have to be analysed with special care. In addition, phases are less reliable when the amplitudes are small. The comparatively short observation period results in larger error bars, also considering the strong inter-annual and short-term variability of the TDT (Younger et al., 2002; Beldon et al., 2006). These aspects have to be taken into account when a comparison with observations made at various latitudes is accomplished.

The results of the mean wind in the measured heights are qualitatively similar to the climatology reported by Fleming et al. (1990); only the observed velocity over Collm shows lower values. An investigation to analyse the dependence between TDT and mean wind was performed, using gate 3 and 4. However, considering the resulting time series (not shown here), no hints were found to support any dependence between mean wind and TDT variability.

Beldon et al. 2006 reported observations made at Castle Eaton, UK (52.6°N, 2.2°W) at 90-95 km (comply with gate 4 and 5) from 1988-2004, using a VHF meteor radar without height finding. The results concerning phase and amplitude are

qualitatively the same than the ones reported here. The zonal amplitude is larger than the meridional, but the general smaller amplitudes are causing closer differences between them. In particular, the zonal peak in October (~5 m/s) is smaller and from May to August the meridional amplitude is more dominant. Furthermore, both components of the amplitude are less synchronic. The seasonal cycles of the phases are identical and also the phase shifts in February/March and September/October are similar. Only the difference between zonal and meridional components in June and July is not that close to +2 h over UK than it is here.

Namboothiri et al. (2004) reported observations made at heights of 76–98 km from 1997-2001, using the MF radar at Wakkanai, Japan (45.4°N, 141.7°E). The amplitudes at 82–98 km there show only one peak in winter (~6-10 m/s) and a minimum in summer (~4-7 m/s). In contrast to Collm, the maxima during the equinoxes are both missing. The phase behaviour is qualitatively similar at Wakkainai and Collm, but vertical wavelengths over Wakkanai are longer.

Thayaparan 1997 presented measurements at London, Canada (43°N, 81°W) from 1992-1996 at heights of 85–94 km, again using a MF radar. The results match with the ones reported by Namboothiri et al. (2004). In general, at each station (Collm, Wakkanai, London) a similar seasonal behaviour of the vertical wavelength is evident, but the observed values show differences. At Wakkanai and London the vertical wavelength reaches the longest values (>1000 km) in winter and autumn. This was also observed over Collm, but the wavelength is significantly smaller (~75–175 km). In spring the wavelength decreases to shorter values, in particular at Wakkanai and London. However, the differences are still large, except during summer when there is no difference between Collm (~30 km) and London (~20–35 km). Particularly noticeable is the strong difference between the zonal and meridional components of the vertical wavelength in London and Wakkanai, indicating an interaction of at least two different modes of the TDT.

Observations of the TDT from October 1999 – April 2001 made by the meteor radar at Esrange, Sweden (68°N, 21°E) at about 81-97 km were reported by Younger et al. (2002). In general, their amplitudes were significant smaller (~3 m/s), except for a strong peak in September and October (~9 m/s). The seasonal behaviour of the amplitude at Esrange shows a missing maximum in spring and a lower variability. The phase also takes defined positions in summer and winter, with shifts during the equinoxes. In contrast to Collm, the phase in winter is later and advances to earlier values in summer. Furthermore, the phase shows a different behaviour with height, resulting in shorter vertical wavelengths during winter and spring (~25–40 km) and longer values in summer (~40–60 km) and autumn (~60–90 km).

Table 2: *Vertical wavelengths of the 8-h tide of every season*

Season	vertical wavelengths [km]	
	meridional	zonal
Winter	100	75
Spring	50	50
Summer	30	30
Autumn	140	175

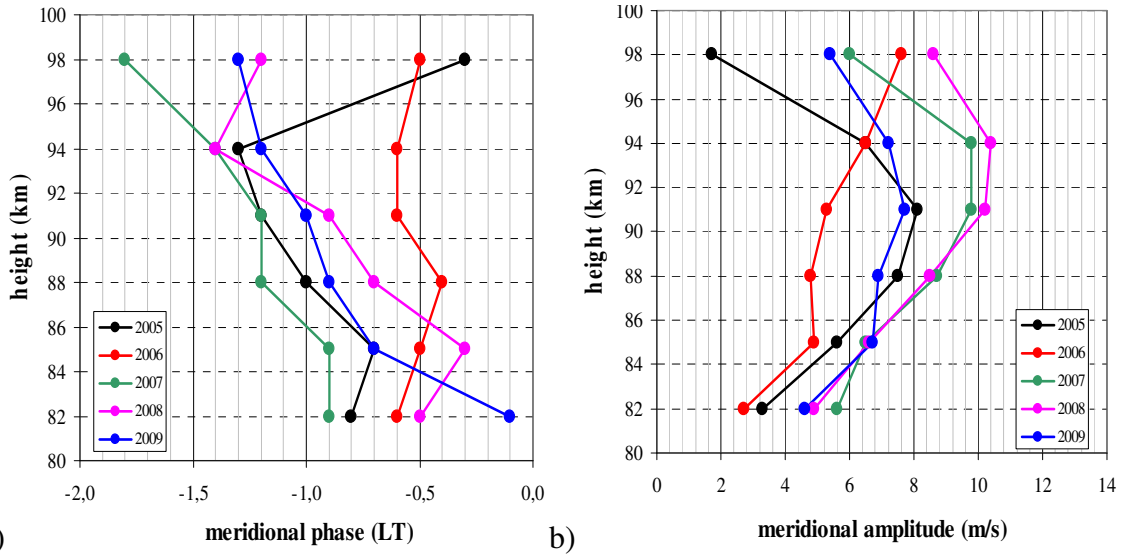

Figure 7: *Height-profile of the meridional a) amplitude and b) phase of the 8-h tide over Collm for October, using the data from 2005 – 2009.*

4.2 Weak meridional amplitudes in October

At the upper height gates, October meridional amplitudes are smaller than zonal ones (see Figure 1b). To investigate this phenomenon in more detail, the meridional amplitude and phase in October for each year is presented in Figure 7. Except for 2006, the amplitudes decrease above 91 km. Due to this similar behaviour, single measurement errors and an effect of a single extreme year can be excluded. The phase is nearly constant with height, which is particularly the case in 2006. The latter one shows an evanescent behaviour (Figure 7b). The amplitudes and phases of the remaining years match each other and no general phase shifts are evident, eliminating the possibility of a superposition between wave modes of the TDT. The phase shift in 2005 in the uppermost gate is most likely due to the small amplitude in gate 6. Therefore, further investigations including interactions with other atmospheric waves are needed to solve this problem of the zonal/meridional amplitude difference in October. But based on the regular occurrence, a physical reason is suggested.

5. Conclusions

The SKiYMET meteor radar located at Collm, Germany (51.3°N, 13°E) has measured the horizontal wind fields at heights about 80–100 km. Here we report results for the 8-hour tide. These are qualitatively similar to those from other observations made at mid-latitudes. Comparisons between mean wind and the 8-hour tide did not show a clear dependence. The amplitudes reach largest values in October (~12 m/s), show a secondary peak in March (~6-7 m/s) and are small during summer (~2-4 m/s). In July, a weak maximum (~5-6 m/s) is observed, and the meridional component shows values comparable to the other two maxima.

The phase shows earlier values in winter and advance to later times in summer. The phase difference between zonal and meridional components is close to +2 h. The amplitudes increase with height, conserving the seasonal cycle. In contrast, the phase profile splits up with height in summer, indicating the presence of two modes. Vertical wavelengths are short in summer and longer in autumn and winter.

Except for the phase behaviour, the results made at other latitudes partly differ from these observations, indicating a dependence of the TDT on latitude. At lower latitudes (43-45°N) the amplitude only shows one peak in winter and smaller values in summer, as well as significantly longer vertical wavelengths. At Arctic latitudes (68°N), a maximum in autumn occurred, but the other maxima were missing. There are also differences in phase and vertical wavelength.

Acknowledgements

The authors are grateful to Peter Hoffmann, Leipzig, for useful discussion, and Falk Kaiser, Leipzig, for maintaining the radar measurements.

References

Andrews, D.G., Holton, J.R., Leovy, C.B., 1987: Middle Atmosphere Dynamics. Academic Press, Orlando, 489 pp.

Beldon, C.L., Muller, H.G., Mitchell, N.J., 2006: The 8-hour tide in the mesosphere and lower thermosphere over the UK, 1988–2004. Journal of Atmospheric and Solar-Terrestrial Physics, 68, 655 - 668.

Chapman, S., Lindzen, R.S., 1970: Atmospheric Tides. Reidel, Dordrecht, 200 pp.

Fleming, E.L., Chandra, S., Barnett, J.J., Corney, M., 1990: Zonal mean temperature, pressure, zonal wind and geopotential heights as functions of latitude. Advances in Space Research, 10(12), 11 – 59.

Hagan, M.E., Forbes, J.M., Vial, F., 1995: On modeling migrating solar tides. Geophysical Research Letters, 22, 893 –896.

Hocking, W., Fuller, B., Vandepeer, B., 2001: Real-time determination of meteor-related parameters utilizing modern digital technology. Journal of Atmospheric and Solar-Terrestrial Physics, 63, 155 – 169.

Namboothiri, S.P., Kishore, P., Murayama. Y., Igarashi, K., 2004: MF radar observations of terdiurnal tide in the mesosphere and lower thermosphere at Wakkanai (45.4°N, 141.7° E), Japan. Journal of Atmospheric and Solar-Terrestrial Physics, 66, 241 – 250.

Teitelbaum, H., Vial, F., Manson, A.H., Giraldez, R., Massebeuf, M., 1989: Non-linear interactions between the diurnal and semidiurnal tides: terdiurnal and diurnal secondary waves. Journal of Atmospheric and Solar-Terrestrial Physics, 51, 627 – 634.

Thayaparan, T., 1997: The terdiurnal tide in the mesosphere and lower thermosphere over London, Canada (43°N, 81°W). Journal of Geophysical Research, 102, 21695 – 21708.

Tokumoto, A.S., Batista, P.P., Clemesha, B.R., 2007: Terdiurnal tides in the MLT region over Cachoeira Paulista (22.7ºS, 45ºW). Revista Brasileira de Geofísica, 25, 69 – 78.

Viehweg, C., 2006: Statistische Analyse von Meteorradardaten. Diploma thesis, Universität Leipzig, 23.

Younger, P.T., Panchva, D., Middleton H.R., Mitchell, N.J., 2002: The 8-h tide in the Arctic mesosphere and lower thermosphere. Journal of Geophysical Research, 107, 1420, doi:10.1029/2001JA005086.

Gravity wave influence on middle atmosphere dynamics in model and satellite data

P. Hoffmann, Ch. Jacobi

Abstract

Numerical results of the Middle and Upper Atmosphere Model (MUAM) for simulating the middle atmosphere conditions during January-February 2006 and 2008 have been compared with SABER/TIMED satellite data. A weaker amplitude of stationary waves in the mesosphere was found in 2008 compared to 2006. By forcing the model with realistic lower boundary conditions from reanalyses, averaged fields of zonal wind and temperature as well as stationary waves were simulated. Through changing of gravity wave (GW) amplitudes in the parameterisation, such a realistic behaviour can be approximately reproduced with model. We conclude that at least part of the middle atmosphere interannual variability is due to changes in GW forcing.

1. Introduction

Mechanistic circulation models of the middle atmosphere include simplified numerical schemes of some dynamical processes such as the gravity wave (GW) interaction with the mean flow. Their application is limited and parts of the input parameters, such as GW sources and the distribution of ozone, only consider zonal symmetric structures. In some models essentially tuned to describe the middle atmosphere like the Middle and Upper Atmosphere Model (MUAM, Pogoreltsev et al., 2007), the scheme that characterises the acceleration of the mean wind due to GW is insufficient to study coupling processes with the thermosphere, because the parameterisation only describes slowly GW with a fixed horizontal wavelength of 300 km, which cannot penetrate the lower thermosphere. Nevertheless, middle atmosphere processes may be approximately reproduced by the model. In this paper we compare two model runs for Jan-Feb 2006 and 2008 with satellite data. In other words, we are interested in how MUAM is able to reproduce the two different observations by simply changing the lower boundary conditions and the amplitude of GW. Figure 1 shows results from satellite data analysis at 45°N, that is the distribution of stationary planetary waves (SPWs) with height over the time from 2002 to 2008. A wave proxy is used based on standard deviations of temperatures from the SABER/TIMED instrument (Mertens and et al., 2001, 2004); a description of this proxy can be found in Hoffmann and Jacobi (2010); Borries and Hoffmann (2010). While in winter (Jan-Feb) 2006 the amplitudes of the mesospheric stationary wave component is well developed, two years later there exists almost no signal of SPW. It is supposed that such behaviour may be indirectly connected with the solar cycle that influences the dynamics of the middle atmosphere. Data analyses of GW potential energy also derived from SABER temperature profiles (Jacobi et al., 2011) of the last years have shown an increase of the mean GW activity in the mesosphere, which might be interpreted for this hypothesis. However, in contrast to the situation in summer, winter conditions are mainly affected by PW activity. GWs play the most important role. Thus, Fig. 2 presents global Jan-Feb mean GW potential energy and its change during the period from 2006 to 2008. Positive

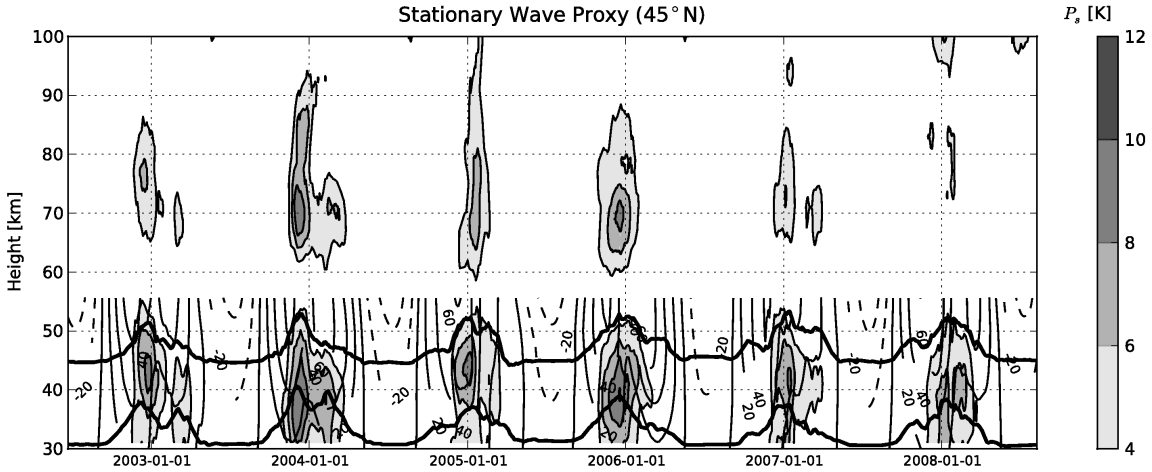

Figure 1: *Height-time cross section of a wave proxy derived from SABER temperatures at 45°N (grey scaling) from 2002-2008. The mean zonal wind (grey contours) and the same proxy at 30 km and 45 km (heavy black lines) obtained by MetO are added.*

deviations (middle panel of Fig. 2) in the upper mesosphere (∼80 km) denote stronger GW activity in 2006 than in 2008. An opposite sign is found in the lower thermosphere, which means a decrease of GW energy between the two years. Although the comparison of GW for these individual years indicates deviations from the current long-term trend the downward shifting of the breaking level (∼90 km) with increasing GW can be seen that motivates us for this comparison study.

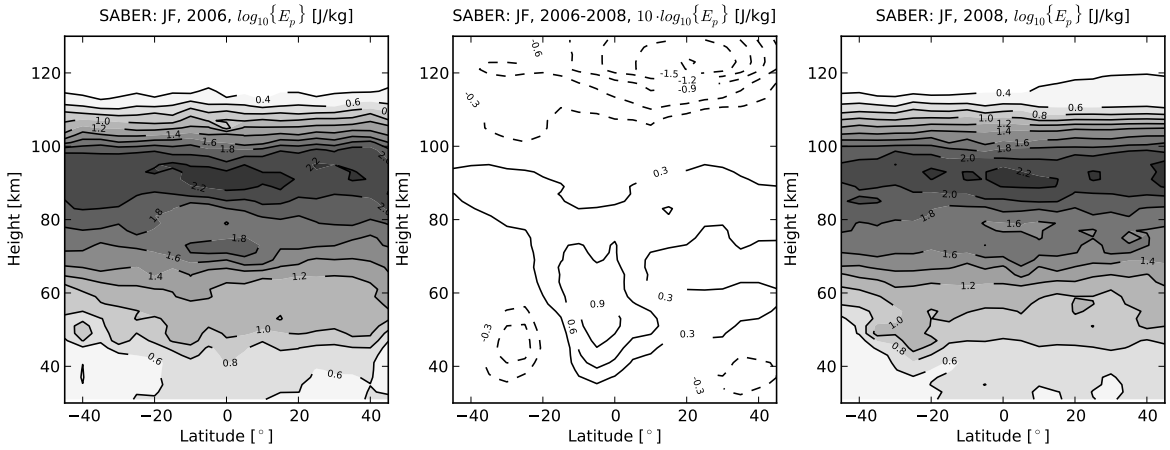

Figure 2: *Height-latitude cross section of Jan-Feb (JF) mean zonal averaged GW potential energy (E_p) for 2006 (left panel) and 2008 (right panel). The 2006-2008 difference pattern is shown in the middle of this figure. Note that the difference values are multiplied by factor of 10.*

In order to simulate the response of middle atmosphere dynamics on GW changes we amplify their amplitude to simulate changes in the middle atmosphere that are in accordance with SABER results and compare the different model results for the mean flow with satellite observations. For that purpose, global data from MetOffice stratospheric reanalyses

(MetO, Swinbank and Ortland, 2003) and unevenly spaced temperature profiles of the stratosphere, mesosphere and lower thermosphere provided by the SABER instrument are analysed with respect to planetary waves (PW) for comparison with the model. The following sections will give a coarse introduction to the circulation model (MUAM) and satellite data (SABER/TIMED) as well as the space-time method for analysing PW.

2. The middle and upper atmosphere model (MUAM)

The MUAM model (Pogoreltsev et al., 2007) was developed on the basis of the Cologne Model of the Middle Atmosphere-Leipzig Institute for Meteorology (COMMA-LIM), which was already applied in previous studies, e.g., by Fröhlich et al. (2003b); Jacobi et al. (2006). It is a so-called mechanistic three-dimensional model, in which the atmosphere circulation is self-consistently generated. Monthly zonal means of the geopotential height and temperature fields, that cover the troposphere and lower stratosphere up to 10 hPa, as well as the monthly averaged amplitude and phase of the first three zonal harmonics at 1000 hPa, taken from reanalysis data, are used as lower boundary conditions. These are typically averaged over 10 years (1992-2002). The radiative heating due to absorption O_3 and O_2 is described in the Strobel-scheme (Strobel, 1978) and the heating of H_2O and CO_2 is adjusted according to (Liou, 1992). The effect of GW on the circulation in the model is parametrised by a scheme based on Lindzen (1981).
The breaking of GW occurs, if the static stability vanishes, which corresponds to $\partial\theta/\partial z = 0$, and causes turbulence, mixing and GW dissipation in the upper mesosphere. Other modifications in this scheme has been implemented by Jacobi et al. (2006) as proposed in Gavrilov and Yudin (1992); Gavrilov and Fukao (1999); Akmaev (2001). A detailed description of the implemented parameterisations can be found in Fröhlich et al. (2003a). Several studies of planetary waves propagation in the middle atmosphere using COMMA-LIM were made by, e.g., Fröhlich et al. (2003b, 2005); Jacobi et al. (2006).
The 60-level version of MUAM allows to include the dynamics of the neutral upper atmosphere (thermosphere) by shifting the upper boundary to a height of about 300 km and incorporating a new scheme for extreme ultra-violet (EUV) heating based on the work of Richards et al. (1994). The 48-level version only considers the middle atmosphere up to about 135 km. The horizontal resolution in latitude and longitude is 5°×5.625° and the vertical levels are given by the non-dimensional height $x = -ln\,(p/1000\,hPa)$. The log-pressure height is obtained by multiplying x the non-dimensional height with the scale height ($H = 7\,km$).

Description	Symbol	Values	Unit
number of gravity waves		48	
horizont. wavelength	λ_x	300	km
phase speed	c_i	5, 10, 15, 20, 25, 30	m/s
azimuth angle	θ	0, 45, 90, 135, 180, 225, 270, 315	deg

Table 4: *Overview about parameters, which determine the spectrum of typical GW as used in the parametrisation scheme of MUAM.*

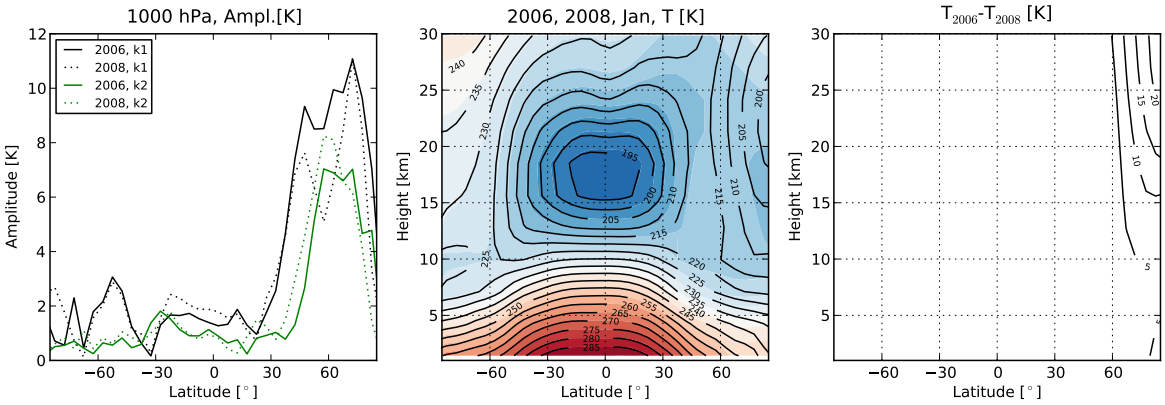

Figure 3: *Lower boundary for January condition of the years 2006 and 2008 that are used in the model runs as a function of latitude and/or height: temperature amplitude distribution for zonal wavenumbers k=1,2 at 1000 hPa (left panel), mean temperature cross sections (mid panel) and the difference (right panel).*

Here, the 48-level version of MUAM is applied in order to study the effect of GW changes on the middle atmosphere dynamics. In Tab. 4 parameters are listed, which indicate the spectrum of GW as considered in the parametrisation. Altogether 48 different kinds of GW are characterised by typical values of phase speed, horizontal wavelength and azimuth angle, which are implemented in 10 km. Their vertical velocity is weighted by frequency and phase speed as described in Jacobi et al. (2006). Latitudinal and seasonal dependencies are also considered in the parameterisation. Though, a stronger GW activity in the winter hemisphere is supposed.

3. Reanalyses and satellite data

Operational reanalyses from MetOffice (Swinbank and Ortland, 2003) and measurements from the SABER instrument on board of the TIMED satellite (Mlynczak, 1997) are analysed here in order to evaluate the model results. While the standard reanalysis products of meteorological parameters are provided on a regular grid up to the lower mesosphere (∼60 km), additional information of the temperature distribution in the stratosphere, mesosphere and lower thermosphere (30-130 km) can be retrieved from satellite (Mertens and et al., 2001, 2004). These data are unevenly spaced according to the orbital geometry. By applying spectral methods (Section 4) harmonic components are extracted from the data and compared with model results.

3.1 Boundary conditions to run the model

For running MUAM for two different Jan-Feb conditions in 2006 and 2008, the monthly mean zonal averaged temperature field up to 30 km and the first three stationary components at 1000 hPa with zonal wavenumber k=1,2,3 in temperature and geopotential height are extracted from NCEP/NCAR reanalyses (Kalnay et al., 1996) and implemented as lower boundary condition.

Figure 3 shows parts of the used lower boundary conditions to setup the model to situations that correspond to Jan 2006 and Jan 2008. The middle panel presents the monthly

zonal mean temperature pattern in the height-latitude cross section. The difference pattern between Jan 2006 and Jan 2008 is shown in the right panel and indicates a 10 K warmer lower north polar stratosphere in 2006. The monthly mean amplitudes of the first two harmonics (left panel), which corresponds to stationary planetary waves SPW1 (black) and SPW2 (green), reveal differences between 2006 (solid) and 2008 (dashed) at the lowest pressure level (1000 hPa). In particular, the SPW1 amplitudes at midlatitudes differ by about 2 K.

3.2 Satellite data analysis

The stratosphere, mesosphere and lower thermosphere satellite-based remote sensing techniques products (e.g. TIMED/SABER) extend the data base provided by reanalyses. In particular, limb-sounding of temperature profiles (Mertens and et al., 2001, 2004) provide useful information about the thermal structure and composition between the height-latitude range of 30-130 km and from 52° to 83° on the other hemisphere. After a 60 days yaw-cycle the latitude range reverses. Thus, since the instrument starts its observations in January 2002, a nearly continuous temperature coverage is available in a latitude range of about 50°S to 50°N.
For analysing the unevenly spaced data, taken from the so-called L2A (V1.07) product, with respect to PW we separated temperature into ascending (T_{asc}) and descending (T_{dsc}) nodes (Oberheide et al., 2003) and arranged the daily orbital information to a regular 3D-grid $[\Delta z, \Delta\phi, \Delta\lambda] = [2\,km, 5°, 10°]$ covering the middle atmosphere from $\phi = [-45° \ldots 45°]$ and $z = [30 \ldots 130\,km]$. By collecting all temperature values within such a grid box and averaging, a data set for analysing PW in the stratosphere and mesosphere is obtained. In the upper mesosphere and lower thermosphere, tidal effects blur a clear picture of PW. Spectral methods for analysing unevenly spaced data in the longitude and time domain (e.g. Hayashi, 1980; Zhang et al., 2006; Pancheva et al., 2009a,b) is applied to decompose PW and tides from polar orbiting satellite data in one step.

4. Analysis of waves

For the analysis of mean fields and wave components with respect to wavenumber (k) and frequency (ω) from unevenly spaced satellite data the method introduced in Pancheva et al. (2009a) is applied. This method also allows to analyse evenly spaced reanalyses and model output data. Based on a two-month data set (Jan-Feb) the algorithm is adopted for each height and latitude separately, in order to obtain a global characteristic of PW activity.
For each analysis, all longitudinal and temporal information $X_{\phi,z}(t, \lambda)$ are arrange in one vector and decomposed into mean (A_m), higher order trends (A_t, A_p) and harmonic components as given next:

$$
\begin{aligned}
X(t,\lambda) &= A_m + A_t \cdot t + A_p \cdot t^2 \\
&+ \sum_{\substack{n=1 \\ 3}} A_v \cdot cos(\omega_n t + \varphi_v) \\
&+ \sum_{\substack{k=1 \\ 16 \quad 3}} A_s \cdot cos(k\lambda + \varphi_s) \\
&+ \sum_{\substack{n=1 \\ 16}} \sum_{\substack{k=0 \\ 3}} A_w \cdot cos(k\lambda + \omega_n t + \varphi_w) \\
&+ \sum_{n=1} \sum_{k=0} A_e \cdot cos(k\lambda - \omega_n t + \varphi_e) \\
&+ R(t,\lambda).
\end{aligned} \tag{1}
$$

A least-squares (LS) method is then applied to determine the extracted spectral wave characteristics with respect to frequencies (ω_n) and zonal wavenumbers (k) for the amplitude and phase of vacillations (A_v, φ_v), stationary waves (A_s, φ_s) and westward (A_w, φ_w) and eastward travelling waves (A_e, φ_e). R gives the residual between analysis model and data. Here, we use this method to exclusively decompose the unevenly spaced SABER temperature profiles into the mean and stationary wave components. Alternatively, we compute proxies of travelling (P_t) and stationary (P_s) waves (Hoffmann and Jacobi, 2010) to compare planetary wave activity between different model runs.

5. Model comparison with data in the winters 2006 and 2008

In this section we present differences between model results for winter conditions (Jan-Feb) of the years 2006 and 2008 in comparison with SABER data. In order to run the model for these two cases, the lower boundary conditions of January 2006 and 2008 were extracted from NCEP reanalysis to replace the climatological data for 1992-2002 (see section 3.1). All runs were carried out without externally forced travelling PW. However, free travelling internal waves are self-consistently generated by the model. There are additional parameters (e.g. the amplitude of GW at the equator) that are adapted to the respective situations.

MUAM runs	year (lower boundary)	GW	figures
1	2006	2.0 cm/s	6, 7, 8, 9
2	2008	2.0 cm/s	6, 7, 8, 9, 11, 12
3	2008	2.2 cm/s	11, 12

Table 7: *List of model runs (330-390 days) and figures that demonstrate our results.*

At first we run the model by using the two different initial data. All other adjustments are equal (see Tab. 7). Although the lower boundaries represent January conditions, the model simulates January and February fields (model day 330-390). The period of time between model day 300 to day 330 corresponds to January 1 conditions over one month.

After that the seasonal variation of the sun begins. All used monthly mean climatological datasets, e.g., the distribution of ozone, represent still January condition. Next, another run is carried out by slightly increasing the GW amplitude from 2.0 to 2.2 cm/s (*run3*). Since the last solar maximum ($\sim$ 2002) an increasing of GW activity in the mesosphere is observed, e.g., by analysing GW potential energy from SABER temperature profiles, which motivates runs with modifies GW amplitudes.

5.1 Synoptic interpretation

Figure 1 shows a strong decrease of the SPW in the mesosphere at 45°N from 2006 to 2008. In order to investigate possible reasons for that we consider the two winter situations in more detail.
In the following Fig. 4 presents the mean zonal wind (contours) and temperature anomalies (color scaling) at 45°N obtained by MetO (lower panels) and SABER (upper panels). The time interval ranges from October 1 to March 31, respectively. The SABER data used here are daily values regridded on an evenly spaced 3-dimensional structure and the geostrophic approximation is applied to derive the zonal wind component from the horizontal pressure gradient. The values above 80 km should be regarded with care due to the tidal signals, which are not removed from the data.

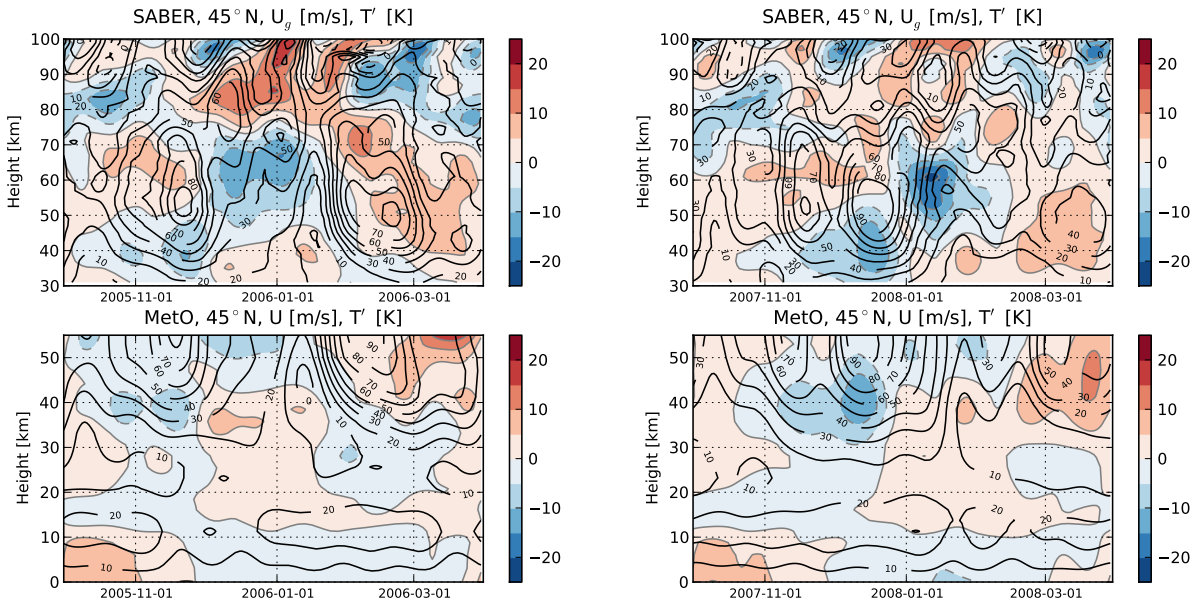

Figure 4: *Height-time cross section of smoothed zonal wind (contours) and temperature anomalies (color scaling) taken from MetO (lower panels) and SABER (upper panels) between the 1st October to 31st March of 2006 (left) and 2008 (right) at 45°N.*

The temporal behaviour in wind and temperature anomalies within the corresponding height range (30-55 km) is similar in the absolute values and the location of the jets. Both cases indicate a warming in the stratosphere (+5 K) connected with cooling in the mesosphere (-10 K) around Dec-Jan 2006 and Jan-Feb 2008. Before the temperature increase occurs, the zonal wind is strong, but much weaker during the warming period. A complete wind reversal, known from sudden stratospheric warming (SSW), is not observed

because this phenomenon is primarily located at higher latitudes (e.g. Labitzke, 1999; Hoffmann et al., 2007).
Figure 5 shows height-latitude patterns of Jan-Feb mean field differences between 2006 and 2008 of SABER temperature (left panel) and the amplitude of SPW1 (right panel). From mean temperature deviations, we may see that the summer hemisphere is hardly affected and the differences are weak. The equatorial region and winter hemisphere indicate a change of positive and negative anomalies, while positive signs correspond to larger values in 2006. Accordingly, a cooling of the tropical mesosphere (50-70 km) is observed, which is accompanied by a warming at midlatitudes. The upper mesosphere (>70 km) shows an opposite behaviour, that is a cooling at 45°N. Considering the change in SPW activity between 2006 and 2008, a decreasing amplitude of more than 2 K is observed in the mesosphere ∼70 km, as already depicted in Fig. 1.

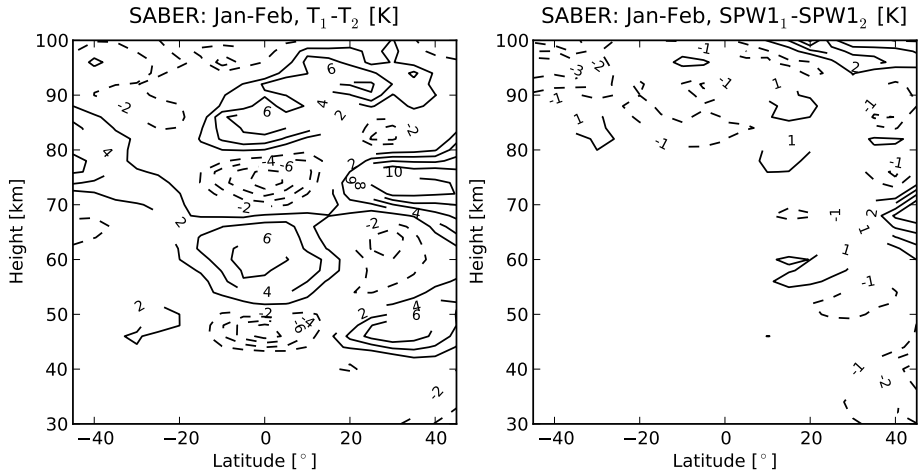

Figure 5: *Height-latitude pattern of 2006-2008 differences of Jan-Feb mean temperature (left panel), and stationary waves (right panel).*

5.2 Modelled differences by changing the lower boundary conditions

In this subsection we compare Jan-Feb mean zonal wind and temperature fields in the middle atmosphere obtained by model simulations (color scaling) with MetO (contours). The following figures show the individual two-monthly mean distributions in height-latitude cross sections of the year 2006 (left) and 2008 (right) as well as the deviations between the two patterns (middle).

Figure 6 compares the 2006 and 2008 mean zonal winds in Jan-Feb. Both model simulations (*run1*, *run2*) represent the known characteristics of the westerly and easterly jets in the middle atmosphere. The height level of the wind reversal in the mesopause region depends on the GW amplitude. In the two considered cases this parameter is set to 2 cm/s at the equator. The comparison between model and reanalyses up to about 55 km reveals a qualitatively better agreement for the summer than for the winter hemisphere. The reason is that no PW are able to exist during easterly winds. In contrast, on the winter hemisphere the mean wind is influenced by waves, which makes it more complicated to reproduce data by model simulations without externally forced travelling PW. For this reason one can sometimes reproduce observations very well (e.g. 2006) and sometimes less satisfactorily (2008).

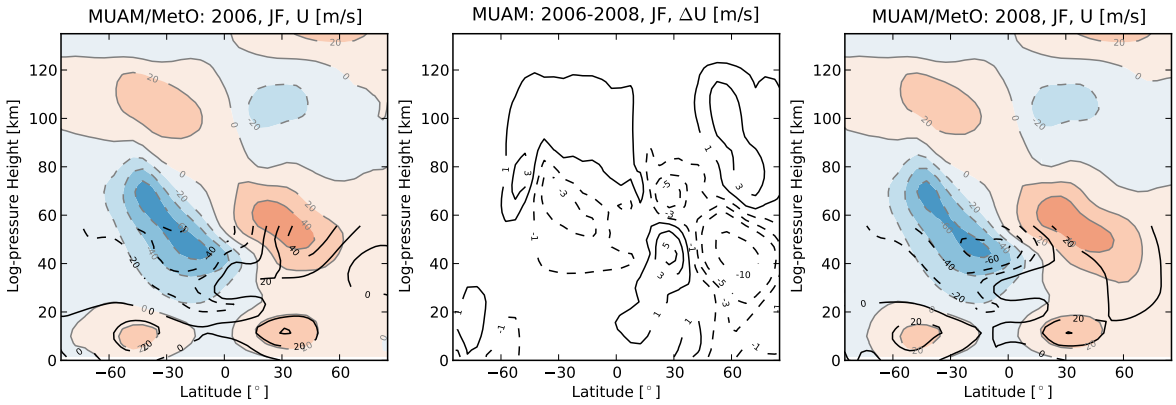

Figure 6: *Height-latitude cross section of mean zonal wind for Jan-Feb 2006 (left panel) and 2008 (right panel) generated by MUAM (colour code). MetO zonal winds are overlayed as isolines. The difference pattern is shown in the middle panel.*

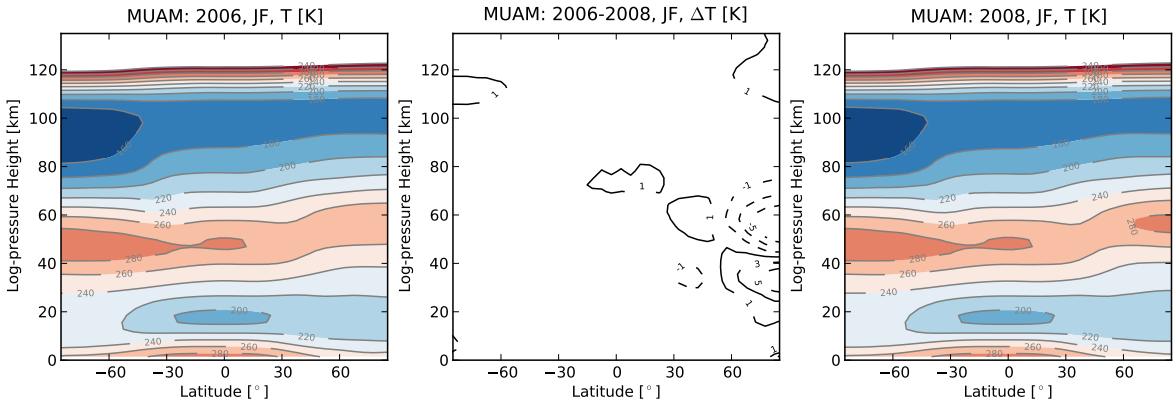

Figure 7: *Height-latitude cross section of mean temperature for Jan-Feb 2006 (left panel) and 2008 (right panel) generated by MUAM. The difference pattern is shown in the middle panel.*

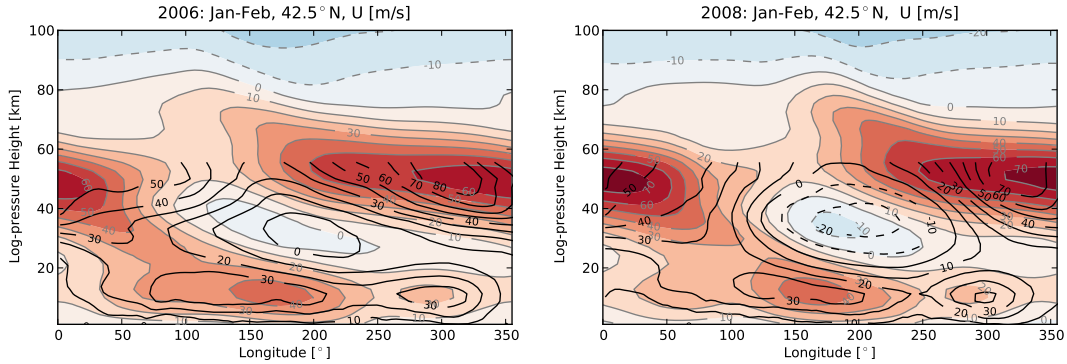

Figure 8: *Height-longitude cross section of zonal wind at 42.5°N modelled by MUAM (color scaling) and MetO (contours).*

Regarding the differences between the same two model simulations (*run1* and *run2*), Fig. 6 (middle panel) reveals negative (dashed lines) and positive (solid lines) anomalies in the zonal wind. Negative anomalies prevail in the region of the middle atmosphere jets, which mean generally stronger westerly winds in 2008 than in 2006 only due to changes of the lower boundary conditions.
Figure 7 presents the temperature distribution of the middle atmosphere for the same cases. The difference of the two patterns reveals a cooling (+5 K) of the stratosphere in 2008 and warming (-5 K) of the mesosphere at high latitudes in 2006. This behaviour can be explained by PW activity. Because externally forced travelling PW are not excited here, differences in SPW activity generated by the lower boundary must be responsible, which is discussed in the following paragraph.

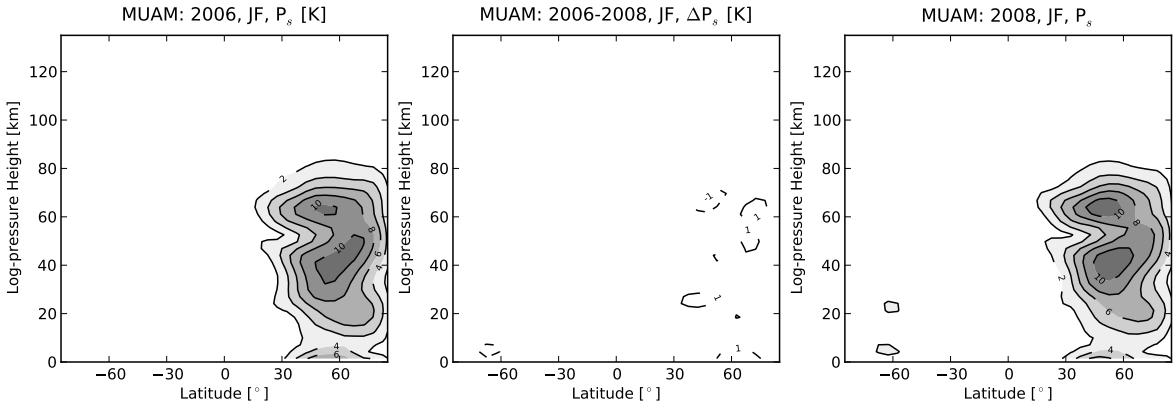

Figure 9: *Height-latitude cross section of the stationary wave proxy in temperature for Jan-Feb 2006 (left panel) and 2008 (right panel) generated by MUAM. The difference pattern is shown in the middle panel.*

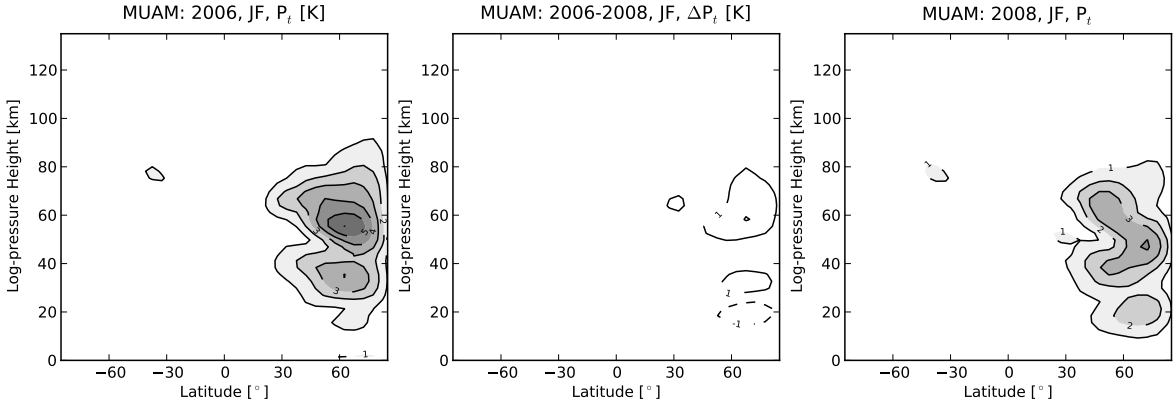

Figure 10: *Height-latitude cross section of the travelling wave proxy in temperature for Jan-Feb 2006 (left panel) and 2008 (right panel) generated by MUAM. The difference pattern is shown in the middle panel.*

It is known that most of the variations caused by PW occur in winter during which westerly winds prevail. Accordingly, we consider the mean zonal wind pattern in the

height-longitude plane at 42.5°N. Figure 8 presents again the two winter situations of 2006 (left part) and 2008 (right part) comparing MUAM (color scaling) and MetO (contours). In 2008 negative values of the zonal wind in the stratosphere over 150°E and 250°E can be observed in both data sets. However, these are stronger in MetO (-20 m/s) than in MUAM data (-10 m/s). In 2006 all values are positive (westerly). The strongest westerly winds with 70 m/s are observed over the Atlantic ocean (300°E to 0°E) in the lower mesosphere in 2008. From Fig. 5 one can estimate the magnitude of the stationary wave 1 in zonal wind to about 30-40 m/s between 50-60 km.
SPW are mainly forced in the troposphere. The amplitude of SPW1 at 1000 hPa may reach 10 K in the winter hemisphere (see Fig. 3). Here, we only consider proxies of stationary waves (P_s). In order to obtain the distribution shown in Fig. 9, we calculate the time mean of an 4-dimensional array that includes temperature data arranged in longitude, latitude, altitude and time. Then the standard deviations w.r.t the longitudes are computed. The outer two panels in Fig. 9 show small differences the standard deviation between the two model runs for 2006 and 2008. From SABER data long-term analysis it is expected that the secondary maximum of the SPW proxy in the mesosphere almost vanishes at midlatitudes. This is not the case comparing *run1* with *run2*.
The travelling PW proxy component is shown in Fig. 10. This proxy mainly represents atmospheric normal modes, for which it is assumed that the source is noise in the meteorological parameters in the troposphere or nonlinear interaction between SPW and the mean flow (e.g. Pogoreltsev et al., 2007).

5.4 Model differences by changing of gravity wave amplitudes

One major uncertainty in numerical models is caused by the parameterisation of small scale processes such as GWs. In Fig. 9 it could be shown that without changes of GW amplitudes one cannot reproduce seasonal or year-to-year variability. Thus, a third model run (*run3*) has been carried out with increased GW amplitudes. One expects in such a case that the breaking level and the zonal mean wind reversal descends.
Figure 11 depicts the acceleration rate (ACC) of the mean zonal wind due to GW for the two situations. A larger amplitude of GW in 2008 (*run*3) leads to a stronger deceleration of the mean flow in the upper mesosphere. We interpret the positive anomalies between 2006 and 2008 in the winter hemisphere around 70 km as a stronger deceleration rate of about 1 m/s/d. The effects in the southern hemisphere are more pronounced.
Recently, analyses of GW potential energy derived from SABER temperature profiles (Jacobi et al., 2011) have shown that the GW activity from 2003 to 2008 is increasing in the mesosphere. Above, in the lower thermosphere a decrease is observed.
The model results using the different amplitudes of GW for Jan-Feb conditions in 2008 are shown in Fig. 12. These patterns obtained by MUAM reveal similarities to the patterns in Fig. 5 obtained by SABER. At first we consider the temperature anomalies. In both the observation and model data one can find negative values at about 40 km over the tropics and positive values around 60 km altitude. At low latitudes (20°N-40°N) of the northern hemisphere one can readoff positive deviations around 40 km (+1 K) and stronger negative values at about 60 km (-5 K), which indicates a warming of the stratosphere. In contrast, the mesosphere is cooling during the two years by +3 K (MUAM) and +10 K (SABER). Note that positive differences represent cooling from 2006 through 2008.
The similar behaviour shows the comparison of SPW between model and data reveals

promising results. Although we use different methods for analysing stationary components, for SABER (one-step) and MUAM (proxies), a positive deviation around 40°N and 70 km is observed in model (*run3*) and SABER analyses. A positive anomaly implicates a stronger secondary maximum in 2006 than in 2008 (about 2-3 K). Due to the stronger GW amplitudes the wind reversal in the mesopause region descends and causes a damping of the SPW in the mesosphere. Figure 12 (left panel) confirms this change in the middle atmosphere circulation by a drop of the westerly jet on the winter hemisphere of about 15 m/s at low-latitudes and at 70 km log-pressure height.

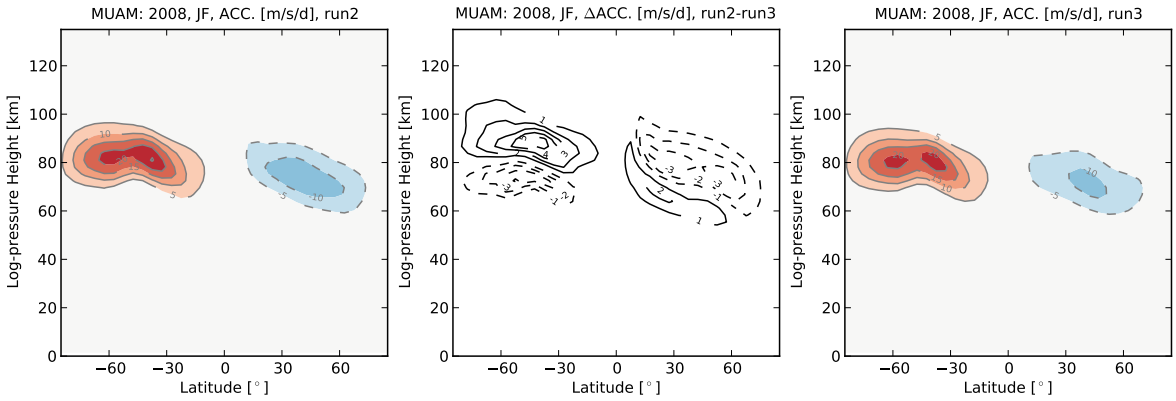

Figure 11: *Height-latitude cross section of acceleration rates for the zonal direction in Jan-Feb 2006 (left panel) and 2008 (right panel) generated by MUAM. The difference pattern is shown in the middle panel.*

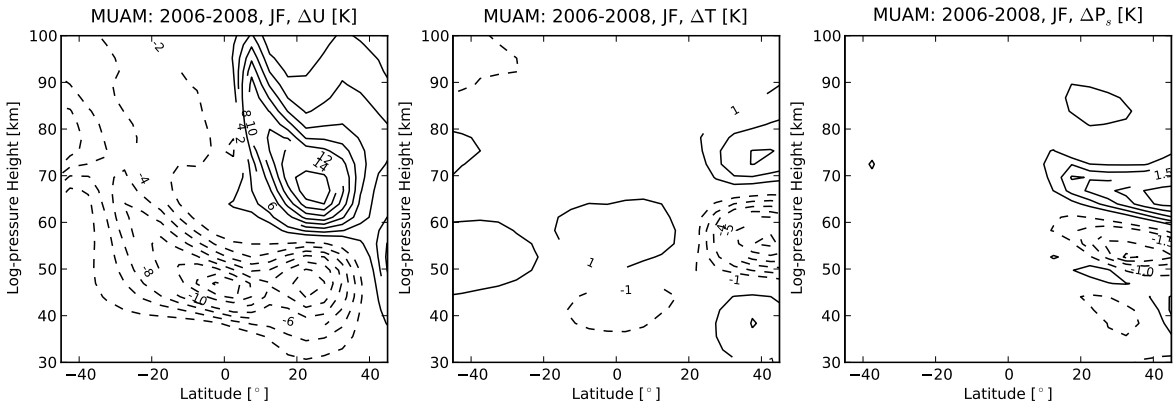

Figure 12: *Height-latitude cross section of differences between model run2 and run3 of mean zonal wind (left panel), temperature (middle panel) and stationary wave proxy (right panel).*

6. Conclusions

A mechanistic model of the middle and upper atmosphere has been applied in order to estimate the differences between two winters. The results has been compared with

observations. Until now such models are mainly used to study processes in middle atmosphere dynamics on the basis of climatological (long-term mean) lower boundary conditions. Here, model sensitivity studies have been carried out with monthly mean reanalyses data of January 2006 and 2008 to simulate individual seasons. For comparison satellite temperature data from the SABER instrument (30-130 km) and MetO reanalyses (0-55 km) were used.
It was shown by two examples for Jan-Feb 2006 and 2008 that current model runs cannot reproduce the observations by only changing the lower boundary mean fields. However, it has been demonstrated that the secondary SPW maximum in the lower mesosphere is reduced by increasing GW amplitudes. This is in accordance with SABER observations in 2008.
From these simulations we conclude that mechanistic models like MUAM require an detailed climatology of GW activity dependent on year, season, latitude, and height. A longitudinal distribution may also help in this context. Thus, the analysis of GW energy from satellite temperature profiles up to 130 km (Hoffmann and Jacobi, 2010) would be suitable to install such a climatological database in the model.

Acknowledgments

This study was supported by Deutsche Forschungsgemeinschaft under grant JA 836/24-1. Many thanks to the British Atmospheric Data Centre (BADC) for providing the MetOffice reanalyses and to NASA for providing the SABER/TIMED satellite measurements. Special thanks to Ekaterina Suvorova and Alexander Pogoreltsev (RSHU) for technical advises for running the MUAM model.

References

Akmaev, R. A. (2001). Simulation of large scale dynamics in the mesosphere and lower thermosphere with Doppler-spread parameterization of gravity waves. 2. Eddy mixing and the Diurnal Tide. *J. Geophys. Res.*, 102:1203–1205.

Borries, C. and Hoffmann, P. (2010). Characteristics of F2-layer planetary wave-type oscillations in northern middle and high latitudes during 2002 to 2008. *J. Geophys. Res.*, 115:A00G10, doi:10.1029/2010JA015456.

Fröhlich, K., Jacobi, C., and Pogoreltsev, A. I. (2005). Planetary wave transience effects on the zonal mean flow: simulations with the COMMA-LIM model. *Adv. Space Res.*, 35:1900–1904.

Fröhlich, K., Pogoreltsev, A., and Jacobi, C. (2003a). The 48-layer comma-lim model: Model description, new aspects and climatology. *Rep. Inst. Meteorol. Uni. Leipzig*, 30:149–155.

Fröhlich, K., Pogoreltsev, A. I., and Jacobi, C. (2003b). Numerical simulation of tides, Rossby and Kelvin waves with the COMMA-LIM model. *Adv. Space Res.*, 32:863–868.

Gavrilov, N. M. and Fukao, S. (1999). A comparison of seasonal variations of gravity wave intensity observed with the middle and upper atmosphere radar with a theoretical model. *J. Atmos. Sci.*, 56:3485–3494.

Gavrilov, N. M. and Yudin, V. A. (1992). Model for coefficients of turbulence and effective Prandtl Number produced by breaking gravity waves in the upper atmosphere. *J. Geophys. Res.*, 97:7619–7624.

Hayashi, Y. (1980). A method for estimating space-time spectra from polar-orbiting satellite data. *J. Atmos. Sci.*, 37:1385–1392.

Hoffmann, P. and Jacobi, C. (2010). Connection of planetary waves in the stratosphere and ionosphere by the modulation of gravity waves. *Rep. Inst. Meteorol. Univ. Leipzig*, 47:23–36.

Hoffmann, P., Singer, W., Keuer, D., Hocking, W. K., Kunze, M., and Murayama, Y. (2007). Latitudinal and longitudinal variability of mesospheric winds and temperatures during stratospheric warming events. *J. Atmos. Solar-Terr. Phys.*, 69:2355–2366.

Jacobi, C., Fröhlich, K., and Pogoreltsev, A. I. (2006). Quasi two-day-wave modulation of gravity wave flux and consequences for planetary wave propagation in a simple circulation model. *J. Atmos. Solar-Terr. Phys.*, 68:283–292.

Jacobi, C., Hoffmann, P., Placke, M., and Stober, G. (2011). Some anomalies of mesosphere/lower thermosphere parameters during the recent solar minimum. *Adv. Radio Sci.*, accepted.

Kalnay, E., Kanamitsu, M., Kistler, R., Collins, W., Deaven, D., Gandin, L., Iredell, M., Saha, S., White, G., Woollen, J., Zhu, Y., Leetmaa, A., Reynolds, R., Chelliah, M., Ebisuzaki, W., Higgins, W., Janowiak, J., Mo, K. C., Ropelewski, C., and Wang, J. (1996). The NCEP/NCAR 40-year reanalysis project. *Bull. Amer. Meteor. Soc.*, 77:437–470.

Labitzke, K. (1999). *Die Stratosphäre*. Springer Verlag.

Lindzen, R. S. (1981). Turbulence and and stress owing ti gravity waves and tidal breakdown. *J. Geophys. Res.*, 86:9709–9714.

Liou, K. N. (1992). *Radiation and Cloud Processes in the Atmosphere*, page 487. Oxford Monographs on Geology and Geophysics.

Mertens, C. J. and et al. (2001). Retrieval of mesospheric and lower thermospheric kinetic temperature from measurements of CO2 15 mm earth limb emission under non-LTE conditions. *Geophys. Res. Lett.*, 28:1391–139.

Mertens, C. J. and et al. (2004). SABER observations of mesospheric temperatures and comparisons with falling sphere measurements taken during the 2002 summer MaCWAVE campaign. *Geophys. Res. Lett.*, 31:L03105, doi:10.1029/2003GL018605.

Mlynczak, M. G. (1997). Energetics of the mesosphere and lower thermosphere and the SABER Experiment. *Adv. Space Res*, 20(6):1177–1183, doi:10.1016/S0273-1177(97)00769-2.

Oberheide, J., Hagan, M. E., and Roble, R. G. (2003). Tidal signatures and aliasing in temperature data from slowly precessing satellites. *J. Geophys. Res.*, 108(A2), doi:10.1029/2002JA009585.

Pancheva, D., Mukhtarov, P., Andonov, B., Mitchell, N. J., and Forbes, J. M. (2009a). Planetary waves observed by TIMED/SABER in coupling the stratosphere-mesosphere-lower thermosphere during the winter of 2003/2004: Part 1 - Comparison with the UKMO temperature. *J. Atmos. Solar-Terr. Phys.*, 71:61–74, doi:10.1016/j.jastp.2008.09.016.

Pancheva, D., Mukhtarov, P., Andonov, B., Mitchell, N. J., and Forbes, J. M. (2009b). Planetary waves observed by TIMED/SABER in coupling the stratosphere-mesosphere-lower thermosphere during the winter of 2003/2004: Part 2 - Altitude and latitude planetary wave structure. *J. Atmos. Solar-Terr. Phys.*, 71:75–87, doi:10.1016/j.jastp.2008.09.027.

Pogoreltsev, A. I., Vlasov, A. A., Fröhlich, K., and Jacobi, C. (2007). Planetary waves in coupling the lower and upper atmosphere. *J. Atmos. Solar-Terr. Phys.*, 69:2083–2101.

Richards, P. G., Fennelly, J. A., and Torr, D. G. (1994). EUVAC: A Solar EUV Flux Model for Aeronomic Calculations. *J. Geophys. Res.*, 99(A5):8981–8992, doi:10.1029/94JA00518.

Strobel, D. F. (1978). Parameterization of the atmospheric heating rate from 15 to 120 km due to O_2 and O_3 absorption of solar radiation. *J. Geophys. Res.*, 83:6225–6230.

Swinbank, R. and Ortland, D. A. (2003). Compilation of the wind data for the Upper Atmosphere Research Satellite (UARS) Reference Atmosphere Project. *J. Geophys. Res.*, 108(D19):4615.

Zhang, X., Forbes, J. M., Hagan, M. E., Russell III, J. M., Palo, S. E., Mertens, C. J., and Mlynczak, M. G. (2006). Monthly tidal temperatures 20-120 km from TIMED/SABER. *J. Geophys. Res.*, 111:A10S08, doi:10.1029/2005JA011504.

Addresses of the Authors:

Peter Hoffmann (phoffmann@uni-leipzig.de)
Christoph Jacobi (jacobi@uni-leipzig.de)

Institute for Meteorology
University of Leipzig
Stephanstr. 3
04103 Leipzig

Appendix

Running MUAM on Linux-server

- MUAM works at LIM server (e.g., passat, anemos) using the Fortran compiler (*ifort*). There, one can run the model in background using the *"nohup"* command. Via vpn-client it is possible to open a tunnel to enter the internal network of the LIM from outside for starting, terminating or modifying model runs. Many scientific analysis programs/software are available on the LIM Linux-server (Debian).
- file system: muam_stud
  - src: includes model source code
    - *model_48.f (main program, most of the subroutines are called here)*
    - *com_main.fc (all common variables are defined here)*
    - *com_grid.f (includes model grid dimensions)*
  - run:
    - include initial data:
      - *f2_0_Jan_new (initial field for January, windless, isotherm)*
      - *TSMo3_v02.data (monthly mean ozone climatology)*
      - *T_lower.dat (height-latitude monthly mean temperature distribution)*
      - *t[1,2,3]_1000mb_Jan9202.dat (include ampl. and phas. of the first harmonics)*
    - files to manage the model run
      - *mod_comma_Alex (includes switches)*
      - *Run32_tst_Alex_data ()*
    - model output (unformatted)
      - *uvt390_jan_tst.dx (zonal- and meridional wind, temperature)*
      - *phi.dx (geopotential height)*
      - *wvel.dx (vertical velocity)*
      - *gwacu.dx; gwacv.dx (gravity wave acceleration)*
      - *gwfluxu.dx; gwfluxv.dx (gravity wave momentum fluxes)*
  - mak: includes shell-scripts to
    - compile source code: *imake48jan.sh*
    - run model in one-step: *run_2006.sh (0-120, 120-210, 210-300, 300-390)*
- analysing model results: *muam_analysis_toolkit*
  - *background fields (*.dx)*
  - *proxies of planetary waves and tides*
  - *difference between two model runs*
  - *calculating amplitude profiles of spectral wave components (one-step method) at fixed latitude*
  - *calculating spectra for westward- and eastward travelling waves at fixed a latitude*
  - *plotting arrows of the meridional circulation*

Peculiarities of mesosphere/lower thermosphere parameters during solar minimum 23/24

Ch. Jacobi[1], P. Hoffmann[1], C. Unglaub[1], M. Placke[2], G. Stober[2]

[1]Institute for Meteorology, University of Leipzig, Stephanstr. 3, 04103 Leipzig, Germany
[2]Leibniz Institute of Atmospheric Physics at the Rostock University, Schlossstraße 6, 18225 Kühlungsborn, Germany

Abstract

The 2009 solar minimum 23/24 has been characterized by an anomalous strong decrease in thermospheric density. We analyze anomalies of mesosphere/lower thermosphere parameters possibly connected with this effect. Nighttime mean low-frequency reflection heights measured at Collm, Germany, show a very strong decrease after 2005, indicating a density decrease. This decrease is also visible in mean meteor heights measured with a VHF meteor radar at Collm. It is accompanied by an increase/decrease of gravity wave (GW) amplitudes in the upper mesosphere/lower thermosphere. On the decadal scale, GWs are negatively correlated with the background zonal wind, but this correlation is modulated in the course of the solar cycle, indicating the combined effect of GW filtering and density decrease.

Zusammenfassung

Das solare Minimum des Jahres 2009 war durch außerordentlich starken Rückgang thermosphärischer Dichte charakterisiert. Hier werden Parameter der Mesosphäre und unteren Thermosphäre untersucht, deren Variabilität eventuell mit diesem Effekt zusammenhängt. Im Einzelnen war ein starker Rückgang der Reflexionshöhe von Langwellen zu verzeichnen, der sich auch in Meteorhöhen zeigt. Dieser Rückgang, verursacht durch geringere Dichte, war mit einer Zunahme/Abnahme atmosphärischer Schwerewellen in der Mesosphäre/unteren Thermosphäre verbunden. Atmosphärische Schwerewellen in der Mesosphäre werden durch den Grundwind gesteuert; der Zusammenhang variiert jedoch im Verlauf des Sonnenfleckenzyklus.

1 Introduction

It is widely known that solar variability influences the atmosphere (e.g., Gray et al., 2010), e.g. the dynamics of the middle and upper atmosphere. In particular, search for an effect of the 11-year solar Schwabe cycle has been undertaken, for example, to partly explain the observed variability of the mesosphere and lower thermosphere (MLT), which can be studied, e.g., by radars. Indeed, indication for a solar effect has been found in MLT radar wind time series over Central Europe (Jacobi and Kürschner, 2006; Keuer et al., 2007).

Solar cycles are different from one to another. Especially, the recent solar minimum 23/24 has been extremely extended and extraordinarily deep. Consequently, it led to extreme upper atmosphere reactions, in particular a decrease in thermospheric

density (Emmert et al., 2010; Solomon et al., 2010) which exceeds the expectations that would have been based on conventional solar indices like the sunspot number or the F10.7 radio flux.

Lower ionospheric electron density reacts on solar extreme ultraviolet (EUV) variations, which leads to a quasi 11-year modulation of radio wave reflection heights. These have been observed, e.g., by Kürschner and Jacobi (2003) who found that low-frequency (LF) radio wave ionospheric reflection heights measured at Collm (177 kHz, distance to transmitter about 160 km) are about 2 km lower during solar maximum than during solar minimum. This is owing to the increased ionisation during solar maximum, however, this effect is superposed by thermal shrinking of the mesosphere during solar minimum, since the middle atmosphere has a solar cycle signal of about 2 K difference between maximum and minimum. However, this thermal shrinking is usually overcompensated by increased ionisation. We are interested, whether the recent extreme solar minimum has led to anomalous signatures either in MLT wind or density. We focus on the summer MLT, which is not that much influenced by stratospheric planetary wave activity.

2 Measurements

2.1 Collm LF lower ionospheric drifts, reflection heights, and GW estimates

At Collm Observatory (51.3°N, 13°E), MLT winds have been obtained by D1 LF radio wind measurements from 1959-2008, using the sky wave of three commercial radio transmitters. The data are combined to half-hourly zonal (u) and meridional (v) mean wind values. The virtual reflection heights have been estimated since late 1982 using measured travel time differences between the separately received sky wave and the ground wave (Kürschner et al., 1987) of one transmitter (Zehlendorf near Berlin, frequency 177 kHz, reflection point at 52.1°N, 13.2°E). More details of the Collm LF system are given in Jacobi (2011).

Since the LF reference height changes in the course of the day, a continuous time series is not available and consequently GW spectra cannot be calculated. However, using the method presented by Gavrilov et al. (2001), horizontal wind fluctuations $u´$ and $v´$ in the period range 0.7-3 h can be estimated from the wind measurements on 177 kHz, which may be taken as GW proxy. Jacobi et al. (2006) has used this method to analyze Collm wind fluctuations from 1984–2003. They found an 11-year solar cycle with larger GW amplitudes during solar maximum, but their dataset did not include the recent solar minimum.

2.2 Collm meteor radar

A SKiYMET meteor radar (MR) is operated at Collm Observatory on 36.2 MHz to measure horizontal winds, meteor rates and heights (height range approx. 80-100 km), and further meteor parameters since August 2004. The radar and the hourly wind detection are described in Jacobi (2011). Monthly mean wind parameters are obtained from half-hourly mean winds applying a multiple regression analysis including the mean wind, and tidal components. Based upon 2-hourly means, GW variances and

fluxes are obtained by fitting the 2-hourly mean GW fluxes to the radial drift variances according to Hocking (2005). Details can be found in Placke et al. (2010).

2.3 GW potential energy from TIMED/SABER temperature profiles

The SABER instrument onboard the TIMED satellite (Russell et al., 1999; Mertens et al., 2001) scans the atmosphere from about 52° on one hemisphere to 83° on the other one. This latitude range is reversed by a yaw manoeuvre every 60-days. Due to the sun-synchronous orbital geometry the spacecraft passes the equator always at the same local time (12LT) on the day side. Each single temperature profile, having a vertical resolution of 0.5 km, is high-pass filtered to analyze waves with vertical wavelength of up to 6 km. From these filtered data, the vertical structure of GW amplitudes and their specific potential energy is obtained. This method has frequently been applied to GPS radio occultations (e.g., Fröhlich et al., 2007). The total energy integrated over a sliding vertical column (10 km) is used to study GWs. Note that limb scanning of the atmosphere as is made by SABER only reveals certain parts of the GW spectrum due to the integration along the line of sight (Preusse et al., 2006). Another limitation is made by the chosen vertical filter, which allows only GWs of short wavelengths to be studied.

3 GW proxy decadal variability

Jacobi et al. (2006) had shown that there is a solar cycle influence on GW activity as measured by LF over Collm. Figure 1 presents the summer (JJA) mean time series of GW variance $\zeta'^2 = u'^2 + v'^2$ at 100 km virtual height, which represents approximately 91 km real height (Jacobi, 2011). The data are an update from Jacobi et al. (2006). The so-called13-monthly mean (which is actually a 12-monthly mean but centered at the respective month) sunspot number is added. Clearly, there is a solar cycle in the GW variance, and from visual inspection a decreasing long-term trend is also visible. We thus added, as a red solid line, a least squares fit of a linear trend b (intercept a) superposed by a solar cycle (coefficient c)

$$\zeta'^2 = a + b \cdot t + c \cdot R \,, \qquad (1)$$

with t as the time in years and R as the 13-monthly mean relative sunspot number. We are only interested in long-term and qualitative connections, so employing other widely used solar proxies as F10.7 are not superior to use of R here. As can be seen in the lower part of the figure, the residuals are not normally distributed, and generally the model is not valid during the 1996 as well as the recent solar minimum. Using the same model, but including only data until 1995 (blue line) reveals that the time interval until the early 2000s is well represented by that model, and after 2004 there is a drastic change. We therefore conclude that there is a change in dynamical regime since about 2004.

In the case of saturated GWs, linear theory predicts amplitudes proportional to the intrinsic phase speed. Consequently, since GW phase speeds must be positive (eastward) in the summer MLT owing to the filtering effect of the stratospheric and mesospheric easterlies, a negative correlation is expected between the background wind and the GW amplitudes. In Figure 2 we present GW variance together with the

background mean zonal wind at 100 km virtual height. Note that the background wind is simply the mean of the zonal wind averaged over those times when GW amplitudes have been calculated, and thus may deviate from the prevailing wind. There is an overall anticorrelation between GW variances and zonal winds, as expected from linear theory.

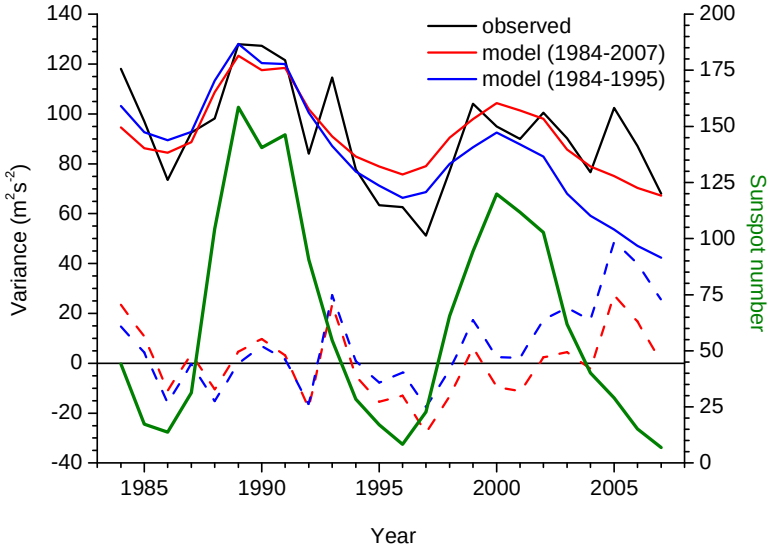

Figure 1: JJA mean LF GW proxy, and fit including linear trend and a solar cycle according to Eq. (1) at 100 km virtual height (approx. 91 km real height). The fit was performed both using the complete dataset 1984-2007 (red curve) and using part of the dataset until 1995 (blue curve). In the lower part the respective residuals are given as dashed lines. The sunspot number is also added as green line.

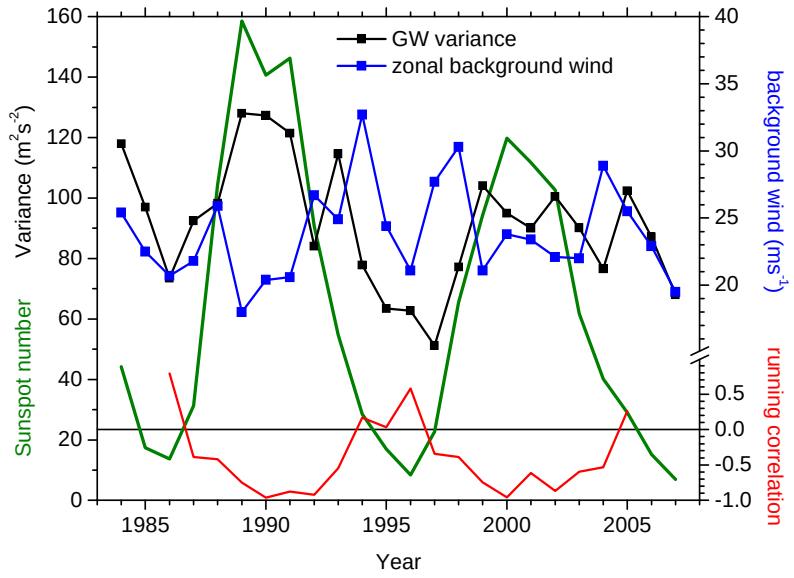

Figure 2: JJA mean LF GW proxy (black) and zonal mean wind (blue) at 100 km virtual height. In the lower part of the figure, running correlation coefficients between GW proxy and mean wind are added. The sunspot number is added as green line.

However, during solar minimum the correlation reverses. The running correlation (Kodera, 1993) between GW proxy and mean zonal wind is added in the lower part of Figure 2. Due to the shortness of the time series, only 5 data points are used for each calculation. A clear solar cycle modulation is visible. The running correlation time series is modulated by the sunspot number cycle with a correlation coefficient of r = -0.80. It is also remarkable that this modulation takes place during each solar minimum since 1986. Note also that that GW variances increase in 2005, when solar flux already decreases and thus decreasing GW variances are expected. This pattern has its counterpart in a GW variance peak in 1993. We may conclude that there is obviously a different regime of mean wind-GW coupling during solar minimum, which is, however, more emphasized during the recent minimum.

LF height measurements at Collm have been terminated after 2007, so that the solar minimum is not covered by them. To analyze winds and waves during the minimum, in Figure 3 MR summer mean zonal prevailing winds at 6 height gates are presented. Clearly, interannual variability of winds in the upper and lower height gates is opposite. This is explained by GW acceleration and filtering in the mesosphere. In the case of strong/weak mesospheric easterlies, GW amplitudes are large/small, which then lead to strong/weak vertical wind shear. Figure 3 also shows that above 91 km winds are decreasing until 2007, which is qualitatively consistent with the decrease of the LF winds during 2005-2007. After 2007, winds are increasing again. This agrees with the zonal LF wind decrease after 1994 (Figure 2). This zonal wind decrease is accompanied by GW proxy amplitude decrease. MR GW analyses of the recent minimum (Figure 4) again show this effect qualitatively. The same is the case for SABER potential energy (Figure 5), although here only the GW amplitudes above ~100 km decrease with time. This may be due to the fact that we present zonal mean potential energy, while Figures 1-4 represent point measurements and non-zonal structures are likely to exist in the MLT. Note that the above mentioned trends are only valid for heights above 90 km, while for the lower height gates the winds and GW amplitudes behave in an opposite manner.

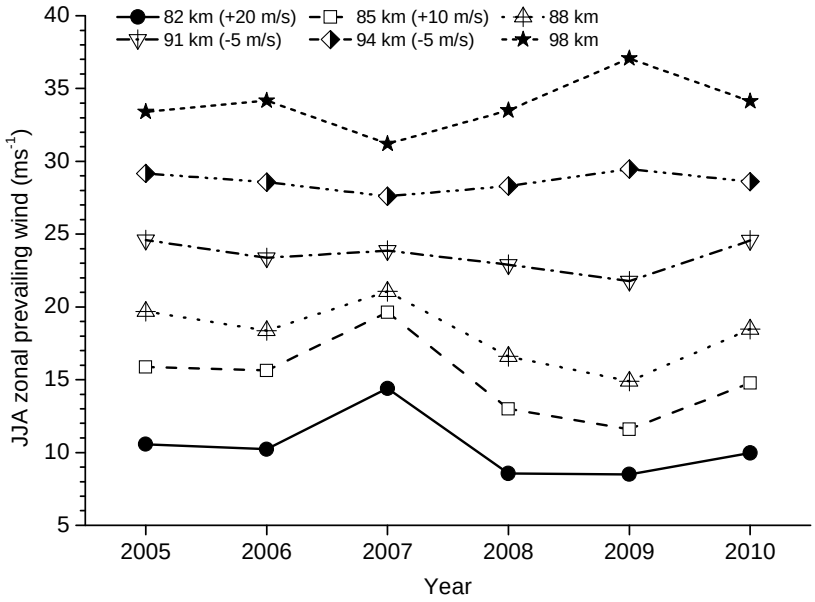

Figure 3: Collm June-August mean zonal prevailing winds measured by meteor radar.

5 LF virtual heights and mean meteor altitudes

The solar modulation of correlation between zonal wind and GW amplitudes suggests that the decrease of reference height of wind systems may play a role. Collm LF virtual nighttime (22-2LT) reflection heights are shown in Figure 6. A multiple linear fit after Eq. (1), but analyzing virtual height instead of variance is added as red line, as well as the residuals (red dashed line). The sunspot number is added as green line. Note that real heights and height differences are much smaller than virtual height differences. Thus, the strong decrease of LF heights after 2005, for example, represents a real height decrease of 2 km only. From the residuals in Figure 6 one can see that the recent minimum is outstanding. Generally, there is an ionization driven solar cycle of reflection heights such that these are lower during solar maximum than during solar minimum. Thus, the strong decrease after 2005 is unexpected. However, a similar variability has already been observed after 1993 during the last solar minimum, although with much smaller amplitudes, LF reflection height variability is influenced by changes in ionization and mesospheric shrinking. According to Figure 6 this would mean that during the recent solar minimum thermal shrinking has overcompensated the ionization effect.

Note that the LF reference height changes shown in Figure 6 do not correspond to the variations of a line of constant pressure or density. A better proxy is the mean height of meteors because these, constant meteor parameters as mean mass and velocity assumed, burn at a height that is determined by the density distribution. Figure 7 shows June-August mean meteor heights from 2005-2010, plotted against the so-called EUV-TEC index (Unglaub et al., 2011), which essentially describes the variability of the normalized solar EUV flux and is based on TIMED-SEE (Woods et al., 2000, 2005) satellite measurements. As expected, the meteor heights increase with solar activity. Note, however, that the mean meteor heights during 2008 and 2010, at the same level of solar EUV flux, are different. This is partly due to the fact that the decrease is

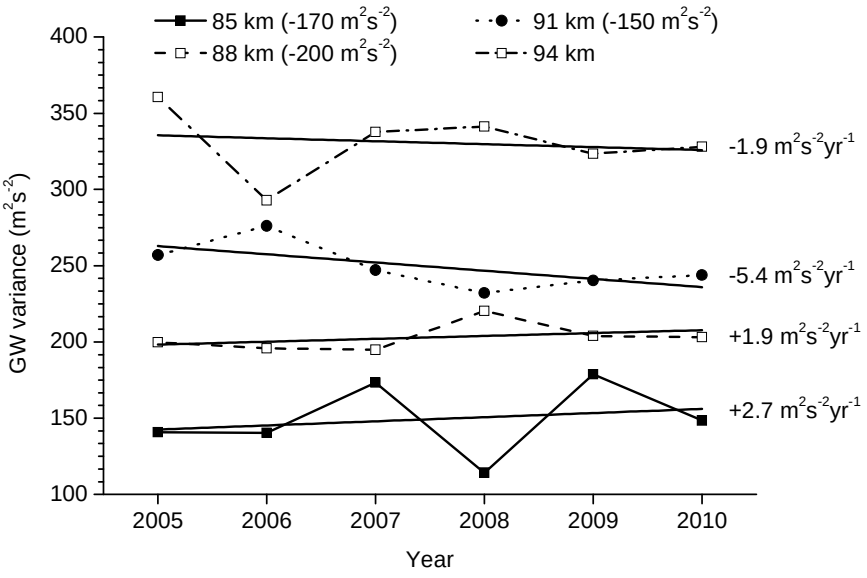

Figure 4: Horizontal wind variance calculated within 2-hr intervals using Collm MR horizontal wind measurements for 4 height gates.

superposed by the long-term changes of mesospheric density. Bremer and Peters (2008) found a long-term decrease of -30 m/yr from LF reflection heights (and excluding the solar cycle). Subtracting this from the measured meteor heights in Figure 7 (red line) shows that then the 2008 and 2010 heights, at the same solar EUV flux, have exactly the same values when long-term cooling of the middle atmosphere is taken into account.

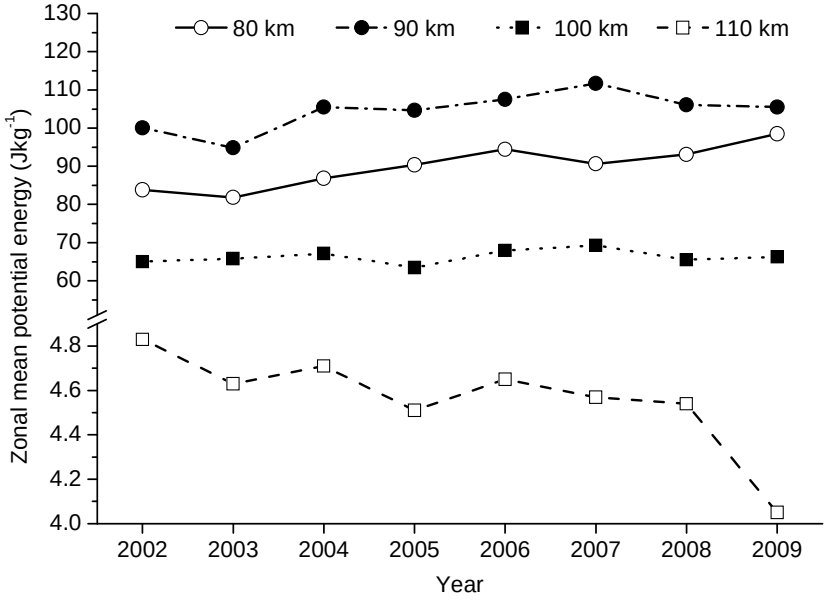

Figure 5: JJA mean potential energy at 45°N from SABER temperature profiles. Data are averages over a 10 km vertical window, and means over all longitudes.

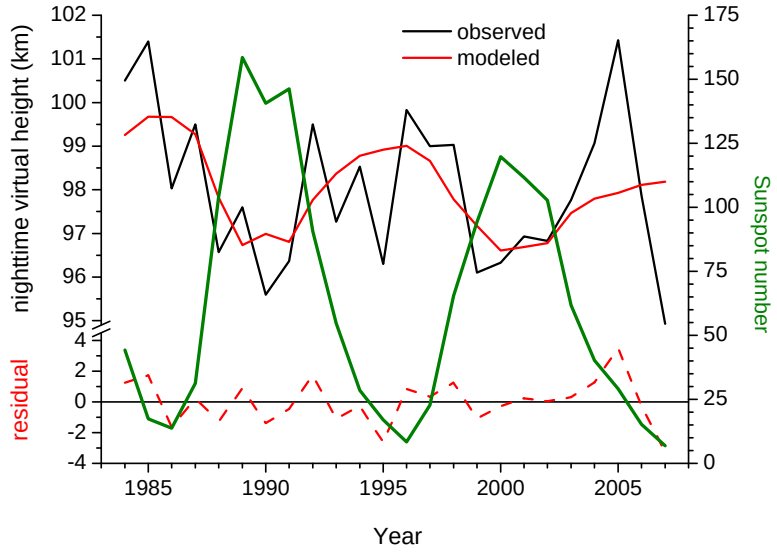

Figure 6: Collm LF virtual nighttime (22-2LT) reflection heights. A linear fit according to Eq. (1) is added as red line, as well as the residuals (red dashed line). The sunspot number is added as green line.

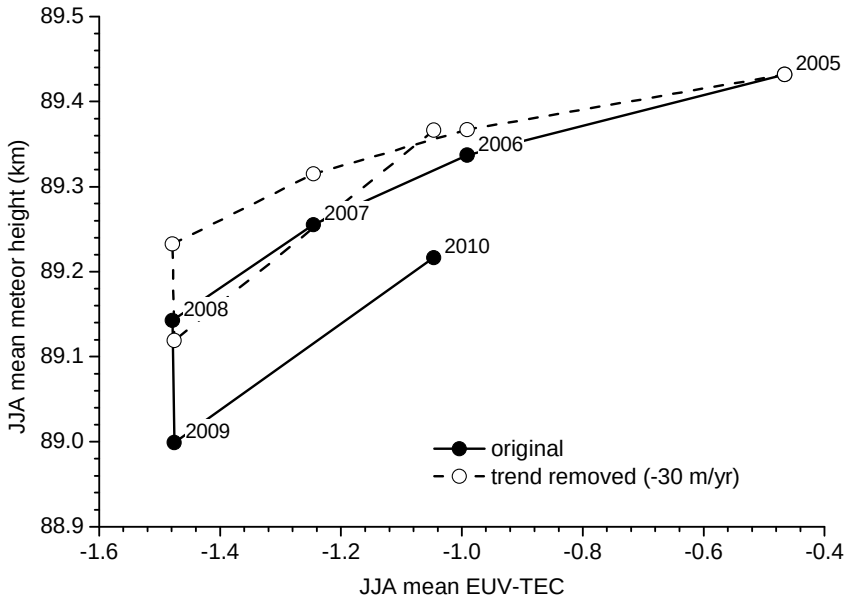

Figure 7: JJA mean meteor heights over Collm vs. EUV-TEC Index. The dashed curve represents meteor heights after removing a linear trend of -30 m/yr.

There remains some hysteresis, so that the density recovers one year later than the solar EUV does. A delay of one year of noctilucent cloud occurrence and solar activity has been reported by DeLand et al. (2006) and Bremer et al. (2009). Ortiz de Adler and Elias (2008) showed a similar hysteresis in ionospheric foF2 data. Jacobi et al. (2008) showed that MLT planetary wave activity lags the solar cycle by 1-3 years.

6 Discussion and conclusions

Linear theory predicts that GW amplitudes are proportional to the intrinsic phase speed and thus, in the case of a given GW with specified phase speed, determined by the zonal wind itself. Since only GWs with positive phase speeds propagate to the MLT, stronger/weaker mean winds mean smaller/larger intrinsic phase speed. The positive correlation between GW amplitudes and zonal winds during solar minimum is thus unexpected at first glance, but may be explained by a downward shift of the GW maximum owing to thermal shrinking of the MLT wind systems. In such a case, GWs already maximize in the upper mesosphere. Then, strong/weak mesospheric easterlies, which are connected with weak/strong lower thermospheric westerlies, are connected with large/small GW amplitudes, large/small GW drag and consequently strong/weak westerly winds at greater altitudes. This may explain the positive correlation during solar minimum, while there is a negative correlation during the other years, then simply in accordance with linear theory.

Whether or not the above mentioned coupling processes really work requires more detailed analyses, including more satellite analyses, further radars, and numerical modeling. However, the observations of MLT GWs, mean winds, and reference heights already suggest that there is a height shift during solar minimum, which may influence vertical coupling between mesosphere and lower thermosphere. The recent solar minimum represents an extreme case, but the fundamental variability, as shown

by the LF measurements, was not qualitatively (although quantitatively) different from the last solar minimum, at least as far as the LF measurements at Collm are concerned. In the thermosphere, however, density decrease during the recent minimum was extreme. Thus, there are still open questions concerning solar variability and its effect on the MLT.

Acknowledgements

This study was supported by DFG under grant JA 836/22-1.

References

Bremer, J., Peters, D., 2008: Influence of stratospheric ozone changes on long-term trends in the meso- and lower thermosphere. J. Atmos. Sol.–Terr. Phys., 70, 1473–1481.

Bremer, J., Hoffmann, P., Latteck, R., Singer, W., Zecha, M., 2009: Long-term changes of (polar) mesosphere summer echoes. J. Atmos. Sol.–Terr. Phys.,71, 1571–1576.

DeLand, M.T., Shettle, E.P., Thomas, G.E., Olivero, J.J., 2006: A quarter-century of satellite polar mesospheric cloud observations. J. Atmos. Sol.-Terr. Phys., 68, 9–29.

Emmert, J.T., Lean, J.L., Picone, J.M., 2010:. Record-low thermospheric density during the 2008 solar minimum. Geophys. Res. Lett., 37, L12102, doi:10.1029/2010GL043671.

Fröhlich, K., Schmidt, T., Ern, M., Preusse, P., de la Torre, A., Wickert, W., Jacobi, Ch., 2007: The global distribution of gravity wave energy in the lower stratosphere derived from GPS data and gravity wave modelling: Attempt and challenges. J. Atmos. Sol.-Terr. Phys., 69, 2238–2248.

Gavrilov, N.M., Jacobi, Ch., Kürschner, D., 2001: Short-period variations of ionospheric drifts at Collm and their connection with the dynamics of the lower and middle atmosphere. Phys. Chem. Earth,26, 459–464.

Gray, L. J., Beer, J., Geller, M., Haigh, J. D., Lockwood, M., Matthes, K., Cubasch, U., Fleitmann, D. , Harrison, G., Hood, L., Luterbacher, J., Meehl, G.A., Shindell, D. , van Geel, B., White, W., 2010: Solar influences on climate. Rev. Geophys., 48, RG4001, doi:10.1029/2009RG000282.

Hocking, W.K., 2005: A new approach to momentum flux determinations using SKiYMET meteor radars. Ann. Geophys. 23, 2433–2439.

Jacobi, Ch., Kürschner, D., 2006: Long-term trends of MLT region winds over Central Europe. Phys. Chem. Earth, 31, 16–21.

Jacobi, Ch., Gavrilov, N.M., Kürschner, D., Fröhlich, K., 2006: Gravity wave climatology and trends in the mesosphere/lower thermosphere region deduced from low-frequency drift measurements 1984-2003 (52.1°N, 13.2°E). J. Atmos. Sol. –Terr. Phys., 68, 1913–1923.

Jacobi, Ch., Hoffmann, P., Kürschner, D., 2008: Trends in MLT region winds and planetary waves, Collm (52°N, 15°E). Ann. Geophys., 26, 1221–1232.

Jacobi, Ch., 2011: Meteor radar measurements of mean winds and tides over Collm (51.3°N, 13°E) - comparison with LF drift measurements 2005-2007. Adv. Radio Sci., in print.

Keuer, D., Hoffmann, P., Singer, W., Bremer, J., 2007: Long-term variations of the mesospheric wind field at mid-latitudes. Ann. Geophys., 25, 1779–1790.

Kodera, K., 1993: Quasi-decadal modulation of the influence of the equatorial quasi-biennial oscillation on the north polar stratospheric temperatures. J. Geophys. Res., 98, 7245–7250.

Kürschner, D., Schminder, R., Singer, W., Bremer, J., 1987: Ein neues Verfahren zur Realisierung absoluter Reflexionshöhenmessungen an Raumwellen amplitudenmodulierter Rundfunksender bei Schrägeinfall im Langwellenbereich als Hilfsmittel zur Ableitung von Windprofilen in der oberen Mesopausenregion. Z. Meteorol., 37, 322–332.

Kürschner, D., Jacobi, Ch., 2003: Quasi-biennial and decadal variability obtained from long-term measurements of nighttime radio wave reflection heights over central Europe. Adv. Space Res., 32, 1701–1706.

Mertens, C.J., Mlynczak, M.G., Lopez-Puertas, M., Wintersteiner, P.P., Picard, R.H., Winick, J.R., Gordley, L.L., Russell III, J.M., 2001: Retrieval of mesospheric and lower thermospheric kinetic temperature from measurements of CO_2 15 μm earth limb emission under non-LTE conditions. Geophys. Res. Lett., 28, 1391–1394.

Ortiz de Adler, N., Elias, A. G., 2008: Latitudinal variation of foF2 hysteresis of solar cycles 20, 21 and 22 and its application to the analysis of long-term trends. Ann. Geophys., 26, 1269–1273.

Placke, M., Stober, G., Jacobi, Ch., 2010: Gravity wave momentum fluxes in the MLT—Part I: Seasonal variation at Collm (51.3°N, 13.0°E). J. Atmos. Sol.–Terr. Phys., doi:10.1016/j.jastp.2010.07.012.

Preusse, P., Ern, M., Eckermann, S. D., Warner, C. D., Picard, R. H., Knieling, P., Krebsbach, M., Russell, J. M., Mlynczak, M. G., Mertens, C. J., Riese, M., 2006: Tropopause to mesopause gravity waves in August: measurement and modelling. J. Atmos. Sol.–Terr. Phys., 68, 1730–1751.

Russell, J. M. III, Mlynczak, M. G., Gordley, L. L., Tansock, J., Esplin, R., 1999: An overview of the SABER experiment and preliminary calibration results. In: Proceedings of the SPIE, 3756, 44th Annual Meeting, Denver, Colorado, July 18–23, 277–288.

Solomon, S. C., Woods, T. N., Didkovsky, L. V., Emmert, J. T., Qian, L., 2010: Anomalously low solar extreme-ultraviolet irradiance and thermospheric density during solar minimum. Geophys. Res. Lett., 37, L16103, doi:10.1029/2010GL044468.

Unglaub, C., Jacobi, Ch., Schmidtke, G., Nikutowski, B., Brunner, R., 2011: EUV-TEC proxy to describe ionospheric variability using satellite-borne solar EUV measurements: first results. Adv. Space Res., 47, 1578–1584.

Woods, T. N., Bailey, S., Eparvier, F., Lawrence, G., Lean, J., McClintock, B., Robie, R., Rottmann, G. J., Solomon, S. C., Tobiska, W. K., White, O. R., 2000: TIMED Solar EUV Experiment. Phys. Chem. Earth (C), 25, 393–396.

Woods, T. N., Francis, G. E., Bailey S. M., Chamberlin, P. C., Lean, J., Rottmann, G. J., Solomon, S. C., Tobiska, W. K., Woodraska, D. L., 2005: Solar EUV Experiment (SEE): Mission overview and first results. J. Geophys. Res., 110, A01312, doi: 10.1029/2004JA010765.

Possible use of television broadcasting signals for wind measurements by the meteor radiolocation method – main theoretical aspects and results of first experiments

V. Kukush, Ch. Jacobi and A. Oleynikov

Summary

The possibility of using terrestrial television (TV) broadcast signals (TVBS) as sounding signals for mesosphere-lower thermosphere (MLT) wind measurements by the radio meteor method is investigated. Such approach allows to use external TV transmitters as sounding signal sources and consequently to reduce costs of measurements. It is shown that meteor trails in the area above the receiver should be selected to eliminate MLT wind measurement ambiguity. Results of experimental observations are presented. Validation of the results has been performed using datasets from the Thermosphere-Ionosphere-Mesosphere Energetics and Dynamics (TIMED) satellite and a SKiYMET meteor radar (Collm Observatory, Germany). It is shown that the obtained experimental results and TIMED mean winds are correlated with a correlation coefficient of 0.58 (significance level 0.95 according to a t-test). The measurements show for the first time that terrestrial television broadcast signals can be used for MLT wind measurements and that the developed technique may be used for MLT wind monitoring on the base of the existing terrestrial TV broadcasting network.

Zusammenfassung

Es wird untersucht, inwieweit terrestrischer Fernsehsignale zur Sondierung des Windes in der Mesosphäre und unteren Thermosphäre genutzt werden können. Ein solcher Ansatz erlaubt es, externe Sender als Quelle zu verwenden und damit Kosten zu sparen. Es wird gezeigt, dass Meteorsignale im Raum über dem Empfänger genutzt werden können, welches die Uneindeutigkeit der Windsignale verringert. Ergebnisse eines Experiments werden gezeigt und anhand von TIMED-Satellitendaten und VHF-Radarmessungen validiert. Die Messungen zeigen zum ersten Mal die Möglichkeit einer Windmessung in der unteren Thermosphäre auf der Basis terrestrischer Fernsehsignale.

1 Introduction

The meteor radiolocation method is one of the main techniques for wind measurements in the mesosphere/lower thermosphere region (MLT, 75-110 km) (Manning et al., 1954; Kashcheyev et al., 1967). The wind measurement principle is the detection of the Doppler shift of the reflected very high frequency **(**VHF) radio waves from ionized meteor trails, which delivers radial wind velocities along the line of sight of the radio wave. For the realization of such measurements special meteor radars (MRs) are used. These radars are actively transmitting and radiate a special sounding signal with a peak power ranging

from few kilowatts to several megawatts and allow to determine the coordinates of meteor trails (elevation ε, azimuth angle φ, altitude h) and its drift velocity along the sounding direction (Hocking et al., 2001; Kashcheyev et al, 2002).

Oleynikov et al. (2010) showed that terrestrial television (TV) broadcast signals (TVBS) can be used as sounding signals for the radiolocation of meteor trails (estimation of meteor daily flux). The use of TVBS allows excluding the transmitter unit from the measurement equipment, because such kind of sounding signals have been already radiated by the existing transmitters of the terrestrial TV broadcasting network. Consequently the equipment for meteor radiolocation with TVBS as sounding signals enables one:

- to reduce operating costs of such by significant reduction of energy consumption, which is essentially determined by the transmitter unit,
- to carry out the measurements without registration of measurement equipment in the State Centres of Radio Frequencies,
- to carry out the measurements also within an urban environment. The use of active VHF MRs is usually allowed only far from urban areas and only in with the vertical direction of the sounding signal radiation. This requirement is caused by the high radiated power of active MR in a frequency band occupied by other users,
- to carry out the measurements without payment of the radio frequency registration fees, which in some countries as, e.g., Ukraine, are collected,
- to save energy (additional using of the energy of the TV transmitters).

The aim of this work is a further development of the work by Oleynikov et al. (2010), including the theoretical and experimental investigation of the possibility to use TVBS for MLT wind measurements by the meteor radiolocation method. Such an approach of TVBS use is, to our knowledge, investigated for the first time.

2 Theoretical aspects

In the case of using TVBS for radiolocation, the distance a between the receiver and the source of the transmitted signal (TV transmitter position) is comparable to or exceeds the range to the target (the meteor trail). Consequently, such kind of a radar-system may be classified as a bistatic radar. The Doppler frequency shift (F_d) can be calculated as (Skolnik, 1970; Chernjak, 1993):

$$F_d = \frac{1}{\lambda} \cdot \vec{V} \cdot (\vec{r_1} + \vec{r_2}) = \frac{1}{\lambda} \cdot \left(\vec{V} \cdot \vec{r_1} + \vec{V} \cdot \vec{r_2}\right), \quad (1)$$

where F_d is the Doppler shift of the sounding signal carrier frequency, $\vec{V}$ is the meteor trail velocity vector; $\vec{r_1}$ are $\vec{r_2}$ the vectors in the directions from the meteor trail to transmitter and receiver; $\lambda = c/f_0$ is the wavelength of the sounding signal carrier frequency f_0, and c is the speed of light. The geometry of the problem is shown in Fig. 1.

Eq. (1) and Fig. 1 show that the Doppler shift of the sounding signal carrier frequency is a sum of two terms, essentially the scalar products $\vec{V} \cdot \vec{r_1}$ and $\vec{V} \cdot \vec{r_2}$, which are

proportional to the meteor trail velocity projection on the sounding signal propagation path between transmitter/receiver and trail. Hence the Doppler shift depends on the geometry of the sounding signal propagation path or, in other words, on the meteor trail location relative to the receiver and transmitter. Thus, for a constant wind velocity vector the Doppler shift can have different values for various locations of the trail (e.g. its *h*, and angular coordinates ε, φ relative to receiver position).

Fig. 2 shows the dependence of the value $D = F_d \big/ \left|\vec{V}\right|$ on the elevation of the meteor trail in the receiver position (ε, Fig. 1). The *D* value characterizes the Doppler shift of the reflected signal relative to the magnitude of the trail velocity vector. The curves in Fig. 2 were calculated by Eq. (1) for the following special cases:

- parallel (||) drift of the meteor trail in the parallel plane, which contains the transmitter and receiver positions and which is orthogonal to the Earth's surface. The drift of the meteor trail is directed from the transmitter to the receiver (plot for $D_{||}$ in Fig. 2 a). Note that in the case the transmitter is located westward or eastward of the receiver, the parallel drift equals the zonal wind component,
- perpendicular ($\perp$) drift of the meteor trail in the perpendicular plane, which contains the receiver position (plot for $D_{\perp}$ in Fig. 2 b). The perpendicular plane is orthogonal to the Earth's surface and to the parallel plane. In the case the transmitter is located westward or eastward of the receiver, the perpendicular drift equals the meridional wind component.

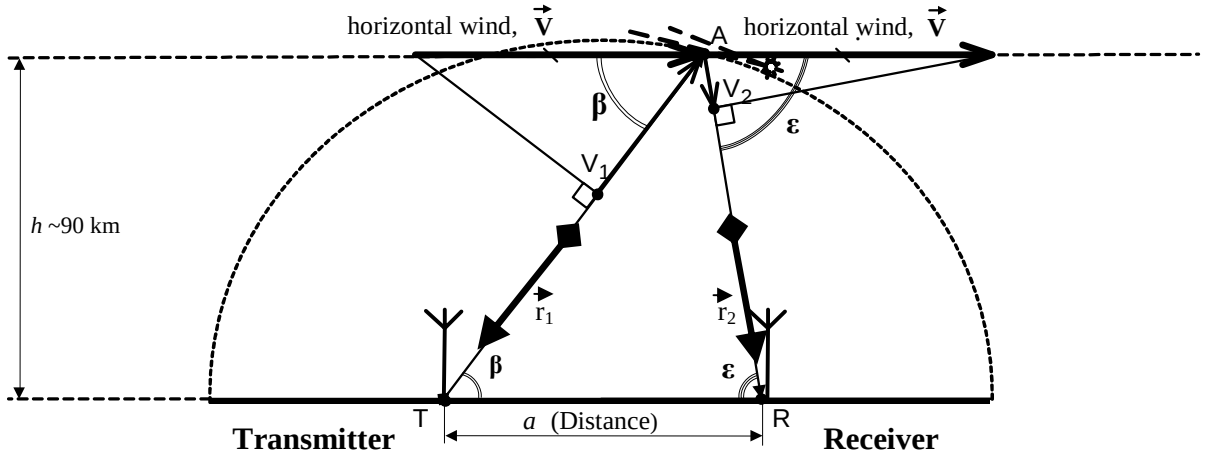

Fig. 1: Two projections of the meteor trail velocity for determination of the Doppler shift of a sounding signal in bistatic radars.

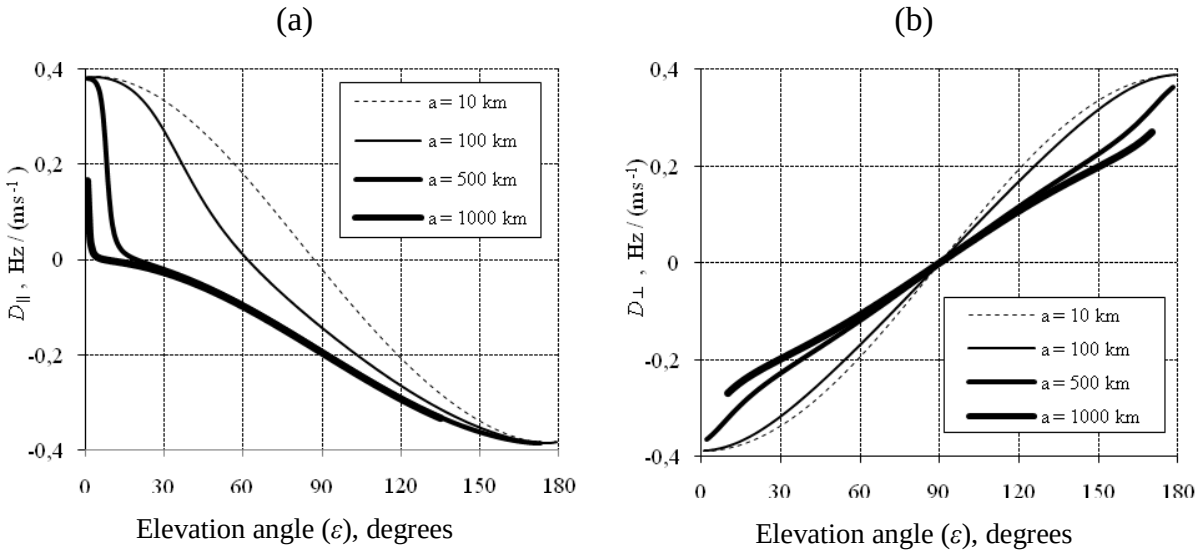

Fig. 2: Relative Doppler shift of reflected signals for different elevation angles ε of the meteor trail in the receiver position. Left panel (a) for $D_{||}$, right panel (b) for $D_{\perp}$.

The calculations for both cases were performed under the assumption that vertical winds are small (Hocking et al., 2001), taking into account the curvature of the Earth's surface, for a constant magnitude of the meteor trail drift velocity vector (1 m/s) at 90 km altitude, and for different *a*. The carrier frequency of the sounding signal corresponds to the nominal value of the second TV channel carrier frequency f_0 = 59.25 MHz, GOST 7845-92 (1992).

Fig. 2 also shows that Doppler shift of the same order of magnitude may be caused by either parallel or perpendicular drift of the meteor trail. Likewise, the same component of the drift vector (parallel or perpendicular) can produce different Doppler shift, even with a different sign, since the sign of the Doppler shift depends on ε. There are also ε values, for which one of the drift components causes no Doppler effect, when $D_{||}$ or $D_{\perp}$, respectively, is equal to zero. In conclusion, the influence of ε and the combination of parallel and perpendicular wind component lead to ambiguity of the meteor trail drift measurements.

To analyse the meteor trail drift velocity measurement ambiguity the selection coefficient of the parallel drift ($S_{||}$) component is used:

$$S_{\parallel} = \frac{|D_{\parallel}|}{|D_{\parallel}| + |D_{\perp}|} , \qquad (2)$$

which quantifies the contribution of the Doppler shift due to the parallel drift component to the overall Doppler shift. Values of $S_{||}$ close to unity/zero mean that the Doppler shift is essentially determined by the parallel/perpendicular drift component. Fig. 3 presents the relation between $S_{||}$ and the angular coordinates (ε,φ) of the meteor trail relative to the re-

ceiver position. The transmitter position (point T in Fig. 2) is chosen a = 500 km westward from the receiver (the transmitter is below the horizon relative to the receiver, φ = 270°, $\varepsilon \approx$ -2.2° or for the same point φ = 90°, $\varepsilon \approx$ 182.2°). The meteor height is taken as h = 90 km. Fig. 3 shows that maximum $S_{||}$ corresponds to meteor trails with ε close to 90° and those in a direction away from the transmitter.

With increasing a the area with $S_{||}$ close to unity increases and the area of minimum $S_{||}$ is shifted to lower ε. However, at very large a the spherical Earth's surface shields the sounding signal propagation path. This effect is negligible for a < 700 km. For example, for a = 500 km receiving of the signals reflected from meteor trails can be impossible for ε > 170° (<10° in the direction opposite to the transmitter, see Fig. 3). For selecting and measuring of the parallel component of the meteor trail drift velocity (and thus the parallel component of MLT wind) only those signals should be used that are reflected from meteor trails within the area with $S_{||}$ close to unity (dashed area in Fig. 3). For a > 100 km the condition $S_{||} \geq 0.5$ corresponds to ε = 90±45°. Such a spatial selection of meteor trails can be realized using a vertically pointing antenna with a beamwidth that should not exceed ~60-90° (Kukush et al., 2011a).

We may conclude that the Doppler shift due to $D_{||}$ has a constant sign in the region above the receiver position (ε = 90±45°, see Fig. 2 for a > 100 km). In contrast to $D_{||}$, $D_{\perp}$ has negative values for ε less than 90° and positive values for ε more than 90°. If the distribution of ε is symmetric about 90°, the average value of $D_{\perp}$ will tend to zero in contrast to the average value of $D_{||}$. Consequently, the mean selection coefficient $S_{||}$ for averaged values of $D_{||}$ and $D_{\perp}$ will exceed $S_{||}$ for single values of $D_{||}$ and $D_{\perp}$. Hence the average Doppler shift for signals from meteors above the receiver are expected to correspond to the average parallel MLT wind component more closely than individual values.

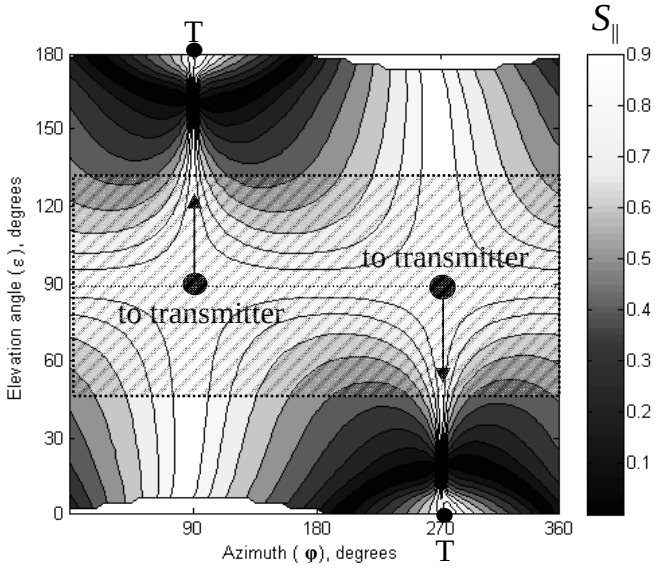

Fig. 3: Relation between the selection coefficient of the meteor trail drift parallel component ($S_{||}$) and the angular coordinates (ε, φ) of the meteor trail.

Tab. 1: Location and working frequencies of sources of TVBS within the second TV channel for Kharkiv, Ukraine.

Transmitter	φ, a (relative to Kharkiv)	carrier frequency, MHz; and CO (rounded to 0.1kHz)	Power, kW
Kyiv	279°; 414 km	59.25; (0 kHz)	340
Stary Oskol	38°; 173 km	59.239583; (–10.4 kHz)	20
Dubki	14°; 865 km	59.239583; (–10.4 kHz)	113
Borisoglebsk	40°; 436 km	59.260417; (+10.4 kHz)	40
Bălți	251°; 656 km	59.239583; (–10.4 kHz)	109
Bryansk	36°; 380 km	59.260417; (+10.4 kHz)	36
Vilnus	309°; 907 km	59.253906; (+ 3.9 kHz)	177
Krasnodar	159°; 593 km	59.244792; (– 5.2 kHz)	27

Receiving signals along the vertical direction has advantages also from a practical point of view: because of the vertically oriented maximum of the directional diagram, the receiver antenna has large attenuation for "terrestrial" signals. These signals can come directly from the transmitter or from other transmitters, which have similar working frequencies (within one octave) and which are located in a similar direction than the receiver. Such signals, owing to their large possible power, could mask the signals reflected from meteor trails or cause nonlinear distortion in the receiver.

A vertically oriented receiver antenna offers equal conditions for receiving of TVBS reflected from meteor trails, which are radiated by different TV transmitters at different φ. For each signal it is then possible to estimate the MLT wind component parallel to the azimuth of the corresponding TV transmitter. Hence various components of the MLT wind can be measured in the same region and the horizontal MLT wind vector can be estimated.

3 Usable transmitters of second TV channel for MLT wind measurements at Kharkiv, Ukraine

There are no TV transmitters of the second TV channel directly in Kharkiv. This enables one to receive signals from remote TV transmitter of the second TV channel (see Tab. 1) by reflection from meteor trails (Oleynikov et. al., 2010). However, receiving TVBS reflected from meteor trails is not always possible in a real environment with substantial noise sources.

Measurements of the meteor trail velocity using reflected TVBS requires the knowledge of φ of a signal source to determine the azimuth of a measured wind component. Initially such kind of information is not defined, because each of the TV transmitters in Tab. 1 can be the source of received TVBS. The signal source, however, can be identified by the carrier frequency (f_0), being the sum of the nominal frequency of the TV chan-

nel (constant for all TV transmitters of the same channel) and the carrier offset (CO), which is individually defined for each TV transmitter in the national standards (e.g., GOST 7845-92, 1992) and has an order of magnitude of 10 kHz. Therefore, the carrier frequency estimation of TVBS reflected from meteor trails allows to obtain the following information:

- a coarse estimation of the frequency (to the order of magnitude of kHz) allows to identify the source of TVBS (TV transmitter). Unambiguous identification is not always possible, because some TV transmitters have the same working frequency/CO, see Tab. 1. However, this estimation can significantly reduce the list of possible transmitters of the received signal,
- an accurate estimation of the frequency (to the order of magnitude of Hz) and its shift from the working frequency of corresponding TV transmitter allows to estimate the Doppler shift, which was caused by the meteor trail drift parallel to the direction from receiver to a defined TV transmitter.

The average duration of a meteor is ~0.1 s and may reach up to 2 s (McKinley, 1961; Hocking et al., 2001). The stability of the TVBS carrier frequencies during such a short time interval is not regulated in the corresponding normative documents such as GOST 7845-92 (1992). However, this parameter is critical for the measurement of meteor trail drift velocity. Kukush and Oleynikov (2010) experimentally estimated the standard deviation δ_{rad} of the TVBS vision carrier frequency. The structure of their instrumentation was similar to the one used here (see section 4 below). For the stability measurements the ground waves of TV transmitters at Stary Oskol (second TV channel) and Kharkiv (third TV channel) were used. The measurement time (τ_{meas}) was chosen equal to the average duration of the meteor trail signal (0.1 s) and more. It was found that $\delta_{rad} = 2$ Hz for $\tau_{meas} = 0.1$ s, $\delta_{rad} = 0.3$ Hz for $\tau_{meas} = 10$ s, and $\delta_{rad} = 1$ Hz for $\tau_{meas} = 24$ h. Thus, δ_{rad} does not exceed the typical values of the Doppler shift (several tens of Hz) owing to meteor trail drift. Hence the vision carrier frequency of TVBS is sufficiently stable for the Doppler shift estimation, being the difference between the working frequency of a TV transmitter and the frequency of its signal, which was reflected from a meteor trail.

4 Description of the test equipment

The test equipment consists of a three-element Yagi receiver antenna, a specialized receiver, standard analog-digital converter (ADC), a reference frequency source and a computer for digital signal processing (Kukush et al., 2011b). The antenna points vertically. The 3 dB beamwidth is 90° (by simulation results from the program MMANA, (Mori, 2000)). The antenna is used for receiving and spatial selection of TVBS reflected from meteor trails above the receiving position. It agrees with the requirements of the measurements of the meteor trail parallel drift velocity component or parallel component of MLT wind (see above).

The receiver is of single superheterodyne type. It has an amplitude detector and amplitude limiter outputs, which are used for the power and carrier frequency estimation of the received signal. The intermediate frequency (IF) of the receiver is 6.5 MHz. The IF

channel bandwidth is 160 kHz. The adjacent-channel selectivity in the IF path is 40 dB. Adjacent and image channel selectivity in the radio path is at least 60 dB. The receiver sensitivity in the antenna input is better than 1 mV (with the output signal-to-noise ratio (SNR) equal to 2). The high adjacent and image channel selectivity makes it possible to receive the meteor trails signals in urban conditions with noisy environment. The reference frequency source is used for the local oscillator and A/D clocking voltage synchronization. The instability of the reference frequency source (type Ч6-31, russ.) is $5 \cdot 10^{-10}$ for τ_{meas} = 10 s, $5 \cdot 10^{-8}$ for τ_{meas} = 24 h, and $5 \cdot 10^{-7}$ for τ_{meas} = 6 months. The on/off frequency setting error is $5 \cdot 10^{-8}$.

A series of test measurements had shown that this test equipment allows to estimate the frequency of a radio signal with few μV amplitude during a measurement time of 0.1 s with a standard deviation error in the order of magnitude of few Hz. The precise error value depends, among others, on the input SNR, and the envelop type of the signal. The expected TVBS carrier frequency Doppler shift due to reflection from meteor trails is much greater than this error and can take values up to several tens of Hz for meteor trails with a drift velocity up to 150 m/s (McKinley, 1961) and $\varepsilon = 90 \pm 45°$. Hence the specifications of the test equipment are sufficient for receiving TVBS reflected from meteor trails and to reveal its carrier frequency Doppler shift.

5 Experimental results

At the Kharkiv National University of Radio Electronics, Kharkiv (50°N; 36.2° E), Ukraine, four series of continuous measurements using the above described test equipment were carried out during April 2010. The dates of the measurements are: 1.-3., 12.-14., 16.-19., 21.-23. April 2010. In total, more than 7,500 meteor echoes from TVBS were recorded. The distribution of the received signal carrier frequencies has a clear peak at 59.25 MHz within 120 kHz bandwidth (the nominal value of the second TV channel vision carrier frequency). The maximums of the distribution correspond to working frequencies of TV transmitters that can be received in Kharkov by reflection from meteor trails (see Tab. 1). The total number of received signals is different for each radio frequency and depends on the power and distance of the respective transmitter. The diurnal variation of the hourly number of signals agrees well with literature (McKinley, 1961; Kashcheyev et al, 1967; Arras et al., 2009).

The width of the received carrier signal frequency distribution in the vicinity of the working frequency for specific TV transmitters (Tab. 1) exceeds more than three times the standard deviation of TVBS carrier frequency variation before reflection. The deviation of the carrier frequency of the TVBS reflected from meteor trails (Δf) reaches 40 Hz, while the standard deviation of the TVBS carrier frequency before the reflection from the meteor trail (the stability of the TV transmitter working frequency) is smaller than 2 Hz for τ_{meas} = 0.1 s (Kukush and Oleynikov, 2010).

The mean diurnal variations for all experimental data of the carrier frequency shift (Δf_{mean}) are shown in Fig. 4. The values are calculated separately by TVBS, which are radiated by transmitters with two different working frequencies. It should be noted that be-

fore the Δf_{mean} calculation the series of Δf was limited within a 10 Hz band centered in the respective TV transmitter working frequency to bring them to a single-mode distribution law. The amount of single Δf for the Δf_{mean} calculation ranges between 32 and 100 values per hour (referred to the mean diurnal variations) for the TV transmitter at Kyiv and from 15 to 80 values per hour for the TV transmitters at Stary Oskol, Dubki, and Bălți.

If the observed Δf and Δf_{mean} are caused by the Doppler effect due to reflection from meteor trails, then these variations should be correlated with the variation of the parallel component of mean meteor zone wind speed. The direction of the parallel component of the wind speed is determined by the azimuth of the source of the received TVBS. Winds from the Thermosphere-Ionosphere-Mesosphere Energetics and Dynamics (TIMED) satellite and the Collm MR are used to reveal the correlation between the experimental Δf_{mean} and variations of the MLT wind.

TIMED is a low-Earth orbiting (625 km) NASA satellite that started its measurements in 2001 (http://www.timed.jhuapl.edu). One of the four experiments on board TIMED is the TIMED Doppler Interferometer (TIDI, Killeen et al., 1999, 2006). It measures horizontal winds and temperatures at 60 – 300 km with a vertical resolution of ~2 km at the lower altitudes and with accuracies that approach ~3 m/s and ~2K, respectively. Each profile takes 100-200 seconds to complete. This results is a nominal horizontal spacing of approximately 750 km between profiles along the orbit. The precession rate of TIMED is such that it will take 60 days to precess 12 hours in local time. Hence, a one-month TIDI dataset is not sufficient to construct a mean diurnal wind variation that covers all local times. During April 2010, TIDI measured up to three wind profiles per day in an area of 10x10 degrees centered around Kharkiv.

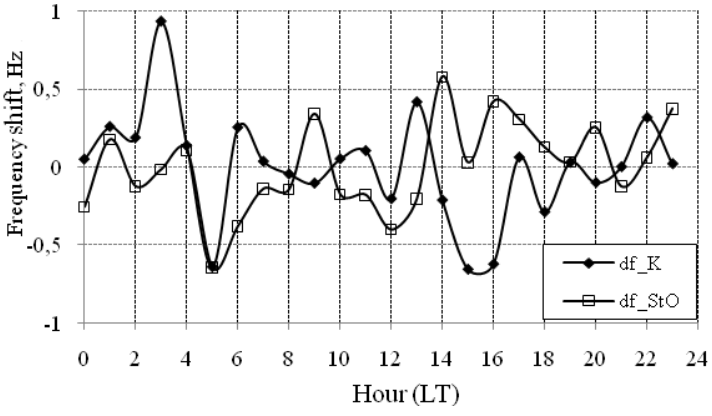

*Fig. 4: Mean diurnal variations of the hourly average TVBS Doppler shifts. The curves show: df_K – transmitter Kyiv, working frequency 59.25 MHz, df_StO – transmitters Stary Oskol, Dubki, and Bălți, 59.239583 MHz (*CO ≈ *–10.4 kHz).*

The low statistical reliability (compared to, e.g., a radar) of the TIDI dataset for a local area is compensated by the following advantages:

- it is possible to reconstruct the horizontal wind vector,
- the TIDI wind profiles were obtained simultaneously in the same volume than the experimental measurements.

The SKiYMET MR at Collm Observatory (51.3°N; 13°E), Germany has been operated nearly continuously since summer 2004 (Jacobi et al., 2005; Jacobi, 2011). The latitude is close to the one of Kharkiv, while the longitude differs by 23.2°. However, the main diurnal variation at higher midlatitudes is owing to the semidiurnal tide, which is known to be essentially migrating. Monthly mean amplitudes and phases (the latter in local time) are similar at different longitudes (e.g., Jacobi et al., 1999). Hence, it is also possible to use the Collm MR winds for comparison with the Kharkiv experimental data. First, however, we use the MR data to validate the TIDI winds. Fig. 5 shows that Collm MR and TIDI mean diurnal wind variations during April 2010 correspond to altitudes above ~90 km. We conclude from that for the altitude of maximum meteor detection rate we may use TIDI winds for comparison with the radio-meteor winds. The distribution of meteor heights has a near Gaussian envelope with a maximum between 85 and 95 km; very often the centroid altitude is near 90 km (Kashcheyev et al., 2002; Stober et al., 2008).

Fig. 6 presents the correlation coefficients between the mean diurnal variation of hourly averaged frequency shift values Δf_{mean} and hourly averaged TIDI vector wind $\vec{V}_{TIDI}$ projections for different azimuths of this projection. Two separate sets of Δf_{mean} are used for TVBS emitted by transmitters with different working frequencies, similar to Fig. 4. $\vec{V}_{TIDI}$ values are averaged between the height range 87.5-92.5 km. Corresponding correlation coefficients using Δf_{mean} and vector wind values of the Collm MR ($\vec{V}_{COLLM}$) are also shown. These are obtained for the same time and altitude range, but refer to the MLT region over Collm. The correlation analysis between the variations Δf_{mean} and projections of $\vec{V}_{TIDI}$ and $\vec{V}_{COLLM}$ at different directions (Fig. 6) shows the following:

- maximum correlation between Δf_{mean} and $\vec{V}_{TIDI}$ or $\vec{V}_{COLLM}$ projection is found for a direction pointing to (or away from) the respective TVBS sources. If the working frequency is used by several transmitters (e.g., for $f_0 = 59.239583$ *MHz*, CO ≈ *-10.4 kHz*; TV transmitters in Stary Oskol, Dubki, and Bălți), the direction for maximum correlation lies "between" the directions to these TV transmitters according to their respective power and distance,
- maximum correlation coefficients exceed 0.58 (significance > 0.95, according to a t-test),
- minimum correlation is found for a direction orthogonal to one to the transmitter,
- the maximum correlation between Δf_{mean} and projections of $\vec{V}_{TIDI}$ is stronger than the corresponding correlation between Δf_{mean} and $\vec{V}_{COLLM}$, owing to the spatial difference of 23.2° in longitude and 1.3° in latitude, giving rise to mean diurnal wind differences at time scales below the semidiurnal tidal one.

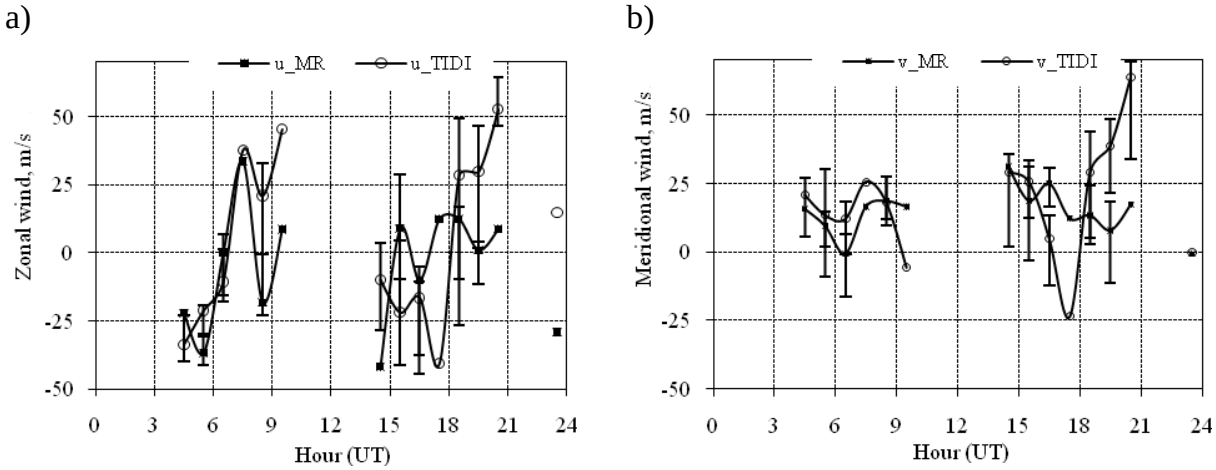

Fig. 5: Monthly mean hourly averaged Collm MR and TIDI zonal (a) and meridional (b) winds for 90 km height. Data are from April 2010 including all profiles when the TIDI profile matches the Collm one.

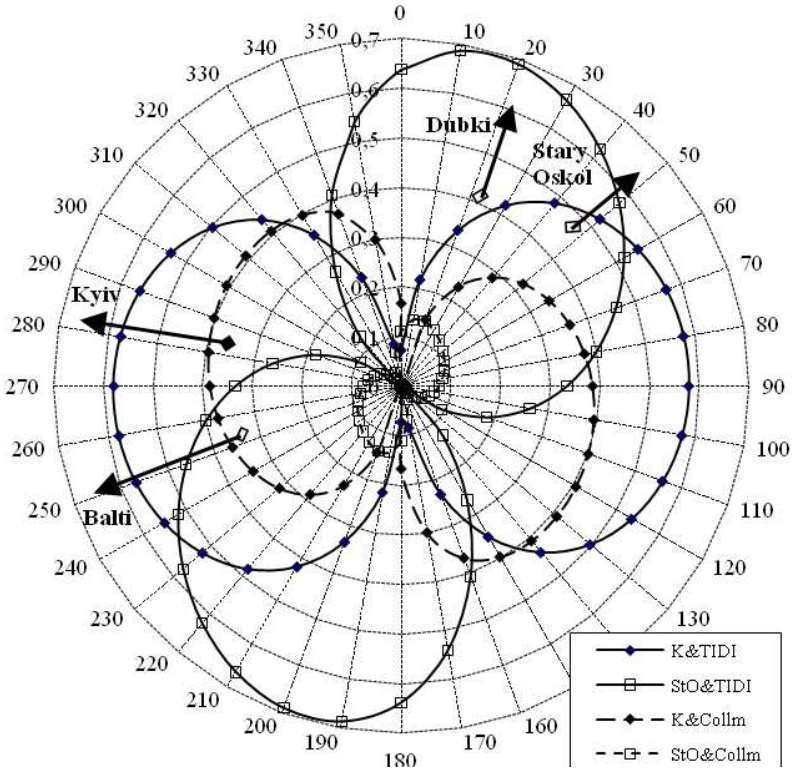

Fig. 6: Correlation coefficients between TVBS frequency shift (Δf_{mean}) and projection of TIDI (solid lines) and Collm MR (dotted lines) MLT wind to different directions. Arrows indicate directions to the corresponding TVBS sources. Solid symbols denote Δf_{mean} for the TV transmitter Kyiv (f_0 = 59.25 MHz); open symbols to TV transmitters Stary Oskol, Dubki, and Bălți (f_0 = 59.239583 MHz, CO ≈ –10.4 kHz).

The experimental results confirm that the measured carrier frequency shifts are caused by the Doppler effect due to meteor trail drift through the MLT wind, because they are proportional to the parallel MLT wind component. Such parallel components nearly correspond to the zonal wind by using signals from the TV transmitter Kyiv and the meridional wind by using a signals from TV transmitters Stary Oskol, Dubki, and Bălți. Hence the TVBS can be used for MLT wind measurements by the MR method.

Conclusions

The possibility of using terrestrial TV broadcast signals (TVBS) as sounding signals for MLT wind measurements by the radio meteor method is investigated for the first time. Use of TVBS allows to use external transmitters and consequently to reduce costs of such measurements. Using a specially developed receiver und digital signal processing tool, observations of TVBS reflected from meteor trails (second TV channel, nominal carrier frequency 59.25 MHz, SECAM colour TV system) and their Doppler shift have been obtained in April 2010 at Kharkiv, Ukraine. Validation of the obtained results has been performed using TIMED/TIDI satellite wind profiles over Kharkiv at the time of the radio measurements and Collm MR data. The hypothesis that the experimental results and TIMED/TIDI winds are uncorrelated can be discarded with a confidence of 0.95 (according to a t-test).

The measurements show that the mean diurnal variation of hourly average values of Δf is proportional to the MLT wind. It confirms that the TVBS can be used for MLT wind measurements by the radio meteor method and that the developed technique can be used for MLT wind monitoring on the base of the existing terrestrial TV broadcasting network. MLT vector wind monitoring is also possible by simultaneous using of several TV transmitters.

But this kind of TVBS usage is still to be further investigated due to relatively short time interval of the experiment TIMED satellite dataset used for validation does not have full time coverage. Validation of the results using a MR in the same area would lead to more reliable results. Further, during the experiment the angular coordinates of corresponding meteor trails are not known. There parameters, however, are necessary to increase the accuracy of MLT wind measurements and for possible wind profile estimation, and could be obtained using multi-channel receiver with spatially distributed antennas, which can be configured to act as an interferometer.

Acknowledgements

This research has been partly supported by a scholarship DAAD, code number A/09/96888. TIDI winds have been kindly provided by NOAA/NCAR through http://timed.hao.ucar.edu/tidi/data.html.

References

Arras, C., Jacobi, Ch., Wickert, J., 2009: Semidiurnal tidal signature in sporadic E occurrence rates derived from GPS radio occultation measurements at midlatitudes. Ann. Geophys., 27, 2555–2563.

Chernjak, V., 1993: Multiposition radiolocation (in russ.), Moskow, 416 p.

GOST 7845-92 (USSR/Russian/Ukrainian National Standard), 1992: Television broadcasting system: Basic parameters. Measurement methods, (in russ.), 36 p.

Hocking, W.K., Fuller, B., Vandepeer, B., 2001: Real-time determination of meteor-related parameters utilizing modern digital technology, J. Atmos. Solar-Terr. Phys., 63, 155-169.

Jacobi, Ch., 2011: Meteor radar measurements of mean winds and tides over Collm (51.3°N, 13°E) and comparison with LF drift measurements 2005-2007, Adv. Radio Sci., accepted 14.2.2011.

Jacobi, Ch., Kürschner, D., Fröhlich, K., Arnold, K., Tetzlaff, G., 2005: Meteor radar wind and temperature measurements over Collm (51.3°N, 13°E) and comparison with co-located LF drift measurements during autumn 2004, Rep. Inst. Meteorol. Univ. Leipzig, 36, 98-112.

Jacobi, Ch., Portnyagin, Yu. I., Solovjova, T. V., Hoffmann, P., Singer, W., Fahrutdinova, A. N., Ishmuratov, R. A., Beard, A. G., Mitchell, N. J., Muller, H. G., Schminder, R., Kürschner, D., Manson, A. H., Meek, C. E., 1999: Climatology of the semidiurnal tide at 52°N-56°N from ground-based radar wind measurements 1985-1995, J. Atmos. Sol.-Terr. Phys., 61, 975-991.

Kashcheyev, B. L., Lebedinets, V. N., and Lagutin, M. F., 1967: Meteoric Phenomena in the Earth‘s atmosphere (in russ.), Moscow, 260 p.

Kashcheyev, B. L., Proshkin, E. G., Lagutin, M. F., 2002: Remote methods and facilities for processes study in atmosphere of the Earth (in russ), Kharkiv, KNURE, 426 p.

Killeen, T. L., Skinner, W. R., Johnson, R. M., Edmonson, C. J., Wu, Q., Niciejewski, R. J., Grassl, H. J., Gell, D. A., Hansen, P. E., Harvey, J. D., Kafkalidis, J. F., 1999: The TIMED Doppler interferometer (TIDI), Proc. SPIE, 3756, 289-301, doi:10.1117/12.366383.

Killeen, T. L., Wu, Q., Solomon, S. C., Ortland, D. A., Skinner, W. R., Niciejewski, R. J., 2006: TIMED Doppler Interferometer: Overview and recent results, J. Geophys. Res., 111, A10S01, doi:10.1029/2005JA011484.

Kukush, V., Oleynikov, A., 2010: Estimation of possibility of meteor trail drift velocity measurements using television broadcast signals (in russ.), Proc. 11-th International Conference “Modern Information & Electronic Technologies”, Odessa, p. 218.

Kukush, V., Oleynikov, A., Makovetskyi S., 2011a: Process of wind measurement by the meteor radiolocation method with use of television broadcast signals (in ukr.). Patent

of Ukraine on the useful model, application number u2010 08168, Ukraine, IPC code (2006.01) G01S 13/58, applicant Kharkiv National University of Radio Elec¬tronics, application filing date 30.06.10, patent accept date 10.03.11.

Kukush, V., Oleynikov, A., Makovetskyi S., 2011b: Device for wind measurement by the meteor radiolocation method with use of television broadcast signals (in ukr.). Patent of Ukraine on the useful model, application number №2010 13684, Ukraine, IPC code (2009) G01S 13/58, applicant Kharkiv National University of Radio Electronics, application filing date 18.11.10, patent accept date 09.02.11.

Manning, L. A, Peterson, A. M., Villard, O. G., 1954: Ionospheric wind analysis by meteoric echo techniques, J. Geophys. Res., 59, 47-62.

McKinley, D.W.R., 1961: Meteor Science and Engineering. McGRAW-HILL, New York, 309 p.

Mori, M., 2000: Official English website for JE3HHT. Amateur Radio Freeware, http://mmhamsoft.amateur-radio.ca/, downloaded 16.03.2011.

Oleynikov, A., Sosnovchik, D., Lykov, Y., Kukush, V., Makovetskyi, S., 2010: Use of television broadcasting signals for processes study in the meteor zone of Earth's atmosphere (in russ.), All-Ukr. Sci. Interdep. Mag. Radiotechnika 160, 47-55.

Skolnik, M. I., 1970: Radar handbook. McGRAW-HILL, russ. transl., book IV, 376 p.

Stober, G., Jacobi, Ch., Fröhlich, K., Oberheide, J., 2008: Meteor radar temperatures over Collm (51.3°N, 13°E). Adv. Space Res., 42, 1253–1258.

Addresses of Authors

Vitalii Kukush, Anatoly Oleynikov
Chair "Basics of Radio Technique", National University of Radio Electronics, Lenin Avenue, 14, 61166 Kharkiv, Ukraine, e-mail vdk86@rambler.ru, ortoan@rambler.ru

Christoph Jacobi
Institut für Meteorologie, Universität Leipzig, Stephanstr. 3, 04103 Leipzig, Germany

Airborne measurements of reflectivity and albedo of urban and rural surfaces of Megacities

B. Mey[1], C. Xingfeng[2], L. Zhengqiang[2], X. Gu[2], Y. Tao[2], and M. Wendisch[1]

Abstract

Spectral reflectivity and albedo are obtained from airborne measurements of spectral irradiance and radiance during two field campaigns in Leipzig, Germany and Zhongshan, China. The data measured above urban and rural areas have been investigated with respect to the heterogeneity and anisotropy of the surface. Furthermore the spectral albedo and reflectivity measured above the same surface but at different flight altitudes have been analyzed. These data is used to estimate the impact of multiple scattering processes by aerosol particles and gas molecules.

Abstract

Spektrale Reflektivität und Albedo wurden aus Flugzeug getragenen Messungen der aufwärtsgerichteten spektralen Strahlungsflussdichte (Irradianz) und Strahldichte (Radianz) während zweier Messkampagnen in Leipzig, Deutschland und Zhongshan, China, bestimmt. Die Daten, die über urbanen und ländlichen Flächen auf konstanter Flughöhe gemessen wurden, wurden in Hinblick auf Heterogenität und Anisotropie der Oberfläche untersucht. Desweiteren wurden die spektrale Albedo und Reflektivität, die über gleichem Untergrund aber während unterschiedlicher Flughöhen gemessen wurden, analysiert. Diese Daten werden verwendet um den Einfluss von Mehrfachstreuprozessen durch Aerosolpartikel und Gasmoleküle abzuschätzen.

1 Introduction

The yearly mean global radiant energy budget is dominated by interactions of the solar radiation with clouds, trace gases, aerosol particles, and the ground surface. The solar radiation is absorbed or scattered by these components, which can locally lead to a cooling or a warming of the atmosphere. Aerosol particles and the ground surface are the largest contributors in the reflection of solar radiation in a cloud free atmosphere Therefore they should be considered especially in the vicinity of strong aerosol sources, like Megacities (cities with more than 10 Million citizens, Molina and Molina, 2004) with high productions of anthropogenic aerosol particles. To obtain a global view on the aerosol distribution satellite measurements are required. To retrieve the Aerosol Optical Depth (AOD) from space borne measurements, the measured reflected radiation has to be separated into the fractions of radiation reflected by aerosol and the surface. This separation needs assumptions which are sources of uncertainties in the satellite aerosol retrieval. The heterogeneity of the urban surface structure enhances the uncertainty of aerosol retrievals from satellite borne measurements, e.g. the AOD retrieval from measurements with the MODerate resolution Imaging Spectroradiometer (MODIS, Justice et al., 1998, Kaufman et al., 1997, Levy et al., 2007) data onboard the NASA satellites Aqua and Terra.

Surface reflectivity and albedo properties retrieved from airborne measurements are an option to estimate the surface albedo (lower boundary condition) in the satellite retrieval algorithm. albedo α_λ describes the hemispheric reflection of radiation on a surface, whereas reflectivity ρ_λ describes the reflection of radiation into a certain solid angle. The physical formulas of albedo and reflectivity are shown in Eq. [1] and [2]:

$$\alpha_\lambda = \frac{F_\lambda^\uparrow}{F_\lambda^\downarrow} \quad [1]$$

$$\rho_\lambda = \frac{\pi \cdot I_\lambda^\uparrow}{F_\lambda^\downarrow} \quad [2].$$

$F_\lambda^\uparrow$ is the spectral upward irradiance (spectral radiant flux density in W m^{-2} nm^{-1}), $F_\lambda^\downarrow$ is the spectral downward irradiance, and $I_\lambda^\uparrow$ is the spectral upward radiance (radiant density in W m^{-2} sr^{-1} nm^{-1}).

Due to lower flight altitudes of the aircraft the spatial resolution of the data is much higher than the resolution of the MODIS data. Although most of the particle load within the atmosphere is in the boundary layer, less atmospheric corrections are necessary for the retrieval of surface albedo and reflectivity in comparison to satellite data. We present measurements conducted during the field campaigns of the Megacities-project of 2007 and 2009.

2 Field campaigns

Airborne measurements of spectral albedo and reflectivity have been conducted during the field campaigns for the framework of the priority program (SPP 1233) "Megacities Megachallenge – Informal Dynamics of Global Change" funded by the German research foundation (DFG) in the years 2007 and 2009. In 2007 the area of Leipzig has been sampled, in 2009 measurements in China (Zhongshan, Guangdong province) have been obtained. The priority program is an interdisciplinary program bringing together scientist from different research area (e.g. economy, geography, engineering, and public health) within the frame of different kind of challenges in Megacities.

The first field campaign took place in September 23-24, 2007 in Leipzig, Germany. During four scientific flights, the spectral upward irradiance and radiance were measured, as well as images of the surface in three wavelength bands, of the urban structure of Leipzig.

The second field campaign was conducted in November/December 2009 in Zhongshan, China. The research flights on December 3 and 4 covered the area over Zhongshan. The flight pattern of December 3 is shown in Fig. 1.

3 Instrumentation

Airborne measurements of upward spectral irradiances and radiances were performed with the Spectral Modular Airborne Radiation measurement system (SMART-Albedometer, Wendisch et al., 2001). The SMART-Albedometer consists of two types of spectrometers which are connected via optical fibers to two kinds of optical inlets, for measuring radiance and irradiance. The two types of spectrometers cover the spectral wavelength range of 0.35 to 2.2 μm.

Ground-based measurements of the downward irradiance in the wavelength range of 350 to 1000 nm were conducted with a ground based version of the SMART-Albedometer, the COmpact RAdiation measurement System (CORAS) during the field campaign in Zhongshan 2009.

Data of downward irradiance could not been obtained during the field campaigns due to aircraft installation limitations and is simulated with the library for Radiative transfer code (libRadtan, Mayer and Kylling, 2005). Previous work (Bierwirth et al., 2008) showed that the simulated irradiance spectra match the measured ones within the measurement uncertainties for cloud free atmosphere and the knowledge of the aerosol optical properties.

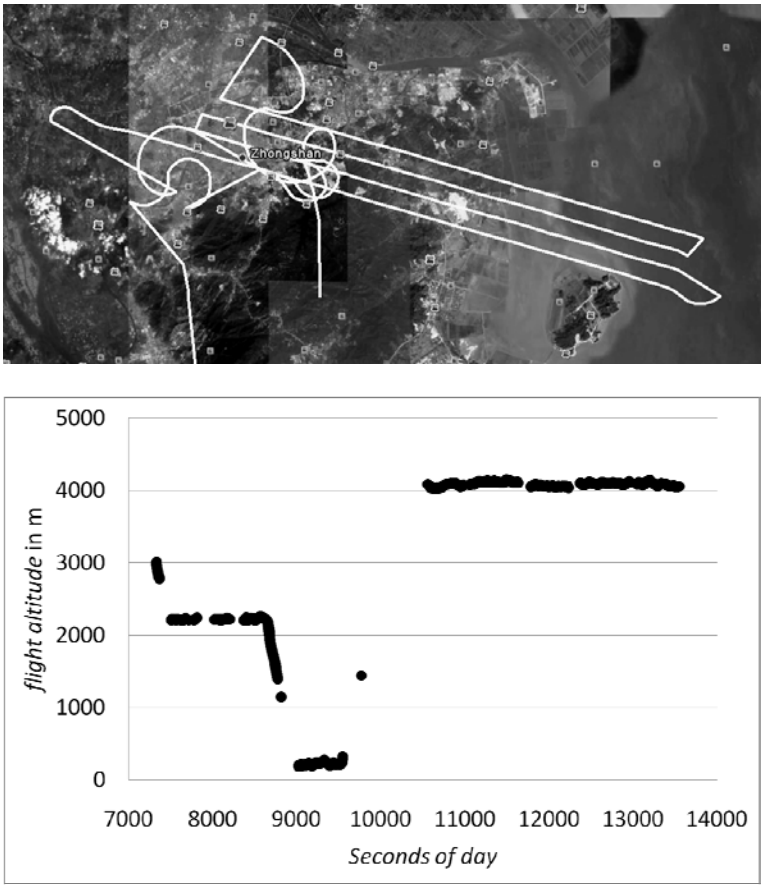

Fig. 1: Flight pattern (upper image) and flight altitude (lower image) of the flight over Zhongshan on December 3, 2009. Urban, rural, and coastal structures were surveyed by this flight pattern as it can be seen in the underlying satellite picture in the upper image.

Measurements of the AOD, the single scattering albedo (SSA), the asymmetry parameter (g) and the vertical extinction profile were retrieved from sun photometer and LIDAR measurements respectively. These measurements have been provided by the Leibniz Institute for Tropospheric research (IfT, Leipzig, Germany) and the Institute of Remote Sensing Applications, Chinese Academy of Sciences (IRSA, CAS, Beijing, China).

4 Results

We present results obtained from the data measured in 2007 in Leipzig, Germany and in 2009 in Zhongshan, China. The presented data at flight level still includes the signal of the solar radiation reflected on gas molecules and aerosol particles in the layer between aircraft and ground; therefore it is not possible to draw any conclusion about surface reflectivity and albedo. Features in the data which could already be observed at flight level without extrapolating albedo and reflectivity to surface level are discussed.

Two major differences between the data sets of Leipzig and Zhongshan can be highlighted. Both locations are characterized by a different aerosol load during measurements. The AOD at 532 nm measured on September 23, 2007 in Leipzig was much lower (AOD = 0.2) in comparison with the AOD on December 3, 2009 in Zhongshan (AOD = 0.9). Furthermore, the flight altitude during the measurements in Leipzig was about 600 m above sea level (approx. 500 m above surface), whereas the flight altitude during the measurements in Zhongshan was mostly 4000 m with two short flight tracks in 2000 m and 200 m flight altitude. This gives the opportunity to analyze the data focussing on different aspects, surface heterogeneity during the first campaign, and flight altitude dependence for the data of the second campaign in Zhongshan.

4.1 Surface heterogeneity and homogeneity

Different surface types with different grade of heterogeneity were observed during the measurements in Leipzig, Germany. The measurements were performed at low flight altitudes of 500 m above ground (600 m above sea level) and only minor corrections are necessary to obtain the surface albedo from the measurements at flight level to reduce the atmospheric masking. A time series of albedo and reflectivity, corresponding to their spatial distribution gives an idea about the heterogeneity of the surface (Fig. 2).

The time series of the albedo is obviously smoother than the time series of the reflectivity which can be explained by the definition of the quantities itself. The albedo data includes the reflection properties of the geographical measurement position and the information of the vicinity. Reflectivity that is calculated by multiplying the radiance with π, is typically locally different from the albedo for anisotropic surfaces. The reflectivity is higher than the albedo, if the surface observed in the field of view is highlighted, or lower than the albedo, if the surface is shadowed. Part (a) in Fig. 2 shows the reflectivity and the albedo of a heterogeneous surface (urban/industrial surface). Fluctuations in the reflectivity data and differences between albedo and reflectivity are clearly visible. These differences show that the surface reflects solar radiation anisotropic. The fluctuations in the reflectivity data indicate that the

measured surface is heterogeneous. Exemplarily, part (b) shows both quantities for a rather homogeneous surface (agriculture). The values of the albedo and the reflectivity are almost constant and correspond within the error bars for most times, which shows that the surface is most likely an isotropic reflecting surface.

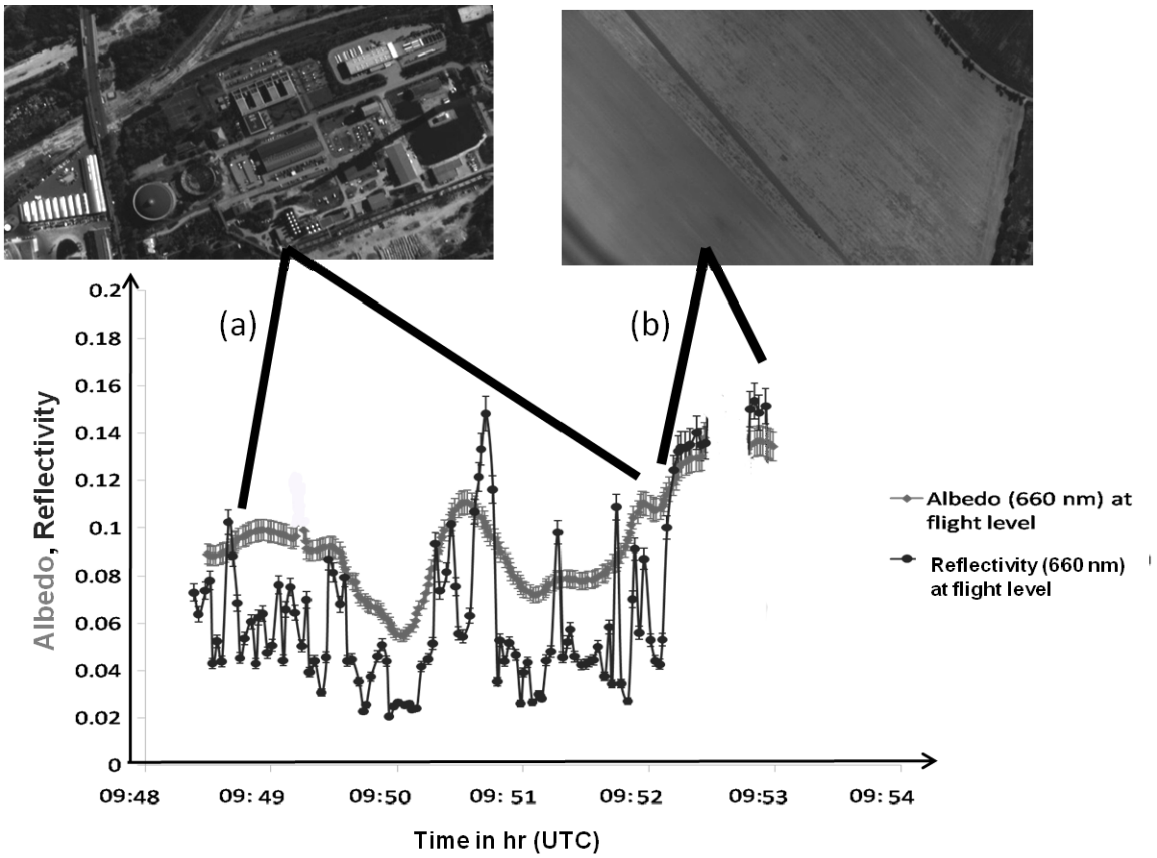

Fig. 2: Time series of albedo (light grey) and reflectivity (dark grey) of 660 nm at flight level, measured on September 23, 2007 over Leipzig, Germany. The time seires corresponds to a spatial data series as the aircraft is moving. Parts (a) and (b) representing different surfaces. (a) Heterogeneous urban surfaces, (b) homogenous agricultural surfaces. The missing data in part (b) was caused by strong aircraft movement (high roll angles) during a turn. The images above are examples for the present surface during the measurements in part (a) and (b).

4.2 Albedo and reflectivity of different surfaces at high flight altitudes

In contrast to the measurements over Leipzig the measurements conducted in Zhongshan have been obtained at a flight altitude of about 4000 m, with two short flight legs (approximately 2 minutes) at 2000 m and 200 m. Two implications on the measured data result from the high flight altitude. Due to the high atmospheric column between surface and optical inlet, the amount of solar radiation scattered by aerosol

particles and molecules into the optical inlet is increased compared to the fraction of radiation reflected by the surface. This effect is enhanced by the fact that the main amount of aerosol was in the layer between the surface and the flight level.

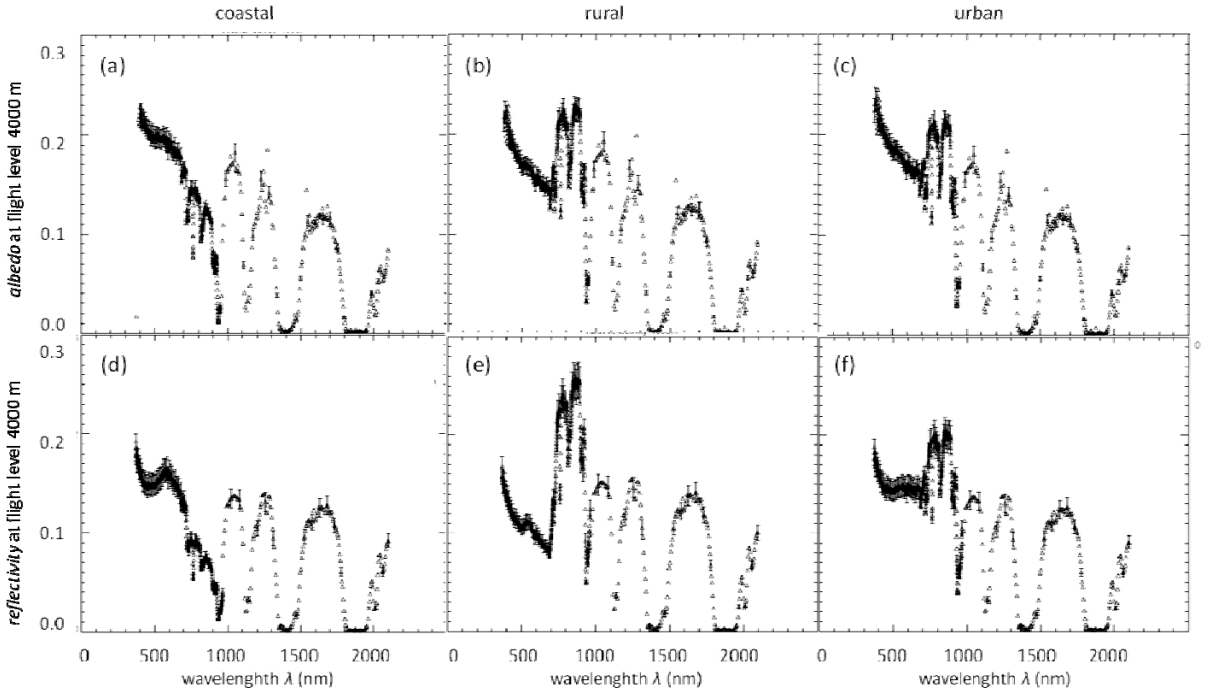

Fig. 3: Albedo (upper row) and reflectivity (lower row) measured at 4000 m flight altitude for different surfaces ((a) and (d) coastal/ocean surface, (b) and (e) rural surface, (c) and (f) urban surface).

Furthermore the surface area relevant for the irradiance measurements is larger compared to measurements obtained at low flight altitude. Therefore, different surface types may be included in one single measurement, e.g. urban surfaces are still visible in the coastal region and vice versa. Figure 3 shows three exemplarily albedo measurements (upper row) and three reflectivity measurements (lower row) of different surfaces. Coastal/ocean surface ((a), (d)) which was observed approximately 7 km away from the coastline, where the sea is relatively shallow and a small island nearby can additionally influence the measurement. Figure 3 (b) and (e) show spectra of rural surfaces in the area between the city of Zhongshan and the coastline. The albedo is therefore influenced both by urban surface and coastal/ocean surface. Spectra of urban reflectivity and albedo are shown in images (c) and (f). Especially the spectra (b) and (c) look similar what can be explained by the mutual influence of the surfaces in the measurements. The reflectivity spectrum in (d) shows a local maximum between 500 and 600 nm which could be caused by four factors: the nearby land surface of the main land, the nearby small island, contamination of the water by green algae, and the ocean surface visible through shallow water.

4.3 Influence of altitude on the observed albedo and reflectivity

The observed albedo and reflectivity at flight altitude is affected by the field of view of the optical inlet and the optical properties of the aerosol below. With increasing flight altitude the observed area is also increasing. Figure 4 shows the spatially averaged spectra of the albedo (upper row) and the reflectivity (lower row). The same surface area of Zhongshan was sampled three times in different flight altitudes (approximately 200 m, 2000 m, and 4000 m). The measured data was averaged for 2 minutes. Additionally to the mean values the standard deviations are shown in Figure 4. The standard deviations indicate the spatial variability of the surface. As expected, the standard deviation of the reflectivity spectra is higher compared to the standard deviation of the albedo spectra, illustrating that the surface heterogeneity is more pronounced in the reflectivity measurements than in the albedo. Especially the reflectivity obtained from measurements at 200 m flight altitude shows high standard deviation values. By contrast, the information of the surface reflectivity is already at 2000 and 4000 m flight altitude and has lower standard deviation values. Both measurements at 2000 and 4000 m ((b), (e) and (a), (d)) look similar and differ from the spectra measured at 200 m ((c), (f)). This can be explained again by multiple scattering processes at higher altitudes, and additionally the stronger influence of the surface in the vicinity of the measured spot in comparison to the measurement at 200 m.

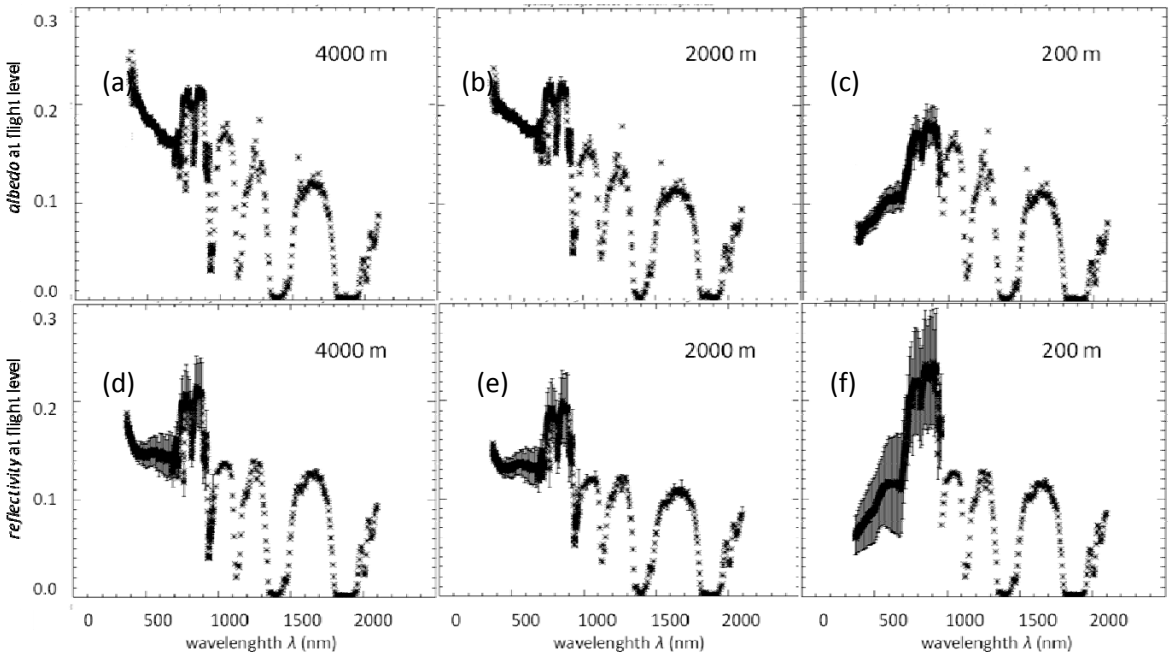

Fig. 4: Spatially averaged albedo and reflectivity at flight level measured at different flight altitudes and corresponding standard deviations as error bars. Only every tenths error bar is displayed for visibility reasons.

5 Conclusions and Outlook

A dataset of reflectivity and albedo measured at flight altitude of the cities Leipzig, Germany and Zhongshan, China was obtained within the framework of the priority program SPP 1233 of the German Research Foundation (DFG) in the years of 2007 and 2009. The simultaneous airborne measurement of albedo and reflectivity allows to draw conclusions about the heterogeneity of a surface, and if a surface is isotropic reflecting or not. It was shown that agricultural surfaces are homogeneous and rather isotropic reflecting surfaces. In contrast, urban surfaces are heterogeneous, visible in the spatial variability of the spectral reflectivity, and not isotropic which is indicated by the difference between spectral albedo and reflectivity.

The measurements of albedo at flight level are strongly influenced by the flight altitude as the area included in the albedo and reflectivity data increases with increasing flight altitude. By this the measurement of urban albedo might for example include ocean albedo information and vice versa. Additionally the effect of multiple scattering increases with increasing flight altitude, as more aerosol particles are available for scattering processes between the observed object and the optical instrument. Same is valid for scattering of radiation on gas molecules.

Atmospheric correction (Wendisch et al., 2004) to obtain surface albedo and reflectivity from the flight level albedo and reflectivity will show if the retrieved spectra are dependent on the flight altitude. Surface reflectivity data of Leipzig and Zhongshan will be used as input parameter in the MODIS AOD retrieval algorithm to check whether it improves the retrieved AOD in comparison to sunphotometer measurements of the AOD (e. g. data from the AErosol RObotic NETwork, AERONET, Holben et al., 1998).

Literature

Bierwirth, E., Wendisch, M., Ehrlich, A. et al., 2008: Spectral surface albedo over Marocco and ist impact on radiative forcing of Saharan dust. Tellus B, Volume 61 (1): 252 – 269

Holben, B.N., Eck, T.F., Slutsker, I. et al., 1998: AERONET—A Federated Instrument Network and Data Archive for Aerosol Characterization. Remote Sensing of Environment, 66 (1): 1 – 16

Justice, C.O., Vermote, E., Townshend, J.R.G, et al., 1998: The Moderate Resolution Imaging Spectroradiometer (MODIS): land remote sensing for global change research. IEEE Transactions on Geoscience and Remote Sensing. 36 (4): 1228 – 1249

Kaufman, Y.J., Wald, A.E., Remer, L.A., et al., 1997: The MODIS 2.1- μm Channel—Correlation with Visible Reflectance for Use in Remote Sensing of Aerosol. IEEE Transactions on Geoscience and Remote Sensing, 35 (5): 1286 – 1298

Levy, R. C., Remer, L. A., Mattoo, S., et al., 2007: Second-generation operational algorithm: Retrieval of aerosol properties over land from inversion of Moderate Resolution Imaging Spectroradiometer spectral reflectance. Journal of Geophysical Research. 112: D13211

Mayer, B., and Kylling, A., 2005: Technical note: The libRadtran software package for radiative transfer calculations – description and examples of use. Atmos. Chem. Phys. Discuss., 5, 1319–1381

Molina, M.J. and Molina, L.T., 2004: Megacities and Atmospheric Pollution. Air & Waste Manage. Assoc. 54:644 – 680

Wendisch, M., Müller, D., Schell, D. et al., 2001: An airborne spectral albedometer with active horizontal stabilization. J. Atmos. Oceanic Technology, 18, 1856-1866

Wendisch, M., Pilewskie, P., Jäkel, E. et al., 2004: Airborne measurements of areal spectral surface albedo over different sea and land surfaces. Journal of Geophysical Research, 109: D08203

Addresses of Authors

[1] Leipzig University, Institute for Meteorology, Stephanstr. 3, 04103 Leipzig, Germany, b.mey@uni-leipzig.de
[2] Institute of Remote Sensing Applications, Chinese Academy of Sciences, No. 20 Datun Road, Chaoyang District, P.O. Box 9718, Bejing 100101, P.R. China

On the overestimation of gas absorption optical depth due to spectral layer-transmissivity averaging

S. Otto

Summary

Absorption of radiation by atmospheric gases is characterised by specific line transition structures. Spectrally high-resolved line-by-line (lbl) spectra of the respective optical depths may vary over several orders of magnitude. To avoid time-consuming lbl simulations spectral averaging is commonly applied to obtain an averaged layer optical depth as a basis for fine- and broad-band absorption parameterisations for input in band radiative transfer models. It is shown that various averaging approaches can be applied but leading to significantly differing optical depth spectra whereby the usually considered method of averaging the layer transmissivity results in strong overestimations.

Zusammenfassung

Die Absorption von Strahlung durch Atmosphärengase ist von spezifischen Linienübergangsstrukturen geprägt. Spekral hochaufgelöste Linie-für-Linie (LfL)-Spektren der entsprechenden optischen Dicken können über mehrere Größenordnungen variieren. Spektrale Mittelungen werden bemüht, um eine gemittelte schichtoptische Dicke als Grundlage fein- und grobbandiger Parametrisierungen der Absorption zu erhalten für den Einsatz in Banden-Strahlungstransportmodellen zur Vermeidung des Rechenaufwands von LfL-Simulationen. Es wird gezeigt, dass verschiedene Mittelungsansätze anwendbar sind, die jedoch zu signifikant unterschiedlichen Spektren der optischen Dicke führen, wobei die im Allgemeinen berücksichtigte Methode der Mittelung der Schichttransmissivität zu starken Überschätzungen führt.

1 Introduction

In the case of isotropic extinction (independence of radiation direction $\mathbf{y}$) and horizontal homogeneity the optical depth at a certain altitude x_3 is defined by

$$\tau := h^{-1}(x_3, \nu) = \int\limits_{[x_3, z_{\mathcal{A}}]} k_e(s, \nu)\, ds \tag{1}$$

where k_e is the (isotropic) extinction coefficient of the medium in units of m^{-1}, ν the frequency in units of Hz and $z_{\mathcal{A}}$ the top of the local (horizontally homogeneous) atmospheric column $\mathcal{S} \subset \mathbb{R}^3$ over a certain place on Earths surface.

Let the column $\mathcal{S}$ be a Gaussian domain (Fischer and Kaul, 1998) and a straight-lined path $C = \{\boldsymbol{\alpha}(x_3) \in \mathcal{S} \,|\, x_3 \in [0, z_{\mathcal{A}}]\}$ given along which the extinction coefficient and hence the optical depth in (1) are defined for all $x_3 \in [0, z_{\mathcal{A}}]$. Let the atmospheric medium in $\mathcal{S}$ also be characterised by stationarity (independence of time), elastic scattering as well as Planckian emission. Suppose that the scattering and absorption coefficient are isotropic and at least one of both are locally positive, that is, $k_a(x_3, \nu) > 0$ and/or $k_s(x_3, \nu) > 0$ for some $x_3 \in [0, z_{\mathcal{A}}]$. Introducing $L(x_3, \mathbf{y}, \nu)$ to be the radiance on $\mathcal{S}$, divided into a direct and diffuse part D and I, respectively, as well as applying the vertical transformation $h^{-1} : x_3 \in [0, z_{\mathcal{A}}] \to [\tau_{\mathcal{A}}, 0] \ni \tau$ and spherical coordinates to represent the unit sphere $S_o = \{\boldsymbol{\omega}(\mu, \varphi) \,|\, (\mu, \varphi) \in [-1, 1] \times [0, 2\pi]\}$, where $\boldsymbol{\omega}$ is one parameterisation (Otto and Trautmann, 2008a,b, 2009), for the diffuse radiance field the equation

$$\mu\, \partial_\tau I(\tau, \mu, \varphi, \nu) - I(\tau, \mu, \varphi, \nu)$$

$$= \begin{cases} -\Big(1 - \varpi(\tau, \nu)\Big)\, \dfrac{B(\tau, \nu)}{\Omega_o} \\ \quad - \dfrac{\varpi(\tau, \nu)}{4\pi} \displaystyle\int\limits_{[0, 2\pi]} \int\limits_{[-1, 1]} P(\tau, \mu' \,|\, \mu, \varphi' \,|\, \varphi, \nu)\, I(\tau, \mu', \varphi', \nu)\, d\mu'\, d\varphi' \\ \quad - \dfrac{\varpi(\tau, \nu)}{4\pi}\, P(\tau, \mu_{_D} \,|\, \mu, \varphi_{_D} \,|\, \varphi, \nu)\, D(\tau, \mu_{_D}, \nu) \qquad \vee\, k_s(\tau, \nu) > 0 \\ \\ -\dfrac{B(\tau, \nu)}{\Omega_o} \qquad \vee\, k_s(\tau, \nu) = 0 \end{cases} \tag{2}$$

holds for all $(\tau, \mu, \varphi, \nu) \in [0, \tau_A] \times [-1, 1] \times [0, 2\pi] \times \mathbb{R}_{>0}$ in case of horizontal homogeneity where ϖ is the single scattering albedo, B the Planck function, P the scattering phase function, Ω_o the unit area (Otto and Trautmann, 2009; Otto and Meringer, 2011) and the direct light D as a function of the solar zenith angle $\vartheta_D = \cos^{-1}(\mu_D) > \frac{\pi}{2}$ satisfies

$$D(\tau, \mu_D, \nu) = F_o(\nu) \exp\left(\frac{\tau}{\mu_D}\right), \qquad \mu_D = \cos\vartheta_D < 0$$

with the solar radiance F_o. The radiative transfer (RT) equation (2) is usually applied to describe the transport of radiation through a terrestrial model atmosphere which is divided into a finite number of horizontally homogeneous layers, that is, a so-called plane-parallel model atmosphere. It is valid for a monochromatic frequency ν or wavelength $\lambda = \frac{c}{\nu}$ with velocity of light in vacuum c and can be solved numerically by standard techniques in the plane-parallel approximation if the so-called optical properties (τ, ϖ and P) are known as a function of altitude as well as frequency and if boundary conditions are determined (Zdunkowski et al., 2007).

2 The averaging and mixing problem

The Earth's atmosphere consists of gas molecules, aerosol particles and cloud elements. All these objects can scatter and absorb solar (0.2 to 4 μm wavelength) and thermal (4 to 40 μm) radiation in characteristic spectral regions. Especially, the absorption coefficient of gases can vary spectrally over several orders of magnitude which results in significant variations of the spectral total optical depth of oxygen which is shown in Fig. 1 (top) where the calculation was performed in a solar band with a high-spectral resolution to resolve the lbl absorption structures. Total optical depth also varies spatially (Fig. 1, bottom).

Weather forecast and climate models contain radiation schemes which calculate radiative heating rates as input for their dynamics schemes. The heating rate is proportional to the spectrally integrated net energy flux density (Zdunkowski et al., 2007), obtained by solid angle integrations (over μ and φ) of the total (direct plus diffuse) radiance $L(\tau, \mu, \varphi, \nu)$. To exactly calculate the heating rate one has to determine L lbl and integrate then spectrally. Such monochromatic lbl calculations of the RT are recently still too time-consuming. To avoid numerical effort, RT is solved only for fine or broad bands, an approximation which implies a certain spectral averaging of

the optical properties. In particular, the optical depth has to be averaged spectrally which is discussed in the following.

Divide the spectral region of interest into a finite number N of pairwise disjoint intervals $I_{\nu_l} := [\nu_{l-1}, \nu_l]$, to be averaged over, with $\Delta\nu_l := \nu_l - \nu_{l-1}$ for all $l = 1, \ldots, N$. Divide also the plane-parallel model atmosphere into a finite number Q of homogeneous layers with $Q+1$ layer boundaries (levels) z_k such that $z_0 = z_{\mathcal{A}}$ and $z_Q = 0$ (or $z_Q > 0$ according to the elevation of the ground above sea level). Let $k_e(x_3, \nu)$ be the extinction coefficient of the plane-parallel atmospheric column and consider the k-th homogeneous layer (Cheruy et al., 1995). Then (i) the quantity

$$\Delta\tau_k(\nu) := \int_{[z_k, z_{k-1}]} k_e(x_3, \nu)\, dx_3, \qquad k = 1, \ldots, Q$$

is called spectral **layer optical depth**, (ii) the term

$$\Delta T_k(\nu) := \exp\left[\, -\Delta\tau_k(\nu)\,\right]$$

is the spectral **layer transmissivity** and (iii) the expression

$$T_i(\nu) := \prod_{k=1}^{i} \Delta T_k(\nu) = \exp\left[\, -\sum_{k=1}^{i} \Delta\tau_k(\nu)\,\right] \equiv \exp\left[\, -\tau_i(\nu)\,\right],$$

$$\tau_i(\nu) = h^{-1}(z_i, \nu), \qquad i = 0, \ldots, Q$$

with h^{-1} from (1) and $\tau_0(\nu) \equiv 0$ is denoted spectral **level transmissivity** for which $T_0(\nu) = 1$ and the recursion formula $T_k(\nu) = T_{k-1}(\nu)\,\Delta T_k(\nu)$ hold. Note that the standard RT solvers require a certain layer optical depth to be applied in fine- and broad-band simulations. This *spectrally averaged* layer optical depth is denoted by $\Delta\tau_k(\Delta\nu_l)$ in the following and refers to the spectral band I_{ν_l}.

If this averaged layer optical depth can be parameterised in a certain way, resimulations of the lbl structures can be avoided and computational effort is significantly reduced, since the RT solver is called only for a small number of bands compared to a much larger number of monochromatic frequencies in a lbl calculation. This is the idea of the exponential-sum fitting technique (Wiscombe and Evans, 1977) and the correlated k-distribution method (Fu and Liou, 1992) which parameterise the spectrally averaged band absorption as a function of temperature, pressure and absorber amount. However, from literature it often becomes not clear how the averaging is really performed.

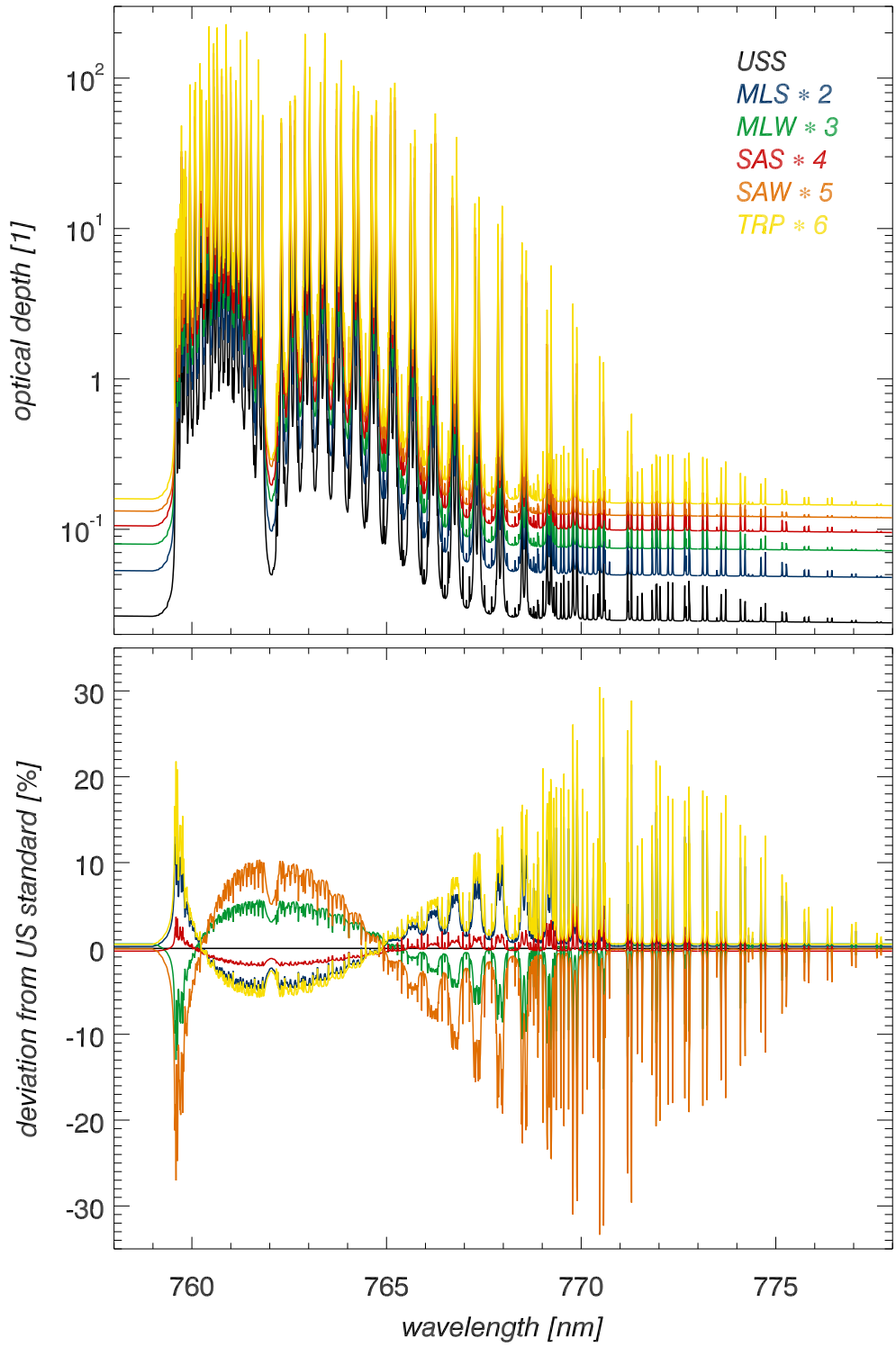

Figure 1: (top) Spectral total extinction optical depth between 758 and 778 nm wavelength (O_2A band) for various only-oxygen-containing standard atmospheres (Anderson et al., 1986) within the altitude range from 0 to 70 km (including Rayleigh scattering): US-Standard (USS), Mid-Latitude Summer (MLS), Mid-Latitude Winter (MLW), Sub-Arctic Summer (SAS), Sub-Arctic Winter (SAW), TRoPical (TRP). For clarity the curves were scaled as indicated by the numbers in the legend. Spectral resolution is 10^{-2} nm according to a moderate lbl calculation. (bottom) Deviations to USS atmosphere caused by oxygen.

That's why I would like to note that the following spectral averaging procedures are conceivable (index k runs from 1 to Q while i from 0 to Q):

1. Averaging of the layer optical depth (ALOD) by

$$\Delta\tau_{k}(\Delta\nu_{l}) := \frac{1}{\Delta\nu_{l}} \int\limits_{I_{\nu_{l}}} \Delta\tau_{k}(\nu)\, d\nu$$

2. Averaging of the layer transmissivity (ALAT) by (Isaacs et al., 1987; Lacis und Oinas et al., 1991; Fu and Liou, 1992; Chou et al., 1995; Bennartz and Fischer, 2000; Cao et al., 2011)

$$\Delta\tau_{k}(\Delta\nu_{l}) := -\ln\left[\frac{1}{\Delta\nu_{l}} \int\limits_{I_{\nu_{l}}} \Delta T_{k}(\nu)\, d\nu\right]$$

3. Averaging of the level transmissivity (ALET) by

$$\Delta\tau_{k}(\Delta\nu_{l}) := -\ln\left[\frac{T_{k}(\Delta\nu_{l})}{T_{k-1}(\Delta\nu_{l})}\right], \qquad T_{i}(\Delta\nu_{l}) := \frac{1}{\Delta\nu_{l}} \int\limits_{I_{\nu_{l}}} T_{i}(\nu)\, d\nu.$$

Third method can be considered as the physically most reasonable one for averaged layer optical depth calculations. The problem of choicing one these three approximations is called *averaging problem*.

Another source of error is the mixing of gases, that is, the averaged layer optical depths for individual gases are calculated separately from each other and then summed by the so-called mixing rule of optical properties to yield the total averaged layer optical depth. It will be shown in the next section that this really leads to certain errors, since the mixing rule is actually only valid for a monochromatic frequency (Otto, 2011) and can strictly speaking only be performed before applying the spectral averaging. This problem is called *mixing problem*.

Note that the before-mentioned two sources of error in averaged layer optical depth calculations of trace gases might accumulate when deriving averaged total optical depths representative for the entire column.

3 Discussion of the two problems

First, the mixing problem is discussed. The averaged total optical depths of various major and minor gases (Rothman et al., 2009) were computed

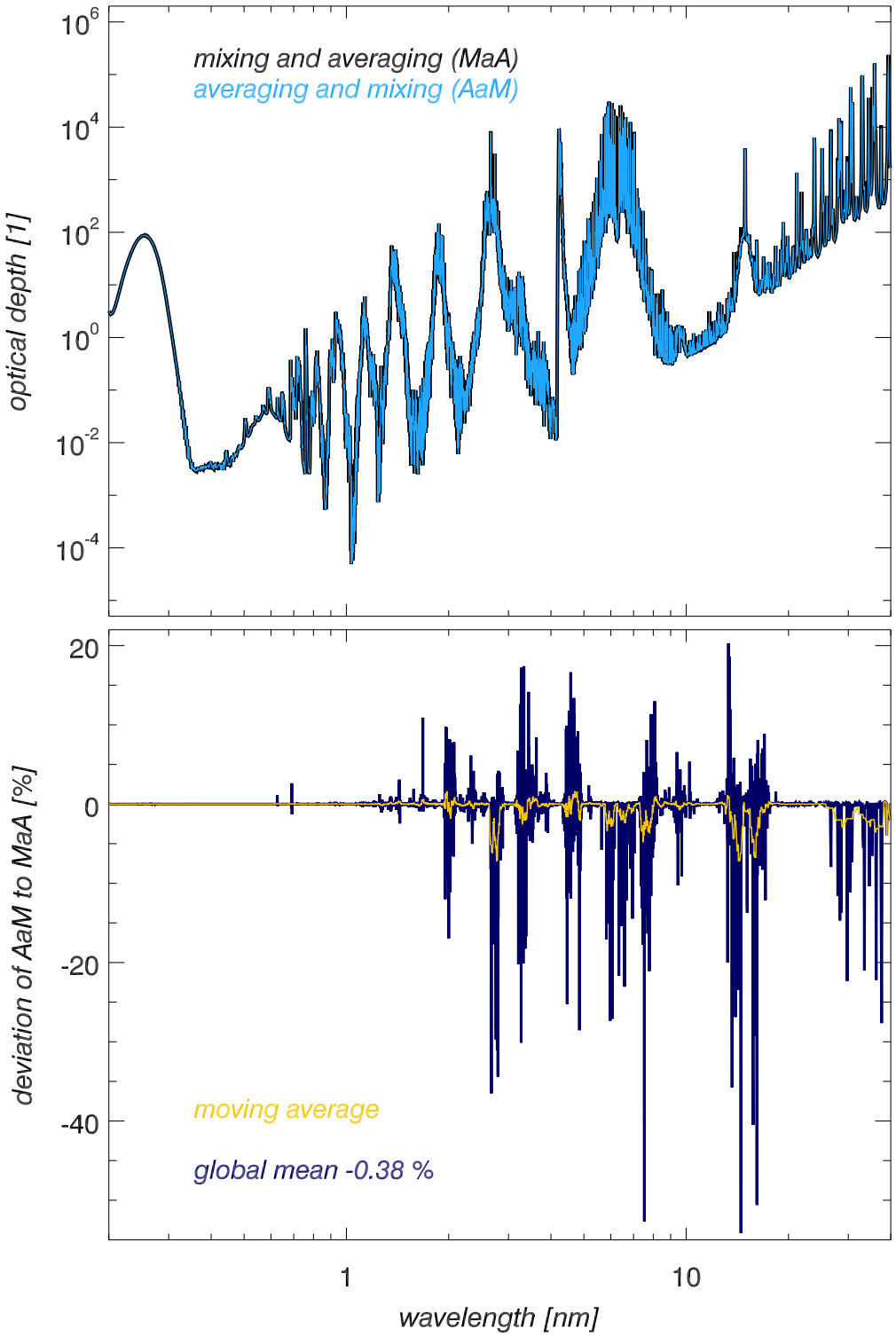

Figure 2: (top) Total absorption optical depth of a tropical standard atmosphere (Anderson et al., 1986) within the altitude range from 0 to 70 km as a function of wavelength with fine-band spectral resolutions of 1 nm (for the spectral range from 0.2 to 1.6 μm wavelength), 2.5 nm (1.6 to 5 μm) and 1 cm^{-1} (5 to 40 μm) applying i) MaA (black curve) and ii) AaM (blue) approach. See main text for details. (bottom) Deviation of AaM to MaA approach (purple curve) with a spectrally global mean of -0.38%. A moving average (yellow) is also drawn just to demonstrate where rather positive or negative spectral deviations occur.

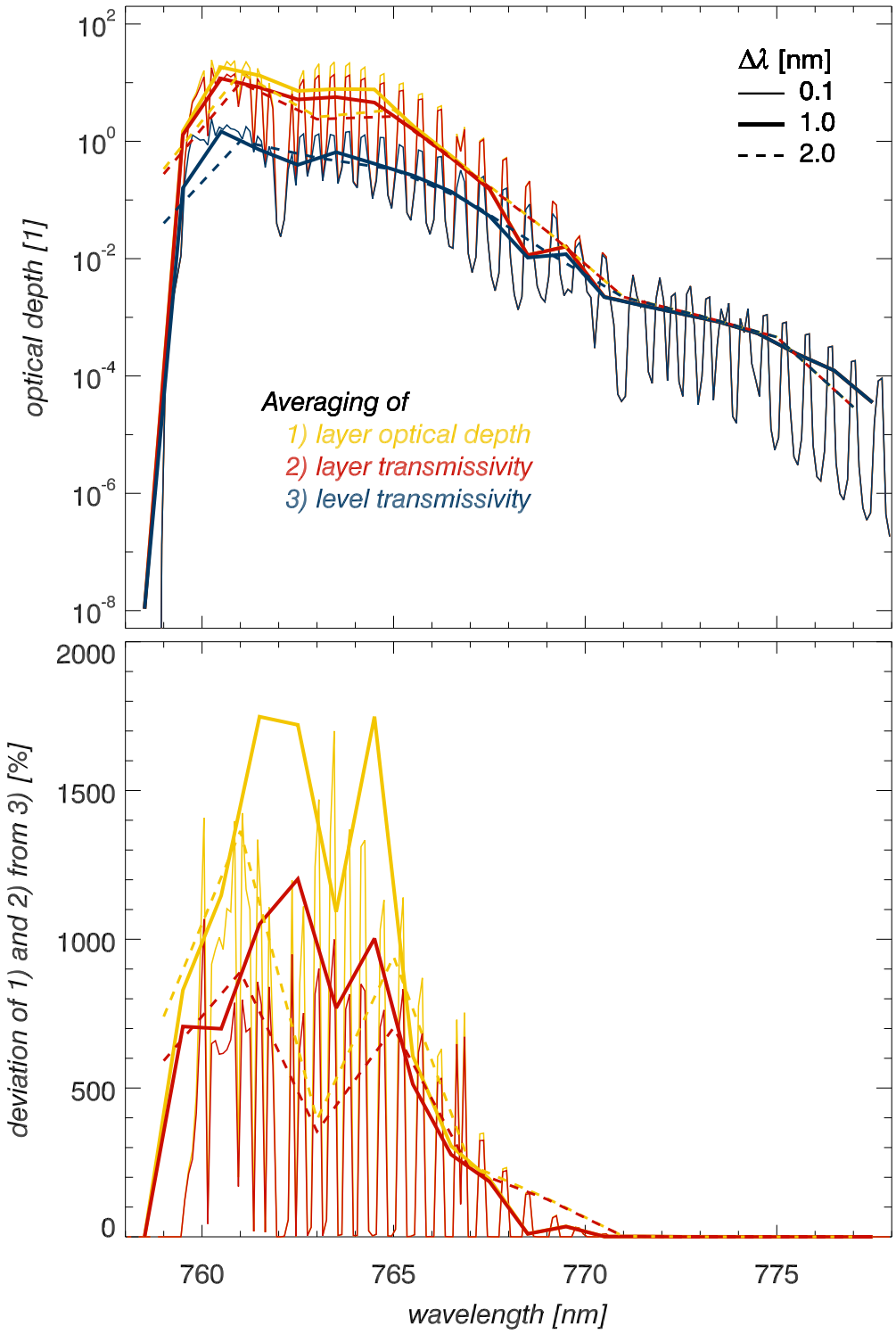

Figure 3: (top) Total absorption optical depth of oxygen for a standard tropical atmosphere (Anderson et al., 1986) within the altitude range from 0 to 70 km between 758 and 778 nm wavelength (O_2A band) applying the three different spectral averaging approaches 1) ALOD, 2) ALAT and 3) ALET as explained in the main text to various spectral resolutions $\Delta\lambda$. (bottom) Deviations of the averaging techniques ALOD, ALAT from ALET.

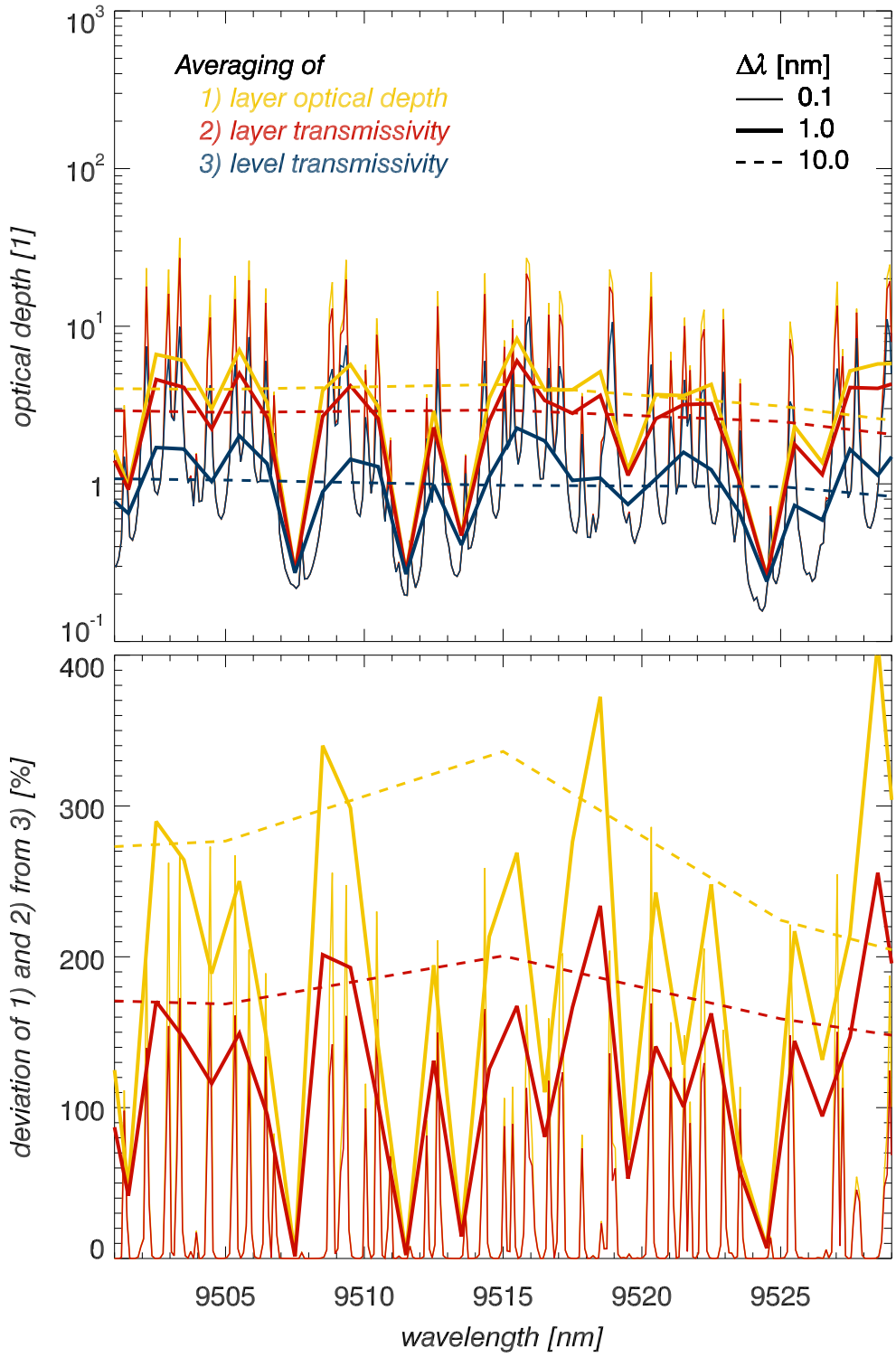

Figure 4: The same as in Fig. 3, but for ozone between 9.5 and 9.53 μm wavelength (within the 9.6 μm band of ozone).

for a tropical standard atmosphere in the solar and thermal spectral range where ALET was applied. All gases were considered independently of each other, that is, always one gas component was assumed for which the spectral averaging was performed. The total optical depth of the gas mixture was then approximated with the help of the mixing rule whereby all the total optical depths of the individual gases were summed. The result is shown in Fig. 2 (top) and represented by the blue curve 'averaging and mixing' (AaM). In a second step all gas components were considered before carrying out the spectral averaging over each fine band such that the mixing rule is correctly applied monochromatically for the sub frequencies of each fine band. This phyisically more reasonable and exact approach is drawn as the black curve 'mixing and averaging' (MaA) in the same figure lying behind the blue one. The bottom panel shows the spectral deviation of the AaM approach to the case of MaA. Obviously, significant deviations between AaM and MaA approach occur depending on the spectral region, which are rather negative (yellow curve), that is, AaM rather underestimates total absorption optical depth by a global mean of -0.38%. Thus, the mixing of averaged layer optical depths should be avoided and parameterisations of the optical depth of individual gas components lead to characteristic errors when deriving the total optical depth of the gas mixture from different parameterisation for the single gases. This mixing problem might also be relevant for situations of aerosols and clouds in the atmosphere.

Second, the averaging problem is considered. To avoid the mixing problem always single gas components are considered for certain smaller spectral regions where they characteristically absorb: i) oxygen in the O_2A band (Fig. 1) in the solar and ii) ozone around its $9.6\,\mu$m band in the thermal window region. The Figs. 3 and 4 present the spectral absorption optical depth of oxygen and ozone, respectively, simulated via ALOD, ALAT and ALET for three different spectral resolutions. Independently of the latter ALOD and ALAT lead to significant overestimations of the optical depth for regions of large magnitudes. The larger the spectral resolution is chosen, the more are the effects smeared over the spectrum resulting in relatively spectrally constant overestimations not to be ignored. Thus, the accuracy of averaged layer optical depth calculations depends significantly on the averaging technique and spectral resolution. Methods ALOD and ALAT should be avoided which is a helpful information for re-evaluating the correctness of absorption parameterisations based on ALAT.

4 Conclusions and outlook

Parameterisations of absorption by atmospheric gases in characteristic fine and broad bands that are based on spectral averaging the layer transmissivity must be revised and incorporate level transmissivity averaging. This will be discussed in a future paper.

References

Anderson, G.P., Clough, S.A., Kneizys, F.X., Chetwynd, J.H., Shettle, E.P., 1986: AFGL atmospheric constituent profiles (0-120 km). AFGL-TR-86-0110, AFGL (OPI), Hanscom AFB, MA 01736.

Bennartz, R., Fischer, J., 2000: A modified k-distribution approach applied to narrow band water vapour and oxygen absorption estimates in the near infrared. J. Quant. Spectrosc. Radiat. Transfer 66, 539-553.

Cao, Y., Zhang, W., Zhang, Y., Chang, H., Cong, M., 2011: A new k-interval selection technique for fast atmospheric radiance calculation in remote sensing applications, J. Quant. Spectrosc. Radiat. Transfer, in press.

Cheruy, F., Scott, N.A., Armante, R., Tournier, B., Chedin, A., 1995: Contribution to the development of radiative transfer models for high spectral resolution observations in the infrared. J. Quant. Spectrosc. Radiat. Transfer 53(6), 597-611.

Chou, M.-D., Ridgway, W.L., Yan, M.M.-H., 1995: Parameterizations for water vapor IR radiative transfer in both the middle and lower atmospheres. J. Atmos. Sciences 52(8), 1159-1167.

Isaacs, R.G., Wang, W.-C., Worsham, R.D., Goldenberg, S., 1987: Multiple scattering LOWTRAN and FASCODE models, Appl. Optics 26(7), 1272-1281.

Fischer, H., Kaul, H., 1998: Mathematik für Physiker 1. Teubner Studienbücher Mathematik/Physik. B.G. Teubner, 584 pp.

Lacis, A.A., Oinas, V., 1991: A description of the correlated k distribution method for modeling nongray gaseous absorption, thermal emission, and multiple scattering in vertically inhomogeneous atmospheres. J. Geophys. Research 96(D5), 9027-9063.

Fu, Q., Liou, K.N., 1992: On the correlated k-distribution method for radiative transfer in nonhomogeneous atmospheres, J. Atmos. Sciences 49(22), 2139-2156.

Otto, S., Trautmann, T., 2008a: Fast analytical two-stream radiative transfer methods for horizontally homogeneous vegetation media, Meteorologische Arbeiten (XIII) und Jahresbericht 2007 des Instituts für Meteorologie der Universität Leipzig 42, 17-32, self-published, ISBN 978-3-9811114-2-2.

Otto, S., Trautmann, T., 2008b: A note on G-functions within the scope of radiative transfer in turbid vegetation media, J. Quant. Spectrosc. Radiat. Transfer 109, 2813-2819.

Otto, S., Trautmann, T., 2009: On a generalised G-function in radiative transfer theory of turbid vegetation media. Meteorologische Arbeiten (XIV) und Jahresbericht 2008 des Instituts für Meteorologie der Universität Leipzig 45, 131-137, self-published, ISBN 978-3-9811114-5-3.

Otto, S., Meringer, M., 2011: Positively homogeneous functions in atmospheric radiative transfer theory. J. Math. Anal. and Applications 376, 588-601.

Otto, S., 2011: Optische Eigenschaften nichtkugelförmiger Saharamineralstaubpartikel und deren Einfluss auf den Strahlungstransport in der Erdatmosphäre. Dissertation to be submitted for University of Leipzig.

Rothman, L.S., Gordon, I.E., Barbe, A., et al., 2009, The HITRAN 2008 molecular spectroscopic database. J. Quant. Spectrosc. Radiat. Transfer 110, 533-572.
http://cfa-www.harvard.edu/HITRAN/

Wiscombe, W.J., Evans, J.W., 1977: Exponential-sum fitting of radiative transmission functions. J. Comput. Physics 24(4), 416-444.

Zdunkowski, W., Trautmann, T., Bott, A., 2007: Radiation in the atmosphere: A course in theoretical meteorology. Cambridge University Press, 496 pp.

Adresse des Autors

Sebastian Otto, Leipziger Institut für Meteorologie der Universität Leipzig, Universität Leipzig, Stephanstr. 3, 04103 Leipzig.
e-mail: sebasotto@gmx.de

Studies of enlarging, anthropogenic lakes to mesoscale modelling

L. Schenk and A. Raabe

Abstract

For a long period of time the need for power in Germany has mainly been and is still covered by coal as a very important resource. To extract the coal, some big holes in the surface were dug. After ending of the coal mining, they were filled with water in order to use them effectively, so anthropogenic lakes will be created. By 2050 the water surface area in the south of Leipzig will be enlarged to 6000 ha as a consequence of human intervention (Berkner, 2003). Due to the changed soil surface, there will be generate a change in the interaction between the atmosphere and the earth. In this article an approach is demonstrated to classify the effects of anthropogenic lakes with help of a mesoscale model.

Zusammenfassung

Über lange Zeiträume und auch noch zur jetzigen Zeit wird der anhaltende Bedarf an Energie in Deutschland vor allem durch die Ressource Kohle gedeckt. Zum Zweck ihrer Gewinnung wurden so teils große Löcher in die Erdoberfläche gebaggert. Diese werden nach Stilllegung zur nachhaltigen Nutzung mit Wasser gefüllt, was zum Entstehen anthropogener Seen führt. Im Leipziger Süden wachsen so bis zum Jahr 2050 durch menschliches Zutun Wasserflächen mit einer Gesamtfläche von 6000 ha. Durch die veränderte Bodennutzung kommt es zu einer veränderten Wechselwirkung zwischen Atmosphäre und Erde. In diesem Artikel wird ein Ansatz vorgestellt, die Wirkung anthropogen entstandener Seen auf ein mesoskaliges Modell zu klassifizieren.

1 Introduction

When anthropogenic lakes are built, there might occur a changing interaction between the atmosphere and the earth. Water has a high heat capacity and a low albedo (α_w=6-12%, global average: α=30%) (Kraus, 2004), which means that water bodies are a reservoir of heat. Water surfaces deliver latent heat, so especially days of high wind and dry air are efficient. Anthropogenic lakes have a direct impact on the equation of energy balance:

$$Q_0 - B_0 - H_0 - E_0 = 0. \quad (1.1)$$

(Q_0-Energy balance, B_0-Soil heat, H_0-Sensitive heat, E_0-Latent heat)

In parts, the influence of anthropogenic lakes can be studied and measured. However, this topic partly is a future topic which will become reality in the middle of this

century. For meteorological processes, different tools are given, for example numeric models. Thus, fictional and future case scenarios can be simulated with the help of those models. Today, the capacity of computers is so advanced that grid points which have less than one kilometre distance, can be simulated. Such simulations can be integrated into regional planning. For those being interested, like the Dam authority of the Freestate of Saxony, information's about the changing water budget, granting drinkable water, and influence on microclimate by the lakes can be simulated and forecasted.

A Long-term objective should be adapting the mesoscale model GeSIMA (Kapitza, 2003) to give an answer for regional planning. Step by step, this model should lead to a system which has to examine its sensitivity for the leading boundary conditions. First, the boundary conditions should be arranged simple, so that the influence of changing soil use parameters like capillary, field capacity, albedo, and roughness length can be tested in order to calculate values like potential temperature θ, absolute temperature T, specific humidity q, and evapotranspiration V. For this case, it is a need to implement an available CLC-dataset (chapter 2.2) and a topography-dataset in GeSIMA to have flexible areas of simulation and, furthermore, to test the new handling of data in a next step. At the end, representative conditions of soil use, topography, and the atmosphere have to be used and there should be a possibility to use GeSIMA with a web 2.0 Homepage.

2 Mesoscale model GeSIMA

GeSIMA is a non-hydrostatic, mesoscale and meteorological model (β- and γ-scale). This mesoscale model of weather is based on the averaged equation of motion for momentum, the partial mass of dry air, the humidity, liquid water in the atmosphere (liquid precipitation, cloud water) and frozen water (cloud ice, solid precipitation). In addition, it is based on the total mass by the equation of continuity and also on the energy balance with the first fundamental theorem of thermodynamic.

2.1 Basics

The conservation of momentum, mass and energy is the base for every modelling, also of modelling with GeSIMA. Complex atmospheric processes have to be simplified or parameterized to have a useful balance between the time of simulation and the needing. An overview of the complete GeSIMA-Basic is given by the GeSIMA Documentation Manual (Kapitza, 2003).

2.2 The CORINE Land Cover (CLC) and the soil parameterization

The CORINE (COoRdinated INformation on the European environment) Land Cover is a dataset for the soil use in Europe which is provided by the European Union (EU). The classification of soil use is split up in five main classes, which in turn are split up in individual intermediate classes. Those are again split up in some subclasses. An

overview is given by (Keil et al., 2005). A total of 43 different classes of soil use are needed to describe Europe, whereby 37 of them are relevant for Germany. The CLC-dataset is available in Gauß-Krüger coordinates. This coordinate system corresponds to the transversal Mercator projection, which means, an angle preserving cylindrical-transformation is created and the central meridian is the only equidistant of its length. In greater distance to these, the distortion is coming bigger. The main axes of the coordinate system are named “northing” or rather “easting”. Through an offset the origin of the ordinates can be shifted for rectification. The mathematic transformation in a Gauß-Krüger coordinates system is based on differential equations, which are approached with a regression of Taylor (Braun, 2009).

In GeSIMA ten parameters for different soil types are given for every CLC-value:

1. Diffusion coefficient [m^2s^{-1}]
2. Heat capacity [$JK^{-1}m^{-3}$]
3. Emissivity
4. Albedo
5. Roughness length [m]
6. Field capacity [m]
7. Capillarity [$kgm^{-3}s^{-1}$]
8. Characteristic of roughness elements
9. Max. Evaporative conductivity [ms^{-1}]
10. Resistance for lead particles [sm^{-1}]

Examples of the parameters of different soil use are given in the table:

Soil use	CLC	1	2	3	4	5	6	7	8	9	10
Continuous urban fabric	111	1.0E-06	2.0E+06	0.90	0.2	2	0.009	0.001	1	0	270
Airports	124	1.0E-06	2.0E+06	0.90	0.2	0.1	0.009	0.001	1	0	270
Non-irrigated arable land	211	8.4E-07	2.1E+06	0.95	0.25	0.05	0.15	0.001	1	0	400
Pastures	231	7.0E-07	2.5E+06	0.95	0.2	0.02	0.195	0.001	0	0.024	260
Broad-leaved forest	311	7.0E-07	2.5E+06	0.97	0.25	1.5	0.255	0.008	0	0.023	130
Mixed forest	313	7.0E-07	2.5E+06	0.97	0.2	1.5	0.255	0.008	0	0.023	155
Lakes	512	1.4E-07	4.2E+06	0.95	0.1	1E-04	1	1	1	0	0

Table 2.1: CLC soil use and corresponding parameters

3 Model area of simulation in Saxony

The south of Leipzig is suited as a model area in Saxony. This area is characterized by enlarging, anthropogenic lakes which were built by flooding of opencast pit with water. The flooding of the area will be finished by the year 2050. Therefore, lakes will arise to a total area of more than 6000 ha.

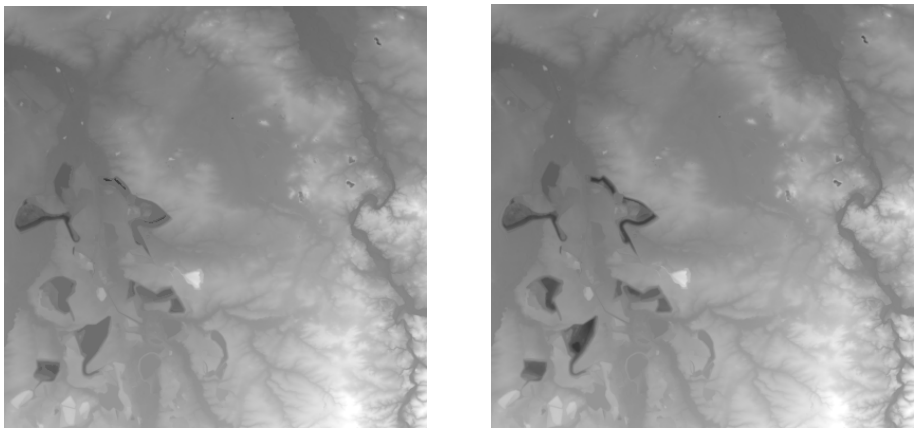

Fig. 3.1: Topography of the south of Leipzig (year 2050 (left), year 2000 (right)) (black→white: valley→hill). Areas of opencast pit are brighter after flooding.

Affected by new lakes, the topography is assimilated to simulate a water surface which is higher than the holes before (Fig 3.1). The soil use changed from opencast pit to lakes (Fig. 3.2).

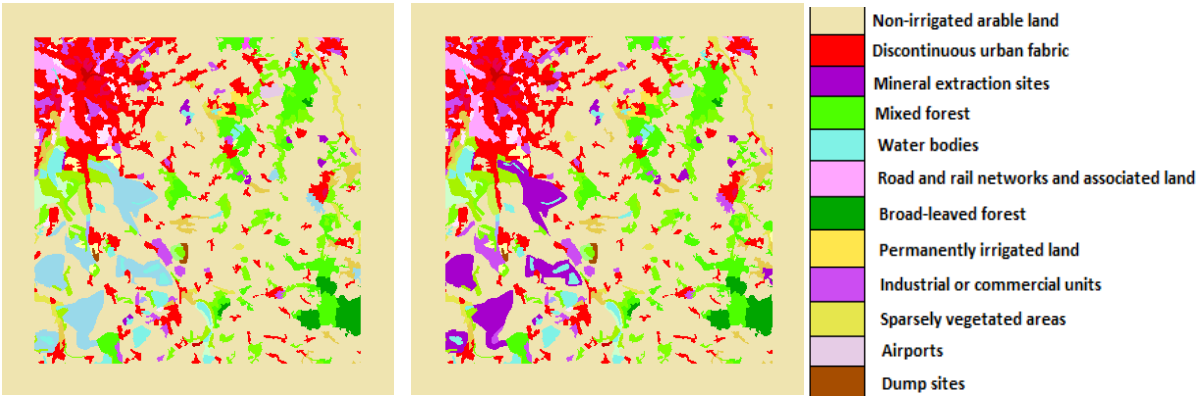

Fig. 3.2: Change of the CLC soil using in the south of Leipzig (2050 (left), 2000 (right).)

4 Differences of meteorological values by arising lakes

In section 4 some examples of differences between the fields of temperature, humidity and evapotranspiration are shown. Those differences result from the arising or new accruements of lakes in the south of Leipzig. In the numeric models, the state of flooding in the year of 2000 has a total area of water of 1500 ha. For the state of flooding in the year of 2050, the total area of water will be nearly 7500 ha.

4.1 Initial conditions (summer atmosphere Leipzig (SAL))

SAL is a fictional summer atmosphere for Middle Germany. The atmospheric layering is stable and the wind has a north-east direction with a velocity of 2-4 ms^{-1} ten meters above the ground. The change of the temperature of the water surface during one day is small contrary to the change of the surface temperature of solid soil, so for 24h-simulations the surface temperature of the lakes is used as a constant (293 K).

4.2 Differences of the field of temperature

Conditioned by the smaller area of water surface in the year 2000, it was calculated in comparison to the year 2050 that the downwind area shows a smaller effect to the field of temperature. By day the differences of the fields of temperature (Fig. 4.1 (right)) only refers to the new area of the lakes. Whereas in the morning (Fig. 4.1 (left)), the difference of the temperature in the lee side of the lakes is clearly distinct. An area of 300 km^2 in the downwind side of the lakes is influenced by the warmer lakes in relation to the air mass. 5 K of heating is the maximum. The maxima of heating occur by the fact, that the air masses which are influenced by one lake are affected by a second lake in the lee side of the first. So, the temperature of the air is still higher. The centre heating rate by the arising lakes in 2050 is 1-3 K higher compared to situation in the year 2000.

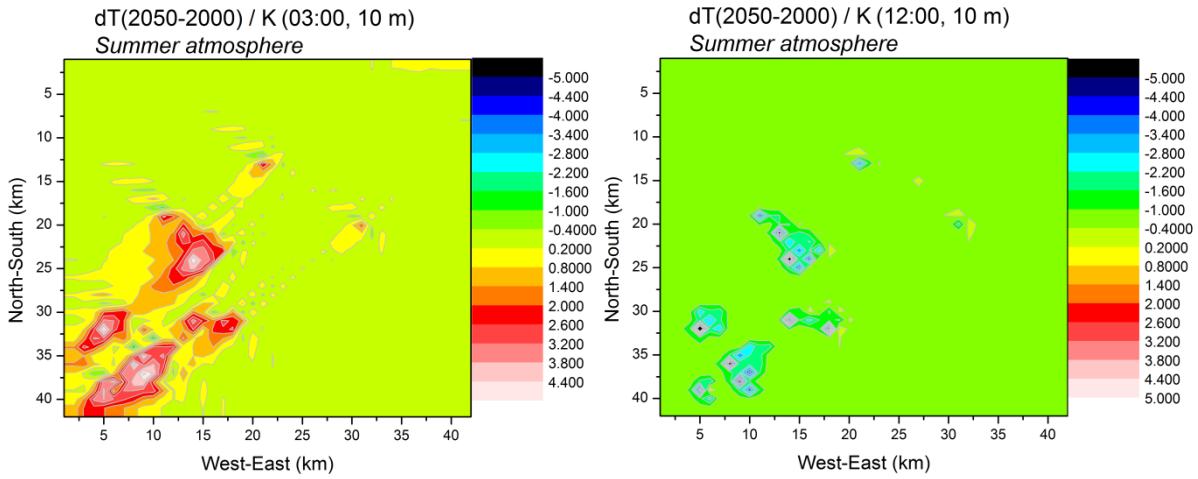

Fig. 4.1.: Differences of the field of temperature/K, due to the lakes becoming larger in the south of Leipzig (state of flooding 2050 minus 2000). The points of time of the situation of the atmosphere are 03:00 left side and 12:00 right side of the figure.

4.3 Differences of the field of humidity

Figure 4.2 illustrates the differences of the field of humidity (mixing ratio) which are due to the enlargement of the lakes until the year 2050. By day (Fig. 4.2 (left)), only the nearest area to the new lakes are influenced by the emitted humidity as well as the field of temperature. Thereby 1-2 gkg^{-1} are the maxima of humidification. By night (Fig. 4.2 (right)), the lakes are warmer than the air mass which is not influenced by the lakes. Thus, the warmer lakes reduce the stability of the atmospheric boundary layer.

Hence, the humidification is larger than by day. The elevation of the mixing ratio, relative to the not influenced air mass of the lakes is situated between 3-4 gkg^{-1} by night. The influenced area beyond (lee side) the lakes, also gets larger.

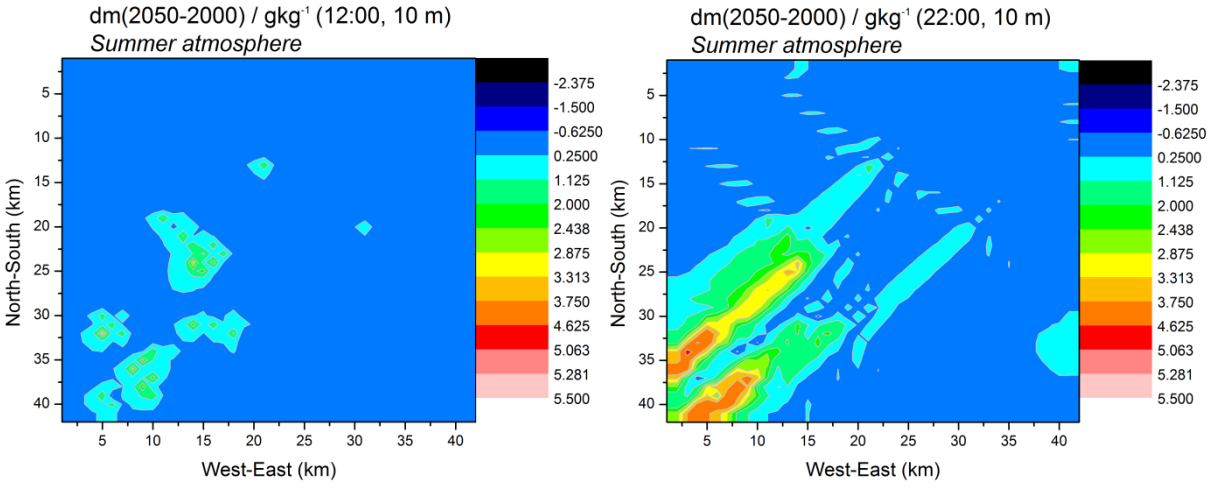

Fig 4.2: Differences of the field of humidity /gkg^{-1}, due to the lakes becoming larger in the south of Leipzig (state of flooding 2050 minus 2000). The points of time of the situation of the atmosphere are 12:00 left side and 22:00 right side of the figure

4.4 Evapotranspiration

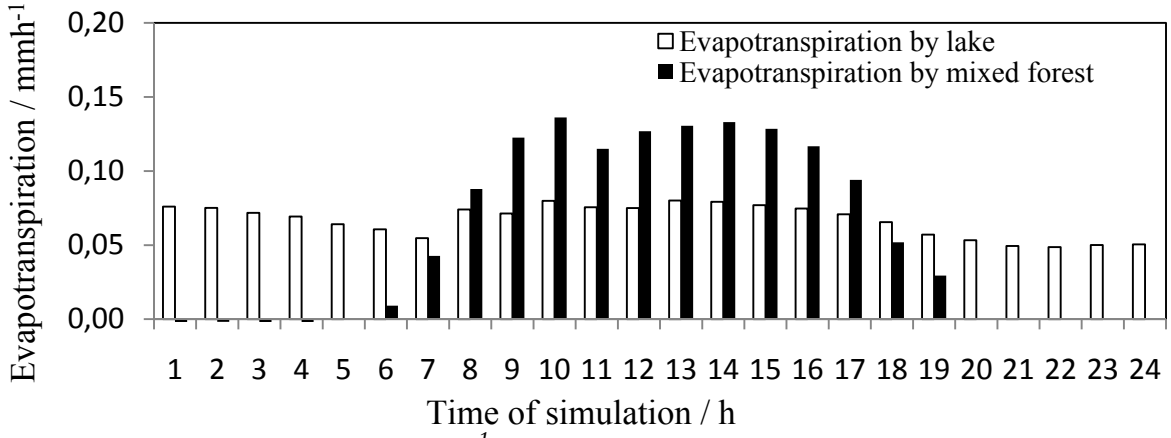

Fig 4.3.: Evapotranspiration / mmh^{-1} by a lake and a mixed forest area over 24 hours.

Fig. 4.3 illustrates the evapotranspiration of a lake and mixed forest for the example of the atmosphere SAL during one day. Lakes have a constant input of water vapour contrary to wet soil uses like mixed forest, which result in different values of evapotranspiration over the day. By night, only the area of the new lakes evaporates. The value by night is less than the value of evapotranspiration by day, but the difference is situated at ca. 0.02 mmh^{-1}. In the afternoon the maximum of the emission of water vapour of the lakes is reached (0.08 mmh^{-1}). Evapotranspiration by mixed forest only occur by day. The maximum value of evapotranspiration is at 0.15mmh^{-1} which is higher than the emission of water vapour by lakes. In total the emission of water of lakes is more efficient because of the continuity of evapotranspiration.

Two reasons for the differences are:

1. Greater roughness by solid soil uses have a raising effect of evapotranspiration (z_0(lakes)=0.01-0.05m, z_0(forest)=1.5m, z_0(city)=1-2m) (Kapitza, 2003).
2. A lake, which is warmer relative to the air mass, damps the temperature of the air above the lake. So, it is possible that the dew point of the air mass over the lake is not been reached, differently to the air mass over solid soil use as in the example SAL. Therefore, evapotranspiration over lakes is possible by night.

To conclude, a lake is not automatically the most evaporative soil use. What matters is the interaction of atmospheric processes like precipitation, the humidity and the temperature of the air, the lake on one hand, and geologic conditions like field capacity of the soil and their soil moisture on the other hand.

5 Conclusions

Simulations with GeSIMA are helpful to get an overview of possible impact of a changed interaction between the atmosphere and a changing soil use. Mesoscale simulations using a resolution of the surface structure (land use, topography) of round about one kilometre are possible. So, conclusions to regional planning for this small scale are feasible (flooding of opencast pit). For the simulation example (SAL) the difference of the temperature between earth and atmosphere is decisive for mesoscale atmospheric processes. So called “cold” lakes, which are colder than the air mass, have only an impact to the nearest areas of the lakes. These cold lakes have a stabilizing effect and this reduce the impact to the regional temperature and humidity fields. In contrast “warm” lakes, which are warmer relative to the air mass, generate an effect of labilization. As a consequence, affected areas are far from the shoreline of the lakes. The evapotranspiration of lakes shows only a slightly variation during one day. In contrast, especially a wet soil surface evaporates much more water during one day. At night the evaporation is zero. As a result the lakes affect the climate condition especially at night and not so much at day.

6 Outlook

A statement to a climate effect with the help of meteorological parameters like direction of wind, velocity of wind, thermal stratification of the atmosphere, and the mean influence of clouds is possible now. Results of the climate effect will be analyzed in the next step of work. So, for instance statements the effect of the evapotranspiration of lakes will be classifiable for different situations of the atmosphere for interested parties like LTV (Landestalsperrenverwaltung Sachsen).

Acknowledgements

We would like to thank N. Braun for a helpful briefing to the Web 2.0 page, also the acoustic group of the LIM (Leipziger Institute of Meteorology) for helpful discussions and last but not least those who helped in translating this manuscript.

References

Berkner, A. 2003: Der Braunkohlenbergbau im Südraum Leipzig, Bergbau in Sachsen, Edition 11, p.11-94

Braun, N. 2009: Optimierung des Downscaling in der Microskala auf der Basis eines 3D-Mesoskalen-Modells, Universität Leipzig, p. 7-28

Kapitza, H. 2003: Gesima Documentation Manual, GKSS Research Centre, p.80-82

Keil, M.: Kiefel, R. Strunz, G. 2005: CORINE Landcover 2000-Europaweite harmonisierte Aktualisierung der Landnutzungsdaten für Deutschland, DLR, p. 17

Kraus, H. 2004: Die Atmosphäre der Erde. Eine Einführung in die Meteorologie, 3. Edition, Springer Verlag, 2004, p. 107 ff

Turbulence and aeolian sand transport

H.-J. Schönfeldt

Summary
A description and some results of the calculated aeolian sand transport including the turbulence intensity and the autocorrelation of the wind field in the transport equation's are presented in this study. The simulated transport related to Sørensen (2004) transport equation varies by more than 100% for one and the same friction velocity and one and the same sand type near the thresholds by variation of turbulence intensity and/or the autocorrelation of the wind. Published results of sand transport measurements are imperfect and not comparable without information about the characteristics of the turbulent wind. An indication of friction velocity, threshold friction velocity and measured transport must be supplement by the specification of the turbulence intensity and the autocorrelation of the wind velocity.

Zusammenfassung
Es wird beschrieben, wie die Turbulenzintensität und die Autokorrelation des Windfeldes in Transportgleichungen des aeolischen Sandtransports berücksichtigt werden kann und es werden einige Ergebnisse vorgestellt. Der simulierte Transport angewandt auf die Sørensen (2004) Transportgleichung variiert um 100 % für ein und dieselbe Schubspannungsgeschwindigkeit und den gleichen Sandtyp in Schwellennähe bei Variation der Turbulenzintensität und/oder der Autokorrelation des Windes. Ohne Informationen über die Eigenschaften des turbulenten Windes sind veröffentlichte Ergebnisse von Sandtransportmessungen unvollständig und nicht vergleichbar. Die Angabe der Schubspannungsgeschwindigkeit, Schwellenschubspannungs-geschwindigkeit und der gemessene Transport müssen durch die Angabe der Turbulenzintensität und Autokorrelation der Windgeschwindigkeit ergänzt werden.

Introduction

Knowledge about the airflow patterns near the surface and the resulting transport of sediment can enhance our understanding of desert sand movement and dust production. Furthermore, aeolian sediment transport is important in redistributing plant nutrients, determining vegetation patterns, and contributing to the change in vegetation type (Schlesinger et al. 1990). A number of equations have been proposed linking horizontal sand fluxes with wind velocities (Bagnold 1941; Zingg 1953; Williams 1964; Kawamura 1964; Owen 1964; Gillette and Goodwin 1974; Gillette 1979; Lettau and Lettau 1978; White 1979; Sørensen 1985; Gillette and Stockton 1989; Leys and Raupach 1991; Shao et al. 1993; Stout and Zobeck 1997; Zheng et al. 2003, 2006; Stout 2004; Leenders et al. 2005). Figure 1 shows data points of measured transport and the calculated results of three transport equations which all meet the measured points more or less good. Bowker et al. (2007) compared the sand flux of model predictions with field measurements and then assess the sensitivity of the simulations to several aspects such as the formulation of the sand flux equation and the specific value of the threshold velocity, u_{*_t}. They used the transport equations of Kawamura (1964)/White (1979) (Eq. 1) and Owen (1964) (Eq. 2), with Q the transport rate, u_* the friction velocity and A, A_1 constants. Kawamura/White's equation has a correction

term reciprocally proportional to the friction velocity but the difference between the measured and simulated data are nevertheless significant as shown in the Table 1.

$$Q = A_1 u_*^3 \left(1 - \frac{u_{*t}^2}{u_*^2}\right)\left(1 + \frac{u_{*t}}{u_*}\right) \quad \text{Kawamura (1964), White (1979)} \quad (1)$$

$$Q = A\, u_*^3 \left(1 - \frac{u_{*t}^2}{u_*^2}\right) \quad \text{Owen (1964)} \quad (2)$$

Eq. (1) and Eq. (2) underestimate the measurement during the storm-event 1 in 2003 (see Table 1) and on the storm 5 in 2003 the equations overestimate the measurements up to 100%. The storm 1 in 2004 is not predictable with this method. Problematic in the prediction equations is the threshold friction velocity. Stout (1998) experimentally and Schönfeldt (2003) theoretically found that the averaging time of wind speed measurement affects the observed threshold. Measurements of this threshold friction velocity have not solved the problem (Bowker et al., 2007).

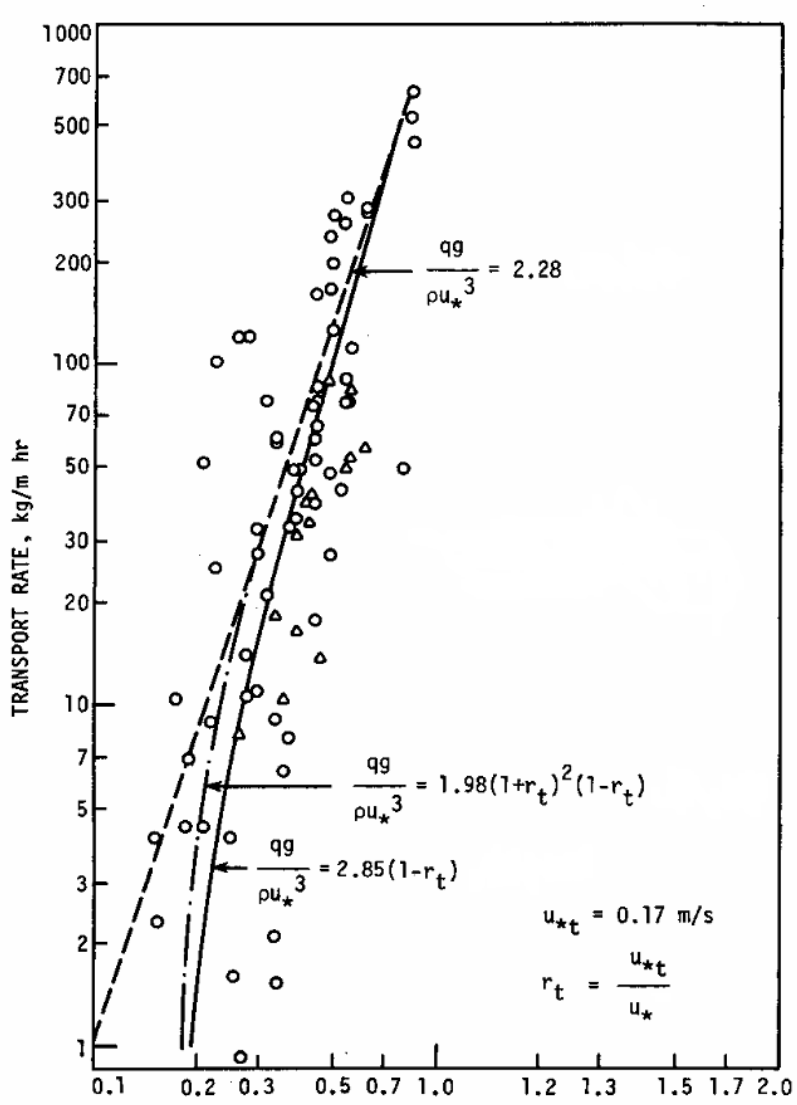

Figure 1. Mass transport rate as a function of friction velocity (Greeley and Iversen, 1985).

The object of this study is to examine the influence of the turbulence intensity on the sand transport. Generally the turbulence is parameterized by the friction velocity, a quantity derived from the law of the wall of fluid dynamics. The law of the wall describes the alteration

of the wind speed with distance or height above the ground surface. Spectral parameters and the relation of standard deviation to mean wind speed (turbulence intensity) are not incorporated in this law. In the following the importance of these parameters on the sand transport is demonstrated.

Table 1. Total accumulated sand flux for each of the eight storms (Bowker et al., 2007).

	Measured (kg m^{-1})	Best fit (Owen) (kg m^{-1})	Best fit (White) (kg m^{-1})
Storm 1, 2003	410.3	245.5	274.7
Storm 2, 2003	95.3	61.8	69.5
Storm 3, 2003	1584.4	1577.9	1595.0
Storm 4, 2003	47.7	39.2	44.8
Storm 5, 2003	279.3	542.8	581.8
Storm 1, 2004	8.0	0.1	0.1
Storm 2, 2004	127.8	59.4	67.6
Storm 3, 2004	264.6	174.7	196.2

Methods

The threshold friction velocity in Equation (1) and (2) is a constant; therefore the normalized saltation velocity V is introduced as the horizontal velocity at the height z divided by the impact threshold velocity at the same height z. Assuming a logarithmic wind profile (according to the law of the wall) then the mean of the normalized saltation velocity is the friction velocity u_* divided by the impact threshold friction velocity u_{*_t}. The normalized saltation velocity V is similar statistically distributed as the velocity u. It can be Gaussian distributed or otherwise.

$$V = \frac{u(z)}{u_t(z)} \quad \rightarrow \quad \overline{V} = \frac{u_*}{u_{*_t}} \tag{3}$$

In order to describe gusts in the turbulent time series of wind, the turbulence intensity I is used. The turbulence intensity I is defined as the standard deviation of the wind speed, σ divided by the mean of the wind speed. Assigned to the normalized saltation velocity V it follows:

$$I = \frac{\sigma_V}{\overline{V}}. \tag{4}$$

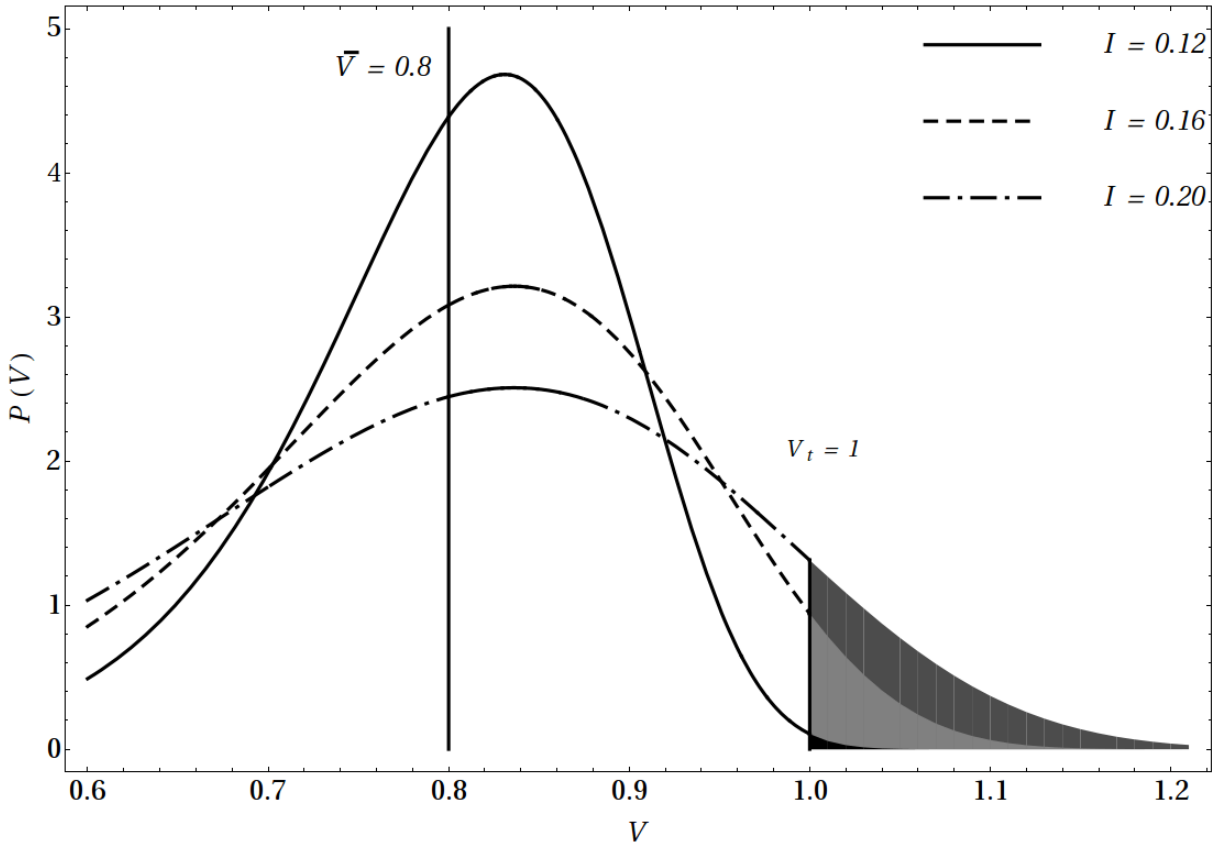

Figure 2. The probability density of exceeding the normalized saltation threshold velocity V_t in dependence of the turbulence intensity (I = standard deviation of the wind velocity divided by the mean of the wind velocity). The mean of the Weibull- distributed wind velocity is always $\overline{V} = 0.8$.

Figure 2 shows different Weibull distributions of wind velocity with the same mean and three different turbulence intensities. The threshold is per definition one. The mean wind speed is chosen to $\overline{V} = 0.8$. This wind speed will not give any transport using such prediction equations as Eq. (2). A wind time series with a turbulence intensity of 0.12 provides some transport and wind with a turbulence intensity of 0.2 results in a rather considerable amount of transport. Note that the mean velocity is constant and therefore u_* is always the same. Every transport equations ignore the gusts and will give one and the same value for the sand transport.
All transport equations such as Equation (2) provide for $u_* < u_{*_t}$ ($\overline{V} < 1$) a negative transport and must actually written as

$$Q = H\left(\overline{V} - 1\right) A u_*^3 \left(1 - \overline{V}^{-2}\right) \tag{5}$$

with $H(x)$ as Heaviside function ($H(x) = 0$ for $x < 0$ else $H(x) = 1$). Introducing a low frequency turbulence and gusts, the Heaviside function in Equation (5) is transferred from a Heaviside function, *H(V-1)*, to a distribution function, *F(V,I)* which describes the probability of saltation. Eq. (5) becomes then

$$Q = F\left(V, I\right) A u_*^3 \left(1 - V^{-2}\right). \tag{6}$$

Schönfeldt (2003) examined the resulting transport determined after Eq. (6). Using Weibull and Gaussian distributions for the horizontal wind speed, Schönfeldt (2003) found that the averaging time, the variance and the form of horizontal wind speed distribution affects the observed threshold. Furthermore, calculations reveal that the sediment transport rate and its increase with the friction velocity above the apparent threshold depends on the variance and the form of horizontal wind speed distribution. The proportionality between streamwise sand flux and friction velocity cubed is a result of the distribution function of the wind strength and the average procedure.

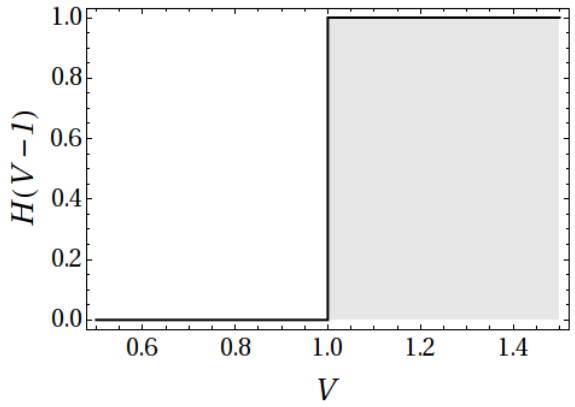

Figure 3a. Heaviside function $H(V\text{-}1)$.

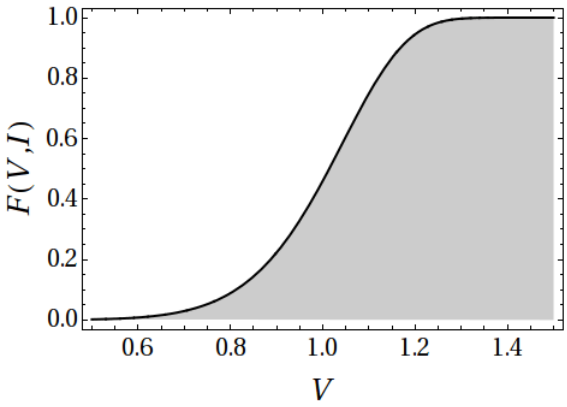

Figure 3b. Probability of saltation *F(V,I)*.

Bagnold (1941) showed that there are two thresholds for saltation: the fluid threshold, which is defined as the speed at which particles start moving due to the forces of wind only, and the impact threshold, which is the speed at which the combined action of wind forces and saltation impacts can just sustain movement, or alternatively, the speed at which the energy received by the average saltating grains becomes equal to that lost (by impact) so that motion is sustained. The impact threshold is smaller than the fluid threshold. After Bagnold the impact threshold is 0.8 of the fluid threshold and therefore the normalized saltation fluid threshold is $V_f = 1.25$ with $V_i = 1.0$, the impact threshold. In the case of intermittent saltation a transport equation must take into account this circumstance. Intermittent saltation is characterized by periods with wind speed falling below that necessary threshold for grain movement, producing a momentary calm followed immediately by gusts. In Figure 4 the explained process is illustrated. There are two thresholds, the impact threshold $V_i = 1.0$ and the fluid threshold $V_f = 1.25$. The saltation process begins when the fluid threshold is overcome (red points) and stops, when the normalized wind velocity falls below the impact threshold (blue points). The saltation process depends on how frequently the wind speed exceeds the fluid threshold and how long the wind speed remains over the impact threshold. Therefore saltation also depends on spectral parameters of the wind velocity time series. The simplest parameter to describe a spectrum is the value of the autocorrelation function at time lag Δt. In the following an interval for the time series of $\Delta t = 1$ second is used.

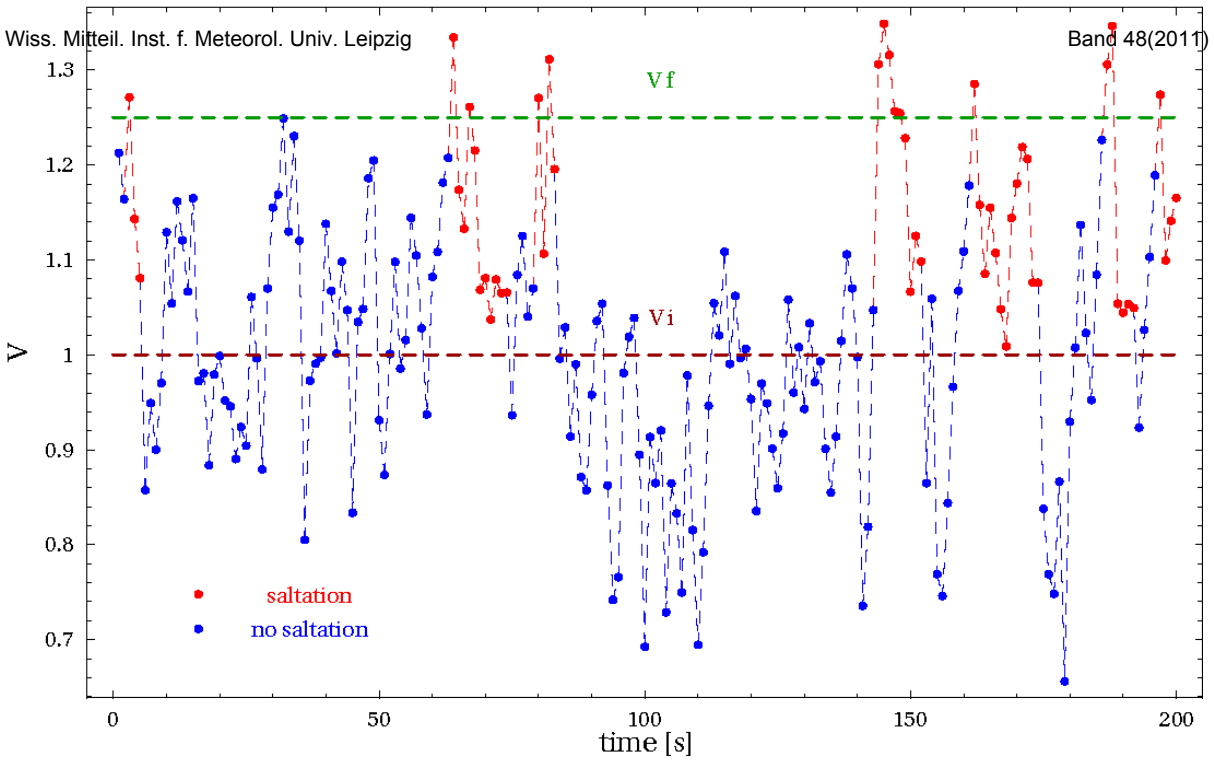

Figure 4. An example of modelled time series of the normalized saltation velocity (Schönfeldt, 2004). After Bagnold (1941) the saltation starts at the red points and stops at the blue points.

From Fig. 4 one can see that the saltation process has a characteristic hysteresis curve and is strongly nonlinear. In a transport equation as Sørensen (2004) recommends for sand of size > 170 µm the non-written Heaviside function in the equation should be replaced by the probability of saltation $F(V,I,r_1)$ (see Fig. (3a,b)) and the normalized saltation velocity V must be replaced by its expected value during saltation, where V during saltation is denoted by V_s.

$$Q = \frac{\rho}{g} u_{*t}^3 \left(\gamma V^2 + \beta V - \gamma - \beta \frac{1}{V} \right) \rightarrow Q = \frac{\rho}{g} u_{*t}^3 F(V,I,r_1) \left(\gamma \varepsilon\{V_s^2\} + \beta \varepsilon\{V_s\} - \gamma - \beta \varepsilon\left\{\frac{1}{V_s}\right\} \right) \quad (7)$$

In Eq. (7) and (8) the expected value of the variable during saltation is denoted by $\varepsilon\{\text{variable}_s\}$, β and γ are constants for a fixed grain size (see also Sørensen, 2004). Other transport equations, which are valid for constant velocities as e.g. derived by a wind tunnel experiment, must be transformed by the following rules:

$$V^2 \rightarrow \varepsilon\{V_s^2\}; \quad V \rightarrow \varepsilon\{V\}; \quad \frac{1}{V} \rightarrow \varepsilon\left\{\frac{1}{V}\right\}; \quad H(V-1) \rightarrow F(V,I,r_1) \quad (8)$$

An analytic solution for the quantities in Eq. (8) as a function of the normalized saltation velocity (or friction velocity) is difficult because of hysteresis in the process. We solved the problem with synthetic time series. The simplest form is the first order Markov chain. A Markov chain is a sequence of random values whose probabilities at a time interval $k + 1$ depend upon the value of the number at the previous time k. A time step of one second was used. The controlling factor in a Markov chain is the transition probability. The first order Markov chain is described by Eq. (9), where ε is a random noise.

$$V_{k+1} - \overline{V} = r_1 (V_k - \overline{V}) + \varepsilon \quad (9)$$

Using r_1 as the autocorrelation of $V(t)$ with a time lag of one second in Eq. (9), the resulting time series has also this autocorrelation r_1. Epsilon can be Gaussian, Weibull or otherwise distributed. In the following the Weibull distribution is used for the noise. Gaussian distributed time series give in principle the same result.

Results

A table of excepted values for the quantities in Eq. (7) as well as for the distribution function $F(V, I, r_1)$ is numerically calculated using turbulence intensities from 0.1 to 0.3, values of autocorrelation from 0.5 to 0.9 and normalized saltation velocities from 0.8 to 4.0. The resulting values are fitted whereas the distribution function of the saltation probability is somewhat complex. The fitted distribution function, $F(V, I, r_1)$ has a form like a Gumbel distribution with an additional quadratic and cubic term in V.

$$F(V,I,r_1) = Exp\left(-Exp\left(f_0(I,r_1) + f_1(I,r_1)V + f_1(I,r_1)V + f_2(I,r_1)V^2 + f_3(I,r_1)V^3\right)\right) \quad (10)$$

The coefficients f_i are polynomial functions of the turbulence intensity I and r_1. The dependency from the autocorrelation is simply linear. The polynomial functions f_i can be expressed as

$$f_i = f_{i00} + f_{i01}c + f_{i02}c^2 + f_{i03}c^3 + \left(f_{i10} + f_{i11}c + f_{i12}c^2 + f_{i13}c^3\right) r_1, \quad (11)$$

There are 32 coefficients to describe the probability of saltation for given V, I, r_1 values. The probability of saltation as function of the normalized saltation velocity V is shown in Fig. 5 with the turbulence intensities from 0.1 to 0.2 and the autocorrelation r_1 from 0.5 to 0.9 as parameters

The expected values of $1/V_s$, V_s and V_s^2 are polynomial functions of the turbulence intensity I and r_1.

$$\varepsilon\left\{\frac{1}{V_s}\right\} = \frac{1}{V}\left(a_{00} + \frac{a_{01}}{V^2} + \frac{a_{02}}{V} + a_{03}V\right), \varepsilon\{V_s\} = V\left(a_{10} + \frac{a_{11}}{V^2} + \frac{a_{12}}{V} + a_{13}V\right), \varepsilon\{V_s^2\} = V^2\left(a_{20} + \frac{a_{21}}{V^2} + \frac{a_{22}}{V} + a_3V\right) \quad (12)$$

$$a_{ij} = a_{ij00} + a_{ij01}c + a_{ij02}c^2 + a_{ij03}c^3 + \left(a_{ij10} + a_{ij11}c + a_{ij12}c^2 + a_{ij13}c^3\right) r_1 \quad (13)$$

The so corrected equation of Sørensen (2004) has 128 coefficients. The implementation of these coefficients in a simple FORTRAN program can be downloaded over the website http://www.uni-leipzig.de/~meteo/de/HANS/hans.htm. This program is written for homogeneous sand of size 242 µm and can be simply adapted to any transport equation by interchanging the prefactors of the expected values (β, γ) in equation (7) or by introducing other linear combinations of the expected values.

The results for the turbulent sand transport using an adapted transport equation compared with the equation by Sørensen (2004) are shown in Fig. 6. It demonstrates that there are combinations of turbulence intensity I and autocorrelation r_1 parameters

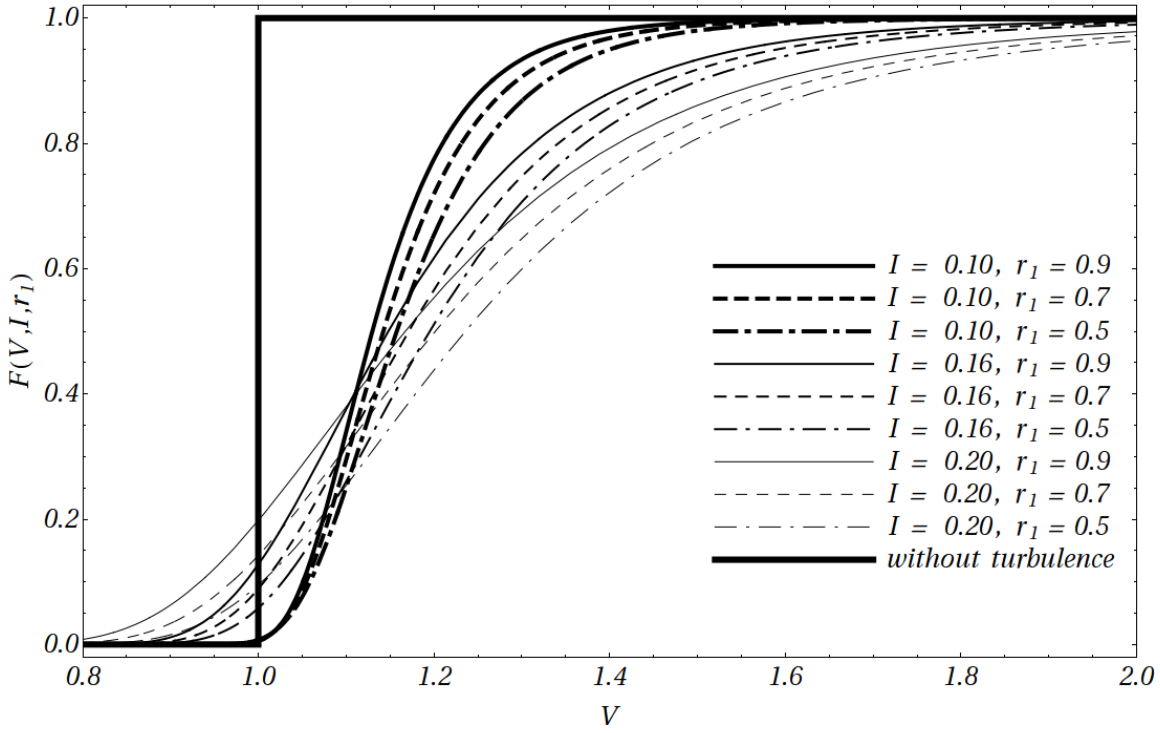

Figure 5. The probability of saltation as function of the normalized saltation velocity V with the turbulence intensity I and the autocorrelation r_1 as parameters.

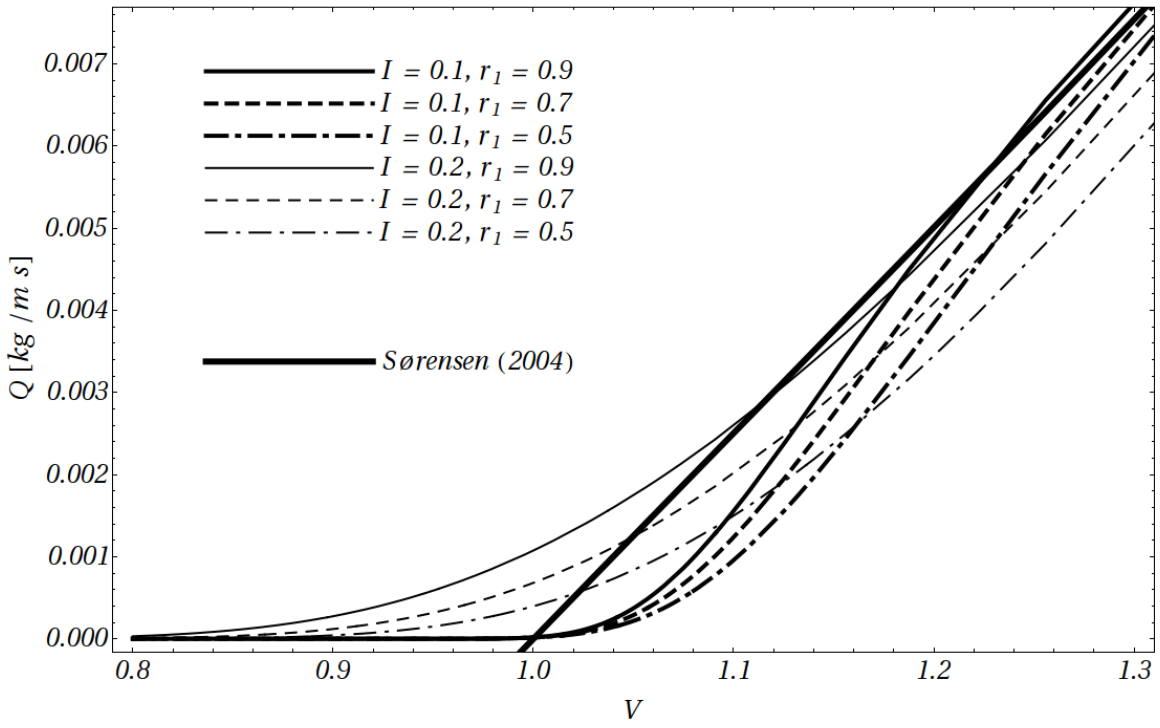

Figure 6. The sand transport Q as function of the normalized saltation velocity V with the turbulence intensity I and the autocorrelation r_1 as parameters.

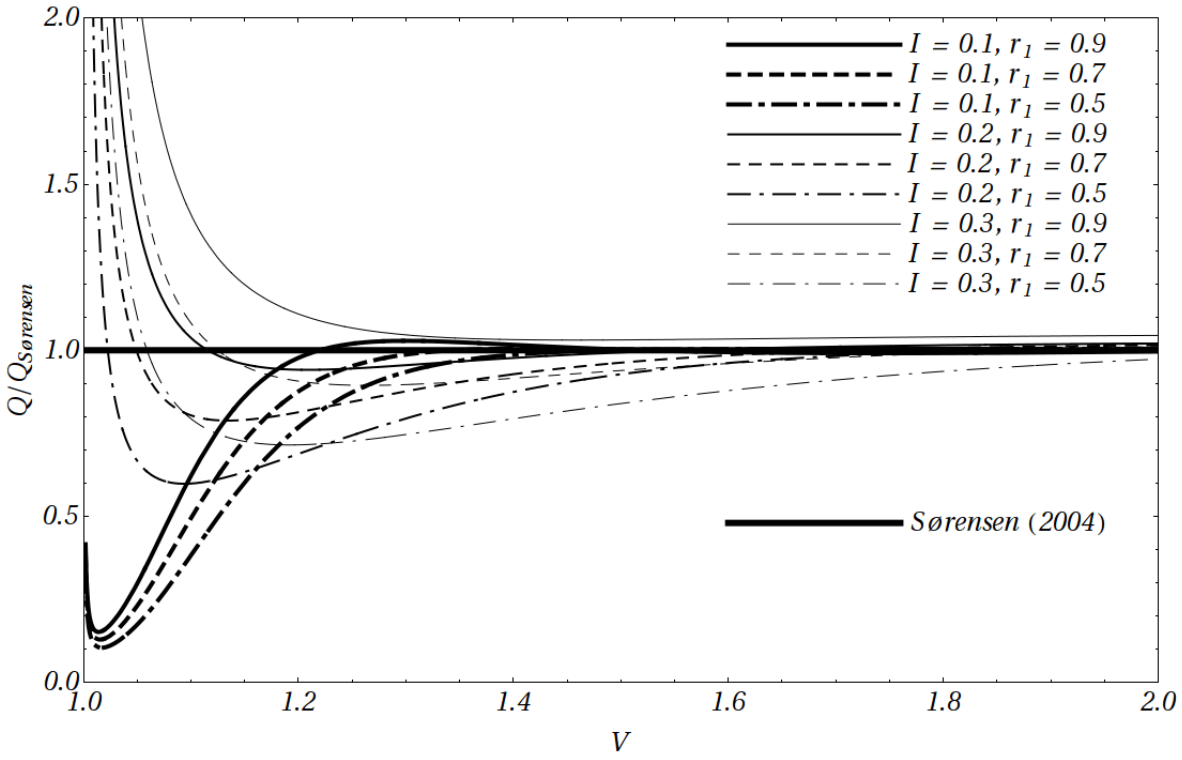

Figure 7. The sand transport Q related to the Sørensen (2004) transport as function of the normalized saltation velocity V with the turbulence intensity I and the autocorrelation r_1 as parameters.

with lower as well as higher transports as predicted by Sørensen (2004). Figure 7 shows the normalized transport and makes clear that the transport near the thresholds can differ by more than 100% for one and the same friction velocity and one and the same sand type. Therefore, measurements as done by Bowker et al. (2007) are imperfect without information about the characteristics of the wind velocity time series (I, r_1).

References

Bagnold, R.A., 1941: The Physics of Blown Sand and Desert Dunes. Methuen, London, 256 pp.

Bowker, G.E., Gillette, D.A., Bergametti, G., Marticorena, B. and Heist, D.K., 2007: Sand flux simulations at a small scale over a heterogeneous mesquite area of the northern Chihuahuan Desert. Journal of Applied Meteorology and Climatology 46(9), 1410-1422.

Greeley, R., Iversen, J.,1985: Wind as a geological process on Earth, Mars, Venus and Titan, Cambridge Planetary Science Series.

Gillette, D. A, Goodwin, P. A., 1974: Microscale transport of sand-sized soil aggregates eroded by wind. J. Geophys. Res., 79, 4080–4084.

Gillette, D. A., 1979: Environmental factors affecting dust emission by wind erosion. Saharan Dust, SCOPE 14, C. Morales, Ed., John Wiley and Sons, 71–91.

Gillette, D. A., Stockton, H., 1989: The effect of nonerodible particles on wind erosion of erodible surfaces. J. Geophys. Res., 94, 12 885–12 893.

Kawamura, R., 1964: Study of sand movement by wind. Translated (1965) as University of California Hydraulics Engineering Laboratory Report HEL 2-8 Berkeley.
Leenders, J. K., van Boxel, J. H., Sterk, G., 2005: Wind forces and related saltation transport. Geomorphology, 71, 357–372.
Lettau, K., Lettau, H., 1978: Experimental and micrometeorological field studies of dune migration. Exploring the World's Driest Climate, K. Lettau and H. Lettau, Eds., University of Wisconsin—Madison IES Rep. 101, 110–147.
Leys, J. F., Raupach, M. R., 1991: Soil flux measurements using a portable wind erosion tunnel. Aust. J. Soil Res., 29, 533–552.
Owen, R.P., 1964: Saltation of uniform grains in air. J. Fluid. Mech., 20, 225-242.
Schlesinger, W.H., Reynolds, J.F., Cunningham, G.L., Huenneke, L.F., Jarrell, W.M., Virginia R.A., Whitford W. G., 1990: Biological feedbacks in global desertification. Science, 247,1043–1048.
Schönfeldt, H.-J., 2003: Remarks on the definition and estimation of the aeolian erosion threshold friction velocity. Meteorol. Z., 12, 137-142.
Schönfeldt, H.-J., 2004: Establishing the threshold for intermittent aeolian sediment transport. Meteorol. Z., 13, 3, 437-444.
Shao, Y, Raupach, M. R., Findlater, P. A., 1993: Effect of saltation bombardment on the entrainment of dust by wind. J. Geophys. Res., 98, 12, 719–12 726.
Sørensen, M., 1985: Estimation of some Aeolian saltation transport parameters from transport rate profiles. Proc. Int. Workshop on the Physics of Blown Sand, Vol. 1, Aarhus, Denmark, University of Aarhus, 141–190.
Sørensen, M., 2004: On the rate of aeolian sand transport. Geomorphology, 59, 53-62
Stout, J. E, Zobeck, T. M., 1997: Intermittent saltation. Sedimentology, 44, 959–970.
Stout, J.E., 1998: Effect of averaging time on the apparent threshold for aeolian transport. Journal of Arid Environments, 39, 395-401
Stout, J. E., 2004: A method for establishing the critical threshold for aeolian transport in the field. Earth Surf. Processes Landforms, 29, 1195–1207.
White, B., 1979: Soil transport by winds on Mars. - J. Geophys. Res., 84, 4643-4651
Williams, G., 1964: Some aspects of the eolian saltation load. Sedimentology, 3, 257–287.
Zheng, X. J., Huang, N., Zhou, Y.-H., 2003: Laboratory measurement of electrification of wind-blown sands and simulation of its effect on sand saltation movement. J. Geophys. Res., 108, 4322, doi:10.1029/2002JD002572.
Zheng, X. J., Huang , N., Zhou, Y., 2006: The effect of electrostatic force on the evolution of sand saltation cloud. Eur. Phys. J. E, 19, 129–138.
Zingg, A. W., 1953: Wind tunnel studies of the movement of sedimentary material. Proc. Fifth Hydraulics Conf., Bulletin 34, Iowa City, IA, Institute of Hydraulics, 111–135.

Address of the Author
Hans-Jürgen Schönfeldt (hans@uni-leipzig.de)
Universität Leipzig
Institut für Meteorologie
Stephanstraße 3
04103 Leipzig

Numerical sensitivity tests of acoustically derived meteorological quantities inside an ‚acoustic chamber‘

A. Ziemann and A. Raabe

Summary
To quantify the energy balance above a lysimeter without disturbance of the measured air volume itself, the applicability of an acoustic-meteorological measurement method is numerically investigated. Several sound paths between transmitters and receivers around the lysimeter border an air volume (‚acoustic chamber') to determine the interaction between the ground surface and the environment with remote sensing.
This study is focused on the sensitivity of the acoustically derived air temperature and wind vector values. To describe the uncertainty of these quantities outgoing from the uncertainty of the acoustic travel time, several effects on the sound propagation, e.g. air absorption, ground reflection, and atmospheric refraction are studied.
Based on the wind and temperature data at several height levels, momentum and heat fluxes can be derived which are important for the energy exchange above the lysimeter surface. First results of the achievable accuracy for the fluxes are summarized in the study using a numerical model of the atmospheric boundary layer.

Zusammenfassung
Um die Energiebilanz oberhalb eines Lysimeters ohne Störung des Messvolumens zu quantifizieren, wird die Anwendbarkeit einer akustisch-meteorologischen Messmethode numerisch untersucht. Verschiedene Schallpfade zwischen Sendern und Empfängern, die um das Lysimeter platziert sind, begrenzen ein Luftvolumen (‚akustische Kammer'), welches fernsondiert wird. Damit wird die Wechselwirkung zwischen Bodenoberfläche und Umgebung bestimmt.
Im Mittelpunkt der vorliegenden Studie steht die Sensitivität der akustisch bestimmten Werte der Lufttemperatur und des Windvektors. Um die Unsicherheit dieser Größen ausgehend von der Unsicherheit einer akustischen Laufzeitbestimmung zu beschreiben, werden verschiedene Schallausbreitungseffekte, z.B. Luftabsorption, Bodenreflexion, Schallbrechung, untersucht.
Ausgehend von Wind- und Temperaturdaten in verschiedenen Höhen können Impuls- und Wärmeflüsse abgeleitet werden, die für den Energieaustausch oberhalb eines Lysimeters von Bedeutung sind. Erste Ergebnisse zur erreichbaren Genauigkeit der Flüsse werden in dieser Studie unter Nutzung eines numerischen Modells der atmosphärischen Grenzschicht zusammengefasst.

1 Introduction

The measurement of the evaporation at the surface is still an important problem for several applications in meteorology, agricultural science or hydrology. One direct measurement method is the lysimeter technique (e.g. DVWK, 1996). An advantage of

a lysimeter is that an adequate measurement of the evaporation is possible using a very small ground surface in comparison to indirect micrometeorological methods. On the other hand, there are no general applicable methods to quantify the total energy and gas exchange at the top of a lysimeter. At present the ground surface of a lysimeter is mostly assembled with sensors and covered with chambers which influence the air flow and the exchange between the lysimeter and the environment (see e.g. Balogh et al., 2007). Otherwise, micrometeorological measurement stations at a distance of decameters are used as a further standard method to describe the energy exchange above lysimeters. The relation between the air flow near the surface of the lysimeter and the micrometeorological measurements is however problematic. In contrast to that, remote sensing techniques do not disturb the sensed air flow and are able to measure contactless, without inertia, and without radiation influence. One possibility is the application of an acoustic measurement system which spans a net of sound paths over the lysimeter surface and gets information about the air flow near the surface. The acoustic paths control and sense an air volume where the energy and gas exchange between the lysimeter and the environment takes place and which is here named as ‚acoustic chamber' in accordance to the conventional chamber measurements for gas exchange between the soil surface and the environment .

The focus of this study lies on the acoustic measurement of meteorological quantities, air temperature and wind vector (see chapter 2). To describe the uncertainty and significance of these measurements theoretically, several effects on the sound propagation have to be studied (chapter 3). Outgoing from the temperature and wind measurements at several height levels it is possible to derive further meteorological quantities, like fluxes, which are important for the energy and gas exchange above the lysimeter surface. In chapters 4 and 5 first results of the investigated uncertainty for momentum and heat flux are summarized applying an atmospheric boundary layer model.

2 Acoustic temperature and wind measurement

2.1 Measurement of the acoustic travel time

For the purpose of acoustic chamber (Fig. 1) measurements we will use line-averaged acoustic travel-time measurements where the sound speed along a defined propagation path can be determined by measuring the travel time of an acoustic signal.

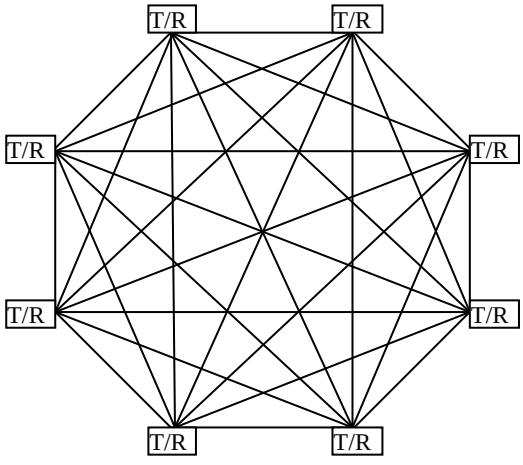

Fig. 1: Top view on the acoustic chamber with 8 measurement places (T…transmitter, R…receiver) for the acoustic travel time along 28 sound paths (black lines between the measurement places).

Thereby we are using transmitters and receivers working with an ultrasonic frequency of 40 kHz. A short sine wave-form signal is sent by the transmitter. This signal is recorded by the receiver after a distinct travel time which depends on the sound speed and the transmitter-receiver distance. The application of this technique to measure meteorological quantities is possible because the sound speed c_{ceff} and therewith the travel time of an acoustic signal is a function of temperature and the wind vector (e.g. Ziemann et al., 1999).

To derive meteorological data outgoing from measurements of the sound propagation between an acoustic transmitter and receiver it is necessary to separate the coupled influences on the effective sound speed, i.e. the influences of acoustic virtual temperature and wind vector. Several separation methods are possible (Ziemann et al, 1999; Arnold, 2000). If the approximation of straight sound rays is applicable (see section 3.3) then the use of reciprocal sound propagation is the simplest and most certain method. Analogous to an ultrasonic anemometer (Schotanus et al, 1983; Kaimal and Gaynor, 1991) the line-averaged wind component along one sound propagation path as well as the temperature-dependent adiabatic sound speed were determined if the travel time will be measured along one and the same path in the downwind direction (τ_{down}) and in the upwind direction (τ_{up}):

$$c_{eff_{down}} = \frac{d}{\tau_{down}} = \sqrt{\gamma_{dry} R_{dry} T_{av}} + v_{ray}\,, \tag{1}$$

$$c_{eff_{up}} = \frac{d}{\tau_{up}} = \sqrt{\gamma_{dry} R_{dry} T_{av}} - v_{ray} \tag{2}$$

with the transmitter-receiver distance d, the wind component along the sound path v_{ray}, the acoustic virtual temperature T_{av}, the adiabatic exponent of dry air γ_{dry}, the specific gas constant for dry air R_{dry}. The acoustic virtual temperature includes the influence of specific humidity q on the sound speed:

$$T_{av} = T(1 + 0.513q) \tag{3}$$

The acoustic travel times are measured at one height level at 8 places. Each measurement place contains one transmitter and one receiver. 56 travel time measurements result at each layer, but with the reciprocal sound propagation analysis there are 28 line-averaged temperature and wind measurements in different directions (see Fig. 1).

2.2 Calculation of line-averaged temperature and wind component

According to the analysis of acoustic measurements of ultrasonic anemometers the travel time data are recalculated together with a known distance between the transmitters and the receivers d into meteorological data (e.g. Kaimal and Gaynor, 1991):

Acoustic virtual temperature $\sqrt{T_{av}} = \frac{d}{2\sqrt{\gamma_{tr} R_{tr}}} \left(\frac{1}{\tau_{down}} + \frac{1}{\tau_{up}} \right)$, (4)

Wind component along the sound path $v_{ray} = \frac{d}{2} \left(\frac{1}{\tau_{down}} - \frac{1}{\tau_{up}} \right)$. (5)

Using wind components into two different directions the horizontal components of the wind vector can be calculated and therewith the horizontal wind vector. Because of the calculation of temperature and wind data along several sound paths one can obtain an

estimation of the horizontal homogeneity of the meteorological fields and possible inhomogeneity influences on the energy balance of the underlying surface.

2.3 Uncertainty of temperature and wind measurements

To test the sensitivity of the acoustic temperature and wind measurements, the (maximal) uncertainty was calculated as following. Assuming that the travel time measurements were carried out outgoing from a known initial state it is possible to eliminate errors of the distance measurement between transmitters and receivers. In this case the uncertainty of the meteorological data is only dependent on the travel time error $\Delta\tau$ (especially the digitalization error depending on the signal frequency, 40 kHz and digitalization frequency, 100 kHz at the moment). If one further assumes that the travel time error along the downwind direction is equal to the error in the upwind direction, the following uncertainties result:

$$\Delta T_{av} = 2\sqrt{\frac{T_{av}}{\gamma_{tr}R_{tr}}}\Delta\tau\left(\frac{(\gamma_{tr}R_{tr}T_{av})+v_{ray}{}^2}{d}\right) \text{ and} \tag{6}$$

$$\Delta v_{ray} = \Delta\tau\left(\frac{(\gamma_{tr}R_{tr}T_{av})+v_{ray}{}^2}{d}\right). \tag{7}$$

The uncertainty of the acoustic virtual temperature is greater, by a roughly constant factor, than that one for the wind component (see Fig. 2).

Acoustic measurements of the temperature, provided along a typical acoustic path length of 1 m through the acoustic chamber volume, results in a temperature uncertainty of about 0.5 K for a travel time uncertainty of 2.5 µs at present (Fig. 2, left side). If this single travel time measurement will be repeated *n*-times, than the uncertainty of the measurements decreases by the factor $\frac{1}{\sqrt{n}}$ (Fig. 2, right side).

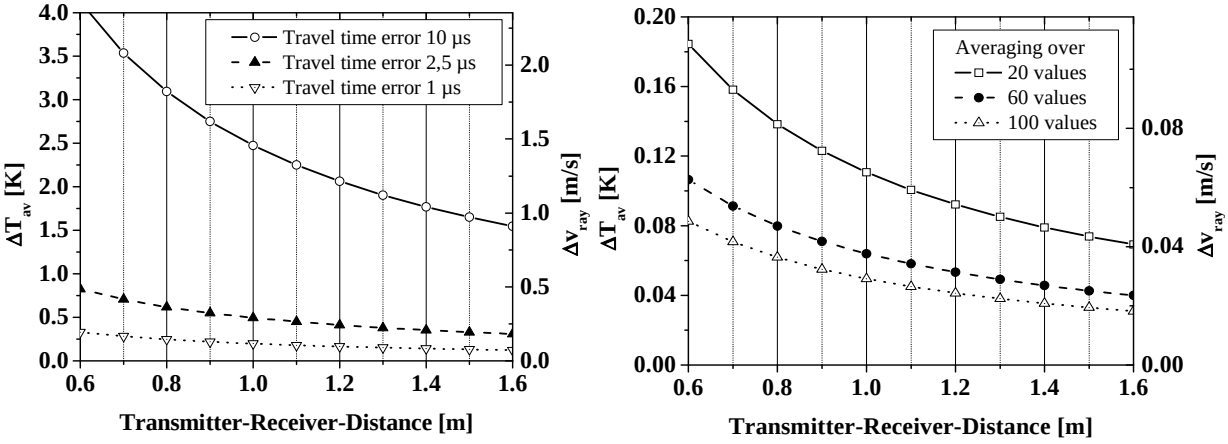

Fig. 2: Temperature and wind uncertainties depending on the sound path length.
Left: instantaneous measurements without averaging, right: with averaging over a distinct number of measurements (travel time error of 2.5 µs for a single measurement).

3 Influences on the acoustic measurement and meteorological analysis

3.1 Air absorption

In the used ultrasonic frequency range around 40 kHz the strongly frequency-dependent influence of atmospheric sound absorption must be investigated. The air ab-

sorption could be divided into the classical absorption because of air viscosity and heat conduction and the molecular absorption because of relaxation processes of nitrogen and oxygen molecules during the sound propagation (see Salomons, 2001). The resulting absorption coefficient depends, besides the frequency, on the air temperature and humidity and leads always to a decreased sound level dependent on the transmitter-receiver-distance. The absorption coefficient amounts, for a sound frequency of 40 kHz, to 1.2-1.3 dB/m for an air temperature of 20°C and a range of 40-80% for the relative humidity. If the spatial divergence of spherical waves will be included in the calculation, then the sound attenuation amounts to about 20 dB already for a sound path of 2 m. From this it can be concluded, that the applied sound frequency of 40 kHz permits only short sound path lengths of a few meters.
Additionally to these two effects there are effects of ground reflected sound paths and meteorological effects (e.g. refraction) which may lead to sound attenuation.

3.2 Ground reflection

In the case of sound propagation near the surface the effect of sound reflection at the ground has to be considered. The received sound signal is made up of two parts, first the direct sound wave travelling through the atmosphere, second the reflected sound wave. Interference effects result under the assumption of coherence of the direct and reflected wave and depend on the acoustic ground surface properties as well as the phase difference between the two waves. Constructive interference appears for a rigid ground (reflection coefficient is equal to 1) and similar path lengths of the direct and the reflected sound wave. Destructive interference occurs e.g. for a grazing incidence, that means a marginal sensor height in comparison to the transmitter-receiver distance. Consequently, the sound level decreases (theoretically an infinitely high attenuation is possible) or increases (by maximally 6 dB) in comparison to an unbounded sound propagation (e.g. Salomons, 2001).

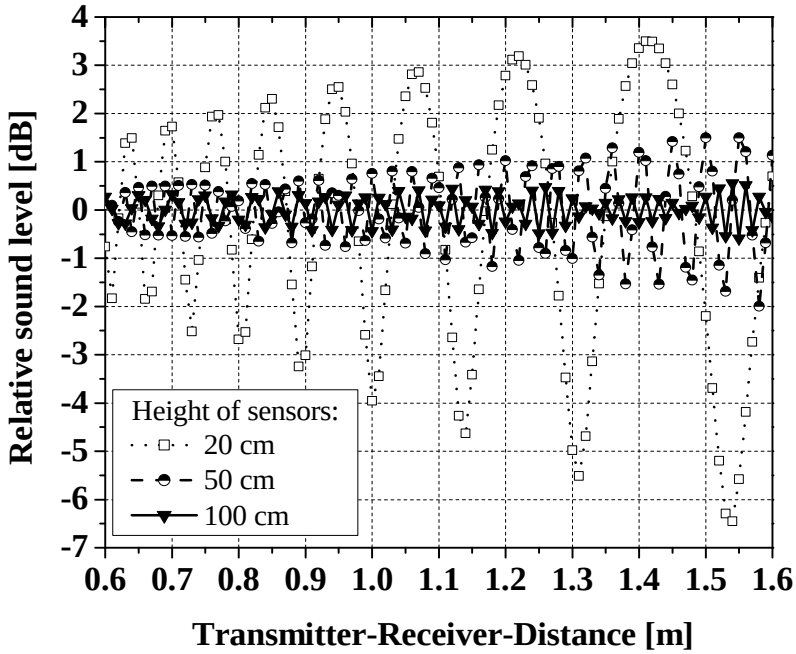

Fig. 3: Relative sound level (in comparison to an unbounded sound propagation) for an ultrasound frequency of 40 kHz, a sound propagation over a grassland surface, and several heights of transmitters and receivers (both at the same height) above the ground.

In Fig. 3 this relative sound level is displayed for a sound frequency of 40 kHz depending on the transmitter-receiver distance and the height of the acoustic sensors. Thereby an one-parameter model of Delany and Bazley (1970) was applied to calculate the reflection factor similar to recently used sound propagation models (e.g., Lihoreau et al., 2006, Ziemann et al., 2007). An absorbing ground (acoustically soft) was assumed, in this special case a grassland site.
The ground influence increases with a decreasing height of the sensors above the ground surface. Furthermore, the amount of the relative sound level and therewith the ground effect increases with an increasing transmitter-receiver-distance. If the height of the sensors is only 20 cm above the ground, the maximal sound attenuation amounts to 6.5 dB for a distance of 1.55 m. Otherwise, the sound level may be enhanced by 3.5 dB for a distance of 1.4 m. If transmitter and receiver are installed at greater heights above surface, the amount of sound attenuation decreases and is negligible for heights of 50 cm and more for the investigated sound frequency.
Because of transmitting of short pulses it will be possible that not any interference effect will occur, but rather consecutive signals of the direct and the reflected waves depending on the path length difference between the two waves. The temporal difference between these signals amounts, for a small sensor height of 20 cm above the ground surface, to about 0.15 ms. This value lies within the range of the signal length (0.125 ms at present), the direct and the reflected wave could interference with each other resulting in a positive or negative sound level attenuation (see Fig. 3). If the height of the transmitter and receiver increases, the time interval between the direct and the reflected wave increases too. The two signals will then be clearly distinguishable at the receiver.

3.3 Atmospheric refraction

The assumption of a reciprocal sound propagation, which means along approximately straight ray paths between a transmitter and a receiver, permits the explicit separation between the two meteorological influences (temperature and wind) on the acoustic travel-time measurement. It remains to investigate, if the atmospheric refraction due to vertical temperature and wind gradients significantly influences the sound paths.
For this purpose a numerical model of the atmospheric boundary layer, HIRVAC (HIgh Resolution Vegetation Atmosphere Coupler), was used to calculate realistically vertical gradients of meteorological quantities for several situations (seasons and times of the day) over a homogeneous grassland site. The one-dimensional model version of HIRVAC was applied here, which was developed in the previous years (Mix et al., 1994), including a vegetation and soil module (Ziemann, 1998), validated and applied for several questions with regard to ground-vegetation-interactions (Goldberg und Bernhofer, 2001; Baums et al., 2004). HIRVAC solves the prognostic equations for momentum, heat, and moisture at 120 height levels through the atmospheric boundary layer. The set of equations is closed using an assumption for the turbulent diffusion coefficient combined with the solution of the equation for the turbulent kinetic energy.

Only positive gradients of the effective sound speed result for a downwind sound propagation for all modeled seasons and day times. This leads to a downward refraction of the sound rays due to the stratified atmosphere.
If one assumes that the curved sound rays can be approximated by arcs of a circle than it is possible to simply calculate the differences of the ray path lengths as well as the travel times between the straight-line and the curvilinear sound propagation (smaller travel time according to Fermat's principle) only using geometrical relations. The greatest differences can be awaited for maximal sound speed gradients which lead to a minimal radius of the curved sound ray. Such conditions could be found on the model day 15th January during the morning and evening hours and for sensor's height of only 20 cm above the ground surface (see Fig. 4). The maximally calculated sound speed gradient of about 5.6 m/(s·m) is caused by the strong temperature inversion together with the strong positive wind speed gradient near the ground surface. For an almost horizontal sound emission a maximal travel time difference of about 0.3 µs results for a transmitter-receiver-distance of 1.6 m. Even this maximal difference is one magnitude smaller than the measurement accuracy of the travel time (2.5 µs at present). It can be concluded that for downwind conditions the assumption of reciprocal sound propagation is applicable.

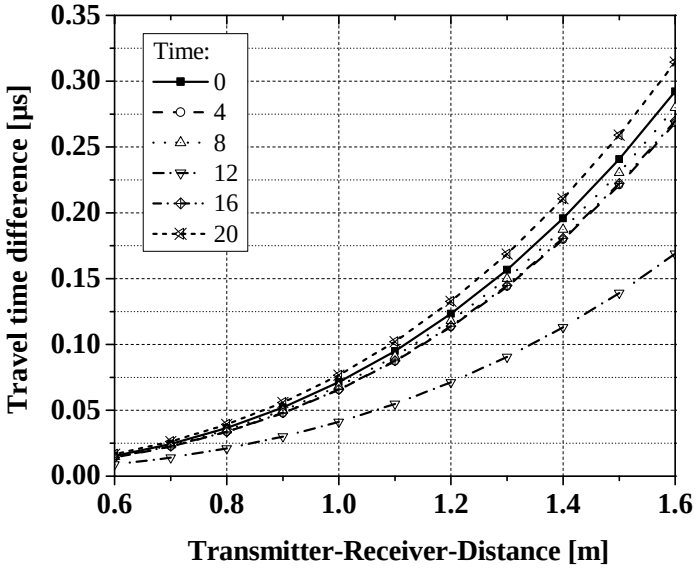

Fig. 4: Travel-time difference between the straight-line and the curved sound path for a downwind sound propagation at several times during a day for a transmitter and receiver height of 20 cm (meteorological data from HIRVAC simulation on 15th January over grassland without clouds). The graphs at 4 and 16 o'clock are nearly identical.

Only negative gradients of the effective sound speed result for an upwind sound propagation for all simulated seasons and day times. This leads to an upward refraction of the sound rays due to the stratified atmosphere. Strictly speaking, no sound signal could be received by a point-shaped receiver for such conditions and neglecting effects of turbulent scattering. If one considers the extension of the receiver (about 2 cm) than it will be possible, that a signal can be received if the height difference between the curved sound ray near the receiver position and the receiver position itself is very small (in our case smaller than about 2 cm). The greatest height differences can be awaited again for maximal amounts of sound speed gradients. Figure 5 demonstrates such a case on the 15th July and again for small sensor heights above the ground.

The maximally calculated amount of the sound speed gradient of about 12.7 m/(s·m) is caused by the strong temperature decrease with height about noon together with the strong negative wind speed gradient near the ground surface.

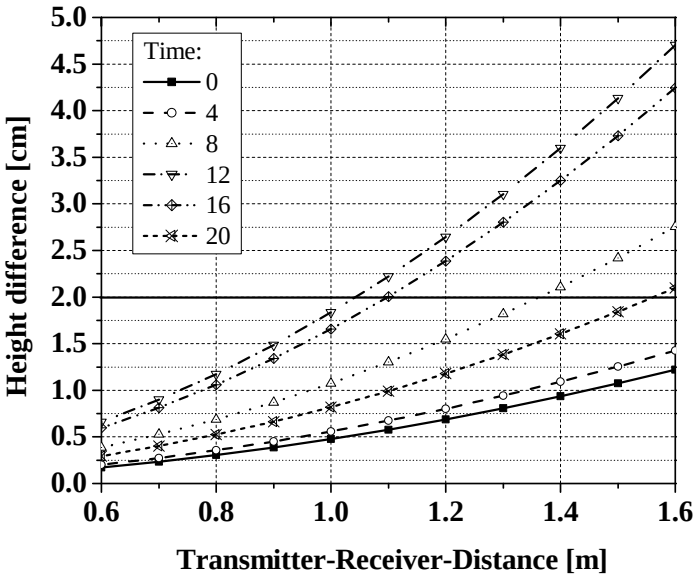

Fig. 5: Height difference between the straight-line and the curved sound path for an upwind sound propagation at several times during a day for a transmitter and receiver height of 20 cm (meteorological data from HIRVAC simulation on 15th July over grassland without clouds).

The maximal height difference occurs for the maximal transmitter-receiver distance and amounts to 4.7 cm. Only up to distance of 1 m it can be awaited that the refraction effect in the upwind direction never influences the measurements. If measurements with acoustic sensors at greater height levels (> 50 cm) will be carried out, than the refraction effect decreases significantly for the investigated transmitter-receiver distances.

4 Derivation of further meteorological quantities

4.1 Calculation of momentum and sensible heat fluxes

The measurements of temperature and wind vector inside the acoustic-chamber volume will be carried out along several sound paths at two height levels. Using these measurements at several heights, vertical temperature and wind gradients can be calculated and following turbulent momentum and heat fluxes applying the profile method (see e.g. Foken, 2006). At first, the applicability of the acoustic measurements to derive relevant vertical gradients of meteorological quantities should be proven. For that purpose the atmospheric boundary layer model HIRVAC was applied again to simulate typical temperature and wind speed profiles for several seasons and daytimes over a grassland site.

The model simulations show the expected result, that the vertical gradients of temperature and wind speed decreases significantly with increasing height levels (here considered: 0.2 m, 0.5 m, 0.7 m, 1.0 m). Furthermore, maximal gradients can be anticipated in the summer season and during cloudless conditions. These vertical temperature and wind speed differences (height layers: 0.5 m–0.2 m, 0.7 m–0.2 m, 1.0 m– 0.2 m) are now compared with the uncertainty of the acoustic measurement to prove the significance of the method. The results of this comparison demonstrate (here not shown) the

general applicability for wind speed measurements along sound path lengths of 0.6 m–1.6 m, because the minimal vertical wind differences (0.65 m/s for height layer 0.5 m–0.2 m) are larger than the uncertainty of the wind measurement along one single sound path without temporal averaging and for a travel time error of 2.5 µs (see Fig. 2). In contrast to that, the uncertainty of temperature measurements is significantly greater than that one for the wind speed. Therefore, the requirements for the acoustic travel time uncertainty together with the minimally possible sound path length are noticeably higher. Typical temperature differences for the height layer 0.5 m–0.2 m amount to 0.2 K during the winter season. Such small temperature differences are only detectable if sound path lengths greater than 1 m and an averaging over at least 20 single measurements will be used.

By means of the acoustically measured temperature and wind speed gradients it will be possible to derive turbulent fluxes of momentum and sensible heat. The basis for that is the profile method (flux-gradient-similarity), in our case a special profile method for two measurement heights, both above the ground surface (see for further information e.g. Richter and Skeib, 1984, Foken, 2006). Presuppositions for the applicability of this method are: a high measurement repetition rate, a homogeneous terrain with uniform fetch, a detectable difference of temperature and wind speed between the two height levels, a turbulent meteorological regime (wind speed at the second measurement level > 1 m/s, wind speed difference between measurement levels > 0.3 m/s), a large ratio of measurements heights (preferably > 4). That means for our application of the profile method, that outgoing from a first measurement height of 20 cm the second measurement level should be situated at heights of 70 cm and greater.

If both measurement heights are smaller than a critical height, similar to the height of the dynamical sub-layer (where the turbulent fluxes are independent on the atmospheric stability), than simplified profile equations can be applied to calculate the friction velocity as measure of the momentum flux

$$u_* = \frac{\kappa\left(u(z_2)-u(z_1)\right)}{\ln\frac{z_2}{z_1}} \quad \text{[m/s]} \tag{8}$$

as well as the sensible heat flux

$$H = -\rho c_p \frac{\alpha_0 \kappa u_* \left(T(z_2)-T(z_1)\right)}{\ln\frac{z_2}{z_1}} \quad \text{[W/m²]} \tag{9}$$

with the von-Kármán-constant κ = 0.4, the horizontal wind speed u at the two height levels z_2 and z_1, air density ρ, inverse Prandtl-number α_0 = 1.35, specific heat capacity for constant pressure c_p = 1005 J/(kg K).

The critical height was estimated to be higher than 1 m for all investigated seasons and daytimes (here not shown). So it is possible to apply equations (8) and (9) if both measurement heights z_1 and z_2 are smaller than 1 m.

Modeled temperature and wind speed values, which were simulated by HIRVAC, were used now to calculate the fluxes applying equations (8) and (9), see Fig. 6.

Minimal and maximal values of the friction velocity and sensible heat flux results for the winter and summer season, respectively (Fig. 6). Please note, that the displayed

graphs represent only one possible scenario (for distinct values of upper and lower boundary conditions, e.g. geostrophic wind speed, soil moisture, vegetation canopy).

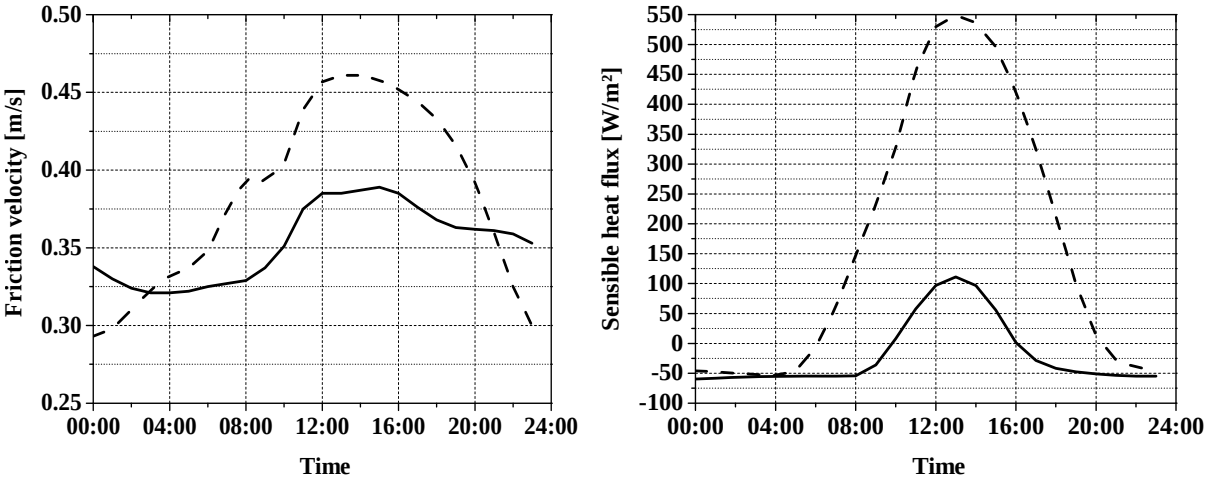

Fig. 6: Friction velocity (left) and sensible heat flux (right) resulting from modeled temperature and wind profiles and the flux-gradient-method for simulations over grassland on the 15th January (continuous line) and 15th July (dashed line), cloudless days.

4.2 Uncertainty of momentum and sensible heat fluxes

The uncertainties for the acoustic measurement of friction velocity (momentum flux) and sensible heat flux are estimated according to chapter 2.3. It is assumed that only the uncertainty of the travel time measurement and therewith the uncertainty of acoustically measured temperature and wind speed contributes to the uncertainty of flux determination. From this it follows the uncertainty of friction velocity

$$\Delta u_* = \left(\left|\frac{\partial u_*}{\partial u(z_2)}\right| \Delta u\right) + \left(\left|\frac{\partial u_*}{\partial u(z_1)}\right| \Delta u\right) = 2\,\frac{\kappa \Delta u}{\ln\frac{z_2}{z_1}} \tag{10}$$

with the wind speed error Δu according to equation (7) and the uncertainty of sensible heat flux

$$\Delta H = \left(\left|\frac{\partial H}{\partial u(z_2)}\right| \Delta u\right) + \left(\left|\frac{\partial H}{\partial u(z_1)}\right| \Delta u\right) + \left(\left|\frac{\partial H}{\partial T(z_2)}\right| \Delta T\right) + \left(\left|\frac{\partial H}{\partial T(z_1)}\right| \Delta T\right) =$$

$$2\rho c_p \frac{\alpha_0 \kappa^2}{\left(\ln\frac{z_2}{z_1}\right)^2} \left(|T(z_2) - T(z_1)|\Delta u + |u(z_2) - u(z_1)|\Delta T\right) \tag{11}$$

with the temperature error ΔT according to equation (6). In the following figures (7 and 8) the results of uncertainties for turbulent fluxes are exemplarily shown for two height differences: 0.5 m–0.2 m and 1.0 m–0.2 m and a travel time uncertainty of 2.5 µs without averaging. This uncertainty decreases in the case of averaging over a distinct number of measurements (here: 20, 60, 100 measurement values).

The investigations show, that an averaging over a number of measurements of minimal 60 values is necessary to get an acceptable uncertainty of the fluxes. Then the uncertainty of friction velocity amounts to about 0.03 m/s for longer sound paths (ca. 1 m) and lies therewith in an adequate range for fully developed turbulence (friction velocity > 0.3 m/s).

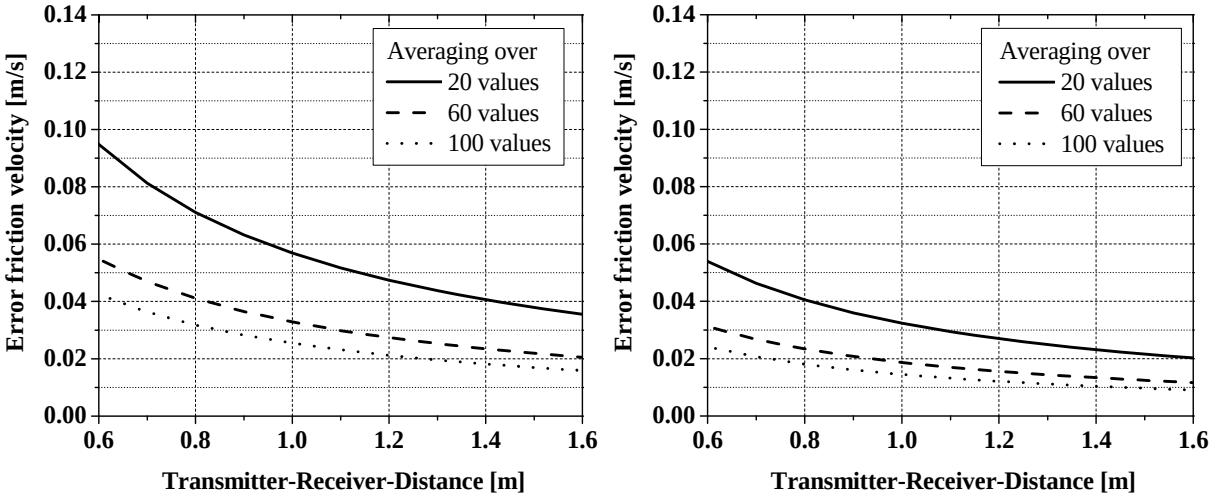

Fig. 7.: Uncertainty of the friction velocity for a measurement height difference of 0.5 m–0.2 m (left) and 1.0 m–0.2 m (right).

An enhancement of the significance of the measurements will be derived if the distance between the height levels increases (left and right picture in Fig. 7). Generally, the uncertainty decreases with an increasing sound path length. This results also for the uncertainty calculation of the sensible heat flux (Fig. 8).

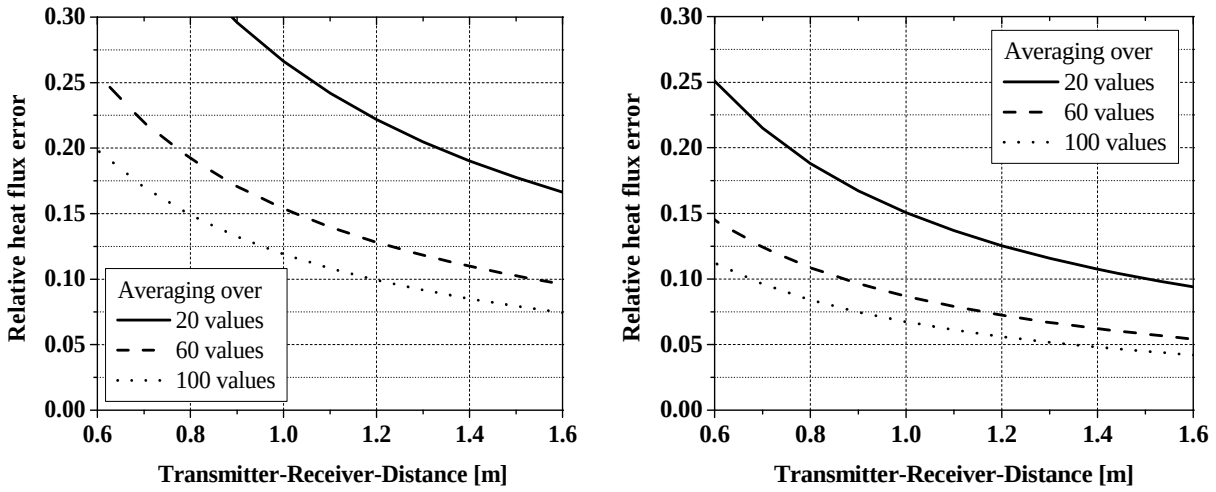

Fig. 8.: Uncertainty (relative error) of the sensible heat flux for a measurement height difference of 0.5 m–0.2 m (left) and 1.0 m–0.2 m (right) on the 15th July (at noon).

To estimate the maximal uncertainty during the vegetation period (planned application of the acoustic chamber measurement), maximal values of the wind speed as well as temperature differences between several heights were used to calculate the uncertainty of sensible heat flux (corresponding to maximal fluxes during the summer season at midday). Because of this dependence of the heat flux uncertainty on the vertical temperature and wind difference, a relative error of the heat flux is calculated (see Fig. 8). The uncertainty of the sensible heat flux is decreasing with a larger height layer comparable to the result derived for the friction velocity (see Fig. 7), although there is a height dependency of the heat flux uncertainty both in the numerator and the denomi-

nator (see Eq. 11). If the height difference between the two measurement levels increases, the temperature and wind speed differences increases too. On the other hand the height ratio in the denominator also increases which leads to a decreased uncertainty altogether.
Please note that for a small uncertainty of the heat flux also a small temperature and wind speed difference between the height levels is desirable. But the minimal detectable wind speed and temperature difference depends on the achievable travel time uncertainty and is therefore given by the properties of the acoustic measurement device (acoustic sensors, digitalization frequency…) itself.

5 Conclusions

For the purpose of studying the energy exchange above a lysimeter surface we will use line-averaged acoustic travel-time measurements. Together with further sensors these acoustic measurements record the mean and turbulent flow field in a volume over the whole surface of the lysimeter. The volume, in which the flow field is detected by the measurements, is here named ‘acoustic chamber’.
To derive meteorological data outgoing from measurements of the sound propagation between acoustic transmitters and receivers it is necessary to separate the coupled temperature and wind influence on the measured effective sound speed. It was demonstrated, that the simplest and most certain separating method of reciprocal sound propagation is applicable for our measurement geometry with measurement heights greater than 20 cm and acoustic path lengths of about 1 m.
Acoustic measurements of the temperature, provided along a typical acoustic path length of 1 m through the acoustic chamber volume, results in a temperature uncertainty of about 0.5 K for an assumed travel-time uncertainty of 2.5 µs. The uncertainty for the acoustically measured wind speed is by a roughly constant factor smaller than that one for the temperature. So it results an uncertainty of a single wind measurement of about 0.3 m/s along an acoustic path length of 1 m. If this single travel-time measurement will be repeated *n*-times, than the uncertainty of the temperature and wind measurements decreases significantly.
Additionally to the inherent uncertainty of acoustic travel-time measurements there are several possible effects, e.g. the sound absorption in air, the reflection of sound at the ground surface, and the sound refraction because of vertical temperature and wind gradients in the atmosphere near the ground, which are able to influence significantly the sound propagation.
The effect of air absorption results always in a sound attenuation. Our study showed that sound signals with the applied sound frequency of 40 kHz permit only short sound path lengths of a few meters.
Furthermore, the sound propagation near the ground surface leads to the effect of ground reflection of sound waves. It is possible that the sound level at the receiver increases or decreases due to the interference of the direct and the reflected sound wave. If the height of the sensors is only 20 cm above the ground, the maximal sound attenuation amounts to 6.5 dB for a distance of 1.55 m and a sound frequency of 40 kHz.

Otherwise, the sound level may be enhanced by 3.5 dB for a distance of 1.4 m. If transmitters and receivers are installed at greater heights above surface, the positive or negative sound attenuation decreases and is negligible for heights above 50 cm. If the height of the acoustic devices increases, the time interval between the direct and the reflected wave increases too and the two signals are then distinguishable at the receiver. It is imaginable to use the reflected signal as an information source on the air layer nearest the ground surface.

The effect of atmospheric refraction determines on one hand the applicability of the reciprocal sound propagation for downwind situations. It has been shown that also for strong vertical temperature and wind gradients near the ground surface the assumption of reciprocal sound propagation is applicable for the used measurement geometry with small sound path lengths of about 1 m. On the other hand, for upwind situations, the detectability of the sound signal is questionable. The results of this study demonstrate that the refraction effect in the upwind direction never influences the measurements at a height of 20 cm only for very small distances up to 1 m. If measurements with acoustic sensors at greater height levels (>50 cm) will be carried out, than the refraction effect decreases significantly and doesn't play a role for the investigated transmitter-receiver distances.

If the certainty of the acoustically measured travel time data is assured, than it is possible to calculate momentum and sensible heat fluxes using the temperature and wind measurements at several height levels. The investigations show, that an averaging over a number of measurements of minimal 60 values is necessary to get an acceptable uncertainty of the momentum and sensible heat fluxes (see Fig. 7 and 8). At least a 10% accuracy is achievable for measurements in an atmospheric surface layer with developed turbulence. Generally, the applicability of the used calculation method for momentum and heat flux (profile method) must be guaranteed for future measurements along acoustic paths within a length scale of 1 m.

To capture all parts of the turbulent spectrum it is necessary to repeat the acoustic measurements with a high frequency of 1-10 Hz and to average the resulting data dependent on the measurement height, the atmospheric stability, and the wind speed. For a height of 1 m and a wind speed of 2 m/s an averaging period of 10 min is adequate (van Boxel et al., 2004) to detect, on one side, the long-wave parts of the turbulent flux but, on the other side, to secure stationarity.

Acknowledgement

The project is funded by the Federal Ministry of Economics and Technology, Central Innovation Programme, funding number KF2709801BN0.

References

Arnold, K., 2000: Ein experimentelles Verfahren zur akustischen Tomographie im Bereich der atmosphärischen Grenzschicht (in German). Wiss. Mitt. Inst. Meteorol. Univ. Leipzig, Inst. Troposphärenforschung, Leipzig 18, 137 pp.

Balogh, J., Nagy, Z., Fóti, Sz.,. Pintér, K., Czóbel, Sz., Péli, E.R., Acosta, M., Marek, M.V., Csintalan, Zs. and Tuba, Z., 2007: Comparison of CO2 and H2O fluxes over grassland vegetations measured by the eddy-covariance technique and by open system chamber. Photosynthetica 45, 288-292.

Baums, A.-B., Goldberg, V. and Bernhofer, C., 2004: Upgrading the Coupled Vegetation Boundary Layer Model HIRVAC by New Soil Water and Interception Modules. Meteorol. Z. 14, 211-218.

van Boxel, J. H., Sterk, G. and Arens, S. M., 2004: Sonic anemometers in aeolian sediment transport research. Geomorphology 59, 131-147.

Delany, M.E. and Bazley, E.N., 1970: Acoustical properties of fibrous absorbent materials. Applied Acoustics 3, 105-116.

DVWK, 1996: Ermittlung der Verdunstung vn Land- und Wasserflächen (in German). DVWK-Merkblätter zur Wasserwirtschaft 238, 134 pp.

Foken, T., 2006: Angewandte Meteorologie – Mikrometeorologische Methoden (in German). 2. Aufl., Springer-Verlag, Berlin, Heidelberg, 325 pp.

Goldberg, V. and Bernhofer, Ch., 2001: Quantifying the coupling degree between land surface and the atmospheric boundary layer with the coupled vegetation-atmosphere model HIRVAC. Annales Geophysicae 19, 581-587.

Kaimal, J.C., Gaynor, J.E., 1991: Another look at sonic thermometry. Bound. Layer Meteorol. 56, 401-410.

Lihoreau, B., Gauvreau, B., Bérengier, M., Blanc-Benon, P. and Calmet, I., 2006: Outdoor sound propagation modeling in realistic environments: Application of coupled parabolic and atmospheric models. J. Acoust. Soc. Amer. 120, 110–119.

Mix, W., Goldberg, V. and Bernhardt, K. H., 1994: Numerical experiments with different approaches for boundary layer modelling under large-area forest canopy conditions. Meteorol. Z. 3, 187-192.

Richter, S.H. and Skeib, G., 1984: Anwendung eines Verfahrens zur Parametrisierung des turbulenten Energieaustausches in der atmosphärischen Bodenschicht (in German). Geod. Geophys. Veröff. RII 26, 80-85.

Salomons, E.M., 2001: Computational atmospheric acoustics, Kluwer Academic Publishers, 355 pp.

Schotanus, P., Nieuwstadt F.T.M. and Bruin, H.A.R., 1983: Temperature measurements with a sonic anemometer and its application to heat and moisture fluxes. Bound. Layer Meteorol. 26, 81-93.

Ziemann, A., 1998: Numerical simulation of meteorological quantities in and above forest canopies. Meteorol. Z. 7, 120-128.

Ziemann, A., Balogh, K. and Arnold, K., 2007: Modelling and measuring the atmospheric excess attenuation over flat terrain during night time conditions. Meteorol. Zeitschrift 16, 429-441.

Ziemann, A., Arnold, K. and Raabe, A., 1999: Acoustic travel time tomography – a method for remote sensing of the atmospheric surface layer. Meteorol. Atmos. Phys. 71, 43-51.

Adressess of authors:

Astrid Ziemann (astrid.ziemann@tu-dresden.de, current affiliation: TU Dresden, Institute of Hydrology and Meteorology) and Armin Raabe (raabe@uni-leipzig.de),
University of Leipzig, Institute for Meteorology, Stephanstraße 3, 04103 Leipzig

Jahresbericht des Institutes für Meteorologie der Universität Leipzig 2010

1. Bearbeitete Forschungsprojekte

AG Atmosphärische Strahlung

Hubschraubergetragene Strahlungsmessungen zur Bestimmung des Einflusses von Wolkeninhomogenitäten tropischer Grenzschichtbewölkung auf die Strahlungsbilanz

Helicopter-borne radiation measurements to investigate the influence of cloud heterogeneities of tropical boundary layer clouds on radiative budget

F. Henrich (f.henrich@uni-leipzig.de), M. Wendisch (m.wendisch@uni-leipzig.de)
H. Siebert (siebert@tropos.de)

Die Vernachlässigung von horizontalen Wolkeninhomogenitäten in Modellen zur Berechnung der solaren Strahlungsbilanz von Wolken kann zu erheblichen Diskrepanzen zwischen Modellergebnissen und Messungen führen. In Zusammenarbeit mit dem Leibniz-Institut für Troposphärenforschung wird der Einfluss von Inhomogenitätseffekten von tiefer Cumulusbewölkung in den Tropen auf den Strahlungshaushalt untersucht. Hierfür wird ein neues, kompaktes Messsystem für spektrale Strahlungsmessungen gebaut, welches zusammen mit einer Messplatform für Aerosol-, Turbulenz- und Mikrophysikalischen Wolkenparametern (ACTOS) erstmals die gleichzeitige Beobachtung von Wolkenmikrophysikischen und Strahlungsgrößen ermöglichen wird. Hierfür wird ein Hubschrauber als Instrumententräger genutzt. Ergänzend sollen dreidimensionale Rechnungen mit einem Strahlungstransfermodell zur Interpretation der Messungen durchgeführt werden.
Das Messgebiet (Barbados) bietet aufgrund seiner Lage zusätzlich die Möglichkeit der Untersuchung von anthropogenen Einflüssen auf den atmosphärischen Strahlungstransfer und die Beeinflussung des solaren Strahlungshaushaltes durch Feuchtigkeits-Halos.

Weiterführung: ja

Finanzierung: Uni Leipzig, DFG WE 1900/18-1, IfT Leipzig

AG Atmosphärische Strahlung

Räumliche Verteilung von Eis- und Flüssigwasser in Arktischen Mischphasenwolken und deren Einfluss auf Energiehaushalt und Fernerkundung

Spatial distribution of ice and liquid water in Arctic mixed-phase clouds and its impact on energy budget and remote sensing

A. Ehrlich (a.ehrlich@uni-leipzig.de), E. Bierwirth (eike.bierwirth@uni-leipzig.de)
M. Wendisch (m.wendisch@uni-leipzig.de)

Mischphasenwolken mit nebeneinander existierendem flüssigem Wasser- und Eisanteil treten häufig in arktischen Regionen auf. Sie können theoretisch in einem Temperaturbereich zwischen -40°C und 0°C über längere Zeit hinweg stabil

existieren. Wie bekannt ist, unterscheiden sich die optischen Eigenschaften von reinen Wasser- und Eiswolken und damit auch ihr Einfluss auf die solare Strahlung. Zur Untersuchung der horizontalen Verteilung von Eis- und Flüssigwasser und deren Einfluss auf den Strahlungstransport wird dieses Projekt in Zusammenarbeit mit dem Alfred-Wegener-Institut für Polar- und Meeresforschung (AWI), Bremerhaven, durchgeführt.
Kern des Projektes ist die internationale Messkampagne „Solar Radiation and Phase Discrimination of Arctic Clouds“ (SORPIC), die vom 30.April bis zum 20.Mai 2010 auf Svalbard (Norwegen) stattfand (Projekt-Webseite http://www.uni-leipzig.de/~sorpic/). Dabei wurden erfolgreich spektrale solare Strahlungsmessungen an Bord des Forschungsflugzeuges Polar-5 des AWI durchgeführt. Die gemessenen Strahlungsdaten sind vollständig korrigiert und kalibriert und stehen den Projektpartnern zur Verfügung.
Simultan wurden Messungen mit der hyperspektralen Kamera AISA Eagle des AWI durchgeführt; die Auswertung erfolgt in Zusammenhang mit den Strahlungsdaten des SMART-Albedometers am LIM. AISA Eagle wurde im Labor des LIM spektral und radiometrisch kalibriert.
Am 15.November 2010 hat das LIM einen Daten-Workshop mit den beteiligten Projektpartnern (AWI Potsdam/Bremerhaven, LaMP Clermont-Ferrand (Frankreich), Freie Universität Berlin) veranstaltet, bei dem der Fortgang der Datenauswertung und das Publikationskonzept für 2011 abgesprochen wurden.

Weiterführung: ja

Finanzierung: DFG WE 1900/17-1

AG Atmosphärische Strahlung

Einfluss von SAHARA-Staubschichten und Biomasseverbrennungsprodukte auf den atmosphärischen Strahlungsantrieb
Influence of Saharan dust layers and biomass burning on atmospheric radiative forcing

S. Bauer (mail@bauerstefan.com), M. Wendisch (m.wendisch@uni-leipzig.de)
B. Heinold (heinold@mail.tropos.de), I. Tegen (itegen@tropos.de)
A. Torge (atorge@ifm-geomar.de), A. Macke (macke@tropos.de)

Das Projekt untersucht den Einfluss von Saharastaub und Biomasseverbrennungsprodukte auf den atmosphärischen Strahlungshaushalt. Dafür stehen flugzeuggetragene und bodengebundene Messungen von solaren Radianzen und Irradianzen während der Kampagne SAMUM 2 (Saharan Mineral Dust Experiment) auf den Kap Verden im Januar/Februar 2008 zur Verfügung. Somit wurden Strahlungsmessungen unter und über Staub- und Biomasseschichten durchgeführt. Die gesammelten Daten werden unter Zuhilfenahme von eindimensionalen Strahlungstransfersimulationen auf Abkühlungs- und Erwärmungseffekte solarer Strahlung in Staub- und Biomasseschichten untersucht.
Die gemessenen aufwärtsgerichteten Radianzen über Staubschichten werden zudem mit Messungen des Meteosat-Second-Generation-Satelliten (MSG) verglichen. Unter Annahme von isotroper atmosphärischer Strahlung können

Irradianzen aus MSG-Radianzen abgeleitet und mit den gemessenen Irradianzen auf dem Flugzeug verglichen werden.
Weiterhin werden Ergebnisse aus Staubtransportmodelle, die im Zuge von SAMUM 1 im Jahr 2006 entwickelt wurde, mit den gemessenen Irradianzen verifiziert.

Weiterführung: ja

Finanzierung: DFG WE 1900/15-1

AG Atmosphärische Strahlung

Bestimmung optischer und mikrophysikalischer Wolkeneigenschaften im Vertikalprofil mittels bodengebundener Fernerkundung
Measurements of vertical profiles of optical and microphysical cloud properties by means of surface-based remote sensing

J. Walter (jwalter@uni-leipzig.de), M. Brückner (mbrueck@rz.uni-leipzig.de)
A. Raabe (raabe@uni-leipzig.de), M. Wendisch (m.wendisch@uni-leipzig.de)

Mittels Kombination eines einfachen Rückstreulidars mit Radianzmessköpfen sollen Vertikalprofile von sowohl mikrophysikalischen als auch optischen Eigenschaften n konvektiver Bewölkung untersucht werden. Hierzu wurde das LIDAR in einem ersten Schritt während einer EARLINET-Messkampagne im Mai 2009 mit anderen LIDAR-Systemen verglichen. In einem zweiten Schritt wird ein Radianzmesskopf zusätzlich im LIDAR implementiert. Neben der Bestimmung optischer Wolkeneigenschaften soll mit Hilfe des LIDAR die thermodynamische Phase der Wolkentropfen bestimmt und mit den Ergebnissen der Bestimmung der thermodynamischen Phase mittels Radianzmessungen verglichen werden. Die Radianzmessungen werden weiterhin zur Bestimmung des effektiven Wolkentropfenradius verwendet. Die gewonnenen Ergebnisse sollen anschließend mit dreidimensionalen Strahlungstransportmodellrechnungen verglichen werden.

****

AG Atmosphärische Strahlung

Megacities - Hochaufgelöste spektrale Albedo-Karten von Megastädten und ihre Anwendung in Aerosol-Satelliten Datengewinnung
Megacities - High-resolution spectral albedo maps of megacities and its application in aerosol retrievals from satellite data

B. Mey (b.mey@uni-leipzig.de), M. Wendisch (m.wendisch@uni-leipzig.de)
H. Jahn (heiko.jahn@uni-bielefeld.de), A. Krämer (alexander.kraemer@uni-bielefeld.de) ,
Chen Xingfeng (chenxf@irsa.ac.cn) , Gu Xingfa (guxingfa@irsa.ac.cn)

Megastädte sind eines der größten Quellgebiete anthropogenen Aerosols. Sie fungieren daher als Punktquellen für Aerosole im globalen Kontext und beeinflussen lokal die Gesundheit der Menschen. Daher ist es wichtig den Aerosolgehalt der Atmosphäre in Megastadt-Regionen möglichst genau zu bestimmen. In Regionen ohne dichtes Messnetz für Spurenstoffe, ist die Satelliten-Fernerkundung ein

geeignetes Mittel, um Spurenstoffe regelmäßig zu messen. Zur Ableitung der Aerosoloptischen Dicke aus Satellitendaten muss das empfangene Signal der reflektierten Strahlung in einen atmosphärischen Anteil und den Bodenanteil getrennt werden. Der Bodenanteil ist durch die Boden-Albedo oder –Reflektivität gegeben, welcher schwierig aus Satellitenmessungen bestimmt werden kann.
Spektral und räumlich hochaufgelöste Messungen der Bodenalbedo wurden mit der Kombination aus den flugzeuggetragenen Messsystemen SMART-Albedometer (400-2100 nm) und einer Kamera (Geospatial Systems, MS 4100) mit 3 spektralen Kanälen gemessen. Der erste Datensatz wurde in Leipzig im Jahr 2007 aufgenommen, der zweite Datensatz konnte im Dezember 2009 in Zhongshan, China, gemeinsam mit unseren chinesischen Kooperationspartnern des Institute of Remote Sensing Applications erfasst werden.
Das Satelliten-Tool IMAPP der Universität Wisconsin wurde auf Computern des Instituts für Meteorologie installiert und steht nun für wissenschaftliche Zwecke in diesem, sowie anderen Projekten bereit.
Es wird erwartet, dass durch Verwendung der hochaufgelösten Messdaten der Bodenalbedo im Aerosol-Retrieval der Satellitendaten das Resultat der Aerosol Optischen Dicke verbessert werden kann.

Weiterführung: ja

Finanzierung: DFG, SPP 1233 (WE 1900/16-2)

****

AG Atmosphärische Strahlung

Räumlich inhomogene Zirren: Einfluss auf die atmosphärische Strahlung
Spatially Inhomogeneous Cirrus: Influence on Atmospheric Radiation
M. Wendisch (m.wendisch@uni-leipzig.de)

Die Strahlungseffekte durch inhomogene Zirren werden mit Hilfe einer Kombination von Flugzeuggetragenen Messungen (Strahlung und mikrophysikalische Eigenschaften), einem 3D Strahlungsmodell und einem dynamischen wolkenauflösenden Zirrus-Modell untersucht. Ein instrumentiertes Flugzeug (Lear-Jet) misst die spektrale Strahlung über Zirren im Rahmen einer Feldmesskampagne. Daraus werden die mikrophysikalischen Felder der Zirren abgeleitet. Diese werden verglichen mit gleichzeitigen in situ Messungen, welche mit einer Schleppsonde gesammelt werden. Diese wird gleichzeitig vom Flugzeug durch die Zirren gezogen wird. Parallel dazu werden die örtlichen Inhomogenitäten der Zirren Felder mit Hilfe einer abbildenden digitalen CCD Kamera beobachtet. Zusätzlich wird ein wolkenauflösendes Zirren-Modell benutzt zur Berechnung der mikrophysikalischen Zirren-Felder. Die aus den kombinierten in situ und indirekten Messungen abgeleiteten sowie modellierten mikrophysikalischen Zirren-Felder werden als Eingabe für ein 3D Strahlungsmodell benutzt, um die 3D-Effekte inhomogener Zirren zu untersuchen.

Weiterführung: ja

Finanzierung: DFG WE 1900/19-1

AG Atmosphärische Strahlung

Solare Strahlungsmessungen auf HALO
Solar Radiation Measurements on HALO
C. Fricke (fricke@uni-leipzig.de)
M. Wendisch (m.wendisch@uni-leipzig.de)

HALO (High Altitude and LOng Range Research Aircraft) ist das Synonym für das neue deutsche Forschungsflugzeug mit dem es möglich sein wird, eine Vielzahl von verschiedensten atmosphärischen Parametern bis hin in die untere Stratosphäre zu messen. Aufgrund seiner Reichweite, sowohl in vertikaler als auch in horizontaler Richtung bietet HALO die Möglichkeit großräumige Strahlungsfelder zu erfassen. Während zwei HALO Demo-Missionen kommen dabei neu entwickelte Spektrometersysteme zur spektralen Erfassung solarer Strahlung zum Einsatz. Die dabei ermittelten Messgrößen sind zum einen die (i) spektrale Strahlflussdichte, welche den solaren Strahlungshaushalt der Atmosphäre bestimmt, sowie die (ii) spektrale aktinische Flussdichte, welche photolytische Prozesse innerhalb der Atmosphäre kontrolliert. Die solare spektrale Strahldichte in Nadir-Richtung wird für Fernerkundungsuntersuchungen zusätzlich simultan gemessen. Für die Strahlflussdichten ist es dabei entscheidend, die aufwärts- sowie abwärts gerichteten Flussdichten, welche mittels der Kosinusempfänger oberhalb und unterhalb des Flugzeugs empfangen werden, zu unterscheiden. Hierfür sind Stabilisierungsplattformen vorgesehen, die die Bewegungen des Flugzeuges aufzeichnen und die Position der Empfänger mit hinreichender zeitlicher Verzögerung korrigieren. Bezüglich der aktinischen Flussdichte ist die Kombination aus hoher zeitlicher Auflösung und hoher Genauigkeit innerhalb des UV-B Bereiches die größte Herausforderung. Realisiert wird selbige durch eine entsprechende Kombination aus Monochromatoren und Detektoren. Die aus allen Daten gewonnenen Erkenntnisse sollen zur Modellverbesserung verwendet werden, um sowohl Oxidationsprozesse als auch die mikrophysikalischen Prozesse, welche für die Bildung und zeitlichen Entwicklung von Zirren verantwortlich sind, besser zu verstehen.

Weiterführung: ja

Finanzierung: DFG WE 1900/21-1

AG Atmosphärische Strahlung

HALO Koordination von "Aerosol, Cloud, Precipitation, and Radiation Interactions and Dynamics of Extra-Tropical Convective Cloud Systems" (ACRIDICON)
HALO coordination of ACRIDICON
D. Rosenow (d.rosenow@uni-leipzig.de)
M. Wendisch (m.wendisch@uni-leipzig.de)

Konvektive Wolken können erheblichen ökonomischen Schaden verursachen aufgrund von starken Windböen, heftigen Schauern und Niederschlagen, welche teilweise mit Hagel, Graupel, und Gewittern verbunden sein können. Die Dynamik und Heftigkeit dieser ausgeprägten Wettererscheinungen werden bestimmt durch mikrophysikalische Prozesse bei der Wolken- und Niederschlagsbildung, welche beeinflusst werden können durch Aerosolpartikel und Wechselwirkungen mit atmosphärischer Strahlung. Weiterhin werden durch konvektive Wolken Spurengase und Aerosolpartikel prozessiert und umverteilt durch vertikalen Transport sowie Ein- und Ausmischen der Wolke mit der Umgebungsluft. Um diese Wechselwirkungen zwischen Spurengasen, Aerosolpartikeln und der Wolken- und Niederschlagsbildung sowie atmosphärischer Strahlung in außertropischen, konvektiven Wolken zu untersuchen, wurde die HALO Demo-Mission “Aerosol, Wolken, Niederschlag, und Strahlungswechselwirkungen sowie Dynamik von außertropischen, konvektiven Wolkensystemen (ACRIDICON)” vorgeschlagen. ACRIDICON trägt bei zu zwei Schwerpunkten des SPP 1294 bei: „Wolken und Niederschlag“ und „Transport und Dynamik in der Troposphäre und der unteren Stratosphäre“. Der vorliegende Antrag beinhaltet hauptsächlich die Organisation und das Management von ACRIDICON sowie teilweise einen Beitrag zur Analyse und Auswertung der Strahlungsmessungen, welche bei dieser HALO Demo-Mission gesammelt werden.

Weiterführung: ja

Finanzierung: DFG WE 1900/22-1

AG Atmosphärische Strahlung

Koordination des Schwerpunktsprogramms 1294 "Atmosphären- und Erdsystemforschung mit dem Forschungsflugzeug HALO (High Altitude and Long Range Research Aircraft)"

HALO coordination project
M. Wendisch (m.wendisch@uni-leipzig.de)
D. Rosenow (d.rosenow@uni-leipzig.de)

Das Projekt dient vornehmlich der Kooperation und der Kommunikation unter den Einzelprojekten des Schwerpunktprogramms. Im Rahmen des Projekts werden ein jährliches Statusseminar sowie jährliche Themen-Workshops geplant und durchgeführt. Die drei Koordinatoren vertreten den SPP gegenüber der DFG, dem Wissenschaftlichen Lenkungsausschuss von HALO (WLA), dem HALO Projektteam des Deutschen Zentrums für Luft- und Raumfahrt (DLR) und nach außen. Das Koordinatoren-Team betreibt Maßnahmen zur Nachwuchs- und Gleichstellungsförderung. Zentrale Initiativen wie gemeinsame Sammelveröffentlichungen in einem Sonderband oder die Durchführung von Sitzungen zu Themenschwerpunkten ("special sessions") bei internationalen Konferenzen sowie der Internetauftritt des SPP werden im Rahmen dieses Projekts koordiniert und durchgeführt.

Weiterführung: ja

Finanzierung: DFG WE 1900/24-1

AG Atmosphärische Strahlung

EUFAR - European Facility for Airborne Research in Environmental and Geosciences

M. Wendisch (m.wendisch@uni-leipzig.de)
D. Rosenow (d.rosenow@uni-leipzig.de)

Im Rahmen dieses Projektes werden die Expert Working Groups koordiniert. Workshops werden organisiert, und ein Buch wird geschrieben: Wendisch, M., and J.-L. Brenguier, Airborne Measurements – Methods and Instruments. In preparation to be published by *Wiley & Sons.*

Weiterführung: ja

Finanzierung: EU

AG Atmosphärische Strahlung

Spektrale Strahlungsbilanz über dem Atlantik aus Modell und Beobachtung

Spectral radiation budget over the Atlantic Ocean from model and observation

A. Macke (macke@tropos.de)
M. Wendisch (m.wendisch@uni-leipzig.de)
M. Brückner (mbrueck@rz.uni-leipzig.de)

Der Stoff- und Energieaustausch zwischen Ozean und Atmosphäre spielt eine entscheidende Rolle für die physikalische, chemische und biologische Entwicklung unseres Klimasystems Erde. Die von den beteiligten Forschungseinrichtungen entwickelten und eingesetzten Technologien zur in-situ Messung im Ozean und zur aktiven/passiven Fernerkundung der Atmosphäre, ermöglichen erstmalig durch eine Kombination dieser Daten eine kontinuierliche Erfassung relevanter Parameter. Im Rahmen des WGL-Verbundprojekts OCEANET wurde in Zusammenarbeit der Forschungseinrichtungen (IFM-GEOMAR, IfT Leipzig, Universität Leipzig, GKSS Geesthacht, AWI) eine autonome Messplattform entwickelt, die langfristig für den operationellen Betrieb an Bord von Fracht- und Forschungsschiffen vorgesehen ist.
Zum Verstehen des Klimasystems Ozean und Atmosphäre spielen Wolken und Strahlung eine wichtige Rolle. Da die Wolkenstrukturen sehr inhomogen sind und damit für Strahlungsübertragungsprozesse entscheidend sind, müssen diese Prozesse in Strahlungsparametrisierungen berücksichtigt werden. Eine Kombination der Beobachtung von physikalischen Eigenschaften und Strahlungseigenschaften von Wolken sind eine Möglichkeit solche Parametrisierungen anzugleichen oder zu validieren. Mithilfe der Erweiterung der breitbandigen Strahlungsflussdichtemessungen auf spektrale Strahldichte- und Strahlungsflussdichtemessungen mit einem bodengebundenem Spektrometer (CORAS) können unterschiedliche Wolkentypen zugeordnet werden. Beobachtete Atmosphärenzustände werden in ein 3D-Monte-Carlo Strahlungstransportmodell eingegeben, sodass die Ergebnisse mit den gemessenen Parametern verglichen

werden können. Die Messungen finden weitestgehend auf FS Polarstern statt.

Weiterführung: ja

Finanzierung: Leibniz-Institut für Troposphärenforschung

****

AG Allgemeine Meteorologie

Entwicklung eines tomographischen Wasserdampfsondierungssystems auf der Basis von GNSS Daten.
Development of a tomographic water vapour sounding system based on GNSS data

Prof. Dr. G. Tetzlaff (tetzlaff@uni-leipzig.de), Dr. A. Raabe (raabe@uni-leipzig.de), Dr, M. Bender
Prof. Dr. M. Rothacher, Dr. J. Wickert, Dr. G. Dick, Dr. G. Gendt, (GFZ Potsdam)

Die hochgenaue Positionsbestimmung mit Hilfe des GPS oder auch demnächst verfügbarem GALILIEO-Systems ist erst möglich, wenn die Atmosphäreneinflüsse auf die Signallaufzeiten korrigiert werden. Diese Korrekturen repräsentieren auch den Einfluss des atmosphärischen Wasserdampfes auf die Laufzeiten der GPS-Signale an der entsprechenden Bodenstation. Die GNSS-Bodennetze (*Global Navigation Satellite System*) in Europa erreichen eine solche räumliche Dichte, so dass es mit Ihnen möglich wird eine dreidimensionale Verteilung des Wasserdampfes in der Atmosphäre unter Zuhilfenahme von tomografischen Rekonstruktionstechniken abzuleiten.
Dazu sind Abschätzungen der Genauigkeiten notwendig und Algorithmen zu erarbeiten, die ein Zusammenfassen der an einzelnen Stationen vorliegenden Daten ermöglicht.
Ziel ist es, den numerischen Wettermodellen quasi Echtzeit-Informationen über die dreidimensionale Wasserdampfverteilung in der Atmosphäre z.B. über Europa zur Verfügung zu stellen.

Weiterführung: Ja

Finanzierung: DFG (TE 51/26-1; RO 2330/5-1)

****

Auswirkung möglicher Klimaänderung auf das Wasserdargebot in verschiedenen Wassereinzugsgebieten Sachsens
Potential climate change impacts on the water supply in different drainage basins of Saxony

Prof. Dr. G. Tetzlaff (tetzlaff@uni-leipzig.de), Dr. A. Raabe (raabe@uni-leipzig.de), Dr. M. Barth (mbarth@uni-leipzig.de)

Klimaveränderungen wirken sich auf das Wasserdargebot im Einzugsgebiet von Talsperren aus. Aus den Langfristvorhersagen unterschiedlicher Klimamodelle, deren Grundlage verschiedene Emissions-Szenarien sind, sollen

Wasserdargebotsaussagen für die Region der sächsischen Talsperren abgeschätzt werden.

Weiterführung: Ja

Finanzierung: Landestalsperrenverwaltung des Freistaats Sachsen (LTV)

****

AG Hochatmosphäre
Upper Atmosphere

Strukturelle Änderungen von langfristigen Trends in dynamischen Parametern der mittleren Atmosphäre
Structural changes in long-term trends of the dynamics of the upper atmosphere

Prof. Dr. Christoph Jacobi (jacobi @ rz.uni-leipzig.de), Dr. J. Lastovicka, P. Krisan (IAP der Akademie der Wissenschaften, Prag), Prof. Yu.I. Portnyagin, Dr. E.G. Merzlyakov (Institut für Experimentelle Meteorologie, Obninsk)

Die Analyse experimenteller Daten hat gezeigt, dass, im Gegensatz zum Verhalten der Temperatur der mittleren Atmosphäre, die Dynamik der Mesosphäre und unteren Thermosphäre (MLT) keinen eindeutigen Trend aufweist, was wahrscheinlich auf das Zusammenwirken verschiedener Einflussfaktoren aus der unteren und mittleren Atmosphäre zurück zu führen ist. Um die Rolle dieser verschiedenen Faktoren zu klären, sollen Windzeitreitreihen der MLT im Hinblick auf Trends und speziell Trendänderungen untersucht werden, wobei aufgrund der relativen Kürze der verfügbaren Datensätze neue statistische Verfahren zum Einsatz kommen werden. Die Analysen werden durch Vergleiche mit stratosphärischen, troposphärischen und ionosphärischen Parametern vervollständigt, sowie die Rolle externer Einflüsse geklärt (solarer Fluss, Geomagnetismus). Numerische Simulation der Antwort der mittleren Atmosphäre auf Änderungen der troposphärischen und stratosphärischen Zirkulation wird ebenfalls zur Klärung der Frage, welche Einflüsse die Windänderung der MLT steuern, beitragen.

Weiterführung: nein

Finanzierung: Drittmittel (DFG JA836/22-1, GA-CR)

****

AG Hochatmosphäre
Upper Atmosphere

Selbstkalibrierende EUV/UV-Spektrophotometer SolACES
Auto-Calibrating EUV/UV Spectrophotometers SolACES

Prof. Dr. Christoph Jacobi (jacobi @ rz.uni-leipzig.de), Dr. B. Nikutowski

Das vom Fraunhofer IPM entwickelte Instrument SolACES (Solar Auto Calibrating EUV / UV Spectrometers), soll die solare Strahlung im Wellenlängenbereich von 17 bis 220 nm spektral aufgelöst mit hoher radiometrischer Absolutgenauigkeit messen. Im Projekt erfolgt neben Unterstützung der Missionsvorbereitung und -begleitung die Aufbereitung der Rohdaten, Datenauswertung, Erstellung empirischer Modelle der EUV-Strahlung, und Analyse der ionosphärischen Reaktion auf EUV-Variabilität.

Weiterführung: ja

Finanzierung: Auftrag (Fraunhofer-Institut für Physikalische Messtechnik)

****

AG Hochatmosphäre
Upper Atmosphere

Aufbau einer Streudatenbank SCATDB
Constructing a scatter characteristics data bank

Prof. Dr. Christoph Jacobi (jacobi @ rz.uni-leipzig.de), Dr. J. Wauer

Es hat sich gezeigt, dass Chebyshev-Teilchen ein gutes Modell zur Beschreibung der Lichtstreuung an rauen Teilchen darstellen. Ziel ist es, mittels Störungstheorie den Konvergenzbereich für diese Teilchengeometrie zu erweitern. In der Datenbank SCATDB am DLR sind bislang die Streueigenschaften von Rotationsellipsoiden enthalten. Diese Streudatenbank wird auf weitere Geometrien ausgedehnt und die dazugehörige Nutzeroberfläche weiter auszubauen.

Weiterführung: nein

Finanzierung: Auftrag (DLR)

****

Arbeitsgruppe Hochatmosphäre
Upper Atmosphere

Variabilität planetarer Wellen
Variability of planetary waves

Prof. Dr. Christoph Jacobi (jacobi @ rz.uni-leipzig.de), Prof. A.I. Pogoreltsev, S.S.. Derugina, Russian State Hydrometeorological University

Das Projekt umfasst experimentelle und numerische Studien atmosphärischer Wellenaktivität insbesondere in den Schichten oberhalb der Tropopause. Innerhalb des Projekts soll die Variabilität der Frühjahrsumstellung in der Stratosphäre im Detail untersucht werden, wobei Reanalysedaten und numerische Simulationen zum Einsatz kommen.

Weiterführung: ja

Finanzierung: DAAD, Leonard-Euler-Stipendienprogramm

****

AG Hochatmosphäre
Upper Atmosphere

Analyse atmosphärischer Zirkulationsmuster
Analysis of atmospheric circulation

Prof. Dr. Christoph Jacobi (jacobi @ rz.uni-leipzig.de), Prof. A.I. Pogoreltsev, V. Nikolaeva, M. Vasilenko, Russian State Hydrometeorological University

Innerhalb des Projekts wird die Variabilität der Atmosphäre der Nordhemisphäre anhand der Quasi-zweijährigen Schwingung im Detail untersucht werden, und Fernwirkungen dieses Zirkulationsmusters analysiert. In einem zweiten Teil wird die Variabilität der polaren Hochatmosphäre aufgrund extraterrestrischer Einflüssen experimentell und numerisch untersucht.

Weiterführung: nein

Finanzierung: DAAD, Leonard-Euler-Stipendienprogramm

****

AG Hochatmosphäre
Upper Atmosphere

Untersuchung der Mesosphäre/unteren Thermosphäre mit Meteorradar
Investigation of the mesosphere/lower thermosphere using meteor radar

Prof. Dr. Christoph Jacobi (jacobi @ rz.uni-leipzig.de), Prof. A. Oleynikov, V. Kukush, Kharkiv Technical University of Radioelectronics

Innerhalb des Projekts werden VHF-Funksignale kommerzieller Fernsehsender zur Analyse von Meteoren zur Ableitung der horizintalen Windgeschwindigkeit in der Mesosphäre und unteren Thermosphäre verwendet. Validierung dieser experimente erfolgt mit Radardaten der Universität Leipzig und Satellitendaten.

Weiterführung: ja

Finanzierung: DAAD,

****

AG Hochatmosphäre
Upper Atmosphere

Analyse von Gezeiten in der Mesosphäre/unteren Thermosphäre mit Meteorradar
Analysis of tides in the mesosphere/lower thermosphere using meteor radar

Prof. Dr. Christoph Jacobi (jacobi @ rz.uni-leipzig.de), Prof. A.I. Pogoreltsev, E. Suvorova Russian State Hydrometeorological University

Mit Hilfe des globalen Zirkulationsmodells MUAM und Reanalysedaten werden die Amplituden migrierender und nichtmigrierender Gezeiten in der Mesosphäre une Thermosphäre untersucht. Besonders berücksichtigt werden Zeiträume stratosphärischer Erwärmungen und der Frühjahrsumstellung

Weiterführung: nein

Finanzierung: Ministerium für Bildung und Forschung der Russischen Föderation

****

AG Akustik
Acoustics

Schallausbreitung in urbanen Gebieten unter Berücksichtigung des Atmosphärenzustandes
Sound propagation in urban areas considering the state of the atmosphere

Dipl. Met. Gabi Fischer (gfischer@uni-leipzig.de), Dr. Astrid Ziemann (ziemann@uni-leipzig.de), Prof. Dr. Manfred Wendisch (m.wendisch@uni-leipzig.de)

Aufgrund der dynamischen Entwicklung von Stadtregionen sind diese verdichteten Räume besonders anfällig gegenüber kurz- und langfristig wirkenden Risikofaktoren, wie z.B. Lärm, für die Gesundheit und Lebensqualität der Stadtbewohner. Vor allem der Straßenverkehrslärm stellt im urbanen Raum ein ungelöstes Umweltproblem mit Langzeitauswirkungen dar.
Zur verbesserten Abschätzung der Kopplung zwischen Atmosphärenstruktur und Schallausbreitung im urbanen Umfeld werden im verwendeten Schallstrahlenmodell neben den vertikalen meteorologischen Profilen auch die horizontal inhomogenen meteorologischen Strukturen integriert, um die Raum-Zeitskalen zu ermitteln, auf welchen der Atmosphäreneinfluss im städtischen Lärmmanagement zu berücksichtigen ist. Untersucht wird dabei die Schallausbreitung ab einigen 10 m Entfernung, da dort die Einflüsse meteorologischer Parameter, wie z.B. Lufttemperatur, Windvektor und Luftfeuchte, signifikant nachweisbar sind. Zur Validierung der Modellergebnisse sowie zur Abschätzung der Fehler und Grenzen des Modells sollen Messergebnisse aus dem urbanen Raum verwendet werden. Die Durchführung von Sensitivitätsstudien mit dem validierten Modell ermöglicht es, charakteristische Längenskalen für die Lärmbelastung abzuschätzen und Lärmindikatoren in Abhängigkeit von verschiedenen atmosphärischen Grenzschichtbedingungen zu bewerten.

Weiterführung: ja

Finanzierung: Wiedereinstiegsstipendium des Freistaates Sachsen

****

AG Akustik
Acoustics

Bestimmung des Energie- und Stoffaustauschs zwischen Bodenoberfläche und Pflanzenbestand, Umgebung und Atmosphäre durch mikrometeorologische Messverfahren der Anemometrie –Thermometrie, Teilprojekt: Akustische Strömungs- und Temperaturmessungen über einer Lysimeterfläche
Determination of the energy and matter exchange between the ground surface and vegetation canopy, environment and atmosphere using micro-meteorological measurement techniques of anemometry and thermometry, sub-project: Acoustic flow and temperature measurements over a lysimeter

Dr. Armin Raabe (raabe@uni-leipzig.de), Dr. Astrid Ziemann (ziemann@uni-leipzig.de), Dipl.-Inf. (FH) Falk Kaiser (fkaiser@rz.uni-leipzig.de),
Dr. Sascha Reth (sascha.reth@ugt-online.de), Dr. Christian Heerdt (christian.heerdt@ugt-online.de), Rick Friedrich (rick.friedrich@ugt-online.de), Umwelt-Gerätetechnik UGT GmbH Müncheberg,
Prof. Dr. Christian Bernhofer (christian.bernhofer@tu-dresden.de), Dipl.-Hydrol. Markus Hehn (markus.hehn@tu-dresden.de), Dipl.-Geogr. David Schaffrath (david.schaffrath@tu-dresden.de), TU Dresden, Professur für Meteorologie

Für die Quantifizierung des Energie- und Gasaustausches am oberen Rand eines Lysimeters existieren bislang keine allseits anerkannten Messmethoden. Derzeit wird die Lysimeteroberfläche mit Sensoren bestückt, die allerdings ihrerseits die Wechselwirkung zwischen Lysimeter und Luftströmung beeinflussen können.
Einen Beitrag zur Quantifizierung dieser Energie- und Stofftransporte können mikrometeorologische Messverfahren leisten, wenn es gelingt, die Sensoren nahe genug über einer Lysimeterfläche zu positionieren, ohne dass die Wechselwirkungsverhältnisse zwischen Lysimeter und Luftströmung gestört werden.
Deshalb wird hier ein über die Messfläche des Lysimeters aufgespanntes akustisches Temperatur- und Strömungsmessverfahren entwickelt, das in einem durch die akustischen Messstrecken begrenzten Volumen über dem Lysimeter die Wechselwirkung zwischen der Oberfläche und den Luftmassen über dem Lysimeter aufzeichnet. Unter Hinzunahme weiterer Sensoren (in erster Ausbaustufe CO2, H2O) soll es gelingen, den Energie- und Massenaustausch in diesem Volumen berührungslos zu sondieren. Dieses kontrolliert behandelte Volumen wird hier als "Akustische Kammer" bezeichnet.

Weiterführung: ja

Finanzierung: BMWi, Zentrales Innvovationsprogramm Mittelstand (ZIM), Förderkennzeichen KF2709801BN0
****

AG Akustik
Acoustics

Wetterabhängige Schallausbreitung, Lärmschutz an Schießplätzen der Bundeswehr

Weather permitting *sound propagation, noise protection at artillery range of the Bundeswehr*

Dr. Armin Raabe (raabe@uni-leipzig.de),
Jun.-Prof. Dr. Astrid Ziemann (ziemann@uni-leipzig.de
Dipl. Met. Michael Wilsdorf (mwils@uni-leipzig.de)

Dieses Projekt setzt die langjährige und erfolgreiche Zusammenarbeit des Institutes für Meteorologie der Universität Leipzig mit der Bundeswehr, hier im speziellen mit dem AGeoBw, fort. Anlass waren Artillerieschießen, bei denen die akustische Belastung in der Nachbarschaft von TrÜb-Plätzen derart erhöht war, dass es zu Beschwerden / Klagen von Bürgern und der Kommunen kam. Ein verstärkender Faktor war in den betreffenden Fällen u.a. die Wettersituation, bei der eine ausgeprägte Temperaturinversion zu einer anomalen Schallausbreitung führte.
Ziel dieser Studie ist deshalb die weitere Verbesserung der bestehenden Schallimmissionsprognose, sowohl in konzeptioneller Hinsicht, als auch in ihrer Praktikabilität sowie in der statistischen Absicherung der zu Grunde liegenden Auswertungen.
Datengrundlagen der schallklimatologischen Untersuchungen sind Radiosondenaufstiege des Deutschen Wetterdienstes und der Bundeswehr, die im Zeitraum 2001 bis mindestens 2007 an 14 Stationen im Bundesgebiet jeweils zu den Terminen 00 UTC und 12 UTC durchgeführt wurden. Damit erweitern diese Daten den untersuchten Datenumfang einschließlich der Vorgängerstudie (von 1990 bis 2000) auf 18 Jahre.

Weiterführung: ja

Finanzierung: AGeoBw; M/UR1M/7A180/7A524

****

2. Wiss. Veröffentlichungen Institut für Meteorologie 2010

Autoren	Titel
Lampert, A., C. Ritter, A. Hoffmann, J.–F. Gayet, G. Mioche, A. Ehrlich, A. Dörnbrack, M. Wendisch, and M. Shiobaro	Lidar characterization of the Arctic atmosphere during ASTAR 2007: four cases studies of boundary layer, mixed-phase and multi-layer clouds, Atmos. Chem. Phys. 10, 2010, 2847-2866
Bierwirth, E., M. Wendisch, E. Jäkel, A. Ehrlich, K. S. Schmidt, H. Stark, P. Pilewskie, M. Esselborn, G. P. Gobbi, R. Ferrare, T. Müller, and A. Clarke	A new method to retrieve the aerosol layer absorption coefficient from airborne flux density and actinic radiation measurements, J. Geophys. Res. 115, 2010, D14211, doi:10.1029/2009JD013636.
I. Tegen, E. Bierwirth, B. Heinold, J. Helmert, and M. Wendisch	The Effect of Measured Surface Albedo on Modeled Saharan Dust Solar Radiative Forcing, J. Geophys. Res. 115, 2010, D24312, doi:10.1029/2009JD013764.
Schmale, J., J. Schneider, T. Jurkat, C. Voigt, H. Eichler, M. Rautenhaus, M. Lichtenstern, H. Schlager, G. Ancellet, F. Arnold, M. Gerding, I. Mattis, M. Wendisch, and S. Borrmann	Aerosol layers from the 2008 eruptions of Mount Okmok and Mount Kasatochi: In situ upper troposphere and lower stratosphere measurements of sulfate and organics over Europe. *J. Geophys. Res.* 115, 2010, D00L07, doi:10.1029/2009JD013628.
Voigt, C., Schumann, U., Jurkat, T., Schäuble, D., Schlager, H., Petzold, A., Gayet, J.-F., Krämer, M., Schneider, J., Borrmann, S., Schmale, J., Jessberger, P., Hamburger, T., Lichtenstern, M., Scheibe, M., Gourbeyre, C., Meyer, J., Kübbeler, M., Frey, W., Kalesse, H., Butler, T., Lawrence, M. G., Holzäpfel, F., Arnold, F., Wendisch, M., Döpelheuer, A., Gottschaldt, K., Baumann, R., Zöger, M., Sölch, I., Rautenhaus, M., and Dörnbrack, A.	In-situ observations of young contrails - overview and selected results from the CONCERT campaign, Atmos. Chem. Phys. 10, 2010, 9039-9056.
Henrich F., H. Siebert, E. Jäkel, R. A. Shaw, M. Wendisch	Collocated Measurements of Boundary-Layer Cloud Microphysical and Radiative Properties - A Feasibility Study, J. Geophys. Res. 115, 2010, D24214, doi:10.1029/2010JD013930.
Schmidt, K. S., P. Pilewskie, B. Mayer, M. Wendisch, B. Kindel, S. Platnick, M. D. King, G. Wind, G. T. Arnold, L. Tian, G. Heymsfield, and H. Eichler	Apparent absorption of solar spectral irradiance in heterogeneous ice clouds, J. Geophys. Res. 115, 2010, D00J22, doi:10.1029/2009JD013124.
Schmidt, K. S., P. Pilewskie, R. Bergstrom, O. Coddington, J. Redemann, J. Livingston, P. Russell, E. Bierwirth, M. Wendisch, W. Gore, M. K. Dubey, and C. Mazzoleni	A new method for deriving aerosol solar radiative forcing and its first application within MILAGRO/INTEX-B. *Atmos. Chem. Phys.* 10, 2010, 7829–7843, doi:10.5194/acp-10-7829-2010
Ehrlich, A., Bierwirth, E., Wendisch, M.	Airborne remote sensing of Arctic boundary-layer mixed-phase clouds, Wiss. Mitt. Inst. f. Meteorol. Uni. Leipzig, Bd. 47, 2010, 173 S.
Fricke, C., Ehrlich, A.	Impact of aerosol particles on measured and simulated polarized solar radiation, Wiss. Mitt. Inst. f. Meteorol. Uni. Leipzig, Bd. 47, 2010, 173 S.
Walter,J., Brückner, M.	Comparison of a Backscatter LIDAR during LICL 2009, Wiss. Mitt. Inst. f. Meteorol. Uni. Leipzig, Bd. 47, 2010, 173 S.
Stober, G., Singer, W., Jacobi, Ch.	Evaluation of absolute radar calibration using cosmic noise (QDC) and simulated signals. Proceedings of the 12th International Workshop on Technical and Scientific Aspects of MST Radar (MST12), 2010, 77-80.
Placke, M., Jacobi, Ch., Hoffmann, P., Singer, W., Becker, E., Rapp, M., Stober, G.	Gravity wave momentum fluxes in the mesosphere/ lower thermosphere at high- and mid- latitudes. Proceedings of the 12th International Workshop on Technical and Scientific Aspects of MST Radar (MST12), 2010, 281-284.
Borries, C., Jakowski, N., Jacobi, Ch.	Observation of Large Scale Waves in the Thermosphere-ionosphere System. WPP-303 Proceedings for ESA's 2nd SWARM International Science Meeting, 2010.
Hoffmann, P., Jacobi, Ch.	Connection of planetary waves in the stratosphere and ionosphere by the modulation of gravity waves. Wiss. Mitt. Inst. f. Meteorol. Uni. Leipzig, 47, 2010, 23-36.

Liu, R.Q., Jacobi, Ch..	Piecewise linear trend detection in mesosphere/lower thermosphere wind time series. Wiss. Mitt. Inst. f. Meteorol. Uni. Leipzig, 47, 2010, 37-50.
Unglaub, C., Jacobi, Ch., Schmidtke, G., Nikutowski, B., Brunner, R.	EUV-TEC - an index to describe ionospheric variability using satellite-borne solar EUV measurements: first results. Wiss. Mitt. Inst. f. Meteorol. Uni. Leipzig, 47, 2010, 51-60.
Arras, C., Wickert, J., Heise, S., Schmidt, T., Jacobi, Ch.	Global sporadic E signatures revealed from multi-satellite radio occultation measurements. Adv. Radio Sci., 8, 2010, 225-230.
Jacobi, Ch. Merzlyakov, E.G., Liu, R.Q., Solovjova, T.V., Portnyagin, Y.I.	Structural changes in lower ionosphere wind trends at midlatitudes. Adv. Radio Sci., 8, 2010, 231-236.
Stober, G., Jacobi, Ch., Keuer, D.	Distortion of meteor count rates due to cosmic radio noise and atmospheric particularities. Adv. Radio Sci., 8, 2010, 237-241.
Lieberman, R.S., Ortland, D.A., Riggin, D.M., Wu, Q., Jacobi, C.	Momentum budget of the migrating diurnal tide in the mesosphere and lower thermosphere. J. Geophys. Res., 115, 2010, D20105, doi:10.1029/2009JD013684.
Liu, R.Q., Jacobi, Ch., Hoffmann, P., Stober, G., Merzlyakov, E.G.	A piecewise linear model for detecting climatic trends and their structural changes with application to mesosphere/lower thermosphere winds over Collm, Germany. J. Geophys. Res., 115, 2010, D22105, doi:10.1029/2010JD014080.
Raddatz, M., Schönfeldt. H.-J.	Ejection and impact angles of saltating particles measured with a high-speed camera. Wiss. Mitt. Inst. f. Meteorol. Uni. Leipzig, Bd. 47, 2010, 133-142
Schönfeldt, H.-J.	Reinforcement of edge waves by beach cusps. Wiss. Mitt. Inst. f. Meteorol. Uni. Leipzig, Bd. 47, 2010, 143-152
Brecht, B., Raabe, A., Ziemann, A.	Acoustic Anemometrie and Thermometrie. Wiss. Mitt. Inst. für Meteorol. Univ. Leipzig, Bd. 47, 2010, 101-110
Friedrich, A., Ziemann, A., Schlink, U.	Measurement and modelling of the cumulated thermal stress in Leipzig. Wiss. Mitt. Inst. für Meteorol. Univ. Leipzig, Bd. 47, 2010, 75-86
Louca, K., Stadler, A., Raabe, A., Ziemann, A.	Comparison of wind flow measurements between the Mini-SODAR PA0, a 99 m tower and a Doppler-SODAR. Wiss. Mitt. Inst. für Meteorol. Univ. Leipzig, Bd. 47, 2010, 111-122
Rösch, C., Ziemann, A., Schlink, U.	Hydrocarbons in indoor air and their health-effects. Wiss. Mitt. Inst. für Meteorol. Univ. Leipzig, Bd. 47, 2010, 61-74
Rost, F., Ziemann, A., Raabe, A.	Investigation and simulation of the influence of turbulence on the sound propagation in the atmosphere. Wiss. Mitt. Inst. für Meteorol. Univ. Leipzig, Bd. 47, 2010, 87-100
Wilsdorf, M., Ziemann, A., Belitz, H.-J., Raabe, A.	Ein Bewertungsverfahren für Schallimmissionsprognosen unter Berücksichtigung der Meteorologie. Lärmbekämpfung 5, 2010,188-195
Bender, M.; Dick, G.; Ge, M.; Deng, Z.; Wickert, J.; Kahle, H.-G.; Raabe, A.; Tetzlaff, G.	Development of a GNSS water vapour tomography system using algebraic reconstruction techniques. Advances in Space Research. doi: 10.1016/j.asr.2010.05.034
Bender, M., Stosius, R., Zus, F., Dick, G., Wickert, J., Raabe, A.	GNSS water vapour tomography – expected improvements by combining GPS, GLONASS and Galileo observations. Adv. Space Res. 2010, Doi: 10.1016/j.asr.2010.09.011
Otto, S., Meringer, M.,	Positively homogeneous functions in atmospheric radiative transfer theory, J. Math. Anal. and Applications, 376,2010 588-601
Otto S., Trautmann T., Wendisch M.	On realistic shape and size equivalence of spheroidal Saharan mineral dust particles applied in solar and thermal radiative transfer calculations, Atmos. Chem. Physics. Discuss., 10
Borries, C. & Hoffmann, P.	Characteristics of F2-layer planetary wave-type oscillations in northern middle and high latitudes during 2002 to 2008 J. Geophys. Res., 2010, 115, A00G10

Wiss. Mitarbeiter am Institut für Meteorologie, 2010

Barth	Manuela	mbarth@rz.uni-leipzig.de
Bauer	Stefan	s.bauer@uni-leipzig.de
Bender	Michael	bender@gfz-potsdam.de
Bierwirth	Eike	eike.bierwirth@uni-leipzig.de
Brecht	Benedict	brecht@rz.uni-leipzig.de
Ehrlich	André	a.ehrlich@uni-leipzig.de
Feck-Yao	Wolfgang	feckyao@uni-leipzig.de
Fischer	Gabi	gfischer@rz.uni-leipzig.de
Fricke	Clemens	fricke@uni-leipzig.de
Hirsch	Kerstin	khirsch@uni-leipzig.de
Hoffmann	Peter	phoffma@rz.uni-leipzig.de
Jacobi	Christoph	jacobi@rz.uni-leipzig.de
Kaiser	Falk	fkaiser@rz.uni-leipzig.de
Mey	Britta	b.mey@uni-leipzig.de
Nikutowski	Bernd	bernd.nikutowski@ipm.fraunhofer.de
Otto	Sebastian	sebastian.otto@uni-leipzig.de
Pospichal	Bernhard	bernhard.pospichal@uni-leipzig.de
Raabe	Armin	raabe@uni-leipzig.de
Rehnert	Jutta	rehnert@uni-leipzig.de
Rosenow	Dagmar	d.rosenow@uni-leipzig.de
Schönfeldt	Hans-Jürgen	schoenfeldt@uni-leipzig.de
Staake	Karin	staake@uni-leipzig.de
Walter	Jörg	jwalter@uni-leipzig.de
Weiße	Frank	weisse@uni-leipzig.de
Wendisch	Manfred	m.wendisch@uni-leipzig.de
Werner	Frank	f.henrich@uni-leipzig.de
Wilsdorf	Michael	mwils@uni-leipzig.de

Immatrikulationen am Institut f. Meteorologie

Immatrikulationen Meteorologiestudenten					BSC								
					MSC								
Datum	Semester	1.FS	2. FS	3.FS	4.FS	5.FS	6. FS	7.FS	8.FS	9. FS	10.FS	>10.FS	Summe
15.10.2010	WS 10/11	64		34		20		20		9		5	152
15.04.2010	SS 10		32		21		20		9		14		96
15.10.2009	WS 09/10	67	0	21	0	20	0	11	0	14		7	140
15.04.2009	SS 09	0	71	0	28	0	12	0	14	0	23		148
15.10.2008	WS 08/09	71	0	28	0	12	0	14	0	23	1	25	174
15.04.2008	SS 08	0	54	0	14	0	19	0	25	1	18	13	144
15.10.2007	WS 07/08	98	0	15	0	22	0	26	1	18	2	19	201
15.04.2007	SS 07	0	23	0	32	0	35	1	19	2	13	12	137
13.12.2006	WS 06/07	31	0	40	0	36	0	24	2	14	1	17	175
15.04.2006	SS 06	0	82	0	46	0	29	3	14	1	17	7	200
15.10.2005	WS 05/06	109	0	49	0	30	2	16	1	17	1	13	237
07.06.2005	SS 2005	0	83	0	33	1	19	0	17	1	12	8	177
08.12.2004	WS 04/05	97	0	35	1	20	0	19	0	12	1	15	200
07.06.2004	SS 04	0	57	0	24	0	18	1	13	0	11	10	134
03.12.2003	WS 03/04	68	1	25	0	20	1	13	1	12	1	13	155
26.05.2003	SS 03	0	42	0	19	0	15	0	14	1	12	6	109
14.10.2002	WS 02/03	45	0	19	0	16	0	15	1	12	1	9	118
29.05.2002	SS 02	0	38	0	20	0	17	1	13	2	7	4	102
06.12.2001	WS 01/02	43	0	21	0	16	0	13	0	7	0	5	105
31.05.2001	SS 01	0	31	1	22	0	19	0	8	0	5	3	89
07.12.2000	WS 00/01	41	1	27	0	22	0	8	0	6	1	6	112
05.05.2000	SS 00	0	34	0	24	0	8	0	8	1	6	3	84
01.12.1999	WS 99/00	40	0	24	0	9	0	9	0	6	1	6	95
31.05.1999	WS 99	0	29	0	11	0	13	0	8	1	5	3	70
16.12.1998	WS 98/99	36	0	11	0	17	1	9	1	5	0	8	88
22.04.1998	SS 98	1	21	0	17	0	8	1	6	0	7	2	63
10.11.1997	WS 97/98	29	0	17	0	10	1	8	0	7	0	4	76

Abschlussarbeiten Institut für Meteorologie 2010

Promotionen

Jens Voigtländer
Hygroscopic growth and CCN activation of slightly soluble organic and inorganic compounds - Evaluation of experimental LACIS data with FLUENT/FPM

Christina Arras
A Global Survey of Sporadic E Layers based on GPS Radio Occultations by CHAMP, GRACE and FORMOSAT-3/COSMIC

Diplom-Abschlüsse 2010

Name / Vorname	DA-Thema
Friedrich, Anett	Messung und Modellierung der kumulierten thermischen Belastung in Leipzig
Lonitz, Katrin	Comparison of MISR and Meteosat-9 Cloud Motion Winds
Groß, Peter	Global Distribution of Submicrometer Aerosol Particles: Comparison between In Situ Measurements and Global Model Outputs
Kinder, Friederike	Hygroscopic properties of atmospheric earosol particles in central Europe
Raddatz, Michael	Messungen von Impaktwinkeln und Auslösewinkeln von Sandkörnern mittels Hochgeschwindigkeitskamera
Rösch, Carolin	Indoor air and health effects
Rost, Florian	Untersuchung und Simulation des Einflusses von Turbulenz auf die Schallausbreitung in der Atmosphäre
Schöne, Luisa	Laboruntersuchungen zur möglichen SOA-Bildung infolge der troposphärischen Isoprenoxidation
Göbel, Tina	Hygroskopizität anthropogener Aerosole bei hohen Feuchten in der nordchinesischen Tiefebene
Schmeißner, Tina	Tropical free tropospheric aerosol microphysical properties measured at a high altitude research station in the Venezuelan Andes
Smalla, Alexander	Hoch aufgelöste Chemietransprot-Modellierung für den Großraum Dresden mit dem WRF/Chem-Modell
Unglaub, Claudia	EUV-TEC: Ein Index zur Beschreibung der ionosphärischen Variabilität
Louca, Kyriakos Yiannakis	Untersuchung der Eigenschaften von Windprofilen in der atmosphärischen Grenzschicht mit verschiedenen Messmethoden am Standort Lindenberg
Schlimper, Susan	Meteorologische und statistische Auswertung von Langzeitmessungen zur Charakterisierung des Aerosols an der Forschungstation Melpitz

Opelt, Claudia	Räumliche Variabilität atmosphärischer Partikelgrößenverteilung im städtischen Ballungsraum Dresden
Stadler, Andreas	Vergleich von Windmessungen mit einem SODAR und anderen Messmethoden am Standort Lindenberg
Stoll, Jens	Kopplung des des Wettermodell WRF (ARW) mit dem Chemietransportmodell MUSCAT: Vergleich mit weiteren meteorologischen Antrieben
Brückner, Marlen	Depolarissationsmessungen in Cirren mit einem konventionellen Rückstreulidar
Brecht, Benedict	Akustische Anemometrie und Thermometrie
Geimecke, Christina	Regionale Modellierung direkter und indirekter Effekte des Saharastaubs über Europa
Fricke, Clemens	Messung und Simulation polarisierter Strahldichten: Einfluss des solaren Zenitwinkels und der Aerosol optischen Dicke
Seelig, Torsten	Vergleich barokliner Moden in Modell und Experiment
Kamilli, Katharina	Hygroscopische Eigenschaften des urbanen Aerosols einer europäischen "Megacity"
Thiem, Elisabeth	Physikalische Eigenschaften des atmosphärischen Aerosols am Polarmeer in Nordalaska
Barthel, Stefan	Modellierung des Lebenszyklus und der Chemie von Seesalzaerosolen in der maritimen Grenzschicht

BSC-Abschlüsse 2010

Name / Vorname	**Thema**
Assmann, Denise	Einfluss von Saharastaub und Biomasseaerosol auf den terrestrischen Strahlungshaushalt der Atmosphäre
Bauditz, Michael	Messungen der Polarisierten Himmels-strahlung mit einem Sonnenphotometer
Becher, Manuela	Klimatologie und Herkunft klimarelevanter Aerosolpartikel über der südafrikanischen Hochebene
Dietzsch, Felix	Charakterisierung der synoptischen Situation während der Messkampagne SORPIC (April/Mai 2010)
Engelmann, Florian	Klimaveränderungen in Thüringen – Mögliche Auswirkungen auf phänologische Phasen wildwachsender Pflanzen
Foth, Andreas	Stadtklima und Luftschadstoffe in Leipzig
Fritsche, Sebastian	Statistische Untersuchungen zu Frontendurchgängen an einer festen Station
Fytterer, Tilo	Klimatologie der 8-stündigen Gezeiten über Collm
Hoff, Michael	Bestimmung des Wolkenbedeckungsgrades mit einer Wolkenkamera

Junghänel, Thomas	Vergleich verschiedener Wasserhaushaltsmodelle mit gemessenen Parametern an Bodendauerbeobachtungsflächen in Sachsen
Lange, Stefan	Windlastberechnungen auf der Basis eines Mikroskala-Windfeldes
Lehmann, Constanze	Klimaveränderungen in Sachsen – Mögliche Auswirkungen auf phänologische Phasen wildwachsender Pflanzen
Leistert, Michael	Analyse der terrestrischen Strahlungsflussdichten aus Pyrgeometermessungen im chinesischen Ballungsgebiet Guangzhou
Pfitzenmaier, Lukas	Einfluss der atmosphärischen Grenzschicht und Luftmassenherkunft auf die Konzentration atmosphärischen Aerosolpartikel an einer Hochgebirgsstatiobn am Beispiel Beo-Moussala, Bulgarien.
Schneider, Richard	Bestimmung der Menge und der Größenverteilung von rollenden Sandkörnern im Saltationsprozess anhand von Videoaufzeichnungen
Tomsche, Laura	Raumzeitliche Verteilung ultrafeiner Aerosolpartikel in der städtischen Rauhigkeitsschicht von Dresden
Weber, Cathleen	Regionale Verteilung von Gewittern im Gebiet von Leipzig auf der Basis von Blitz-registrierungen
Wiesner, Anne	Analyse optischer Eigenschaften von urbanem Aerosol während der Feldmessung MEGAPOLI
Wolf, Veronika	Experimentelle Methoden zur Bestimmung der Schubspannung
Zenker, Katrin	Analyse feuchter Partikelgrößenverteilungen im urbanen Aerosol

Wissenschaftliche Mitteilungen aus dem Institut für Meteorologie der Universität Leipzig

Band 1 *A. Raabe, G. Tetzlaff* und *W. Metz* (Edn.), 1995: Meteorologische Arbeiten aus Leipzig I

Band 2 *R. Devantier*, 1995: Wolkenbildungsprozesse über der südwestlichen Ostsee - Anwendungen eines neuen Wolkenschemas in einem mesoskaligen Modell

Band 3 *J. Laubach*, 1996: Charakterisierung des turbulenten Austausches von Wärme, Wasserdampf und Kohlendioxid über niedriger Vegetation anhand von Eddy-Korrelations-Messungen

Band 4 *A. Raabe* und *J. Heintzenberg* (Edn.), 1996: Meteorologische Arbeiten aus Leipzig II

Band 5 Wind- und Seegangsatlas für das Gebiet um Darß und Zingst
D. Hinneburg, A. Raabe und *G. Tetzlaff*, 1997: Teil I: Windatlas

Band 6 *W. von Hoyningen-Huene* und *G. Tetzlaff* (Edn.), 1997: Sediment and Aerosol
Teil I: Beiträge zur Alfred-Wegener-Konferenz, Leipzig 1997
Teil II: Aktuelle Beiträge aus dem Institut für Meteorologie

Band 7 *B.-R. Beckmann*, 1997: Veränderungen in der Windklimatologie und in der Häufigkeit von Sturmhochwassern an der Ostseeküste Mecklenburg-Vorpommerns

Band 8 *P. Posse*, 1997: Bestimmung klimarelevanter Parameter des maritimen Aerosols unter besonderer Berücksichtigung der Nichtkugelform realer Aerosolteilchen

Band 9 *A. Raabe, K. Arnold* und *J. Heintzenberg* (Edn.),1998: Meteorologische Arbeiten aus Leipzig III

Band 10 Wind- und Seegangsatlas für das Gebiet um Darß und Zingst, Teil II, 1998:
D. Hinneburg, A. Raabe und *G. Tetzlaff*: Vergleich Windatlas –Beobachtungsdaten; *M. Börngen, H.-J. Schönfeldt, F. Riechmann, G. Panin* und *G. Tetzlaff:* Seegangsatlas; *M. Stephan* und *H.-J. Schönfeldt*: Sedimenttransportatlas

Band 11 ***J. Rissmann, 1998:*** Der Einfluss langwelliger Strahlungsprozesse auf das bodennahe Temperaturprofil

Band 12 *A. Raabe, K. Arnold* und *J. Heintzenberg* (Edn.), 1999*:*Meteorologische Arbeiten aus Leipzig IV

Band 13 *U. Müller, W. Kuttler* und *G. Tetzlaff* (Edn.), 1999: Workshop Stadtklima 17. / 18. 02. 1999 in Leipzig

Band 14 *R. Surkow*, 1999: Optimierung der Leistungsverfügbarkeit von Windenergie durch ihre Integration in Wind-Biogas-Hybridanlagen

Band 15 *N. Mölders*, 1999: Einfache und akkumulierte Landnutzungsänderungen und ihre Auswirkungen auf Evapotranspiration, Wolken- und Niederschlagsbildung

Band 16 *G. Tetzlaff* und *U. Grünewald* (Edn.), 1999:
2. Tagung des Fachausschusses Hydrometeorologie 15./16. 11. 1999 in Leipzig

Band 17 *A. Raabe* und *K. Arnold* (Edn.), 2000: Meteorologische Arbeiten aus Leipzig V

Band 18 *K. Arnold*, 2000: Ein experimentelles Verfahren zur Akustischen Tomographie im Bereich der atmosphärischen Grenzschicht

Band 19 *A. Ziemann*, 2000: Eine theoretische Studie zur akustischen Tomographie in der atmosphärischen Grenzschicht

Band 20 *Ch. Jacobi*, 2000: Midlatitude mesopause region dynamics and its coupling with lower and middle atmospheric processes

Band 21 *M. Klingspohn*, 2000: Interdekadische Klimavariabilität über dem Nordatlantik – Statistische Analysen und Modellstudien –

Band 22 *A. Raabe* und *K. Arnold* (Edn.), 2001: Meteorologische Arbeiten aus Leipzig VI

Band 23 *K. Arnold, A. Ziemann, G. Tetzlaff, V. Mellert* und *A. Raabe* (Edn.), 2001: International Workshop Tomography and Acoustics: Recent developments and methods 06. - 07.03.2001 in Leipzig

Band 24 *O. Fanenbruck*, 2001: Ein thermophysiologisches Bewertungsmodell mit Anwendung auf das Leipziger Stadtgebiet

Band 25 *M. Lange*, 2001: Modellstudien zum CO_2-Anstieg und O_3-Abbau in der mittleren Atmosphäre und Einfluß des Polarwirbels auf die zonale Symmetrie des Windfeldes in der Mesopausenregion

Band 26 *A. Raabe* und *K. Arnold* (Edn.), 2002: Meteorologische Arbeiten aus Leipzig VII

Band 27 *M. Simmel*, 2002: Ein Modul zur spektralen Beschreibung von Wolken und Niederschlag in einem Mesoskalenmodell zur Verwendung auf Parallelrechnern

Band 28 *H. Siebert*, 2002: Tethered-Balloon Borne Turbulence Measurements in the Cloudy Boundary Layer

Sonderband *G. Tetzlaff* (Hrsg.), 2002:- Atmosphäre - Aktuelle Beiträge zu Luft, Ozon, Sturm, Starkregen und Klima

Band 29 *U. Harlander*, 2003: On Rossby wave propagation in atmosphere and ocean

Band 30 *A. Raabe* und *K. Arnold* (Edn.), 2003: Meteorologische Arbeiten aus Leipzig VIII

Band 31 *M. Wendisch*, 2003: Absorption of Solar Radiation in the Cloudless and Cloudy Atmosphere

Band 32 *U. Schlink*, 2003: Longitudinal Models in Biometeorology: Effect Assessment and Forecasting of Ground-level Ozone

Band 33 *H. Heinrich*, 2004: Finite barotrope Instabilität unter synoptischem Antrieb

Band 34 *A. Raabe* und *K. Arnold* (Edn.), 2004: Meteorologische Arbeiten aus Leipzig IX

Band 35 *C. Stolle*, 2004: Three-dimensional imaging of ionospheric electron density fields using GPS observations at the ground and onboard the CHAMP satellite

Band 36 *A. Raabe* und *K. Arnold* (Edn.), 2005: Meteorologische Arbeiten (X) und Jahresbericht 2004 des Institutes für Meteorologie der Universität Leipzig

Band 37 *A. Raabe* und *K. Arnold* (Edn.), 2006: Meteorologische Arbeiten (XI) und Jahresbericht 2005 des Institutes für Meteorologie der Universität Leipzig

Band 38 *K. Fröhlich,* 2006: The Quasi Two-Day Wave – its impact on zonal mean circulation and wave-wave interactions in the middle atmosphere

Band 39 *K. Radtke*, 2006: Zur Sensitivität von Starkwindfeldern gegenüber verschiedenen meteorologischen Parametern im Mesoskalenmodell LM

Band 40 *K. Hungershöfer*, 2007: Optical Properties of Aerosol Particles and Radiative Transfer in Connection with Biomass Burning

Band 41 *A. Raabe* (Hrsg.), 2007: Meteorologische Arbeiten (XII) und Jahresbericht 2006 des Institutes für Meteorologie der Universität Leipzig

Band 42 *A. Raabe* (Hrsg.), 2008: Meteorologische Arbeiten (XIII) und Jahresbericht 2007 des Institutes für Meteorologie der Universität Leipzig

Band 43 *A. Kniffka , 2008*: Einfluss der Inhomogenitäten von Aerosol, Bodenalbedo und Wolken auf das aktinische Strahlungsfeld der Atmosphäre

Band 44 *M. Barth, 2009*: Akustische Tomographie zur zeitgleichen Erfassung von Temperatur- und Strömungsfeldern

Band 45 *A. Raabe* (Hrsg.), 2009: Meteorologische Arbeiten (XIV) und Jahresbericht 2008 des Institutes für Meteorologie der Universität Leipzig

Band 46 *G. Stober, 2009:* Astrophysical Studies on Meteors using a SKiYMET All-Sky Meteor Radar

Band 47 *A. Raabe* (Hrsg.), 2010: Meteorologische Arbeiten (XV) und Jahresbericht 2009 des Institutes für Meteorologie der Universität Leipzig

Band 48 *A. Raabe* (Hrsg.), 2011: Meteorologische Arbeiten (XVI) und Jahresbericht 2010 des Institutes für Meteorologie der Universität Leipzig